Search for Vector Boson Scattering in semi-leptonic final states, with the ATLAS detector and the Run-2 Dataset. Contribution to the Inner Tracker Upgrade in view of the High-Luminosity LHC

Anastasia Kotsokechagia

université PARIS-SACLAY

Search for Vector Boson Scattering in semi-leptonic final states with the ATLAS detector. Contribution to the Inner Tracker Upgrade in view of the High-Luminosity LHC

Recherche de la diffusion de bosons vecteurs dans l'état final sémi-leptonique avec le détecteur ATLAS. Contribution à la construction du Détecteur Interne pour la phase à haute luminosité du LHC

Thèse de doctorat de l'université Paris-Saclay

École doctorale n° 576 Particules, Hadrons, Energie et noyau : instrumentation, imagerie, cosmos et simulation (PHENIICS)
Spécialité de doctorat : Physique des Particules
Graduate School : Physique, Référent : Faculté des sciences d'Orsay

Thèse préparée dans les unités de recherche **IJCLab** (Université Paris-Saclay, CNRS) et **CERN**, sous la direction de **Lydia FAYARD**, Directrice de recherche, et le co-encadrement de **Dimitris VAROUCHAS**, Chargé de recherche

Thèse soutenue à Paris-Saclay, le 17 Mars 2022, par

Anastasia KOTSOKECHAGIA

Composition du jury

Marie-Hélène SCHUNE Directrice de recherche, IJCLab	Présidente
Susanne KUEHN Chercheure eq. HDR, CERN	Rapporteure & Examinatrice
Claude CHARLOT Directeur de recherche, LLR	Rapporteur & Examinateur
Kevin EINSWEILER Professeur, LBNL	Examinateur
Steven SCHRAMM Assistant Professeur, University of Geneva	Examinateur
Lydia FAYARD Directrice de recherche, IJCLab	Directrice de thèse

THESE DE DOCTORAT
NNT : 2022UPASP029

université PARIS-SACLAY

ÉCOLE DOCTORALE
Particules, hadrons, énergie et noyau : instrumentation, imagerie, cosmos et simulation (PHENIICS)

Titre : Recherche de la diffusion de bosons vecteurs dans l'état final sémi-leptonique avec le détecteur ATLAS. Contribution à la construction du Détecteur Interne pour la phase à haute luminosité du LHC
Mots clés : Analyse de données, LHC, Modèle standard, Construction, Trajectographe interne, ATLAS

Résumé :

Dans cette thèse, la mesure de la diffusion de bosons vecteurs (VBS) dans le canal semi-leptonique est étudiée. Dans ce canal, l'un des deux bosons se désintègre leptoniquement tandis que le second se désintègre de manière hadronique en une paire de quarks. En raison de la section efficace de production très faible, le VBS est un canal très difficile à mesurer. Ce qui distingue ce processus des autres processus du LHC, ce sont les deux jets vers l'avant qui accompagnent la diffusion des bosons. Au cours de ma thèse, j'ai travaillé dans de nombreux aspects de l'analyse tels que : la modélisation du bruit de fond, le discriminant MVA, les incertitudes systématiques prises en compte dans la mesure ainsi que l'analyse statistique des résultats.

La performance du jet vers l'avant est d'une importance primordiale dans cette analyse. Par conséquent, le travail de thèse commence par une étude détaillée de l'optimisation de la reconstruction du jet, en particulier le développement d'un algorithme pour atténuer les jets d'empilement dans la région d'avant ; dans ATLAS, afin d'utiliser des données physiques valides, dans toute analyse, le processus physique (à savoir le processus de diffusion dure) doit être distingué des processus de collision secondaires (à savoir les interactions d'empilement). Ceci est principalement réalisé par l'utilisation d'informations du trajectographe interne. Pour la partie avant du détecteur ATLAS, dépourvue de cette information, cette distinction est donc très difficile. Un autre moyen de marquage dans la région avant, basé sur la conservation de l'impulsion entre l'activité avant et l'activité se produisant dans la couverture du trajectographe, est utilisé dans cet algorithme. L'algorithme a été optimisé et diverses méthodes ont été testées.

Le trajectographe interne d'ATLAS actuel est compatible avec la luminosité de conception du LHC de 10^{34} cm^{-2} s^{-1}. L'augmentation prévue de la luminosité vers la phase LHC à haute luminosité (HL) nécessite une refonte fondamentale du détecteur interne complet en raison à la fois de l'augmentation des dommages causés par le rayonnement et de l'occupation substantielle des sous-détecteurs. Pour le HL-LHC, le détecteur interne actuel d'ATLAS sera remplacé par un Inner Tracker (ITk) tout silicium. La conception du détecteur de pixels ITk présente une zone active et une granularité beaucoup plus élevées par rapport au détecteur de pixels actuel. Deux technologies de détecteurs différents à base de silicium sont considérées ; capteurs à pixels planaires et capteurs à pixels 3D. Les capteurs sont équipés d'une nouvelle puce de lecture, capable de répondre à toutes les exigences requises pour le LHC à haute luminosité. Une version prototype de la puce de lecture, appelée RD53A, a été conçue par la collaboration RD53. Dans la troisième partie de cet te thèse, une caractérisation de la puce de lecture RD53A est effectuée.

Le nombre beaucoup plus important de modules et la granularité beaucoup plus fine utilisée par ITk, se traduit par une augmentation significative de la densité de puissance dans le détecteur. Pour cette raison, un schéma d'alimentation en série a été choisi. Dans ce schéma, les puces de lecture des modules de pixels sont alimentées en série par un courant constant ; tandis que les capteurs de plusieurs modules seront connectés à une ligne d'alimentation commune pour la tension d'épuisement. Cette architecture se traduit par une polarisation directe efficace sur certains capteurs dans certaines conditions de fonctionnement. Bien que la polarisation directe soit faible, elle peut toujours conduire à des courants non négligeables entre la face arrière du capteur et la puce de lecture, en particulier pour les capteurs irradiés avec des courants de saturation importants. Par conséquent, le comportement d'une telle chaîne d'alimentation en série est également étudié.

université PARIS-SACLAY

ÉCOLE DOCTORALE
Particules, hadrons, énergie et noyau : instrumentation, imagerie, cosmos et simulation (PHENIICS)

Title : Search for Vector Boson Scattering in semi-leptonic final states, with the ATLAS detector. Contribution to the Inner Tracker Upgrade in view of the High-Luminosity LHC
Keywords : Data analysis, LHC, Standard Model, Construction, Tracking detector, ATLAS

Abstract : In this thesis the Vector Boson Scattering (VBS) process in semileptonic final states is studied. In semileptonic VBS final states, one of the two bosons decays leptonically while the second hadronically into a pair of quarks. Due to the very low production cross section, VBS is a very challenging channel to measure. What makes this process distinguishable with respect to other processes in LHC, is the two forward jets that accompany the boson scattering. During my thesis I worked in many aspects of the analysis such as ; the background modelling, the MVA discriminant, the systematic uncertainties considered in the measurement, as well as, the statistical analysis of the results.

Forward jet performance is of paramount importance in this analysis. Therefore, the thesis work starts with a detailed study of optimizing the jet reconstruction, in particular developing an algorithm to mitigate the pileup jets in the forward region ; in ATLAS, in order to make use of valid physics data , in any analysis, the physical process (namely hard-scatter process) has to be distinguished from secondary collision processes (namely pile-up interactions). This is mainly achieved by the use of tracking information. The forward part of the ATLAS detector, lacking this information is thus highly challenging. An alternative way of tagging in the forward region, based on momentum conservation between forward activity and activity happening within the tracking coverage, is being employed in this algorithm. The algorithm has been optimized and various methods have been tested.

The actual ATLAS Inner Tracker is compatible with the LHC design luminosity of 10^{34} cm^{-2} s^{-1}. The foreseen increase of luminosity towards the High Luminosity (HL) LHC phase requires a fundamental re-design of the complete inner detector due to both, increased radiation damage, and substantial occupancy of the sub- detectors. For the HL-LHC, the current inner detector of ATLAS will be replaced by an all-silicon Inner Tracker (ITk). The ITk pixel detector design features a much higher active area and granularity with respect to the current pixel detector. Two different silicon based detector technologies are considered ; planar-pixel sensors and 3D-pixel sensors. The sensors are equipped with a new readout chip, able to meet all the requirements needed for the high luminosity LHC. A prototype version of the readout chip, called RD53A, was designed by the RD53A collaboration. In the third part of this thesis a characterization of the RD53A readout chip is performed.

The much larger number of modules and the much finer granularity used by ITk, results in a significant increase in the power density in the detector. For this reason a serial powering (SP) scheme has been chosen. In this scheme, the readout chips of the pixel modules are powered in series by a constant current ; while the sensors of several modules will be connected to a common supply line for the depletion voltage. This architecture results in an effective forward bias on some sensors under certain operating conditions. Although the forward bias will be small, it can still lead to non negligible currents between the sensor backside and the readout chip, in particular for irradiated sensors with large saturation currents. Therefore, the behavior of such a serial powering chain is also studied as part of this thesis.

The Collatz conjecture
By Philipp W.

Στον πολυαγαπημένο μου
πατέρα
με την ελπίδα πως με βλέπει..

Acknowledgements

It has been a long journey of discovering and learning new things and there are several people I need to thank for that..

I would like to start by thanking all the members of my jury: Claude Charlot, Kevin Einsweiler, Susanne Kuehn, Steven Schramm and Marie-Helene Schune for kindly accepting to be part of this thesis defense and for their detailed feedback on my manuscript. With some of the members I had the chance to meet and collaborate during my phd (others were more lucky). In that aspect I would like to deeply thank Susanne Kuehn who was the first one to introduce me to the pixel world (when I was still in my master degree) and since then she has been extremely welcoming and supporting at CERN. I would also like to express my deepest thanks to Steven Schramm for transmitting his knowledge and great expertise in jets, as well as, for always being supportive of my efforts. With the rest of my jury members I unfortunately didn't have the chance to meet before. However, I really hope we get to meet and collaborate in the future!

This thesis work would not have been possible without the great help and support of my two amazing supervisors Lydia Fayard and Dimitris Varouchas. I feel extremely lucky I met them and had the chance to collaborate with them. They haven't only been great advisors but also great friends to me, always encouraging and helping me in many difficult moments during my phd. I have no words to express my gratitude and I hope they will both remain in my life.

There are several more people from whom I have learned great amount of things and therefore a big thank you goes to them as well. I would like to greatly thank Jean-Francois Grivaz for the countless discussions we had over the analysis and his precious feedback in almost every aspect of it. I would also like to deeply thank Matthew Klein for his great guidance and help regarding the jet reconstruction studies I performed. A big thank you also goes to Aishik Ghosh for his valuable feedback on BDTs and machine learning in general. I would also like to thank my colleagues in ITk; I would like to express my deepest thanks to Benedikt Vormwald for his great help and guidance over the serial powering studies I performed. I would also like to deeply thank Matthias Hamer for kindly answering all my questions regarding serial powering. It was a great pleasure collaborating with all of you and I hope we meet again in the future!

My phd days would be much more boring without my wonderful friends: Ana, Anastasia, Araceli, Christina, Philipp, Reem and Sabrina. I would like to deeply thank all of you for your love and support all these years and for the many beautiful memories you have given me. I feel really lucky to have you all.

I would like to specially thank my dear friend Philipp Windischhofer not only because he has always been a caring and thoughtful friend but also for his willingness to always help and kindly share his great deep knowledge and understanding over several physics matters with me. His excitement, love and attitude against physics is always inspiring for me.

At this point I should also apologize to all the above for my perpetual state of grouchiness that might have caused you headaches sometimes.

Last but not least, I would like to express my deepest gratitude to my beloved family: my mother Kyriaki, my sister Maria and my father Avraam, for their unconditional love and support all these years, for always believing in me and supporting my dreams. I would like

to dedicate this thesis work to my adored father who is unfortunately not with us anymore but his attitude, morality and determination will always accompany me.

Contents

1. Introduction

The non-abelian nature of the electroweak (EW) sector of the standard model (SM) predicts the existence of triple and quartic gauge couplings (QGC), consequently allowing self-interactions between W and Z bosons. Theories of new physics beyond the SM foresee the modification of such couplings with respect to the SM predictions, resulting in an enhancement of processes like vector boson scattering (VBS). Moreover, the VBS amplitude, being proportional to the centre of mass energy, in a SM without the presence of Higgs, would violate unitarity at high energies (1TeV). Unitarity is only restored after considering the Higgs boson and its specific couplings to the vector bosons (assuming that the Higgs to gauge boson couplings are as prescribed by the Brout-Englert-Higgs mechanism). Consequently, VBS processes could give direct insights to the electroweak symmetry breaking through the Brout-Englert-Higgs mechanism, study the SM nature of the Higgs boson and even probe new physics (through modifications of the Higgs to gauge boson couplings, or anomalous QGC). For these reasons, VBS processes have been of paramount interest to the high-energy physics community since a long time ago.

The VBS process is identified experimentally by the presence of two bosons (W, Z) and two jets in the opposite hemispheres with a large di-jet invariant mass. Due to the very low production cross section, VBS is an extremely challenging channel to measure. In this thesis, VBS in semileptonic final states is studied. In the semileptonic VBS final states, one of the two bosons decays hadronically into a pair of quarks while the other decays leptonically. Depending on the leptonic decay of the boson three analysis channels are considered; 0-lepton,1-lepton and 2-lepton. The advantages of semileptonic final states, with respect to other fully leptonic searches, is the higher branching ratio as well as the exploitation of substructure techniques, for the W/Z identification, which allow high reconstruction efficiency in the high- p_{T} regimes where we are mostly sensitive to anomalous quartic gauge couplings (aQGC). However, the large background contributions coming mainly from $W+$jets, $Z+$jets and tt-bar events, is the largest drawback. What makes this process distinguishable with respect to other processes in LHC, is the two forward jets that accompany the boson scattering. As part of this thesis work, the entire 2-lepton channel analysis was performed with the full Run-2 data of the ATLAS detector. My work includes a study of the background modeling, the event selection optimization, the MVA discriminant development and optimization, a study of the systematic uncertainties considered in the measurement as well as the statistical analysis of the results. The results of this analysis will be detailed in Chapter 6

Forward jet performance is of paramount importance in this analysis. Therefore the thesis work starts with a detailed study of optimizing the jet reconstruction, in particular developing an algorithm to mitigate the pileup jets in the forward region; in ATLAS, in order to make use of valid physics data , in any analysis, the physical process (namely hard-scatter process) has to be distinguished from secondary collision processes (namely pile-up interactions). This is mainly achieved by the use of tracking information. The forward part of the ATLAS detector, lacking this information is thus highly challenging. An alternative way of tagging in the forward region, based on momentum conservation between forward activity and activity happening within the tracking coverage, is being employed in this algorithm. The algorithm has been optimized and various methods have been tested. The results of this work are summarized in Chapter 5.

The current ATLAS Inner Tracker is compatible with the LHC design luminosity of $10^{34}\ cm^{-2}s^{-1}$.

The foreseen increase of luminosity towards the High Luminosity (HL) LHC phase requires a fundamental re-design of the complete inner detector due to both, increased radiation damage, and substantial occupancy of the sub-detectors. For the HL-LHC, the current inner detector of ATLAS will be replaced by an all-silicon Inner Tracker (ITk). The ITk pixel detector design features a much higher active area and granularity with respect to the current pixel detector. Two different silicon based detector technologies are considered; planar-pixel sensors and 3D-pixel sensors. The sensors are equipped with a new readout chip, able to meet all the requirements needed for the high luminocity LHC. A prototype version of the readout chip, called RD53A, was designed by the RD53A collaboration. In the third part of this thesis a characterization of the RD53A readout chip is performed (in Chapter 8). Moreover, the much larger number of modules and the much finer granularity used by ITk, results in a significant increase in the power density in the detector. For this reason a serial powering (SP) scheme has been chosen. In this scheme, the readout chips of the pixel modules are powered in series by a constant current; while the sensors of several modules will be connected to a common supply line for the depletion voltage. This architecture results in an effective forward bias on some sensors under certain operating conditions. Although the forward bias will be small, it can still lead to non negligible currents between the sensor backside and the readout chip, in particular for irradiated sensors with large saturation currents. Therefore, as part of this thesis work, the behavior of such a serial powering chain is also studied in detail in Chapter 9 .

Before diving into the details of this thesis, an overview of the theoretical context and a description of the experimental setup is given in Chapters 2-4.

2. Theoretical Overview

This chapter introduces the basic theoritical concepts that give a better understanding and motivate the studies of this thesis. In the first section a brief introduction of the Standard Model (SM) and its particle content will be given, followed by a more detailed description of the electroweak theory (EW) that directly provokes the necessity of Vector Boson Scattering (VBS) studies done in this thesis.

2.1 The Standard Model of particle physics

The Standard Model [1] is a Quantum Field Theory (QFT) that embodies all known fundamental particles and describes their main interactions [2] [3]. Despite their difference (in terms of strength and action range) three of the major interactions that played a leading role in the evolution of the universe (the electromagnetic, weak and strong interactions) are successfully integrated within the SM. The most exciting part and beauty in such a theory still lies in its renormalizability [4] (in the leading expansion in the dimension of operators in quantum field theory). This makes the theory highly predictive up to high energy scales , allowing us to perform high precision tests of the SM, with any deviations from it (found experimentally) to be treated as hints of new physics. However, as mentioned above, only three out of the four major forces are currently included in the SM. The last one being gravity, is currently understood only in aspects of classical physics, through General Relativity. The non-renormalisability of gravity makes the integration into the SM a difficult task which is still pending solution. Fortunately, the effects of gravity can be considered negligible at the energies where the SM is tested experimentally.

In the QFT theory of the SM, elementary particles, appear as quantized excitation states of their underlying fields. These particles are classified as either fermions, or bosons, depending on their spin: fermions have a half-integer spin while bosons carry an integer-spin. Moreover, particles are characterized by their mass and by various quantum numbers such as their electric, colour and hyper-charge as well as the lepton and baryon number. Each particle has an associated antiparticle with the same mass and spin but opposite electrical charge, as well as lepton and baryon number. A summary of the particle content in the SM can be seen in Figure 2.1.

Fermions are the particles composing matter. The SM predicts the existence of 12 fermions, that can be further classified as quarks [5] and leptons [6] based on their color charge. Quarks are strongly interacting particles (thus carrying a color charge) while leptons are "colorless" particles not participating in strong interactions. Among the 12 fermions there are 6 different quark and 6 different lepton types, or as they are usually called different "flavours". Both quarks and leptons are paired into three generations. The first generation includes the lightest leptons and quarks which are stable particles that participate in the formation of atoms. The next two generations contain mostly unstable particles of increasing mass. Each of the 12 fermions has also it's corresponding anti-particle that carries the same properties as its corresponding particle but with an opposite charge.

In more detail, in each of the quark generations there is a quark with a $+\frac{2}{3}$ and another quark with a $-\frac{1}{3}$ electric charge. The first generation, consists of the up and down flavour quarks, while the remaining flavours include the charm and strange quarks of the second generation and the top and bottom quarks of the third generation. Quarks have a color charge

that can take 6 discrete values (red, green, blue and anti-red, -green and -blue). In nature quarks cannot be found isolated (due to confinement) and thus they always form colourless states, called hadrons. Hadrons can be categorised in two classes, the mesons that consist of a quark-antiquark system, and the baryons, that are made of 3 quarks. It has been observed experimentally a conservation of the number of baryons in particle interactions and therefore each quark has also it's own baryon number (+1/3 for quarks and -1/3 for anti-quarks) .

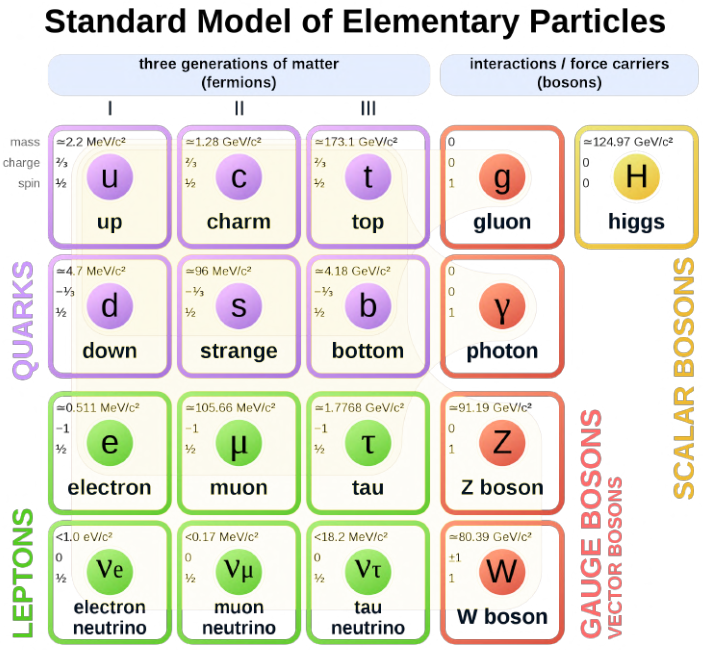

FIGURE 2.1: The particle content of the Standard Model.

Similarly to the quarks, three generations of leptons exist, each of ones composed of a charged, massive particle, and a neutral, light particle. The first generation includes the electron and the electron neutrino, while in the second and third generations there are the muon - muon neutrino and tau - tau neutrino particles respectively. Similarly to the baryon number conservation, a lepton number conservation has also been observed. Lepton number conservation states that the sum of lepton numbers before and after the interaction must be the same. There are three different lepton numbers (one for each generation): the electron-lepton number L_e, the muon-lepton number L_μ and the tau-lepton number L_τ. Each of these quantities has to be conserved separately during any interaction. However, although the total lepton number seems (until now) to be conserved in nature there are observations of violation of family lepton number conservation in phenomena like neutrino oscillations.

Bosons, are integer spin particles with either a spin of 1 for the vector bosons, or spin of 0 for the scalar Higgs boson. The vector bosons are the carriers of the gauge interactions between fermions; photons are the carriers of the the electromagnetic interactions, the weak interactions are propagated by Z and $W^{\pm}$ bosons while the strong force is mediated by gluons. The Higgs boson [7] [8] [9], which is a direct consequence of the existence of the Higgs field in the SM isn't associated to any fundamental force. However as discussed in 2.1.5, the Higgs field through the Brout-Englert-Higgs (BEH) mechanism is responsible for the mass of the fermions and the weak interacting bosons in the SM.

2.1.1 The SM Theory

In the SM theory, particles described in 2.4 and their interactions are expressed through a gauge theory based on a special unitary group $SU(N)$(Yang-Mills theory [10]). The electromagnetic and weak interactions between quarks and leptons, is a Yang-Mills theory based on the symmetry group $SU(2)_I \times U(1)_Y$ [1]. The strong interactions between quarks are described by the $SU(3)_C$ gauge theory of Quantum Chromo-Dynamics (QCD). Combined together the $SU(3)_C \times SU(2)_I \times U(1)_Y$ group forms the quantum field theory of the SM, able to describe the three fundamental forces described above. Symmetries are also fundamental for the theory. This is to a large extent due to the Noether theorem [11], which states:

To any continuous symmetry of a physical system, it corresponds a conserved current and an associate conserved charge.

For example, theories that respect symmetries like time and space translation lead to conservation of energy and momentum, respectively, which are fundamental laws of nature. In the case of the SM, the Lagrangian is invariant under the local symmetries of the $SU(3)_C \times SU(2)_I \times U(1)_Y$ group, where the color charge C, weak isospin I and hypercharge Y are conserved. An example of how a symmetry can lead to a conserved charge is given in 2.1.2 for the case of Quantum Electrodynamics (QED) assuming a rotation of the field phase.

2.1.2 Conservation of charge in QED

Let's take a freely propagating fermion of mass M which is described by a four component spinor Ψ of the fermion field. For the Lagrangian of the fermion we have:

$$\mathscr{L} = \bar{\Psi}(i\gamma^\mu \partial_\mu - M)\Psi \tag{2.1}$$

Now let's consider a local U(1) transformation which corresponds to a phase rotation of the field by an angle $a(x)$:

$$\Psi(x) \rightarrow \Psi'(x) = e^{iqa(x)}\Psi(x), \tag{2.2}$$

under which the Dirac Lagrangian becomes:

$$\mathscr{L} = \bar{\Psi}(i\gamma^\mu \partial_\mu - M)\Psi - \bar{\Psi}\gamma^\mu \partial_\mu q a(x)\Psi \tag{2.3}$$

In order for the Lagrangian to remain invariant under the imposed transformation, the derivative has to be replaced with the covariant derivative D_μ defined as:

$$D_\mu = \partial_\mu - iqA_\mu, \tag{2.4}$$

where A_μ is a vector field which transforms under local U(1) transformation in the following way:

$$A_\mu \rightarrow A'_\mu = A_\mu + \partial_\mu a \tag{2.5}$$

For the modified Lagrangian we now have:

$$\mathscr{L} = \bar{\Psi}(i\gamma^\mu D_\mu - M)\Psi = \bar{\Psi}(i\gamma^\mu \partial_\mu - M)\Psi + q\bar{\Psi}\gamma^\mu \Psi A_\mu \tag{2.6}$$

The first term of the equation corresponds to the Dirac equation for a non-interacting particle while the second part can be interpreted as the interaction of the fermion with the gauge field A_μ, which can be identified as the photon field. The corresponding Noether current for

[1] due to the chiral nature of the weak interaction the $SU(2)_I$ is more often mentioned as $SU(2)_L$

this transformation is defined by:

$$j^{\mu} = q\bar{\Psi}\gamma^{\mu}\Psi \tag{2.7}$$

and is proven to satisfy:

$$\partial_{\mu} j^{\mu} = 0 \tag{2.8}$$

By integrating the current of 2.7 over a volume at a constant time we get the charge which is also conserved due to 2.8 .

2.1.3 The SM Lagrangian

In the SM Lagrangian (without the electroweak symmetry breaking mechanism which will be introduced later) there are two type of fields;

First, there are the matter fields which are the three generations of left-handed and right-handed chiral fermions. The left-handed quarks and leptons are organized in doublets, while the right-handed ones in singlets. This is due to the chiral nature of the weak interaction, which implies that left- and right-handed particles do not interact in the same way.

Next, there are the gauge fields that mediate the interactions. In the so called Electroweak (EW) sector, which provides a unified description of the electromagnetic and weak force, we have the field B_{μ} which corresponds to the generator Y of the $U(1)_Y$ group and $W_{\mu}^{1,2,3}$ which correspond to the generators τ_a, (where a=1,2,3) of the $SU(2)_L$ group. The covariant derivate for the EW sector is:

$$D_{\mu} = \partial_{\mu} - ig\frac{\tau_a}{2}W_{\mu}^{a} - ig'\frac{Y}{2}B_{\mu}, \quad a = 1,2,3 \tag{2.9}$$

where g an g' are coupling constants of the $SU(2)_L$ an $U(1)_Y$ groups, respectively. The EW Lagrangian is then defined:

$$\mathscr{L}_{EW} = i\bar{\Psi}\gamma^{\mu}D_{\mu}\Psi - \frac{1}{4}W_{\mu\nu}^{a}W_{a}^{\mu\nu} - \frac{1}{4}B_{\mu\nu}B^{\mu\nu} \tag{2.10}$$

where $\frac{1}{4}B_{\mu\nu}B^{\mu\nu}$ and $\frac{1}{4}W_{\mu\nu}^{a}W_{a}^{\mu\nu}$ are the kinetic terms for the vector fields B_{μ} and $W_{\mu}^{1,2,3}$ respectively.

In the strong interaction theory, described by QCD [12] [13], we have eight gluon fields $G_{\mu}^{1,..,8}$ corresponding to the eight generators λ_a of the $SU(3)_C$ group. The covariant derivative in the case of QCD is written:

$$D_{\mu} = \partial_{\mu} - ig_s\frac{\lambda_a}{2}G_{\mu}^{a}, \quad a = 1...8 \tag{2.11}$$

where g_s is the strong coupling constant. For the QCD Lagrangian we have:

$$\mathscr{L}_{QCD} = i\bar{\Psi}\gamma^{\mu}D_{\mu}\Psi - \frac{1}{4}G_{\mu\nu}^{a}G_{a}^{\mu\nu} \tag{2.12}$$

By combining equations 2.10 and 2.12, the SM Lagrangian, without mass terms for fermions and gauge bosons, is written in the following way:

$$\mathscr{L}_{SM} = \mathscr{L}_{EW} + \mathscr{L}_{QCD} = i\bar{\Psi}\gamma^{\mu}D_{\mu}\Psi - \frac{1}{4}G_{\mu\nu}^{a}G_{a}^{\mu\nu} - ig\frac{\tau_a}{2}W_{\mu}^{a} - ig'\frac{Y}{2}B_{\mu} \tag{2.13}$$

where D_μ is here defined as:

$$D_\mu = \partial_\mu - ig_s\frac{\lambda_a}{2}G^a_\mu - ig\frac{\tau_a}{2}W^a_\mu - ig'\frac{Y}{2}B_\mu \tag{2.14}$$

In all the above considerations fermions and gauge fields have been kept massless. However we know experimentally that fermions and weak bosons are massive particles. In the case of QCD, someone could add a mass term of the form $-m_q\Psi\bar{\Psi}$ in the right side of equation 2.12, without violating the $SU(3)$ symmetry. However, things are more complicated in the EW theory. When trying to add mass terms of the form : $\frac{1}{2}M_V^2W_\mu W^\mu$ in the EW Lagrangian the local $SU(2)_I \times U(1)_Y$ gauge invariance is violated. This can be easily proven in the case of QED when considering a mass term for the photon field:

$$\frac{1}{2}M_\gamma^2A_\mu A^\mu \rightarrow \frac{1}{2}M_\gamma^2(A_\mu + \partial_\mu a)(A_\mu + \partial_\mu a) \neq \frac{1}{2}M_\gamma^2A_\mu A^\mu \tag{2.15}$$

which violates the local U(1) symmetry of QED. In a similar way, when attempting to add mass terms for fermions in the EW Lagrangian, due to the chiral nature of the EW sector, the isospin symmetry is violated.

For a long time the generation of masses in the SM theory was an open question. After the discovery of the Higgs boson and through the Higgs mechanism of spontaneous symmetry breaking the mystery of mass generation within the SM is finally solved. This mechanism will be briefly described in the following subsections.

2.1.4 The Higgs mechanism in an abelian theory

In order to understand the basic ideas behind the mechanism of mass generation through spontaneous symmetry breaking a simple example is first considered. This is an abelian gauge theory invariant under local $U(1)$ transformations and we will assume a complex scalar field coupled to itself and to the vector field A_μ. For the Lagrangian of the system we have:

$$\mathscr{L} = -\frac{1}{4}F_{\mu\nu}F^{\mu\nu} + |D_\mu\phi|^2 - V(\phi) \tag{2.16}$$

where $F_{\mu\nu}F^{\mu\nu}$ is the kinetic term for the vector field, $D_\mu = \partial_\mu + ieA_\mu$ is the covariant derivative and $\phi = \frac{1}{\sqrt{2}}(\phi_1 + i\phi_2)$ is a complex scalar field. The term containing $D_\mu\phi$ can be understood as the kinetic term related to the scalar field ϕ. For the potential $V(\phi)$ we have:

$$V(\phi) = \mu^2\phi^2 + \lambda\left(\phi^2\right)^2 = \frac{\mu^2}{2}\left(\phi_1^2 + \phi_2^2\right) + \frac{\lambda}{4}\left(\phi_1^2 + \phi_2^2\right)^2 \tag{2.17}$$

In order for the potential to have a finite minimum, λ should be positive. If μ^2 is also positive the potential takes the form shown in fig 2.2a, and has a minimum at $\phi = 0$. In this case the vacuum state occurs when both fields ϕ_1 and ϕ_2 are zero and the Lagrangian simply represents a particle with mass μ and self interactions of the form ϕ^4. However, if μ^2 is chosen to be negative the potential takes the form of fig 2.2b. In this case the potential can have many different set of minima given by:

$$\phi_1^2 + \phi_2^2 = \frac{-\mu^2}{\lambda} = v^2 \tag{2.18}$$

These minima correspond to the dashed circle in fig 2.2b. By choosing any point on this

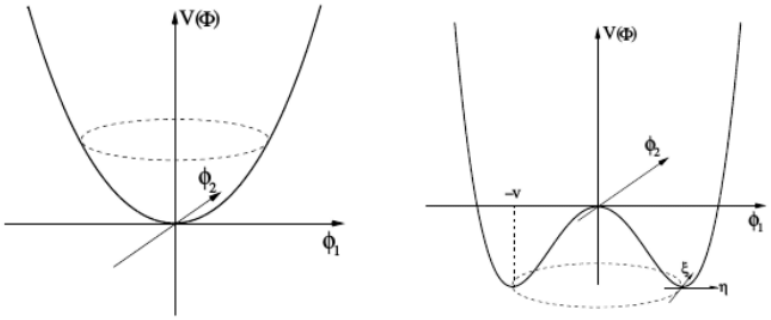

FIGURE 2.2: The $V(\phi)$ potential for a scalar field for (a) $\mu^2 > 0$ and (b) $\mu^2 < 0$

circle to be the physical vacuum state the symmetry of the Lagrangian is spontaneously broken and the Lagrangian doesn't anymore represent a particle with mass μ. Since the particle states are described as excitation states of their underlying fields we expand the Lagrangian around the vacuum state $\frac{v}{\sqrt{2}}$:

$$\phi(x) = \frac{1}{\sqrt{2}}(v + \eta_1 + i\eta_2) \tag{2.19}$$

For the kinetic term of the scalar field ϕ we have:

$$|D_\mu \phi|^2 = \frac{1}{2}(\partial_\mu \eta_1)^2 + \frac{1}{2}(\partial_\mu \eta_2)^2 + e v_\mu \partial^\mu \eta_2 + \frac{e^2 v^2}{2} A_\mu^2 + ... \tag{2.20}$$

By looking at equation 2.20 we now see that there is a mass term $\frac{e^2 v^2}{2} A_\mu^2$, for the previously massless gauge field A_μ. Therefore, by considering a spontaneously broken symmetry of the Lagrangian we have managed to give a mass to the vector boson. However, there is still a problem appearing; in the initial Lagrangian we had four degrees of freedom (two for the complex scalar field ϕ and two for the vector boson A_μ), while now we have five (since the vector boson has become massive there is an extra longitudinal degree of freedom). This suggests that there should be one degree of freedom absorbed by the Lagrangian corresponding to a not physical field (Goldstone boson). This is indeed achieved by performing appropriate gauge transformations such as only physical fields are left in the Lagrangian (unitary gauge).

2.1.5 The SM Higgs mechanism

In the case of the SM, the situation is slightly more complex; we need to generate masses for the three gauge bosons $W^\pm$ and Z, and at the same time keep the photon field massless. On that account, we need at least three degrees of freedom for the scalar field. The simplest choice is a complex scalar doublet. Similarly to the methodology followed in 2.1.4, we add the scalar field (denoted as Higgs) to the SM Lagrangian of 2.13 in the following form:

$$\mathscr{L}_{Higgs} = (D^\mu \phi)^\dagger (D_\mu \phi) - V(\phi), \quad with \quad V(\phi) = \mu^2 \phi^\dagger \phi + \lambda (\phi^\dagger \phi)^2 \tag{2.21}$$

where $\lambda > 0$ and $\mu^2 < 0$.

Next, we arbitrarily choose a vacuum state from the infinite number of degenerate states, and we expand the scalar field around this vacuum state:

$$\phi(x) = \frac{1}{\sqrt{2}} \begin{pmatrix} 0 \\ v + h(x) \end{pmatrix} \tag{2.22}$$

The kinetic and potential terms of the Higgs field are written in this case:

$$(D_\mu \phi)^\dagger (D_\mu \phi) = \frac{1}{2}(\partial_\mu h)(\partial^\mu h) + \frac{g^2}{4}(v+h)^2 W_\mu^+ W^{\mu -} + \frac{1}{8}(g^2 + g'^2)(v+h)^2 Z_\mu Z^\mu \tag{2.23}$$

$$V(\phi) = \frac{\mu^2}{2}(v+h)^2 + \frac{\lambda}{4}(v+h)^4 \tag{2.24}$$

The new fields $W_\mu^\pm$, Z_μ and A_μ are defined as:

$$\begin{aligned} W_\mu^\pm &= \frac{1}{\sqrt{2}}(W_\mu^1 \mp i W_\mu^2) \\ Z_\mu &= \frac{g W_\mu^3 - g' B_\mu}{\sqrt{g^2 + g'^2}} \\ A_\mu &= \frac{g' W_\mu^3 + g B_\mu}{\sqrt{g^2 + g'^2}} \end{aligned} \tag{2.25}$$

and they correspond to our well-known : $W_\mu^\pm$, Z_μ and γ bosons. By looking at the kinetic term of equation 2.23 we can easily identify the mass terms of the W and Z bosons (being quadratic in the fields), while the photon remains massless. Therefore, by spontaneously breaking the symmetry, three Goldstone bosons have been absorbed by the $W_\mu^\pm$ and Z_μ bosons of equations 2.25 which at the same time have acquired mass.

Beyond the mass generation for the bosons, the higgs field is also able to generate the fermion masses by introducing the invariant Yukawa Lagrangian:

$$\mathscr{L}_Y = -y_d \bar{Q_L} \phi d_R - y_u \bar{Q_L} \bar{\phi} u_R - y_l \bar{L_L} \phi l_R + h.c., \tag{2.26}$$

where $\bar{Q_L} = (\bar{u_L}, \bar{d_L})$ and $\bar{L_L} = (\bar{\nu_L}, \bar{l_L})$ are the quark and lepton left-handed doublets (for a single family) and u_R, d_R and l_R are the corresponding right-handed fermion singlets.

Following the same exercise as previously, we have for the fermion masses:

$$m_f = y_f \frac{v}{\sqrt{2}} \tag{2.27}$$

To summarize, by spontaneously breaking the $SU(2)_I \times U(1)_Y$ symmetry we have managed to generate masses for the weak bosons and fermions. It is worth mentioning that the $SU(2)_I \times U(1)_Y$ gauge symmetry is not really removed from the SM Lagrangian, but it is rather hidden, when expanding the vector fields around the non-zero vacuum expectation value. The $U(1)_C$ symmetry of the Lagrangian remains unbroken and therefore no mass is generated for the photon field, which thus remains massless. The $SU(3)$ gauge symmetry of QCD remains unbroken as well.

2.1.6 Weak mixing angles and gauge bosons

In subsection 2.1.5 the mixing of the B_μ and W_μ fields was introduced. The outcome of this mixing is our common $W^\pm$, Z and γ bosons with masses:

$$\begin{aligned} M_W &= \frac{1}{2}gv \\ M_Z &= \frac{v}{2}\sqrt{g^2+g'^2} \\ M_A &= 0 \end{aligned} \tag{2.28}$$

We can now introduce the electroweak angle:

$$cos\theta_w = \frac{g}{\sqrt{g^2+g'^2}} = \frac{M_W}{M_Z}, \quad tan\theta_w = \frac{g'}{g} \tag{2.29}$$

which rotates from the weak basis to the mass basis:

$$\begin{pmatrix} Z_\mu \\ A_\mu \end{pmatrix} = \begin{pmatrix} cos\theta_w & -sin\theta_w \\ sin\theta_w & cos\theta_w \end{pmatrix} \begin{pmatrix} W_\mu^3 \\ B_\mu \end{pmatrix} \tag{2.30}$$

It is worth noticing that the ratio:

$$\rho = \frac{M_W^2}{M_Z^2 cos\theta_w^2} \tag{2.31}$$

is equal to 1 at tree level in the SM and belongs to one of the precision tests of the Standard Model physics.

In addition to introducing the new vector bosons of equation 2.25, due to the non-commuting nature of the $SU(2)$ group generators, self-couplings of the bosons are predicted. Two types of couplings exist: triple gauge coupling (TGC) and quartic gauge couplings (QGC). The possible triple gauge boson vertices are: γW^+W^- and ZW^+W^- , while the quartic boson vertices are: $W^+W^-W^+W^-$, W^+W^-ZZ and $W^+W^-\gamma\gamma$. Moreover triple couplings arise from equation 2.23 between the gauge bosons and the Higgs, and are proportional to the boson masses. The Higgs to boson couplings are of paramount importance especially when considering boson scatterings of the form $W_LW_L \rightarrow W_LW_L$, where L stands for longitudinal. It is proven that such processes have a cross section proportional to the energy term and therefore violate unitarity at high energies. This phenomenon is briefly discussed in the following section.

2.2 WW scattering and unitarity

The tree-level Feynman diagrams contributing to the WW scattering amplitude are summarized in Figure 2.3. For a W gauge particle of momentum q, the free boson field can be written in terms of a plane wave and a four-vector ϵ^m for the polarisation state m,

$$A_\mu = \epsilon_m e^{ikx}$$

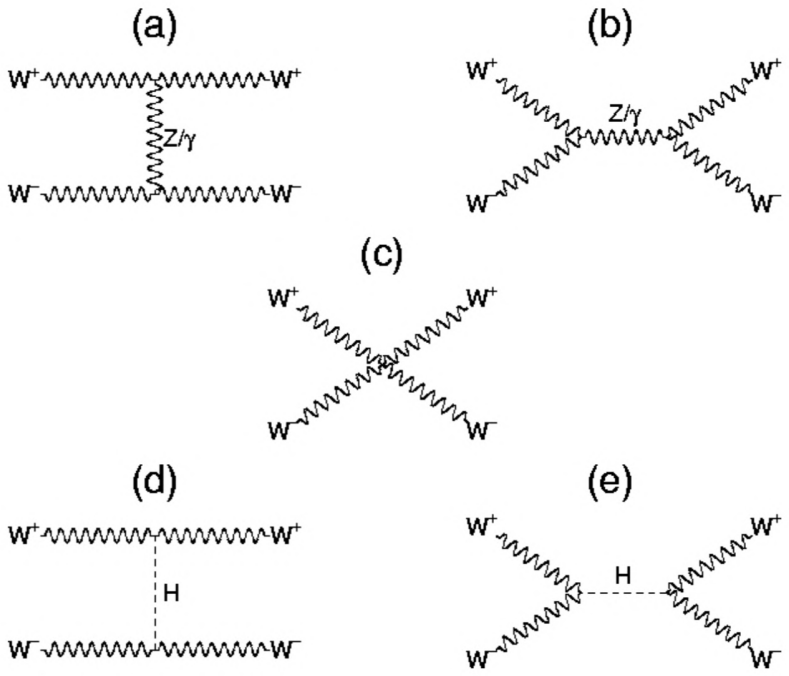

FIGURE 2.3: Tree level diagrams contributing to the $W_L W_L \to W_L W_L$ scattering process.

For a massless W boson the polarisation vector is always transverse to the direction of motion. In that case, the massless particle can be described by two orthogonal polarisation states :

$$\epsilon_1^m = (0,1,0,0) \; and \; \epsilon_2^m = (0,0,1,0)$$

For a massive W boson particle of momentum q and mass M_W, an extra longitudinal polarization should be considered. It can be written as:

$$\epsilon_L^m = (\frac{q}{M_W}, 0, 0, \frac{E}{M_W})$$

The high-energy behavior of the individual graphs of Figure 2.3 is at worse $\sim (\frac{E}{M_W})^4$. Consequently, the contribution of each graph to the tree level amplitude can be written as:

$$\mathcal{A} = A(\frac{E}{M_W})^4 + B(\frac{E}{M_W})^2 + C$$

As described in [14], the first term is vanishing thanks to the gauge cancellation between the contact graph and the s- and t-channel γ/Z exchange graphs of Figure 2.3. However, for the cancellation of the second term, which is proportional to E^2, the Higgs boson needs to be involved. More specifically, in order for all high energy divergencies to cancel, the s- and t-channel exchanges of the Higgs boson, shown in Figure 2.3 d-e, should be considered.

2.3 Factorization of hard processes in QCD

The study of processes such as vector boson scattering is made possible thanks to particle collider experiments. One of the most important quantities when studying a physics process in a collider experiment is the cross section, which gives an estimation of how likely is

the process to occur. In a renormalizable perturbation theory, any such physical quantity is expected to be a function of three variables: the kinematic energy scale of the process (Q), the masses (m) of the particles participating in the scattering, and a renormalization scale (μ_R) [15]. The renormalization scale dependance arises from regularization techniques, which ensure the non-divergence of the process [16]. Given the asymptotic freedom of QCD, one would typically choose a large renormalization scale, such as the effective coupling constant ($a_s(\mu) \sim 1/ln(\mu/\Lambda_{QCD})$) would be small (short-distance behavior) [17]. However, the renormalization scale appears in ratios of the form Q/μ_R and μ_R/m, which would lead to at least one of these terms being large at high energy [15]. Another option would be to choose the renormalization scale to be of the order of Q (long-distance behavior). However, in this regime perturbation theory is not applicable anymore.

When estimating a cross-section, both the short- and long-distance behaviors should be considered. However, due to the long-distance contributions, such cross sections are not directly calculable through perturbation theory. The problem is resolved by considering factorization theorems [15], which allow to derive cross-section predictions by separating, or factorizing, the long-distance from the short-distance behavior. As an example let's consider a process of the form $A + B \rightarrow C + X$ happening in LHC. In this process, A and B are the colliding hadrons, protons in our example, which result in a final state C. The term "X" denotes anything additional produced to the hadron C, which is not originating from the hard-scattering process. Such contributions can arise from different sources, such as interactions between beam remnants, initial state radiation of partons, multiple parton interactions, and are collectively referred to as the underlying event.

In the above example, the non-perturbative long-distance behavior at low scale ($\sim O(1GeV)$), can be factorized into a term composed of parton density functions (PDFs), which describe the partons momentum distribution within the protons. The benefit of such approach is that PDFs can be determined experimentally from fits to data and then applied to any process of the above form. The estimation is performed by assuming a given functional form for the parton content of the proton at a low scale of $O(1GeV)$ and by extrapolating to the process energy scale through the so-called DGLAP evolution equations [16]. The remaining short-distance cross-section term is then describing the hard-scattering process of the partons and is usually calculated theoretically at some order of perturbation theory. In this case, emissions of additional particles or particle loops are described by higher oder terms in the perturbation series. Based on the above, the cross-section can be written as:

$$\sigma_{A+B\rightarrow C+X} = \sum_{a,b} \int dx_1 dx_2 f_a(x_1, \mu_F^2) f_b(x_2, \mu_F^2) \hat{\sigma}_{a+b\rightarrow C}(x_1, x_2, \mu_R^2)$$

where a and b are the partons within the protons A and B, respectively, while terms of the form $f_i(x, \mu_F^2)$ are the corresponding PDFs, parametrizing the probability of finding a parton of flavour i carrying a fraction x of the proton momentum, with μ_F being the factorization scale. The factorization scale μ_F can be understood as the boundary between the short- and long-distance behavior, and is usually chosen to be at the scale that the hard-scattering process takes place. The remaining term, $\hat{\sigma}_{a+b\rightarrow C}$, is the short-distance cross section for the hard-scattering of partons a and b and it depends on the momentum of partons, as well as, the renormalization scale μ_R. The μ_R is usually chosen at the energy scale of the process.

It is worth noting here that the factorization and renormalization scales are artificial scales, introduced due to the methods used for estimating cross-sections. In the ideal case where the cross sections could be fully estimated from perturbation theory, in all orders of the perturbative expansion, these artificial scales would disappear [18]. In an analysis level, one typically

wants to include uncertainties due to missing higher order corrections. This is usually done by varying the renormalization and factorization scales by some amount and by comparing to the nominal predictions. In this case, small differences from nominal, indicate that the missing orders have little impact on the cross-section and the perturbative series is well converging.

Another artificial scale usually arises when trying to overlay fixed-order predictions to a parton shower. The parton shower is added to describe the hadronisation of partons produced during the collision. During the hadronisation process, partons usually emit additional partons, such as gluons, until the produced partons have low enough energy to bound into hadrons. This process is usually estimated separately, by a parton shower algorithm, and is overlaid to the process predictions. However, when overlaying, some extra care has to be taken in order to not double count parton emissions. This is typically done by introducing an extra artificial scale, the matching scale, which defines the boundary between the fixed order calculation and the parton shower regime. Similarly to the previous scales discussed, it has to be chosen carefully in order not to ruin the perturbative convergence of the result.

2.4 Experimental results on VBS

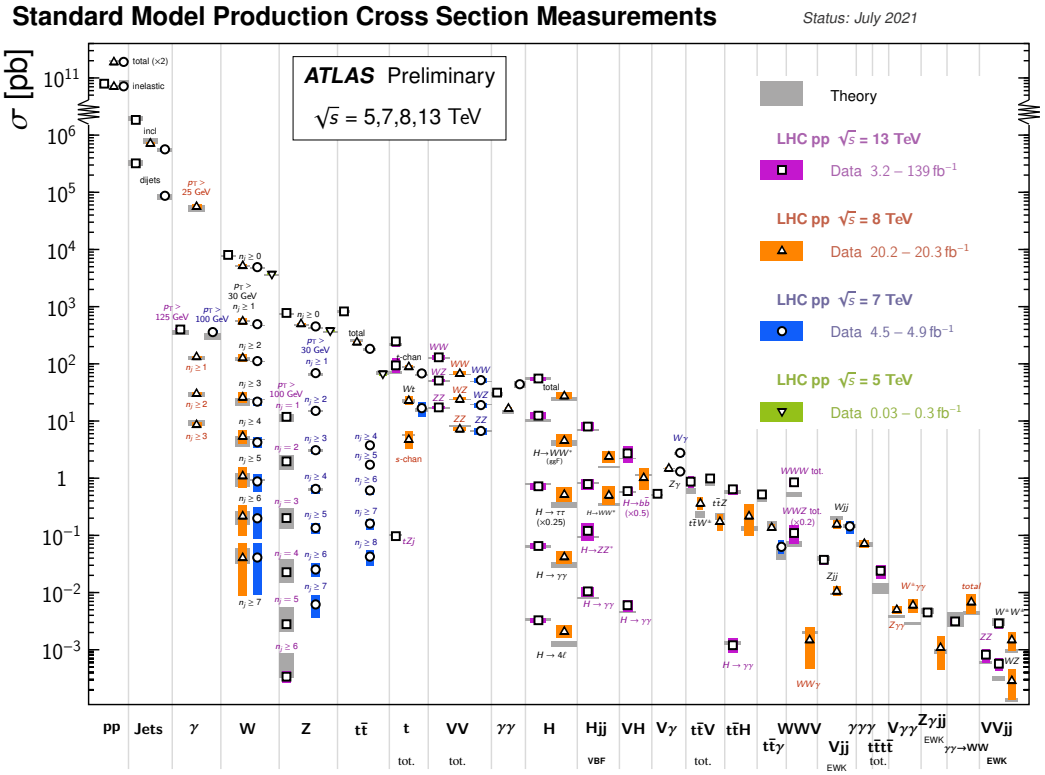

FIGURE 2.4: Summary of several SM total and fiducial production cross-section measurements. The measurements are corrected for branching fractions, compared to the corresponding theoretical expectations. In some cases, the fiducial selection is different between measurements in the same final state for different centre-of-mass energies $\sqrt{s}$, resulting in lower cross section values at higher $\sqrt{s}$.

The vector boson scattering process has been of great interest both on theoretical and experimental levels for a long time. As already discussed, the non-abelian nature of the electroweak sector of the SM predicts the existence of triple and quartic gauge couplings, consequently allowing self-interactions between W and Z bosons. The EW theory determines the self-couplings of the vector bosons. However, new phenomena beyond the SM can alter

the couplings of vector bosons, generating additional contributions to the QGC compared to the SM predictions. More importantly, the Higgs boson regularizes the VBS amplitude by canceling out the divergencies arising from longitudinally polarized vector bosons at high energy. These cancellations depend on the gauge structure of the theory and are exact in the SM [19]. Therefore, measurements of the VBS process constitute a fundamental tool to probe the EW sector of the SM and search for new physics. At the same time, the low cross section of the process, in combination with the rather large background of other diboson productions, makes such a measurement extremely challenging at an experimental level. In Figure 2.5 a summary of several ATLAS SM total and fiducial production cross-section measurements are presented [20]. The VBS measurements, plotted in the last column, have the lowest cross section values. Several VBS channels are defined, based on the final-state bosons after the scattering. At LHC, the VBS searches started already in Run1, after the discovery of the Higgs boson. With an integrated luminosity of $20 fb^{-1}$, accumulated at $\sqrt{s} = 8$ TeV, both ATLAS and CMS reported evidence on the EW production of two same sign $W^{\pm}$ bosons accompanied by two jets ($ssWWjj$) [21, 22], as well as, on the electroweak $Z\gamma jj$ production [23, 24]. The increased energy and statistics of Run2 allowed the first observation of the electroweak $ssWWjj$ production in 2018 by CMS [25], with a significance of 5.5σ, and on the electroweak $W^{\pm}Z$ boson pair production accompanied by two jets in 2019 by ATLAS [19], with a significance of 6.5σ. Semileptonic $VVjj$ final states, where one of the two bosons, V =(W,Z), decays leptonically and the additional boson decays hadronically into a pair of quark - antiquark, have also been investigated. A first measurement of this final state was reported by ATLAS in the 2019 publication using $35.5 fb^{-1}$ of the Run2 dataset, with a significance of 2.7σ, combining all lepton multiplicities (0-,1- and 2-lepton) [26]. Recently, CMS published a 4.4 sigma evidence on the same channel, using the full Run2 dataset, and by considering the 1-lepton final state only [27]. As part of this thesis work, the semileptonic $VVjj$ production in the 2-lepton final state is studied. A detailed description of the analysis strategy and results is given in Chapter 6.

Although constraints on anomalous QGC (aQGC) are not covered as part of this thesis work, they are nevertheless of paramount interest. Many of the VBS channels mentioned above have set limits on aQGC by constraining the parameters of an extended SM Lagrangian, in the frame of an Effective Field Theory (EFT). Variables that are sensitive to the energy scale of the process, such as the diboson mass, are usually exploited to search for signs of higher-energy modifications to the vector boson interactions. In Figure 2.5, an example summary plot of the current constraints set by CMS at 95% confidence level on dimension 8 EFT operators $f_{M,i}$, is shown [28]. As it is shown, in the majority of channels such limits are statistically dominated, with the exception of semileptonic final states (WV ZV) which highly benefit from the larger branching ratio of hadronically decaying bosons.

Boson polarization studies are also of paramount importance. As already discussed in 2.2 the divergent behavior of the scattering amplitude at high energies is more relevant for the scattering of longitudinally polarized vector bosons. Such divergencies cancel thanks to the Higgs boson couplings to the vector bosons, given that they are as prescribed by the SM. In the case that such couplings deviate from the SM predictions, these cancellations might not be exact, resulting in an increase of the scattering amplitude with energy. Several beyond the SM scenarios predict such increase, through modifications to the Higgs sector or new resonances. A direct study of the scattering of longitudinal polarized bosons would therefore probe fundamental Higgs boson properties and set limits on anomalous Higgs couplings. Several polarization measurements of vector bosons have been performed by both ATLAS and CMS [28]. The polarization of a gauge boson can be determined from the angular distribution of its decay products. Polarization measurements are not unique and depend on the reference frame in which they are defined [28]. In many cases the diboson center of mass

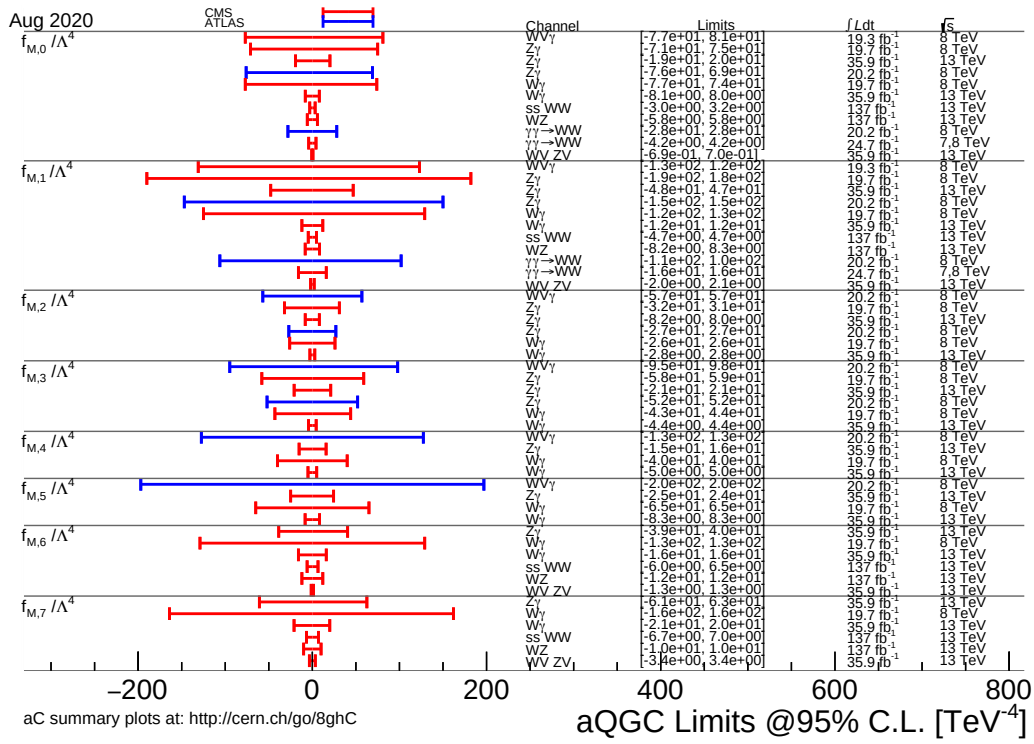

FIGURE 2.5: Limits on dimension 8 mixed transverse and longitudinal parameters $f_{M,i}$ by CMS [28].

frame is chosen, since in that case the line-of-flight of the two bosons coincides with the longitudinal polarization vectors, and the decay products are directly related to the scattering process. However, the measurement of scattering of longitudinal polarized vector bosons is still a long term goal since it is difficult to separate out the contributions from different polarizations. It is therefore important to understand how increases in the $W_L W_L \rightarrow W_L W_L$ amplitude through modifications of the higgs-boson couplings translate to the un-polarised cross section measured by the experiments. In Figure 2.6 a summary of several cross sections is given, estimated at a center-of-mass energy of 2 TeV [29]. The notation $0, +, -$ indicates longitudinally polarized gauge bosons, while un-polarized bosons are denoted as $Z, W^{\pm}$. The table shows two groups of cross-sections: assuming no modification to the higgs-boson couplings (first column) and modified couplings (second column). As it is shown even a small deviation of the couplings from the SM predictions (a=b=1) results in a huge increase of the longitudinal boson scattering cross-section. This huge increase however, translates only into a small rise of the corresponding un-polarized cross-sections, indicating the necessity of separating longitudinal from transversed bosons.

channel	$a = b = 1$ (SM)	$a = 0.9; b = 1$
$00 \to +-$	0.13	295
$ZZ \to W^+W^-$	610	655
$00 \to + - h$	2.0×10^{-3}	350
$ZZ \to W^+W^-h$	10.9	46.2
$00 \to hh$	0.18	158
$ZZ \to hh$	7.61	15.7
$00 \to hhh$	4.9×10^{-4}	112
$ZZ \to hhh$	4.65×10^{-2}	13.6

FIGURE 2.6: Comparison of $2 \to 2$ and $2 \to 3$ cross sections at $\sqrt{s} = 2$ TeV.

3. The Large Hadron Collider and the ATLAS Detector

This chapter manly includes a brief introduction to the experimental setup used to record the data used in the physics analysis of this thesis. It consists of three main parts: the accelerator complex in charge of accelerating and colliding protons, the particle detectors responsible for recording the outcome of the collisions and the object reconstruction which includes advanced reconstruction techniques in order to identify and reconstruct particles from the recorded detector hits. The accelerator complex, mostly known as the Large Hadron Collider (LHC) [30], is a circular accelerator consisting of a 27-kilometre ring, located on the French-Swiss border at CERN. Its large size and the high center-of-mass energy proton-proton collisions it provides, makes it the world's largest and most powerful particle accelerator. In the first data taking period (Run 1), between 2010 and 2013, the accelerator achieved a center-of-mass energy of 8 TeV while it was pushed to 13 TeV for the second data-taking period (Run 2), between 2015 and 2018. A third upcoming data-taking period (Run 3) is also planned, at a center-of-mass energy of 13.6 TeV. The proton particle beams of LHC collide at four points around the accelerator ring where four large-scale particle detectors are installed [31] [32]. The two largest ones ATLAS and CMS, primarily designed as "Higgs" detection machines, are targeting a wide spectrum of physics processes. The other two experiments are LHCb [33], which is mostly studying flavor physics processes, and ALICE [34] which is focusing on heavy ion physics (through heavy ion collisions). The work of this thesis is mainly focuses on the ATLAS experiment and therefore a detailed description of the detector and reconstruction techniques will be given in the following sections.

3.1 The LHC acceleration complex

In order for the proton beams to reach the desired center of mass energy mentioned above, they are accelerated in several steps through interconnected linear and circular accelerators shown in fig 3.1. The acceleration process proceeds with ionised hydrogen atoms which are first guided to the first accelerator, LINAC 2, where they reach an energy of 50 MeV. The protons then pass to the first circular accelerator (called the BOOSTER), accelerating them to an energy of 1.4 GeV. Next, they pass through the Proton Synchrotron (PS) and the Super Proton Synchrotron (SPS) after which they leave with an energy of 450 GeV. Finally, protons are injected into the LHC, where they split into two beams. Since the LHC is mainly a proton-proton collider, separate rings for the counter-rotating beams are needed. The proton beams are accelerated to their final energy of 6.5 TeV by a series of Radio Frequency (RF) cavities. It is worth noting here that the field in the RF cavities is not stable but rather oscillates at a given frequency (400 MHz for the LHC). This way particles with slightly different energies will be decelerated or accelerated achieving a more uniform energy beam. In addition, in order to keep the protons in the circular trajectory during acceleration as well as to have properly collimated beams, superconducting dipole and quadrupole magnets are used respectively. The beams are injected in LHC in the form of bunch trains separated by 25 ns and each containing 1.15×10^{11} protons. During a so-called fill, the LHC has around a few thousands of such proton bunches. Once the desired energy is achieved, collisions at a 40 MHz rate occur in each of the four colliding points of the accelerator.

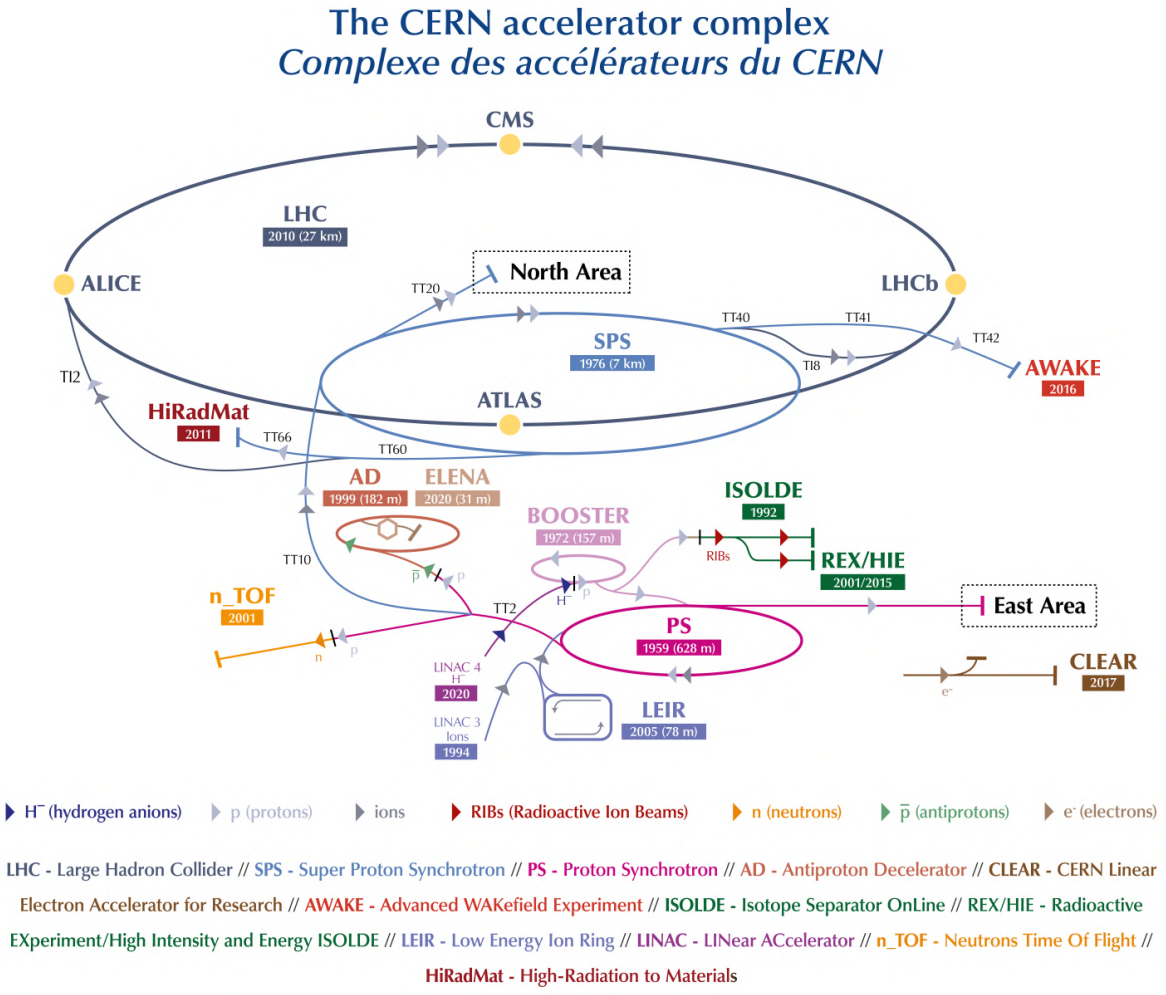

FIGURE 3.1: A representation of the CERN accelerator complex [35].

3.1.1 Luminosity and pile-up

The number of collisions achieved is also of paramount importance for a collider (together with the centre-of-mass energy). Since the physics processes usually studied are extremely rare, sufficient number of collisions is needed in order to observe such processes. This quantity, referred to as Luminosity (L), is defined as:

$$L = \frac{1}{\sigma}\frac{dN}{dt} \tag{3.1}$$

where σ corresponds to the cross-section for a given proton-proton inelastic interaction process and $\frac{dN}{dt}$ to the proton-proton interaction rate.

However, the luminosity can also be expressed in terms of the beam parameters as follow:

$$L = \frac{N_1 N_2 f N_b}{4\pi\sigma_x\sigma_y} S \tag{3.2}$$

where N_1 and N_2 are the number of protons per bunch, N_b is the number of bunches per fill, f is the revolution frequency of the bunches and σ_x and σ_y correspond to the transverse

width of the beam at the collision point. Finally, the factor S is the geometric luminosity reduction factor to account for the crossing angle between the two beams.The evolution of the instantaneous luminosity during the year 2018 is shown in fig 3.2(a). It is worth noting that LHC has managed to go above its design specifications achieving luminosity values above 10^{34} cm^{-2}s^{-1}. This corresponds to an integrated luminosity of 156 fb^{-1} during the full Run 2 data taking period, between 2015 and 2018, as shown in fig 3.2(b).

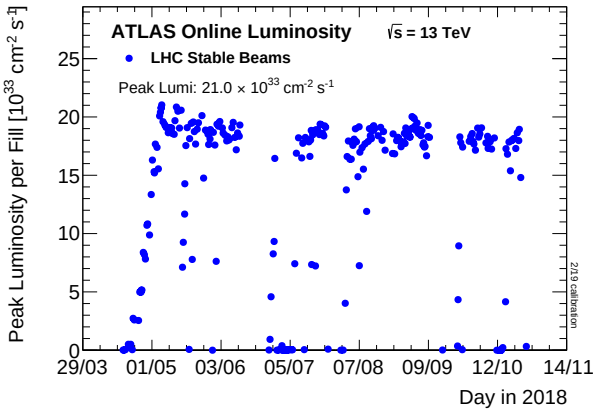

(a)

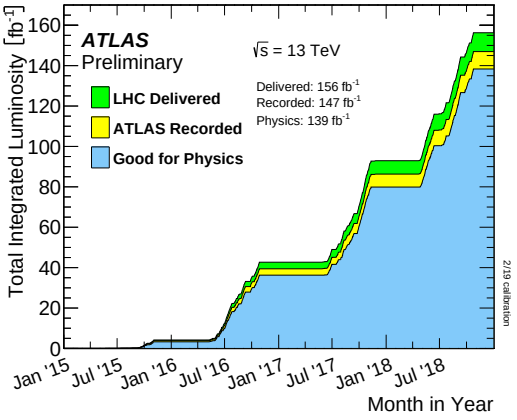

(b)

FIGURE 3.2: (a) Peak instantaneous luminosity delivered to ATLAS as a function of time for the 2018 data-taking period. (b) Cumulative luminosity versus time delivered to ATLAS (green), recorded by ATLAS (yellow), and certified to be good quality data (blue) during stable beams for pp collisions at 13 TeV centre-of-mass energy in 2015-2018 [36].

Even though high luminosity is in general desirable, it comes with an important drawback; that being the several collisions occurring per bunch crossing. This phenomenon is usually referred to as pile-up. The LHC experiments are usually focusing in a single interaction per bunch crossing, the most promising one in terms of physics, usually referred to as the hard-scatter process . In this case, pile-up effects introduce serious contamination for the physics process of interest. The average number of simultaneous interactions per bunch crossing for each year of the Run 2 is shown in fig 3.3. The average pile-up for the full Run 2 period was $< \mu >= 33.7$ interactions per bunch crossing. The corresponding one from Run 1 was around 21. This large increase in the pile-up conditions in Run 2 make physics measurements extra challenging.

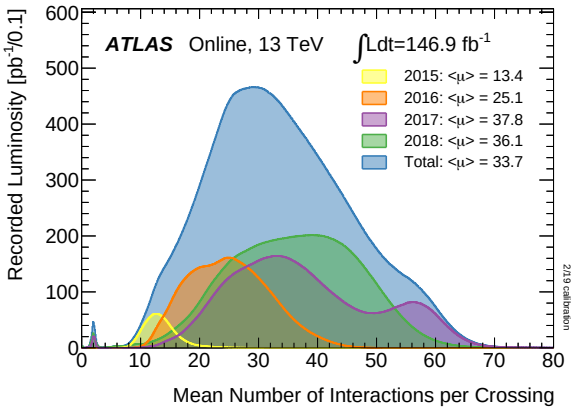

FIGURE 3.3: Mean number of interactions per bunch-crossing in pp collisions recorded by the ATLAS experiment during Run 2 [36].

3.2 The ATLAS detector

The ATLAS detector [31] is the largest of the four large-scale experiments at the LHC. It is composed of six different detecting subsystems organized in layers around the collision point. The different detector systems are able to record the trajectory, momentum, and energy of incoming particles with high precision, allowing them to be individually identified and measured. The detector has a cylindrical geometry and is symmetrical in the forward and backward regions with respect to the interaction point, offering an almost 4π solid angle coverage. The central region of the detector is usually addressed as barrel while the forward regions as end-caps. Due to its design, ATLAS is a general purpose detector able to study a wide range of physics phenomena within and beyond the SM of particle physics. A schematic view of the detector is shown in fig 3.4. More details about the detector coordinate system and subsystems are given in the following sub sections.

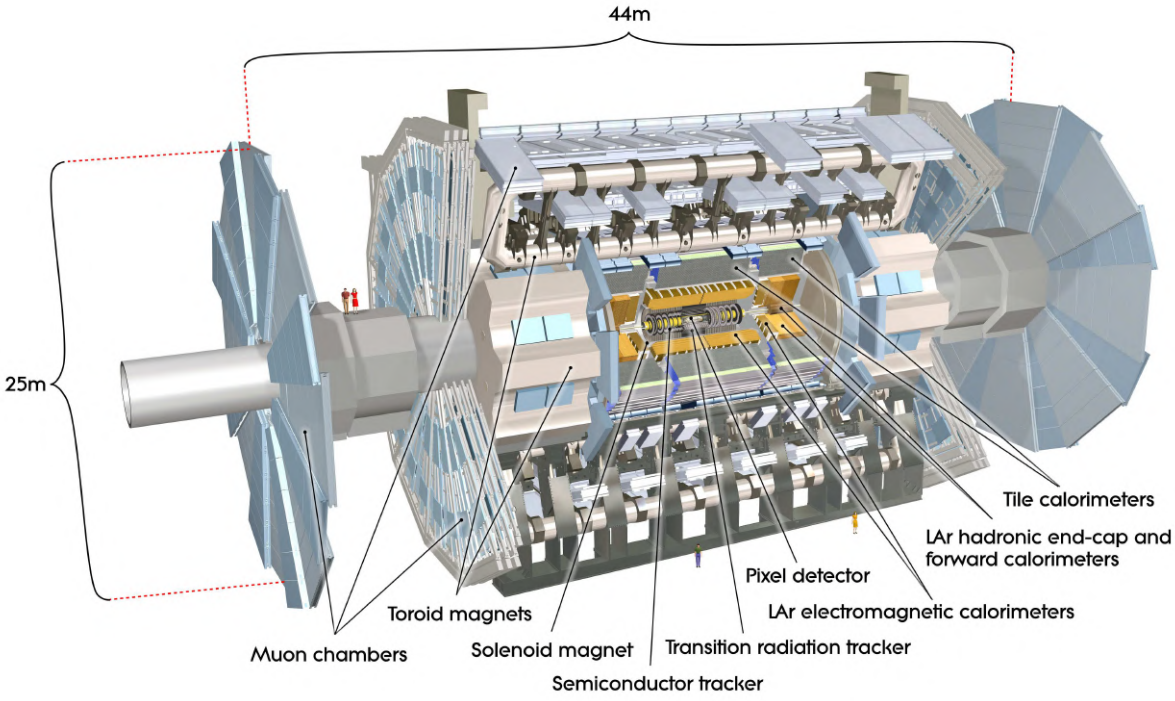

FIGURE 3.4: Schematic view of the ATLAS detector.

3.2.1 Coordinate system

The ATLAS detector is using a right-handed coordinate system centered on the nominal interaction point. In this coordinate system the x-axis points to the center of the LHC ring, the y-axis points upward while the z-axis is on the direction of the beam pipe. Due to its cylindrical geometry, the cylindrical coordinate system (z, θ, ϕ) is more often used. A schematic view of the ATLAS coordinate system is given in fig 3.5. The azimuthal angle around the beam pipe ϕ usually ranges from $-\pi$ to π, while the polar angle θ is usually replaced by the rapidity y defined as:

$$y = \frac{1}{2} ln(\frac{E + p_z}{E - p_z}) \tag{3.3}$$

where E is the energy of the measured object, and p_z its momentum along z. This is a convenient choice because the difference in the rapidity (Δy) between two objects is a Lorentz-invariant quantity under boosts along the beam axis. In the case of massless particles or for negligible masses (in the highly relativistic case), the rapidity can be replaced by the pseudorapity defined as:

$$\eta = \frac{1}{2} ln(\frac{|p| + p_z}{|p| - p_z}) = -\frac{1}{2} ln(tan(\theta/2)) \tag{3.4}$$

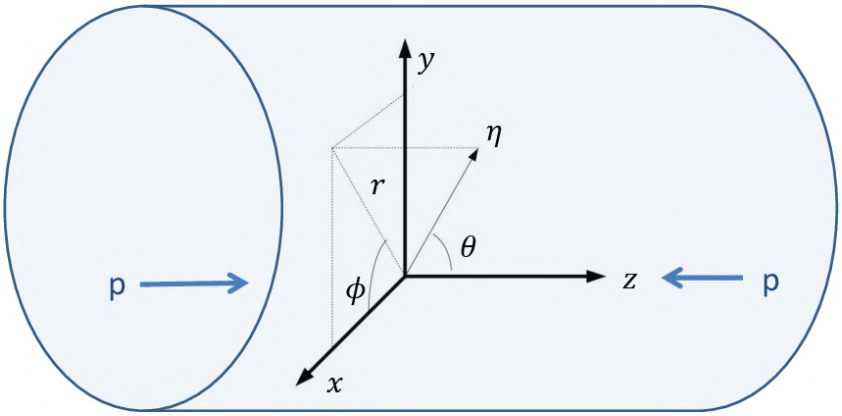

FIGURE 3.5: The ATLAS coordinate system.

The pseudorapity η is very often the preferred option since it offers some advantages like the particle production rate being approximately constant per pseudorapidity unit. The angular separation between two particles is also expressed in terms of pseudorapidity using the formula:

$$\Delta R = \sqrt{(\Delta\eta)^2) + (\Delta\phi)^2)} \tag{3.5}$$

In addition the transverse particle momentum p_T and energy E_T are very often used and are defined in the $x - y$ plane as:

$$p_T = \sqrt{p_x^2 + p_y^2} \tag{3.6}$$

and

$$E_T = \sqrt{p_T^2 + m^2} \tag{3.7}$$

3.2.2 The Inner Detector

Goal of the Inner Detector (ID) is to provide precise tracking information for charged particles coming out of the collisions. Using this information a precise track-to-vertex association can also be achieved; tracks are first reconstructed using a pattern recognition algorithm and their origin can then be extrapolated back to the interaction point. Track-to-vertex association is of paramount importance because it allows identifying the hard-scatter vertex of interest, while rejecting activity coming from other less energetic pp interactions happening in PU vertices, as well as, from secondary vertices coming from decays of long-lived particles.

The ID starting a few centimetres around the beam axis is 6.2 m long and has a radius of 1.2 metres. It covers a psedorapidity up to $|\eta|$ = 2.5. It is able to detect the momentum of particles down to $p_T = 0.1$ GeV with a resolution of:

$$\frac{\sigma_{p_\mathrm{T}}}{p_\mathrm{T}} = 5 \times 10^{-5} p_T[GeV] \oplus 0.01 \tag{3.8}$$

As expected, the momentum resolution deteriorates with the particle p_T, since the first highly depends on the curvature of the particle which is decreasing with p_T. As already mentioned, the ID also plays the leading role on the vertex reconstruction through the track-to-vertex information it provides. Vertices are reconstructed by grouping tracks with overlapping extrapolated positions. Therefore, the ID is additionally required to have an excellent resolution of the extrapolated position of the track to the interaction plane usually quantified by the the longitudinal and transverse impact parameters z_0 and d_0 respectively.

The ID consists of three sub-detectors: the pixel detector, the Semi-Conductor Tracker (SCT) and the Transition Radiation Tracker (TRT). The layout of the ID system is shown in Figure 3.6. The sub-detectors are surrounded by a superconducting solenoid, that provides a 2 T magnetic field, allowing for the measurement of the track momentum through the track's bending radius, and of its charge, through the bending direction.

The Pixel detector

The pixel detector is the innermost layer of the ID and it mainly consists of semiconducting silicon (Si) pixel devices. In the barrel region, it is composed of four silicon pixel layers spanning a distance from 3.3 cm to 15 cm with respect to the beam axis while in each of the two end-cap regions there are three disk layers. In the three outermost barrel layers, the installed pixel sensors are covering an area of $50\,\mu\mathrm{m} \times 400\,\mu\mathrm{m}$ in r and z each, allowing a track reconstruction with a resolution of $14\,\mu\mathrm{m} \times 115\,\mu\mathrm{m}$. This is making the pixel detector the most granular subdetector in ATLAS able to deal with the high particle density expected. The innermost layer, called the insertable B-layer (IBL) [37], was installed before the start of Run 2 and it uses Si sensors with a surface of $50\,\mu\mathrm{m} \times 250\,\mu\mathrm{m}$ in r and z. IBL was installed in order to reassure good tracking and vertex reconstruction performance in view of the instantaneous luminosity increment, as well as, potential radiation damages caused to the existing detector. Due to its higher granularity, IBL was able to improve the spatial resolution and thus enhance the tracking capability as well as vertex reconstruction performance.

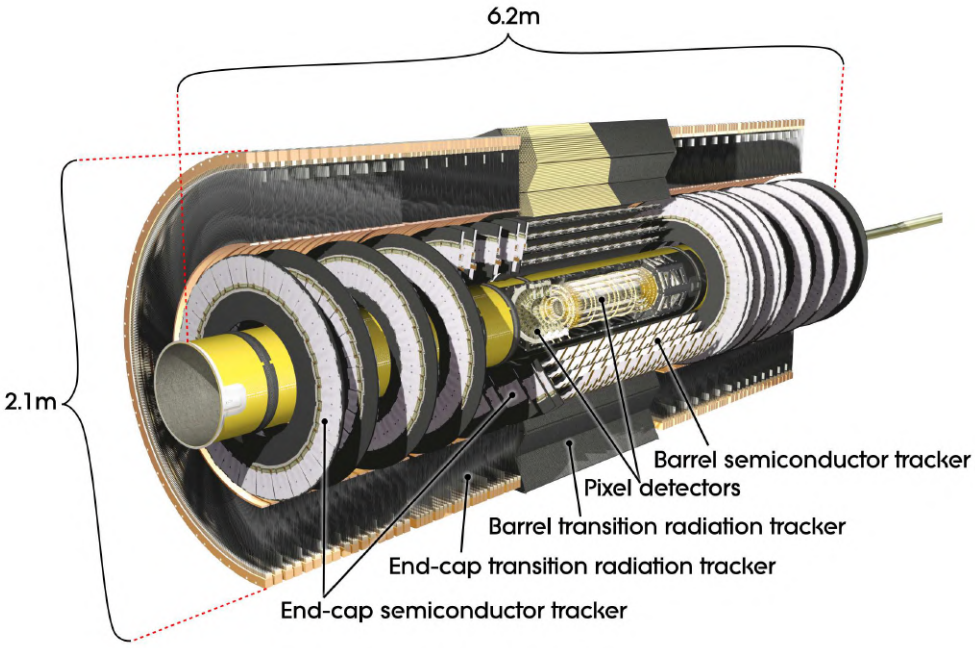

FIGURE 3.6: Cut-away view of the ATLAS Inner Detector.

The Semi-Conductor Tracker (SCT)

The SCT is located right after the pixel detector at a radius range of 30 to 56 cm. Similarly to the pixel detector, it is composed of detection layers, four for the barrel and nine for each of the end-caps. Instead of silicon pixels, it uses silicon strips which are $80\,\mu m$ long in r and 64 mm long in z. The larger surface of the strips, compared to the pixels, make the coverage of larger detector areas much more practical but with the cost of a much coarser resolution of $17\,\mu m$ in r and $580\,\mu m$ in z. However, such a coarser resolution is still sufficient considering the lower particle densities SCT has to deal with.

The Transition Radiation Tracker (TRT)

The TRT is the outermost part of the ID providing coverage up to $|\eta| = 2$. It is composed of 4 mm-diameter straw tubes filled with Xe-CO2-O2 gas and interleaved with polypropylene material which is acting as a radiator. In the barrel region, the tubes are placed in parallel to the beam axis while in the end-cap regions are radial. When a charged particle passes through the straw tube, it ionizes the gas. The ionized particles drift to the anode wire located on the center of the tube with the help of an external electric field. The motion of particles induces a signal to the anode wire while the drift time provides extra information about the location of the particle in the r-ϕ plane.

The TRT has in general a low hit position resolution. Its main advantage is coming from its ability to distinguish between particles. The polypropylene material in between the tubes is creating transition-radiation photons. The amount of transition radiation is highly affected by the mass of the incoming particle. Therefore the crossing particle can be identified based on the intensity of the radiated photons. For this reason the TRT is of particular use when separating electrons from pions.

3.2.3 The Electromagnetic Calorimeter

A schematic cut-away view of the ATLAS complete calorimeter system is shown in fig 3.7. It consists of three main subsystems: the Electromagnetic Calorimeter (EMCal), the Hadronic Calorimeter (HCal) and the Forward Calorimeter (FCAL).

The ATLAS EMCal [38] is the innermost part of the system. Its primary goal is to identify and measure the energy of electrons and photons. It is a sampling calorimeter with Liquid Argon (LAr) layers used as the active material while lead (Pb) plates act as the absorbers. The LAr is kept in a temperature of 89K in order to maintain its liquid state. Incoming particles initiate electromagnetic showers in the absorber plates. The shower particles pass through the LAr layers sandwiched in-between the absorber plates, ionising the LAr. The ionised particles drift with the help of an external electric field to closest electrode, inducing a signal. The absorber plates have a variety of thicknesses depending on pseudorapidity, in order particles to cross approximately the same amount of material in radiation lengths.

The EMCal is composed of two parts : a central region (or barrel) covering a pseudorapidity range up to $|\eta|$ = 1.46 and a forward region (or end-cap) ranging from 1.36 $< |\eta| <$ 3.2. The barrel features a characteristic accordion geometry that allows a full azimuthal coverage without cracks and is organized in three layers with different granularities. In particular, the innermost layer which has the finest granularity allows for particle identification, for instance distinguishing between pions (π_0 and $\pi^{\pm}$. The EMCal provides an energy measurement with a measured resolution of:

$$\frac{\sigma_E}{E} = \frac{a}{\sqrt{E}} \oplus \frac{b}{E} \oplus c \tag{3.9}$$

where a is the stochastic term accounting for statistical fluctuations in the shower detection due to not fully contained showers, b is is the electronic noise term and c is a constant term related to detector instabilities and mis-calibration effects. In the case of EMCal, a= 10%, c is around 270 MeV and c is less than 1% in the barrel and around 1-2% in the end-cap regions.

Hadronic calorimeter

The hadronic calorimeter (HCAL) [39] located right after EMCAL is aiming the energy measurement of hadronic particles. Different calorimeter systems are used for the barrel and the end-cap regions. In the barrel, covering $|\eta| < 1.7$, steel absorbers and plastic scintillators are used forming the Tile Calorimeter (TileCal). Particles going through the scintillators ionize the polystyrene material consequently producing an ultraviolet scintillation light. The light is guided through fibers to photo-multipliers (PMTs) where is converted to a readable electronic signal. In the Hadronic End-Caps (HEC), covering 1.7$< |\eta| <$3.2, a LAr based sampling configuration is used instead.

The HCAL resolution is estimated [40]:

$$\frac{\sigma_E}{E} = \frac{52\%}{\sqrt{E}} \oplus 5.7\% \tag{3.10}$$

The HCAL has in general a much lower resolution comparing to EMCAL. The large stochastic term value is mainly coming from two challenges that HCAL has to face. On one hand, a large amount of the initial energy is converted to low energy nuclear processes, occurring in a relatively large time-scale, and thus are poorly measured. On the other hand, the different

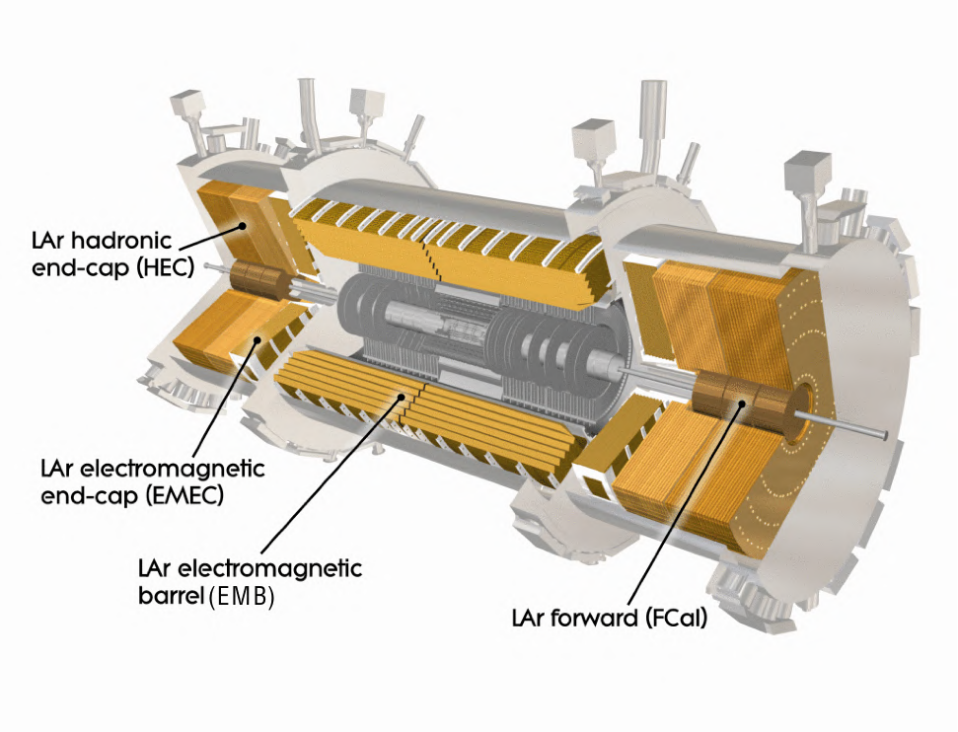

FIGURE 3.7: Cut-away view of the ATLAS calorimeter system.

response of the calorimeter to the electromagnetic and hadronic components of the hadronic showers, constitutes a second challenge. Both components, contribute to the stochastic term of equation 3.11, decreasing the energy resolution.

Forward calorimeter

The Forward Calorimeter (FCAL) [41] is covering $3.1 < |\eta| < 4.9$. FCAL is also a sampling calorimeter and is composed of three layers; the first one optimized for electromagnetic shower measurements uses copper as the absorber material, while the other two focusing on hadronic showers are using tungsten absorbers. Due to the need of extra radiation hard materials in the forward region where particle occupancy is extremely high, LAr is used as the active material for all layers. FCAL has an energy resolution of:

$$\frac{\sigma_E}{E} = \frac{100\%}{\sqrt{E}} \oplus 10\% \tag{3.11}$$

3.2.4 Muon Spectrometer

Muons are Minimum Ionizing Particles (MIPs), therefore cross the Inner Detector and calorimeters depositing a minimum amount of energy. In order to be efficiently detected they need a further detector. For this reason the Muon Spectrometer (MS) [42] dedicated for the detection of muons is the outermost subsystem of ATLAS.

A schematic view of the ATLAS muon system is shown in fig 3.8. The MS system is composed of four different sub-detector technologies:

- The Monitored Drift Tubes (MDTs) designed for precise tracking of muons in pseudorapidity range -2.7 $< \eta <$ 2.7. Each of the drift tubes has a diameter of 30 mm and is filled

with gas. A high voltage of 3kV is applied between the anode wire located in the center of the tube and the ground in order to maximize the charge collection efficiency. Each of the MDT chambers is composed of layers of such tubes and can achieve a hit resolution of about $35\,\mu\mathrm{m}$.

- The Cathode Strip Chambers (CSCs) are multi-wire proportional chambers also filled with gas and covering $|\eta|$ = [2,2.7]. The chambers feature strip-segmented cathodes where the signal readout is performed. The CSCs have in general a better time resolution and can cope with high particle rates better than the MDTs. Therefore, they are used in regions where the particle flux is higher.
- The Resistive Plate Chambers (RPCs) are installed in the barrel, in pseudorapidity range $|\eta| < 1.05$. A single RPC detector consists of two parallel resistive plates separated by a thin gas gap. A high electric field is applied between the two plates, to create an electron avalanche out of the primary ionization electron. Due to the very small distance of the two plates such chambers have a high time resolution. Therefore they are mainly used for trigger purposes.
- The Thin Gap Chambers (TGCs) are also multi-wire proportional chambers similar to the CSCs. They have similar functionality as the RPCs but in the forward region.

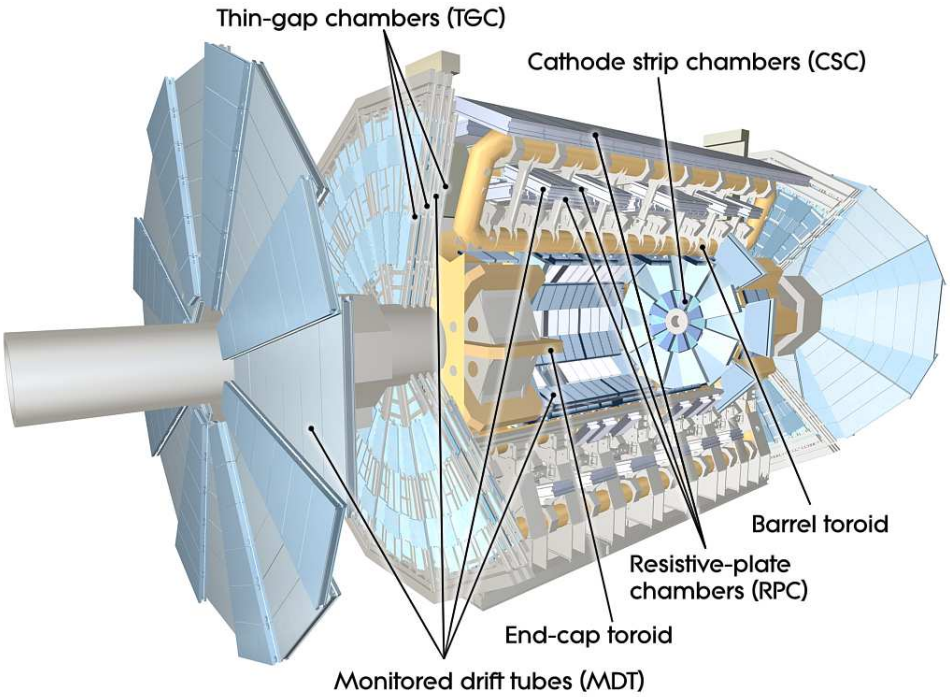

FIGURE 3.8: Cut-away view of the ATLAS muon system.

3.2.5 The Trigger system

The LHC operates at a bunch crossing rate of 40 MHz, i.e. collisions occur every 25 ns. This high collision rate makes the record of each single event extremely difficult. Therefore a selection must be applied in order to reduce the input data rate to a more manageable one while maintaining all the interesting in terms of physics data events. This task is performed by the trigger system.

The ATLAS trigger system [43] consists of two separated trigger levels. The first one, called Level1 (L1), is a hardware trigger that uses data from the calorimeter and the muon

spectrometer systems only. The data are handled by two subsystems, the L1Calo and L1Muon respectively. The L1Calo is looking for regions with significant transverse energy deposits in the calorimeter, while the L1Muon checks for coincidence of hits on the MS trigger detectors. The L1 single-bit decision is transferred to all sub-detector systems demanding either the full read-out or the rejection of the event . The L1 trigger alone reduces the event rate from 40 MHz to around 100 kHz.

Data passing the L1 trigger are temporarily buffered and the second trigger level is employed in order to decide if the data should be saved or not. This is a software-based high level trigger (HLT). It consists of two layers: the level 2 trigger (L2) and the event filter (EF). L2 is doing a similar search as L1, but with higher granularity and with the addition of ID measurements up to $|\eta| < 2.4$. The event filter has access to the complete event data and is using reconstruction and physics algorithms offline. The list of selection criteria for the HLT is defined in the trigger menu. These can vary based on the physics process of interest. Special trigger options are also available for performance measurements and calibration studies. For example in the so-called zerobias trigger, random events are selected without any extra kinematic specifications in order to study the pileup interactions.

3.3 The High-Luminosity LHC and the ATLAS upgrade

The High-Luminosity LHC (HL-LHC) upgrade program is aiming to increase the accelerator luminosity by a factor of approximately 5 to 7 beyond its current value, thus increasing the potential for new physics discoveries. Such an increase of accelerator luminosity impose the need of detector experiment upgrades as well, in order to cope with the increased particle rate and radiation damages expected. In fig 3.9 a summary of the LHC schedule, including the HL-LHC plan, is shown. The HL-LHC installation and commissioning is expected to start in 2026 and last three years followed by the first data taking period, Run4, which is expected to start in 2029. Before the start of HL-LHC, a last four year data taking period, the Run 3, is foreseen, where the nominal instantaneous luminosity will be the same as in Run 2. By the end of Run 3 an integrated luminosity of 450 fb^{-1} is expected, while it is anticipated to reach a value of 4000 fb^{-1} at the end of the HL-LHC operation. LHC is planned to operate at a center of mass energy of 13.6 TeV during Run 3, while for HL-LHC, 14 TeV center of mass energy will be used.

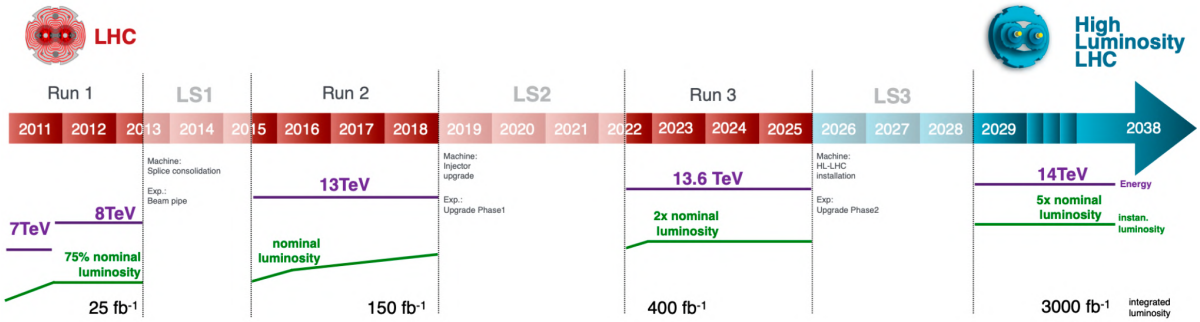

FIGURE 3.9: The LHC baseline programme including the HL-LHC run [44].

3.3.1 Accelerator upgrade and beam conditions

In order to achieve the high luminosity values desired, the beam intensity has to increase by a factor of 3 and remain well focused. For this purpose, new more powerful quadrupole magnets will be installed close to each detector. The new magnets will be niobium-tin (Nb_3Sn)

based, able to generate a 12 Tesla magnetic field, comparing to the current Ni-Ti based ones, able to provide up to 8.3 Tesla. Thanks to their strong magnetic field, the new magnets can effectively squeeze the beams before colliding, increasing the instantaneous luminosity.

An important drawback of the use of such magnets is that it entails the increase of crossing angle of the bunches at the interaction point. As a consequence the probability of collisions is decreasing and therefore the luminosity is reduced. In order to correct for that, radio-frequency crab cavities are planned to be used. The crab cavities are able to tilt the proton bunches before they meet maximizing their overlap. A total of sixteen crab cavities is foreseen to be installed on both sides of the ATLAS and CMS experiments. An illustration of the main idea is shown in fig 3.10

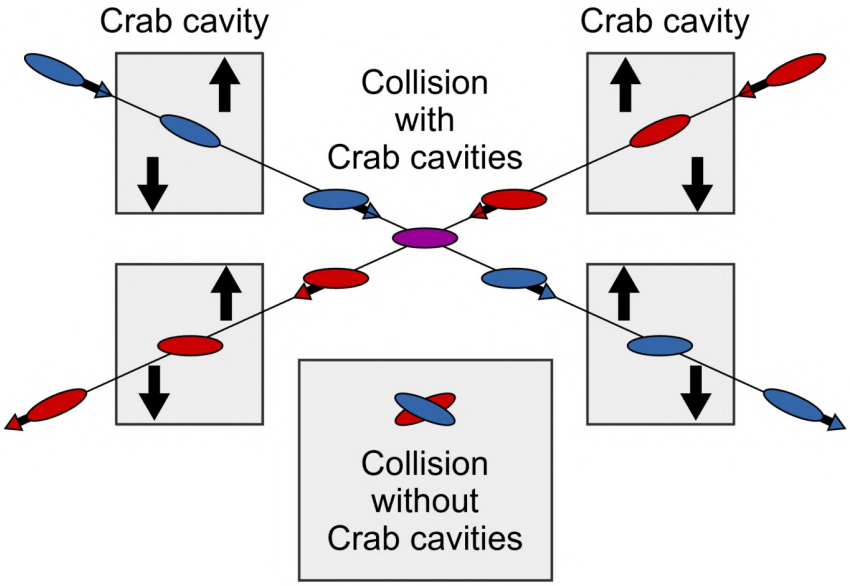

FIGURE 3.10: Effect of the crab cavities on the proton colliding bunches.

3.4 The ATLAS upgrades

In HL-LHC an average number of 200 proton-proton interactions happening per bunch crossing is expected. This is a huge increase with respect to the current average interaction number which is around 30. The detector has to overcome two main challenges in order to maintain its excellent performance; the radiation damage caused due to the high integrated luminosity and the increased pile-up due to the high instantaneous luminosity. Significant upgrades to the ATLAS sub-detector systems is foreseen in order to deal with these challenges. The major upgrades are described in the following sub sections.

3.4.1 ITk

For the HL-LHC, the current ID of ATLAS will be replaced by an all-silicon Inner Tracker (ITk). The layout of ITk in the r-z projection is shown in fig 7.1; it consists of five-layers of pixel detectors (drawn in red) with about 5 billion readout channels and four layers of strip detectors (drawn in blue) with around 50 million readout channels. The ITk design provides a high tracker pseudorapidity coverage up to $|\eta| = 4$ which is a big improvement with respect to the previous ID coverage up to $|\eta| = 2.5$. This will allow for the track reconstruction of forward objects, which was not possible before, and therefore allow the more precise study of physics processes that are expected to have experimental signatures in the forward region, like the VBS process studied in this thesis. Moreover the ITk design offers a much reduced

material budget with respect to the previous ID as shown in Figure 3.12. This is an important improvement that is expected to minimize effects of multiple scattering and energy losses.

For the five-layered pixel detector of ITk [45], two different silicon pixel detector technologies are considered; 3D sensors for the innermost layer and planar sensors for the rest of layers. The innermost layer will use a mixture of pixel geometries; a $25\,\mu\text{m} \times 100\,\mu\text{m}$ pixel size for the barrel region, and a $50\,\mu\text{m} \times 50\,\mu\text{m}$ pixel size for the endcaps. Planar sensors will have a pixel size of $50\,\mu\text{m} \times 50\,\mu\text{m}$ in all regions. Both planar and 3D sensors will use an n-implant in p-substrate technology with a thinner thickness compared to the current pixel detector. The n-in-p sensors are in general more radiation hard since they do not suffer from type inversion of the substrate material, while the thin sensor design allows for charge and hit efficiency saturation at lower bias voltages, leading to a reduction of dissipated power.

The Strip Detector [46] covers a pseudo-rapidity of $|\eta| < 2.7$ and is composed of four layers in the barrel and 6 disks in the end-caps. It will be instrumented with silicon-strip modules of different lengths; short-strips with a length of 24.1 mm for the innermost layers and long strips with length of 48.20 mm for the outmost layers. The combined strip plus pixel detector provides a least nine hits for all particles with $p_T > 1$ GeV allowing for tighter track selections without compromising the reconstruction efficiency.

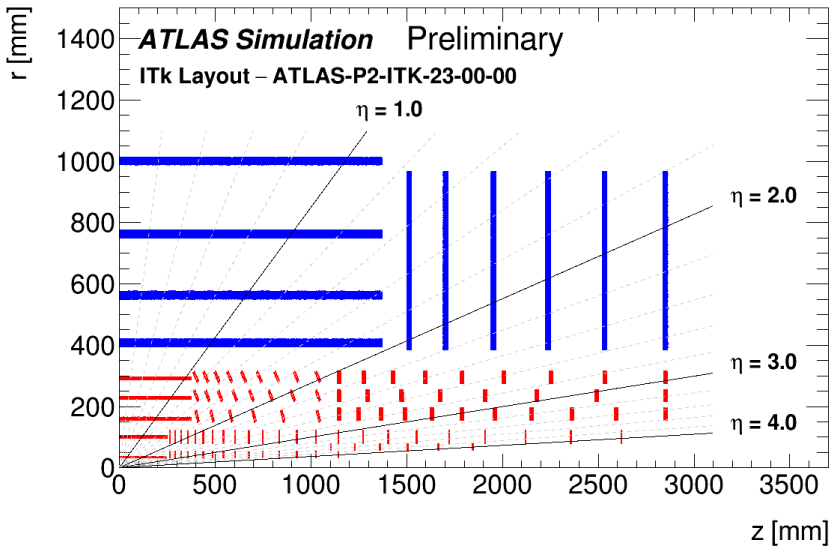

FIGURE 3.11: The ITk layout

3.4.2 High Granularity Timing Detector

The High Granularity Timing Detector (HGTD) [47] is a novel detector planned to cover a pseudorapidity range of 2.4< η <4.0. Its main purpose is to improve the tracking and pile-up mitigation in the challenging forward region by providing precise timing information. The detector is foreseen to be installed between the ITk and the LAr forward calorimeter and is expected to have an excellent timing resolution of 50 ps. It will use Low Gain Avalanche Detector (LGAD) silicon sensors with pixel size of 1.3 mm $\times$ 1.3 mm.

3.4.3 Calorimeter

The calorimeter upgrade mainly includes the upgrade of the readout electronics and is scheduled in two stages: Phase-1 [48] and Phase-2 [49]. The Phase-1 upgrade is related to the

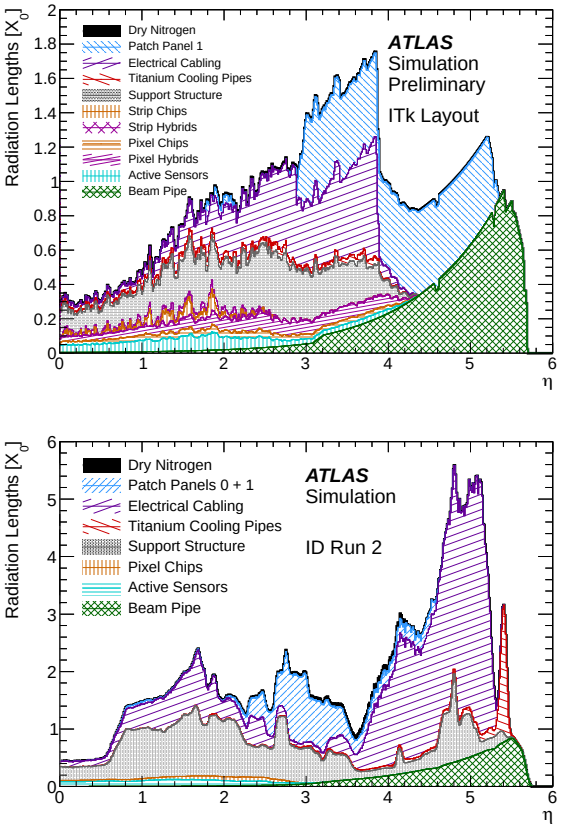

FIGURE 3.12: Comparison of the material budget measured in radiation lengths X_0 versus η for the ITk design (top) and the current Inner Detector during Run 2 (bottom).

trigger electronics and is programmed during the second Long-Shutdown (LS2) from 2019-2021. A finer granularity of the trigger readout is foreseen, which will improve by a lot the sensitivity to the electro magnetic shower development in the calorimeter. In this way shower shape related variables can be reconstructed allowing for additional selection criteria based on these variables, which can significantly improve the background rejection and decrease the trigger rate. The Phase-2 upgrade, planned during LS3, from 2026 to 2028, includes a replacement of the main read-out electronics as well as the low-voltage powering system of the LAr calorimeter in order to cope with the high-radiation environment expected in HL-LHC.

3.4.4 Muon spectrometer

The muon spectrometer of the ATLAS detector will be significantly upgraded in two Phases. In Phase-1, the CSC and the MDT chambers of the innermost end-cap wheels will be replaced by the New Small Wheels (NSWs) [50], which are a combination of two detector technologies; the small-strip Thin Gap Chambers and the Micromegas (Micro Mesh Gas Detectors). The new TGCs are an improved version of the currently used ones, but with a better resolution. Micromegas are micro pattern gaseous detectors and will be installed for the first time in ATLAS. They are composed of two parallel plates, filled with gas and separated by a micro pattern mesh which is located at a distance of about $100\,\mu\mathrm{m}$ from the anode plate. A strong electric field of about 40-50 kV/cm is applied between the mesh and the anode (amplification region), while a much lower electric field is used between the mesh and the cathode (drift region). A charged particle going through the drift region will ionize the gas and the liberated electrons will drift towards the mesh passing in the amplification region where the avalanche happens. The created signal is finally read out by the well segmented anode plate. Due to their fast amplification process Micromegas have a time resolution of a few nanoseconds. The slower signal induced on the anode is coming from the typically slow positive ions produced in the amplification process and moving back to the mesh. Due to the short distance they have to cross they are usually collected fast. The fast evacuation of the ions constitute Micromegas particularly suitable for high particle rate operations.

In the Phase-2 upgrade [**MuonsPhase2:2017**], a large fraction of the frontend and on- and off-detector readout and trigger electronics for the RPCs, TGCs, and MDTs chambers will be replaced so they are able to cope with the higher trigger rates and longer latencies necessary for the new trigger. Additional RPC chambers will be installed in order to increase the trigger acceptance, while part of the MDT chambers will also be replaced by newer small-diameter MDTs. A Number of the currently used TGC doublets is also foreseen to be replaced by TGC triplet chambers, especially in the barrel-endcap transition regions where high trigger rates coming from random coincidences usually occur.

3.4.5 Trigger upgrade

A new trigger and data acquisition system (DAQ) is foreseen for the HL-LHC period. This is composed of a hardware-based Level-0 (L0) trigger running at 40 MHz input rate and a CPU farm-based Event Filter (EF) running at 1 MHz input rate. This trigger is based on a hardware system composed of the L0 Calorimeter Trigger (L0Calo), the L0 Muon Trigger (L0Muon), the Global Trigger and the Central Trigger (CTP) sub-systems [51]. L0Calo provides reconstruction of calorimeter objects exploiting the full calorimeter coverage of ATLAS, while L0Muon provides muon reconstruction with sophisticated algorithms. A new feature of the L0Muon trigger is that it will include MDT information for the muon transverse momentum estimation. After L0Calo, calorimeter objects are improved at the Global Trigger through energy data

coming directly from upgraded calorimeter pre-processors, as well as, by exploiting offline-like algorithms such as anti-k_t jet finding. Additionally, the Global Trigger combines inputs from L0Calo and L0Muon in order to apply selections based on kinematic requirements. The output of L0 is then provided to the EF. The main function of the EF is to refine the selection of the 1 MHz L0 output events using sophisticated offline-like reconstruction techniques allowing to reduce the final output rate to a proper disk storage value [51].

4. Particle reconstruction with the ATLAS detector

This chapter is dedicated to the techniques developed by the ATLAS collaboration in order to reconstruct meaningful physics objects (e.g. electrons, muons) from the raw data collected by the current ATLAS detector. In Section 4.1 the track and vertex reconstruction procedure is first described. Next the reconstruction of electrons and muons are detailed in Sections 4.2 and 4.3 respectively. Following an overview on the reconstruction of hadronic objects, namely jets, is given in Section 4.4. Finally, the reconstruction of neutrinos is discussed, through the missing transverse energy estimation, in Section 4.5

4.1 Track and Vertex Reconstruction

Tracks are trajectories left by charged particles in the ID. The track reconstruction [52] begins with the formation of clusters from hits in the pixel and SCT detectors. Three-dimensional space points are created from these clusters, representing the interaction points between the charged particle and the active material of the ID. In the pixel detector, each cluster equates to one space-point, while in the SCT, clusters from both stereo views of a strip layer must be combined to obtain a three-dimensional measurement [53]. Track seeds are then formed by combining the 3D space points of the four pixel layers and the first SCT layer. Track candidates are next built by employing a combinatorial Kalman filter [54] , which uses additional space points from the rest of ID layers. Multiple track candidates per seed are created in case more than one space points are found to be compatible with the preliminary trajectory. The arising ambiguities are resolved by assigning each track candidate a score based on different quality criteria; like the intrinsic resolutions and multiplicities of the clusters assigned to the track, the χ^2 of the track fit or the track momentum. Tracks with bad scores are rejected. The ambiguity algorithm is also employing an artificial neural network (NN) trained to identify merged clusters. Cases where clusters are not identified as merged and are used by multiple tracks candidates, are most probably due to wrong assignments. After all ambiguities are resolved, a high-resolution fit is performed and the fitted tracks are added to the final collection.

The quality of the reconstructed tracks is usually defined by two parameters; the transverse impact parameter significance, d_0/σ_{d_0}, given by the distance between the proton beam and the track's closest approach point to the beam and divided by its significance. The second is the longitudinal impact parameter z_0, defined as the distance of the track from the primary vertex measured along the beam axis. An illustration of these two parameters is shown in Figure 4.1.

The vertex reconstruction [55] is performed in two stages; the vertex finding and fitting. In the first stage, tracks satisfying specific selection criteria (e.g. having similar impact parameters) are used to identify vertex seed positions. An iterative fit is then performed in the second stage using the tracks and vertex seed as inputs in order to find the best vertex position. Tracks that are less-compatible with the estimated vertex are down weighted during the fit and the vertex position is recalculated. After the vertex position is fixed, tracks that are highly incompatible with it are removed, and used for the reconstruction of other vertices. By the end of the procedure, all tracks are associated to a vertex. The vertex of biggest interest, the so-called hard-scatter (HS) vertex, is chosen by convention to be the one with the largest sum of transverse momentum square of associated tracks. The rest, less energetic vertices, are

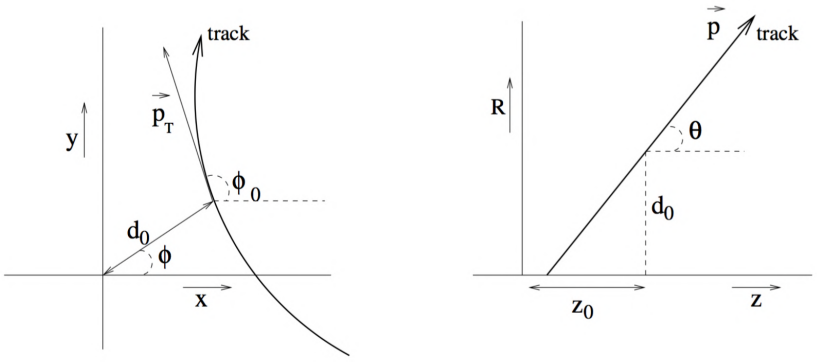

FIGURE 4.1: Illustration of the perigee parameters of a track in the transverse plane (left) and RZ-plane (right), as defined in the global ATLAS tracking frame

referred to as pile-up (PU) vertices.

4.2 Electrons and photons

Electrons and photons are reconstructed within $|\eta|$ <2.47, excluding the barrel-to-end-cap transition region between 1.37< $|\eta|$ <1.52, using information from the EMCAL and the ID. Since they have different charges, they interact with the detector in different ways. Electrons being charged, are expected to leave a signature both in the ID and calorimeter, while photons are primarily expected to leave a signature in the calorimeter system only. However, in the case that a photon is converted to an electron-positron pair before reaching the calorimeter a pair of tracks originating from a dis-placed conversion vertex are also expected in the ID. These characteristics are taken into account during the reconstruction. A schematic illustration of the path of an electron through the detector is shown in Figure 4.2.

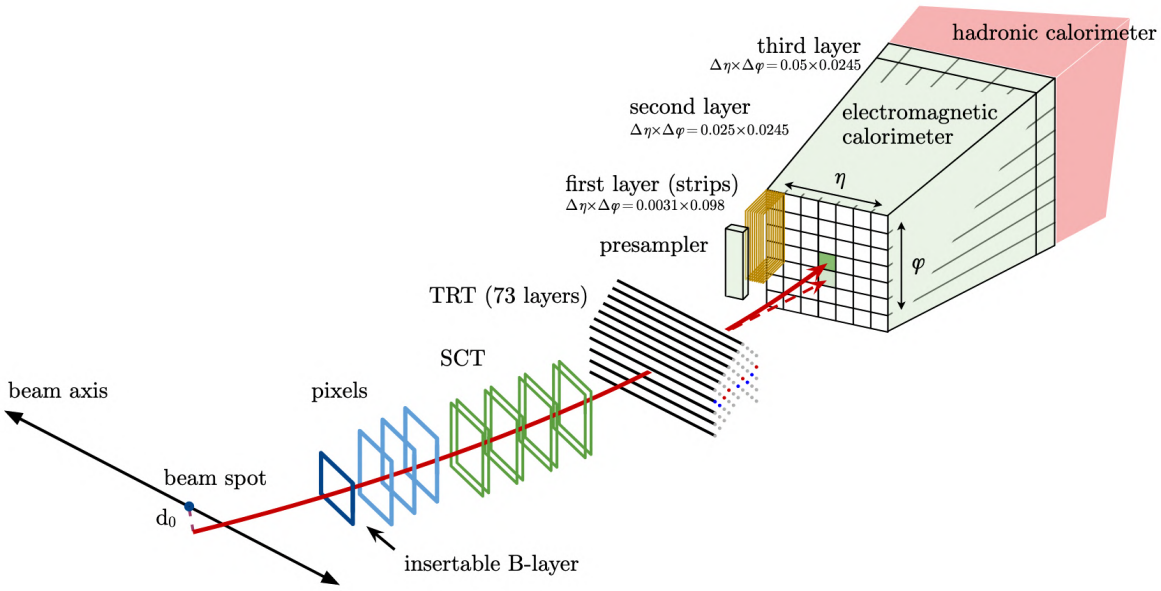

FIGURE 4.2: Schematic representation of the path of an electron through the detector. The red line shows the hypothetical path of an electron as it passes through the tracking system (pixel detectors, then silicon-strip detectors and lastly the TRT) and then enters the electromagnetic calorimeter. The dashed red trajectory shows the path of a photon produced by the interaction of the electron with the material in the tracking system [53].

The electron reconstruction [53] starts by employing a clustering algorithm to form cluster seeds from energy deposits in the various calorimeter layers. Electron candidates are reconstructed by matching seed clusters to ID tracks. Tracks are built from hits in the ID layers, similarly to what is discussed in 4.1. Electrons can lose a significant amount of energy due to bremsstrahlung when interacting with the material they traverse [53]. The radiated photons can convert into electron-positron pairs which can further interact with the detector material. Thanks to their, rather collimated way of emission, they are usually reconstructed as part of the same electromagnetic cluster. However, such interactions may occur before the inner-detector volume, generating multiple tracks in the inner detector. Therefore, it is possible to produce and match multiple tracks to the same electromagnetic cluster, all originating from the same primary electron [53]. If several ID tracks are found to fulfill the matching criteria, the track which is closest in ΔR to the cluster and has at least four hits in the silicon detector, is selected to be the primary electron-track candidate. The electron candidate is required to originate from the HS vertex and have no association with a vertex from a photon conversion. In case a seed cluster can't be matched to any of the tracks, it is tagged as an unconverted photon. Finally, if there is a track pair matched to the seed cluster, compatible to an electron-positron pair, the cluster is identified as a converted photon. Clusters with single tracks that have no hits in the silicon detector are also tagged as converted photons in order to increase the detection efficiency of converted photons.

Electrons are further classified to three categories: loose, medium or tight based on a likelihood-based discriminant response. The purpose of the discriminant is to reduce the misidentification of other objects as electrons by taking into consideration the typical shape of electromagnetic showers. The three defined working points: tight, medium and loose, correspond to an efficiency of 80%, 88% and 93%, respectively, for an electron with E_T = 40 GeV. Photons on the other hand are classified into two categories; loose or tight.

4.3 Muons

Muons [56] are picked out by matching ID to MS tracks. Following, the muon reconstruction proceeds by performing a simultaneous fit to the ID and MS information, taking also into account energy losses in the calorimeter. Muon candidates are required to pass additional selection criteria to be identified as prompt particles like the number of hits in each individual sub-detector and the quality of the fit. Similarly to electrons, they are classified in three categories or working points ; loose, medium and tight which correspond to an efficiency of 98.1%, 96.1% and 91.8% for muons with p_{T} = [20, 100] GeV.

4.4 Jet Reconstruction

Due to colour confinement, partons which carry color charge can not be observed isolated in nature. Instead, they hadronise to form colourless states which are then reconstructed as jets of relativistic particles. Several clustering algorithms are available for the purpose of jet reconstruction. The most common one employed by ATLAS is the so-called anti-kT algorithm [57]. The anti-kT is an iterative cone algorithm. It proceeds by identifying the most energetic entity and then merging to it neighboring ones, in descending transverse momentum order, if they satisfy:

$$d_{ij} = min(\frac{1}{k_{ti}^2}, \frac{1}{k_{tj}^2})\frac{\Delta_{ij}R}{R^2} < d_{iB} \tag{4.1}$$

where

$$d_{iB} = \frac{1}{k_{ti}^2} \tag{4.2}$$

In the above equations, k_{ti} and k_{tj}, are the transverse momentum of entities i and j, respectively, and $\Delta_{ij}R$ is the corresponding relative distance between them. The parameter R describes the radius of the reconstructed jet. An important benefit of the anti-kT algorithm with respect to other jet reconstruction methods is that the output jets have a circular shape, allowing for a much easier jet calibration. At the same time, the anti-kT algorithm ensures collinear and infrared safety, meaning that the reconstruction is independent of the particle multiplicity within the hadronic shower, as well as, independent of the initial parton?s soft radiations.

Depending on the selected reconstruction radius R, jets in ATLAS are categorized as small-R jets and large-R jets. Both categories are employed in this thesis. Moreover, the inputs for jet reconstruction are of paramount importance. Historically, the ATLAS experiment has been using solely calorimeter or solely tracker information to reconstruct hadronic jets. During Run 1, the majority of analyses used jets built from topological clusters of calorimeter cells (topo-clusters) [58]. Topo-clusters of calorimeter cells are usually seeded by first selecting cells whose absolute energy measurements exceed the expected noise by four times its standard deviation, and then by merging with neighboring cells with absolute energy about twice the expected noise [58]. The energies of the resulting clusters are calibrated at the electromagnetic(EM) scale and all clusters are considered to be massless. The resulting jets are usually referred to as EMTopo jets. For this thesis work, an alternative approach is used for the jet reconstruction of small-R jets, in which inputs to the clustering algorithm are the so-called particle flow (PFlow) objects, formed from a combination of calorimeter to ID information. More details about the jet reconstruction of small-R jets and large-R jets are given in the following sub-sections.

4.4.1 Small-R Jets

Small-R jets are reconstructed using the anti-k_t algorithm [57] with a radius parameter of R = 0.4. The particle flow algorithm [59] is employed in order to prepare the inputs for the jet reconstruction. The goal of the PFlow algorithm is to remove overlaps between the momentum and energy measurements made in the inner detector and calorimeters, respectively. A schematic of the main algorithm steps is shown in Figure 4.3. As the first step, the algorithm selects well-measured tracks and tries to geometrically match each of the tracks to a single topo-cluster in the calorimeter. The system of track and topo-cluster ideally represents a single particle passing through the detector. Clusters that can not be matched to tracks, usually correspond to neutral particles and are referred to as unmodified neutral clusters. For the matched track/topo-clusters, the expected energy deposited by the particle in the calorimeter is estimated based on the particle momentum and the topo-cluster position. At this stage, the probability that the particle deposited energy in more than one topo-clusters, is also estimated. If this is found to be high, the algorithm adds more topo-clusters to the system, in order to recover the entire shower energy. Finally, the expected energy deposited in the calorimeter by the particle is subtracted cell by cell from the topo-clusters assigned to the track. All the information regarding the passing particle is now entirely described by the single track's kinematics. After the subtraction step, energy left-overs in the calorimeter might be found. If the remnants are compatible with the expected shower fluctuations of a single particle, they are removed. In the case they are found to be significant, they are kept, assuming they were created by another neutral particle and are referred to as modified clusters. From the collection of

tracks, those associated to the hard-scatter vertex of interest, as well as, the full list of unmodified and modified neutral topo-clusters are used as inputs to the jet reconstruction. The PFlow approach is found to improve the jet energy resolution at low p_{T}, where the inner detector has a better resolution [59].

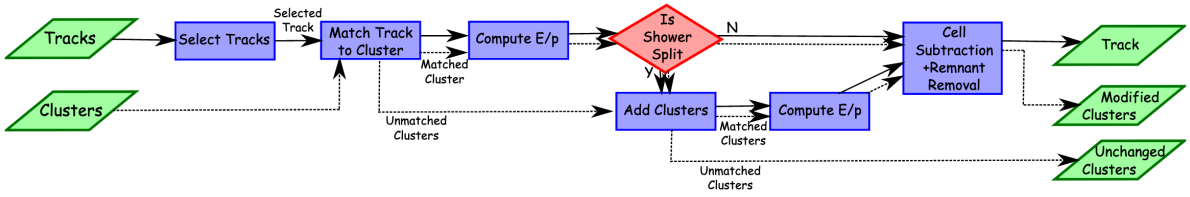

FIGURE 4.3: Schematic of the particle flow algorithm steps.

Calibration

After the PFlow jets are reconstructed, a sequence of corrections are applied, in order to calibrate the jets to the particle-level energy scale [60]. The procedure heavily relies on Monte Carlo simulation and closely follows the scheme used for EMTopo jets described in Refs. [61, 62, 63, 64, 60]. The reconstructed jets are first corrected for pile-up contamination. The corrected jet p_{T} is written:

$$p_{\mathrm{T}}^{corr} = p_{\mathrm{T}}^{reco} - \rho A - \alpha(N_{PV} - 1) - \beta\mu \tag{4.3}$$

where ρ is the median pile-up momentum density, A is the jet area, while N_{PV} and μ are the reconstructed primary vertices and number of pp interactions in the event, respectively. The last two terms are added to account for the linear increase of the jet response with respect to the pile-up conditions. The coefficients α and β are therefore derived from fits to the jet response as a function of N_{PV} and μ, respectively. As discussed above, the tracks associated to pile-up vertices are not considered during jet reconstruction in the PFlow approach. Therefore, the pile-up subtraction, mainly corrects for the pile-up contamination arising from neutral particles. Moreover, due to the reduced pile-up contribution, ρ usually takes lower per-event values for PFlow compared to EMTopo jets [59]. It is worth noting here, that additional pile-up suppression algorithms are also applied to calibrated jets, in order to further mitigate pile-up. These are described in Chapter 5.

Following the pile-up correction, the reconstructed jet energy is brought to the particle level energy scale by comparing the energy of simulated jets in truth and reconstruction level. Truth jets are built from stable particles in the MC generator event record. The corrections to the jet energy response, defined as $R = E_{reco}/E_{truth}$, are derived in bins of truth jet energy E_{truth} and η, with the last added in order to also account for geometrical effects of the detector, such as dead material. This procedure, referred to as numerical inversion calibration, restores the average reconstructed jet energy to the mean value of the truth jet energy. However, differences in the response can arise from other jet characteristics, such as the jet flavour. Such variations are corrected through the so-called global sequential correction that uses additional observables to adjust the jet energy calibration, improving the jet resolution without changing the jet energy scale. Finally, an in-situ calibration of JES is performed, where differences between data and MC simulation are accounted for. Such differences can arise from both the imperfect simulation of the detector response and dead material, as well as, the imperfect knowledge of the physics processes involved (hard-scatter event, pile-up, particle interactions with the detector). The in-situ calibration is usually performed by estimating the jet response in data and MC simulation, separately, and using the ratio to derive additional

corrections [65]. The jet response is estimated by balancing the jet p_{T} to a well measured recoil object. There are three stages of in situ measurements. The first stage, called η intercalibration, corrects the JES of forward jets to agree with that of central jets, by exploiting the p_{T} balance in dijet events. In the second stage, corrections are derived by balancing the jet p_{T} against a calibrated Z boson or photon (Z+jet and γ+jet analyses). In the last step, called the multijet balance (MJB), a system of well-calibrated low p_{T} jets is used to calibrate a single high p_{T} jet. The second and third stages are usually estimated only for central jets. However, thanks to the eta-intercalibration stage the corrections are applicable to forward jets as well. The jet energy resolution (JER) is also measured in-situ. The JER is usually derived in dijet events by exploiting momentum conservation.

A few uncertainty sources are considered related to the various jet calibration steps described above. The full uncertainty in the jet energy scale consists of 125 individual terms. The majority of these terms originate from the in situ measurements. Since there are three stages of in situ calibrations, performed one after the other, uncertainties are propagated from each to the next. These uncertainties mainly account for effects of event topology dependence, MC mis-modelling of the physics process, statistical limitations, as well as, uncertainties associated with the measurement of the reference objects used in the calibration [65]. Additional uncertainties to account for the pile-up mis-modelling in MC, and the flavour dependance, are also considered. The pile-up effects are represented by four nuisance parameters associated to the offset and p_{T} dependance in N_{PV} and μ, as well as, the event topology dependance of the median pile-up momentum density. The pile-up uncertainties are derived from data as described in [65]. The flavour dependance uncertainties are described by two nuisance parameters, and are derived from MC simulation. The first is the jet flavour composition which accounts for the different response of quark- and gluon-initiated jets. It is defined as:

$$\sigma_{composition} = \sigma_g^f \frac{|R_q - R_g|}{f_g R_g + (1 - f_g) R_q}$$

where R_q and R_g are the quark and gluon initiated jet response, respectively, estimated in PYTHIA. The term f_g is the fraction of gluon-initiated jets in the sample, while σ_g^f is the corresponding uncertainty on the gluon fraction. The second uncertainty, referred to as jet flavour response, is added to account for the significantly different response of gluon-initiated jets between different generators. It is defined as:

$$f_g(R_g^{\mathrm{PYTHIA}} - R_g^{Herwig})$$

where R_g^{PYTHIA} and R_g^{Herwig} is the gluon jet response in a MC sample generated with PYTHIA and Herwig, respectively. The flavour uncertainties are usually derived assuming a 50% gluon fraction with a 100% uncertainty.

As already discussed, the JES uncertainties are derived in great detail with a set of 125 nuisance parameters associated to them. However, many times this level of detail is far more than what is required by the majority of analyses. For this reason, alternative uncertainty schemes are also available, which contain a reduced number of nuisance parameters. This reduction is usually performed by combining together only the p_{T} dependent in situ uncertainty components. This combination is usually done in two different ways which results in two different reduction schemes: the so called "global reduction" which combines all p_{T} dependent in situ uncertainties regardless of their origin, and the "category reduction" which combines the p_{T} dependent in situ uncertainties in groups, based on their source (detector, statistical, modelling, or mixed) [65]. The "global reduction" results in a total of 23 nuisance parameters, while the "category reduction" in a total of 30. The "category reduction" scheme is chosen for

the VBS analysis described in Chapter 5.

It is worth noting here, that a single JES component could also be used instead, by adding in quadrature all of the independent components. In that case a single JES uncertainty value would be propagated equally to all jet p_{T} bins. The problem of such approach, appears when the data statistics increases significantly. In that case, low p_{T} regions, containing the majority of statistics, and therefore having the largest statistical power, would constrain the JES uncertainty in the low p_{T} bins. Since a fully correlated approach is chosen (that of a single JES across all p_{T} bins), this constraint would be uniformly propagated to all p_{T} bins. However, such approach is based on an important assumption: that the reduced JES uncertainty is also valid in the high p_{T} bins, which can not be justified.

b-jet tagging

A b-tagging algorithm is used for the identification of jets originating from the hadronisation of b-quarks (b-jets). This is allowed thanks to the relatively long lifetime of b-hadrons (for an energy of about 50 GeV, the average flight length will be 3 mm before the decay) which results to b-hadron decays within the inner detector volume. The tagging of b-jets highly depends on reconstruction of the secondary displaced vertex of the b-hadron decay [66]. Additional kinematic properties of b-jets, such as the mass and their momentum are also employed in order to enhance separation with c- or light-jets originating from u-, -d, -s quarks or gluons. In ATLAS, three complementary algorithms are employed. The first algorithm exploits the large impact parameter of b-jets due to the long lifetime of the b-hadrons, while the second algorithm tries to reconstruct the secondary vertex from the b-hadron decay. Finally, the last algorithm (JetFitter) attempts to reconstruct the full b-hadron decay chain. The b-hadrons are more likely to decay into c-quarks, therefore the algorithm attempts to reconstruct both the b and c decay vertices. The information coming from these algorithms is used as inputs to a Boosted Decisions Tree (BDT) algorithm that uses the ROOT Toolkit for Multivariate Data Analysis (TMVA) [67]. The output BDT score ranges from -1 to 1, and gives an estimation of how much b-quark like is the tested jet (with 1 being closer to a b-quark). Several working points are defined based on their average efficiency on b-jets. The medium working point [68], corresponding to a 70% b-tagging efficiency is chosen for the VBS analysis (Chapter 6). The corresponding mis-tag rate is 16% for c-jets and 0.77% for light-jets [68].

4.4.2 Large-R Jets

High energy particle collisions can result in the production of heavy particles, such as W/Z/H bosons and top quarks, with large Lorentz boosts [69]. The decay products of such particles tend to be highly collimated, or "boosted", in the direction of the parent particle. For such cases, it is preferable to reconstruct the particle's hadronic decay products as a single large-R jet. These large-R jets are expected to carry a characteristic multi-pronged substructure originating from the two- or three-body decay of the hadronically decaying particle. Large-R jets are reconstructed in ATLAS using the anti-k_t algorithm with a radius parameter of R = 1.0. Several different inputs are available for jet reconstruction. Each jet definition provides some benefits over others, depending on the jet p_{T}. The decision of which jet definition to use, is usually made at the level of a physics analysis. A common metric to compare the relative performance of the different definitions is the tagging performance of W/Z bosons and top quarks. The baseline jet definition approach uses topological clusters calibrated at the correct particle-level scale using the so-called local cell re-weighting (LCW) scheme [58]. Similarly to small-R jets, the PFlow reconstruction is also available, offering a better W/Z tagging performance at low p_{T} regions. Alternative approaches use Track-CaloClusters (TCCS) which exploit the energy measurements from topo-clusters and the angular information from

tracks. The TCC reconstruction is found to improve the jet substructure reconstruction in the highest p_{T} jets, allowing for better boosted object identification. A most recent approach by ATLAS combines desirable aspects of PFO and TCC reconstruction in order to achieve optimal performance over the full kinematic range [69]. The new inputs are referred to as Unified Flow Objects (UFOs) and UFO jets are found to greatly improve the tagging performance at high jet p_{T} regions [69]. For the VBS analysis presented in Chapter 6, the baseline LCTopo jet reconstruction is employed. The choice is motivated by the relatively low p_{T} range of the large-R jets studied (of about 200 GeV). In this low p_{T} region, no significant improvements are expected by considering alternative jet definitions.

In order to correct for pile-up effects and soft radiation in the reconstructed large-R jet substructure, a trimming algorithm is used. The trimming algorithm proceeds by re-clustering each large-R jet using the k_t algorithm and a radius of R=0.2 resulting in a collection of subjets for each jet. Sub-jets with a p_{T}^{subjet} less than 5% of the initial jet p_{T} are then removed and the large-R jet four momentum is recalculated. This procedure is usually referred to as "Jet grooming". The sensitivity of searches and measurements that use large-R jets depends on an accurate knowledge of both the transverse momentum and mass responses of the detector [70]. Therefore, a calibration of both the large-R jet energy (JES) and mass scale (JMS) is performed. The calibration, derived from MC simulations, is done in a similar fashion to the small-R jet calibration described previously. The in-situ calibration is performed in two separate steps. In the first step, corrections are derived for the JES, similarly to the in-situ calibration performed for small-R jets. In the second step, the in-situ JMS calibration is performed, after the application of the in-situ JES corrections. The jet mass response is measured from fits to the jet mass peaks formed from by high p_{T} W bosons and top quarks decaying hadronically. A second measurement is done with the so-called R_{trk} method which exploits the independent measurements by the calorimeter and the inner tracker [70]. Similarly to the small-R jets, uncertainties in the JES and JMS are derived by propagating uncertainties from the individual steps to the statistical combination. An overview of the large-R jet reconstruction and calibration procedure is shown in Figure 4.4.

The jet energy resolution (JER) and jet mass resolution (JMR) are also measured in-situ. The JER is derived in dijet events like for small-R jets, while the JMR is extracted from fits to the W boson and top quark mass peaks in tt-bar events.

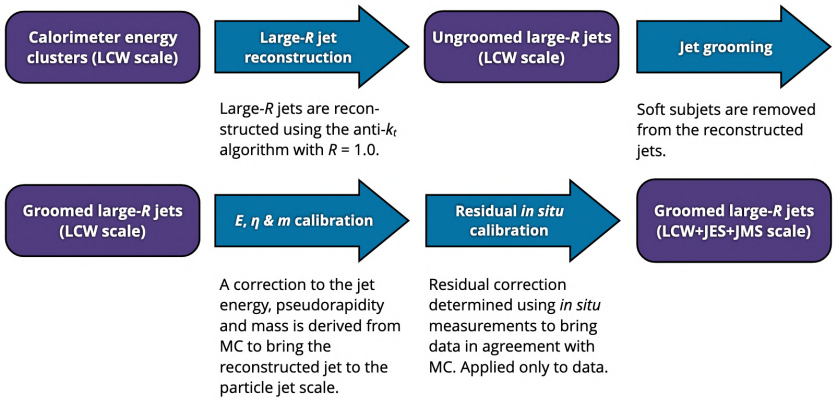

FIGURE 4.4: Overview of the large-R jet reconstruction and calibration procedure [70].

4.5 Missing Transverse Energy

Particles that interact weakly with matter, such as neutrinos, can not be directly measured in the detector. Alternatively, they can be detected indirectly, by exploiting momentum conservation. In the longitudinal direction the initial momentum carried by the quarks is unknown, therefore momentum conservation can not be utilized. However in the transverse direction, the momentum is guaranteed to be zero. Therefore, the total transverse momentum of the final state is expected to be compatible with zero. A significant deviation from a null value can indicate the presence of non-interacting particles. The missing transverse momentum, $\mathbf{E}_{\mathrm{T}}^{\mathrm{miss}}$, is estimated as the negative of the vectorial momentum sum of all reconstructed objects in the detector. In more detail, it given by the following formula:

$$\mathbf{E_T^{miss}} = -\sum_{i\in\{hard\,objects\}} \mathbf{p_{T,i}} - \sum_{j\in\{soft\,objects\}} \mathbf{p_{T,j}} \tag{4.4}$$

The first sum runs over all hard final state objects, while the second sum is added to account for soft objects, like tracks that are not associated to any physical particles, but still contribute to the total event transverse momentum. In order to avoid double counting of energy, only mutually exclusive objects should be considered in the $\mathbf{E}_{\mathrm{T}}^{\mathrm{miss}}$ calculation. Therefore, objects are added in the formula in a particular order, giving priority to electrons, followed by photons, muons and taus, while jets are rejected if they found to overlap with the higher priority particles. The lowest priority is given to the soft-term tracks.

The $\mathbf{E}_{\mathrm{T}}^{\mathrm{miss}}$ resolution is highly affected by the jet component. Jets are objects that are prone to pile-up contamination, which might lead to $\mathbf{E}_{\mathrm{T}}^{\mathrm{miss}}$ mis-estimations. For that reason different $\mathbf{E}_{\mathrm{T}}^{\mathrm{miss}}$ calibrations are available which make use of different working points of the pile-up taggers described in Chapter 5.

5. Forward Jet Vertex Tagging in ATLAS using the particle flow algorithm

In order to enhance the capability of experiments to discover physics beyond the Standard Model, the Large Hadron Collider (LHC) operates at the conditions yielding the highest possible integrated luminosity. As a result, the collisions of proton bunches result not only in large transverse-momentum transfer proton-proton (pp) interactions, but also in additional collisions within the same bunch crossing, primarily consisting of low-energy quantum chromodynamics (QCD) processes. These additional pp collisions are referred to as *in-time pile-up* interactions. Apart from the *in-time pile-up*, there is also the so called *out-of-time pile-up*, which corresponds to energy leftovers in the ATLAS calorimeter from previous or following bunch crossings with respect to the triggered event[1].

In this instance, one is typically concerned about identifying and reconstructing a single primary collision where a physics event of interest occurs amongst the background of the additional proton-proton collisions. For mitigating pile-up jets both ATLAS and CMS use similar techniques based on vertex and jet shape information. However, vertex information can only used for jets within the coverage of the tracking detector, $\mid \eta \mid < 2.5$, which excludes the crucial, for many analyses forward region. Therefore, other techniques for mitigating pile-up in the forward region, $2.5 < \mid \eta \mid < 4.5$, should be employed; topological correlations among particles originating from a pile-up interaction can be exploited in order to identify and reject pile-up jets beyond the coverage of the tracking detector.

In this chapter, the development and performance of such a technique, referred to as the forward jet-vertex-tagger (fJVT) algorithm, using the particle flow (PFlow) algorithm is presented for the first time in ATLAS. In Run 1 of the LHC, the ATLAS experiment used either solely the calorimeter or solely the tracker to reconstruct hadronic jets and soft particle activity. The vast majority of analyses utilised jets that were built from topological clusters of calorimeter cells (topo-clusters) [58]. These jets were then calibrated to the particle level using a jet energy scale (JES) correction factor [61, 62, 63, 64, 60]. For the final Run 1 jet calibration and the beginning of Run 2, this correction factor also took into account the tracks associated with the jet, as this was found to greatly improve the jet resolution [61]. Particle flow introduces an alternative approach, in which measurements from both the tracker and the calorimeter are combined to form the signals, which ideally represent individual particles. The energy deposited in the calorimeter by all the charged particles is removed. Jet reconstruction is then performed on an ensemble of "particle flow objects" consisting of the remaining calorimeter energy and tracks which are matched to the hard interaction. More details on the particle flow algorithm in ATLAS can be found in Ref. [59].

My contribution to this chapter is the development and performance studies of fJVT for PFlow jets, described in sections 5.2 - 5.4. The calibration of the tool, presented in section 5.5, was not performed as part of this thesis work and is presented only for completeness.

5.1 Introduction

[1] In this thesis in-time and out-of-time pile-up are referred as pile-up (PU)

5.1.1 Origin of pile-up jets

Reconstructed small-R jets can be classified into three categories;

- Hard-scatter jets, which have the majority of particles associated to them originating from the hard-scatter interaction vertex of interest.
- QCD pile-up jets, which have the majority of their particles originating from a single QCD pile-up interaction vertex.
- Stochastic pile-up jets, which do not usually receive contributions from a single prevalent source, e.g. can contain particles originating from several pile-up vertices.

A schematic example of the different jet categories is shown in Figure 5.1. Stochastic pile-up jets do not represent, in general, jets with a physical meaning (originating from a single interaction vertex), instead they are built accidentally. The majority of stochastic pile-up jets is due to *out-of-time pile-up*. Such jets are expected to have intrinsic differences in shape and timing with respect to the hard-scatter or QCD pile-up jets, and these differences can be used in order to tag and remove them [71]. On the contrary, QCD pile-up jets can't be distinguished from hard-scatter jets in this way. The most common technique for tagging a QCD pile-up jet relies on vertex association of its particle components. The technique, referred to as Jet Vertex Tagger, is briefly discussed in the following sub-section.

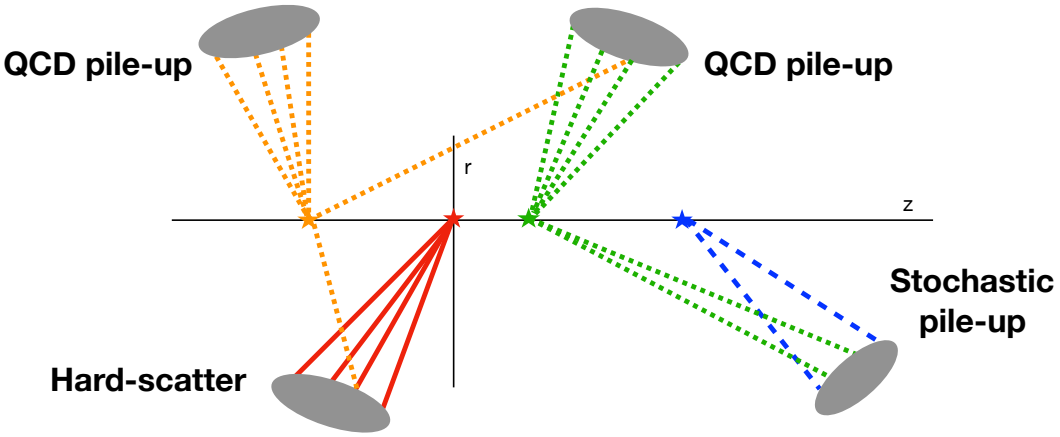

FIGURE 5.1: Schematic example of different jet types.

5.1.2 The Jet Vertex Tagger algorithm

The Jet Vertex Tagger (JVT) algorithm [71] uses a two-dimensional likelihood constructed from the combination of two jet variables, corrJVF and $R^0_{p_T}$, defined as:

$$\text{corrJVF} = \frac{\sum p_T^{\text{track}}(\text{PV}_0)}{\sum p_T^{\text{track}}(\text{PV}_0) + \frac{\sum_{i\geq 1}\sum p_T^{\text{track}}(\text{PV}_i)}{k\cdot n_{\text{trk}}^{\text{PU}}}} \tag{5.1}$$

and

$$R^0_{p_T} = \sum_{\text{trk}} \frac{p_T^{\text{trk}}(\text{PV}_0)}{p_T^{\text{jet}}} \tag{5.2}$$

where PV_i corresponds to the reconstructed vertex i of the event (with $i = 0$ corresponding to the identified hard-scatter vertex). The term $\sum p_{\mathrm{T}}^{\mathrm{track}}(\mathrm{PV}_0)$ seen in both relations is the scalar p_{T} sum of the tracks that are associated to the jet and originate from the hard-scatter vertex, while the $\sum_{i\geq 1}\sum p_{\mathrm{T}}^{\mathrm{track}}(\mathrm{PV}_i)$ term in equation 5.1 represents the scalar p_{T} sum of the tracks that are associated to the jet and originate from pile-up vertices. The last, is divided by a factor $k \cdot n_{\mathrm{trk}}^{\mathrm{PU}}$, with $k = 0.01$, in order to correct for the linear increase of the numerator as a function of the total number of pile-up tracks per event [71]. Finally, the term $p_{\mathrm{T}}^{\mathrm{jet}}$ in equation 5.2 represents the full calibrated jet p_{T}.

As already discussed in 5.1.1, hard-scatter jets are expected to have the majority of the tracks associated to them originating from the hard-scatter vertex (PV_0). Therefore, corrJVF is expected to take values close to 1 for hard-scatter jets, while have much smaller values for pile-up jets. Similarly, $R_{p_{\mathrm{T}}}^0$ is expected to take larger values for hard-scatter jets. In the final JVT discriminant, jets with JVT values close to one are accepted as most likely being hard-scatter jets, while jets with smaller JVT values are tagged as pile-up and are removed. For PFlow jets, two working points are defined, "medium" and "tight", corresponding to JVT > 0.2 and JVT > 0.5 cuts, and yielding high HS efficiencies of 97% and 96% respectively.

5.2 Event Reconstruction

5.2.1 Monte Carlo samples

Dijet events produced from pp collisions at $\sqrt{s} = 13$ TeV are simulated with the PYTHIA8 [72] event generator. Besides the generated primary pp collision, a set of additional, pile-up, interactions are overlaid for each event. Both the effect of in-time as well as out-of-time pile-up is simulated using minimum-bias events generated with PYTHIA8 to reflect the pile-up conditions during the 2017 data-taking period with a mean number of overlaid interactions of $\sim$39, using the A3 tune [73] and the NNPDF23LO [74] PDF set. A sample of Z bosons decaying into a pair of opposite charge muons, produced with jets (($Z \rightarrow \mu\mu$) + jets) is generated with POWHEG + PYTHIA8 [75] interfaced with the AZNLO tune [76] and the CTEQ6L1 [77] PDF set. All generated events are processed with a detailed simulation of the ATLAS detector response, based on GEANT 4 [78], and subsequently reconstructed and analysed in the same way as the data.

Vertices and tracks

The reconstructed primary vertex with the largest $\sum p_{\mathrm{T}}^2$ of constituent tracks is defined to be the hard scatter primary vertex in each event, as described in Ref. [71]. To avoid the convolution of the results of this study with the selection efficiency of the primary vertex, the reconstructed primary vertex z-coordinate is required to be within 0.1 mm ($|\Delta z|$ <0.1 mm) of the position of the true hard-scatter interaction. Note that for QCD events this distinction is arbitrary as all the overlaid in-time pile-up events also produce QCD-like collisions. Since the primary interaction is of the same type as the overlay interactions[2], the hardest interaction will sometimes be one of the pile-up interactions. When this happens, the reconstructed primary vertex with the largest $\sum p_{\mathrm{T}}^2$ will correspond to the hardest pile-up interaction, and not to the primary interaction. Since the MC samples do not contain any truth particle information of the overlay interactions, it is not possible to identify which jets originate from the true hard scatter in these events. The potential bias from the $|\Delta z|$ <0.1 mm cut, rejecting events for which the pile-up vertex is more energetic than the primary interaction vertex, was studied

[2]The primary event is a non-diffractive QCD process, commonly referred to as a "dijet event", while the overlay events are inelastic processes that consist to about 25% of diffractive and 75% non-diffractive pp interactions.

and found to be negligible.

Tracks originating from the hard-scatter primary vertex are required to have $|z_0 \sin(\theta)|$ <2 mm, where z_0 is the distance of closest approach of the track to the hard-scatter primary vertex along the z-axis. All tracks are required to have $p_{\mathrm{T}} > 0.5$ GeV and to satisfy quality criteria designed to reject poorly measured or fake tracks. Tracks are assigned to primary vertices based on the track-to-vertex matching resulting from the vertex reconstruction. Tracks that are not matched to any vertex are not considered.

Inputs to jet reconstruction

The particle flow (PFlow) jet reconstruction algorithm is employed in this study (Section 4.4). In particle flow, a cell-based energy subtraction algorithm is applied in order to remove overlaps between the momentum and energy measurements made in the inner detector and calorimeters, respectively.

The inputs to the jet reconstruction are the PFlow objects, which are the ensemble of positive energy topo-clusters surviving the energy subtraction step of the PFlow algorithm, within $|\eta| < 2.5$, and the selected tracks that are matched to a primary hard-scatter or pile-up vertex. Prior to jet-finding, the topo-cluster η and ϕ are recomputed with respect to the primary vertex (PV) position, rather than the detector origin.

Outside the geometrical acceptance of the tracker, $|\eta| > 2.5$, only the calorimeter information is available. Hence, in the forward region, the topological clusters, formed from calorimeter cells with significant energy depositions, are used as inputs to jet reconstruction.

Jets

Jets are reconstructed using the anti-k_t algorithm [57] as implemented in FastJet [79], with a radius parameter of $R = 0.4$. The inputs to FastJet are the particle flow objects discussed above. After jets are built, a sequence of corrections are applied to calibrate the jets to the particle-level energy scale, as described in Ref. [60]. The calibrated jets are required to have a $p_{\mathrm{T}} > 20$ GeV and are divided into two categories: those with $|\eta| < 2.5$, in order for most of their charged particles to be within the tracking coverage (central jets), and those with $|\eta| > 2.5$ (forward jets).

Jets built from particles in the Monte Carlo generator event record ("truth particles") are also considered. Truth-particle jets are reconstructed using the anti-k_t algorithm with a radius parameter of $R = 0.4$ from stable[3] final-state truth particles from all interactions (hard scatter and in time pile-up).

The reconstructed jets are classified as hard-scatter or pile-up jets based on truth particle information. More specifically; jets are labelled as hard-scatter (HS) if a truth-particle hard-scatter jet with $p_{\mathrm{T}} > 10$ GeV is found within ΔR <0.3[4] and as pile-up jets if no truth-particle hard-scatter jet with $p_{\mathrm{T}} > 10$ GeV is found within ΔR <0.6. A schematic of the geometrical matching is shown in Figure 5.2.

Pile-up jets built from the truth-particle container by construction do not account for out-of-time pile-up effects.Therefore the truth particle information can further be used to label the

[3]Truth particles are considered stable if their decay length $c\tau$ is greater than 1 cm. A truth particle is considered to be interacting if it is expected to deposit most of its energy in the calorimeters; muons and neutrinos are considered to be non-interacting.

[4]Angular distance is measured in units of $\Delta R = \sqrt{(\Delta\phi)^2 + (\Delta\eta)^2}$.

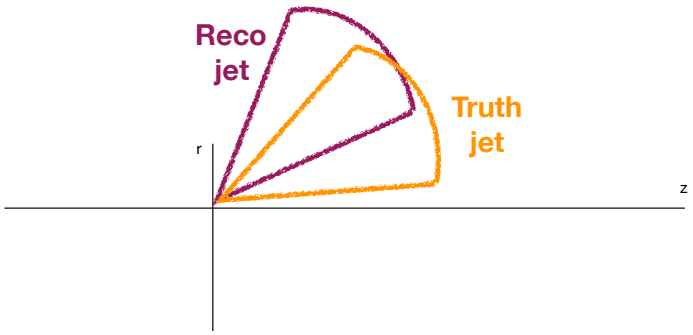

FIGURE 5.2: Schematic example of geometrical matching of reconstructed and truth jets

pile-up jets as QCD or stochastic. The reconstructed pile-up jets are classified as QCD pile-up jets if they are matched within ΔR <0.3 to a truth-particle pile-up jet or as stochastic pile-up jets if no truth-particle pile-up jet is found within ΔR <0.6. A truth-particle $p_{\mathrm{T}} > 10$ GeV requirement is applied in both cases.

Muons

Muons are built from an inner detector track (for $|\eta| < 2.5$) and a muon spectrometer track. Muons are required to satisfy $p_{\mathrm{T}} > 10$ GeV as well as reconstruction quality and isolation criteria [56]. A veto on cosmic-ray muons is also applied. For selecting the $Z \to \mu\mu$ events, two muons of opposite charge are further required, such that their invariant mass lies within the Z boson mass[5].

5.3 The Forward Jet Vertex Tagger algorithm

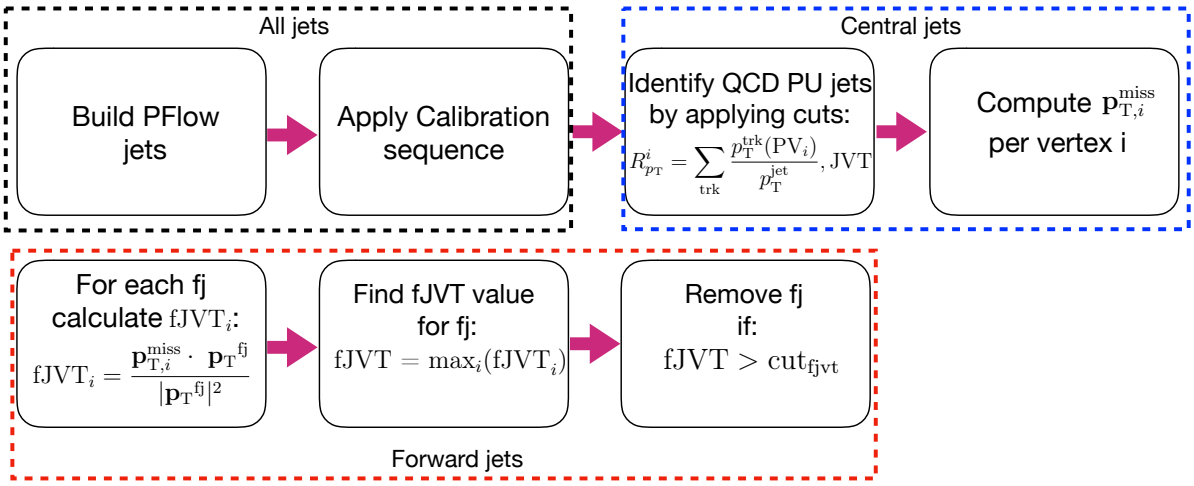

FIGURE 5.3: The forward JVT algorithm using particle flow jets. Central jets correspond to jets with $|\eta| < 2.5$. Forward jets (referred to as fj) correspond to jets with $2.5 < |\eta| < 4.5$.

The main algorithm steps are summarized in Fig. 5.3. The forward JVT algorithm employs momentum conservation for each pile-up vertex of the event in order to tag a forward PFlow jet as pile-up. For this purpose jets associated to pile-up vertices are necessary. In the PFlow approach, jets associated to pile-up vertices are removed [6]. Therefore, as the first step, central

[5] $|m_{\mu^+\mu^-} - m_Z| < 25$ GeV.
[6] only jets associated to the hard-scatter vertex are available

jets are reconstructed for every pile-up vertex i[7] and the relevant energy calibration is applied. This "per-vertex" jet reconstruction is required by the particle flow algorithm, and is different with respect to the fJVT algorithm applied to calorimeter jets, for which calorimeter jets are reconstructed "per-event" and then matched to vertices [71]. In order to re-assure that the jet reconstruction employed here is in agreement with the nominal reconstruction employed by ATLAS, hard-scatter jets are reconstructed and are compared to the baseline ATLAS pflow jets. In Figure 5.4 the corresponding maps in p_{T} and η bins are plotted for reconstructed and baseline PFlow jets. The baseline 2D map is subtracted from the reconstructed one in Figure 5.4(c). In general a good agreement is observed. Most of the difference comes at high eta since the algorithm explicitly rejects clusters with $\mid \eta \mid > 2.5$.

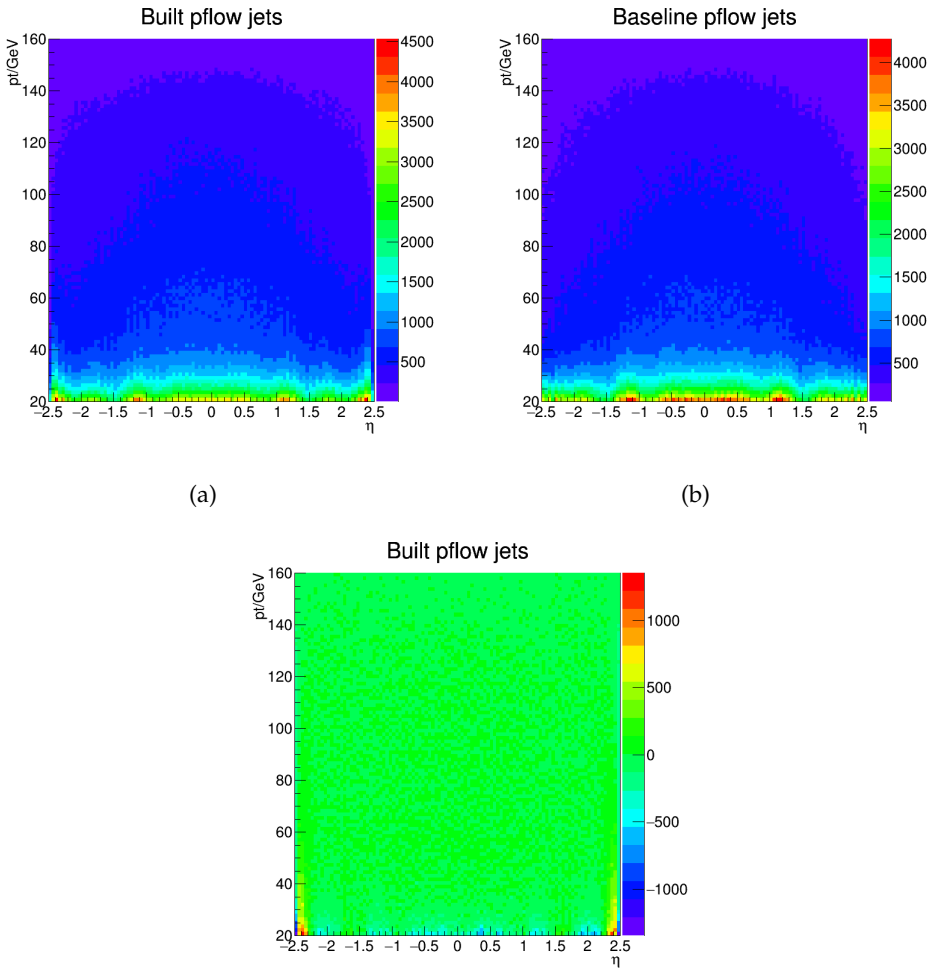

FIGURE 5.4: (a)Reconstructed PFlow jets originating from the hard-scatter vertex (b) Baseline ATLAS PFlow jets (c) difference between the two maps.

Following the particle flow jet reconstruction and calibration, the QCD pile-up jets are distinguished from stochastic pile-up jets in the central region. This step is of paramount importance since stochastic pile-up jets are not objects with a physical meaning, therefore we don't want to include them in the missing transverse momentum estimation happening in the next step. Different discriminants have been tested;

[7]The positive-energy topo-clusters (described in section 5.2.1) are treated inclusively for all vertices here.

- An extension of the $R^i_{p_T}$ variable defined in 5.2 is calculated with respect to any pile-up vertex i:

$$R^i_{p_T} = \sum_{\text{trk}} \frac{p_T^{\text{trk}}(\text{PV}_i)}{p_T^{\text{jet}}} \tag{5.3}$$

  QCD pile-up jets are expected to have the majority of the tracks associated to them originating from the same pile-up vertex (PV_i), and thus have large values of $R^i_{p_T}$. Tracks associated with stochastic pile-up jets are not likely to originate from the same pile-up vertex, thus yielding small $R^i_{p_T}$ values. In the case of PFlow, the stochastic pile-up jets seen, are due to the positive-energy topo-clusters participating in the jet reconstruction. Jets for which a large fraction of their momentum is due to topo-clusters, are more likely to be stochastic jets. The $R^i_{p_T}$ variable for all the reconstructed pile-up jets with $p_T > 20$ GeV and $|\eta| < 2.5$, is plotted in Figure 5.5(a). As expected, $R^i_{p_T}$ tends to take larger values for QCD pile-up jets.

- Jet timing defined as the energy square weighted average of the timing of the constituent topo-clusters: $t_{jet} = \frac{\sum E^2_{clus} t_{clus}}{\sum E^2_{clus}}$. The cluster timing is defined with respect to the bunch crossing time. The jet timing distribution is shown in Figure 5.5(b) for jets with $p_T > 20$ GeV and $|\eta| < 2.5$. QCD pile-up jets usually have a timing close to 0 ns. On the other hand, stochastic pile-up jets, receiving large contributions from out-of-time pile up, have a wider timing distribution.

- Cluster timing where we require the timing of the topo-clusters, participating in the jet reconstruction step described above, to have a timing $t_{pfo} < 12$ ns.

- Jet width defined as: $w = \frac{\sum_k \Delta R(jet,k) p^k_T}{\sum_k p^k_T}$ where the index k runs over the jet constituents and $\Delta R(jet, k)$ is the angular distance between the jet constituent k and the jet axis. The jet width is considered a useful observable for identifying stochastic jets, as the average width is significantly larger for jets with a smaller fraction of energy originating from a single interaction [71]. However, as shown in Figure 5.5(c), the jet width is found to have small discrimination power in this study.

Several cut values on the R_{p_T}, jet timing and cluster timing were tested and the performance was evaluated in the final discriminant. A jet timing cut of 12 ns and $R_{p_T} > 0.1$ are found to have equally good performances. For simplicity, a value of $R^i_{p_T}$ greater than 0.1 is chosen to optimally reject stochastic pile-up jets. Moreover, a cut of $JVT < 0.2$, as described in 5.1.2, is also applied in order to ensure that hard-scatter central jets are not taken into account. The efficiency of the JVT cut is very high, rejecting 98.8% of the hard-scatter central jets.

The missing transverse momentum per vertex i, ($\mathbf{p}^{\text{miss}}_{\text{T},i}$), is then calculated as

$$\mathbf{p}_{\text{T},i}^{\text{miss}} = -\Big(\sum_{\text{jets, } p_T^{\text{jet}}>20 \text{ GeV}} \mathbf{p}_T{}^{\text{jet}} + \sum_{\text{tracks, } p_T^{\text{jet}}<20 \text{ GeV}} \mathbf{p}_T{}^{\text{track}} + \sum_{\text{tracks, jets fail } R^i_{p_T} \text{ cut}} \mathbf{p}_T{}^{\text{track}} \Big) , \tag{5.4}$$

where the components correspond to:

- The vector sum of all the central jets with transverse momentum $p_T^{\text{jet}} > 20$ GeV,

- The vector sum of the tracks transverse momentum for the jets with $p_T^{\text{jet}} < 20$ GeV,

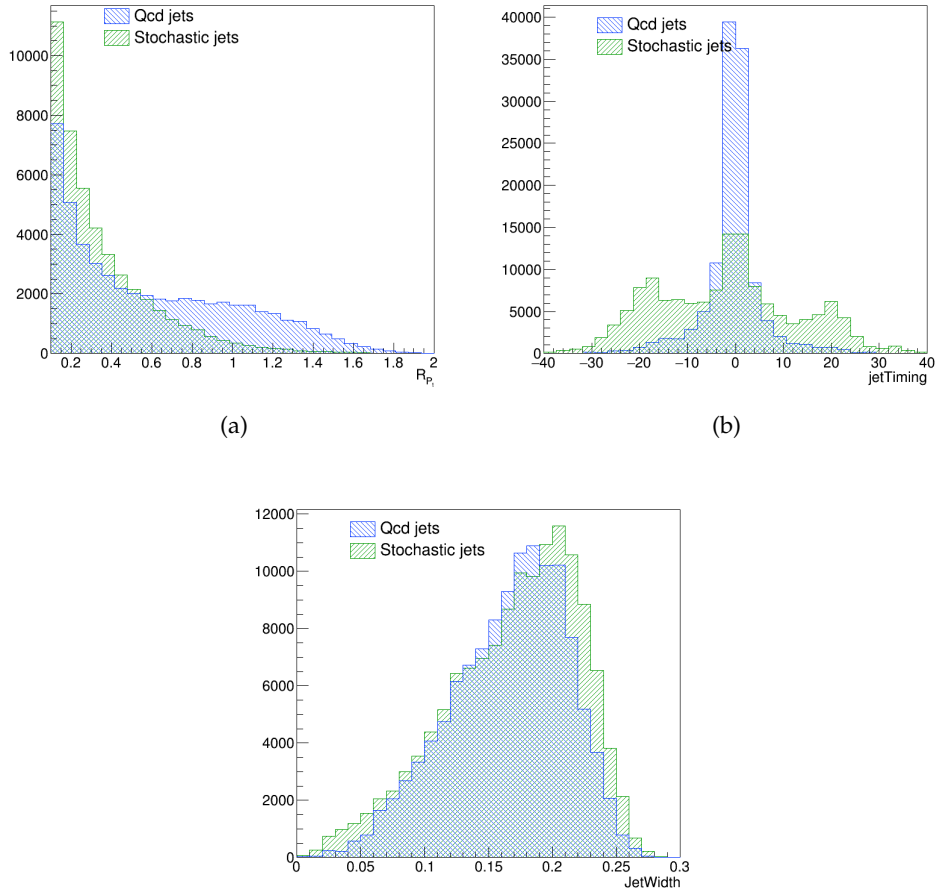

(a) (b)

(c)

FIGURE 5.5: Variables tested for QCD pile-up versus stochastic pile-up jet discrimination.

- The vector sum of the tracks transverse momentum of the tracks associated to the jets that were rejected with the $R^i_{p_T}$ cut at the previous step of the algorithm.

Finally, for every forward jet, the normalized projection of $\mathbf{p}^{\text{miss}}_{\text{T},i}$ on the direction of the forward jet,

$$\text{fJVT}_i = \frac{\mathbf{p}^{\text{miss}}_{\text{T},i} \cdot \mathbf{p}_{\text{T}}{}^{\text{fj}}}{|\mathbf{p}_{\text{T}}{}^{\text{fj}}|^2} \tag{5.5}$$

is computed. The final forward JVT (fJVT) discriminant is then defined as

$$\text{fJVT} = \max_i(\text{fJVT}_i)\ . \tag{5.6}$$

For a forward pile-up jet, it is expected that its energy will be balanced by the $\mathbf{p}^{\text{miss}}_{\text{T},i}$ of a pile-up vertex i, leading to fJVT values close to 1. A schematic view of the algorithm is shown in Figure 5.6. In this example, the missing momentum of pile-up vertex 1 is fully balancing the forward jet p_{T}. On the contrary, this effect is not present at the case of hard-scatter forward jets, resulting in fJVT values closer to 0. Therefore, a forward jet is tagged as pile-up if its fJVT value is above a given threshold (cut_{fjvt}).

In order to avoid potential bias from training and evaluating the performance on the same

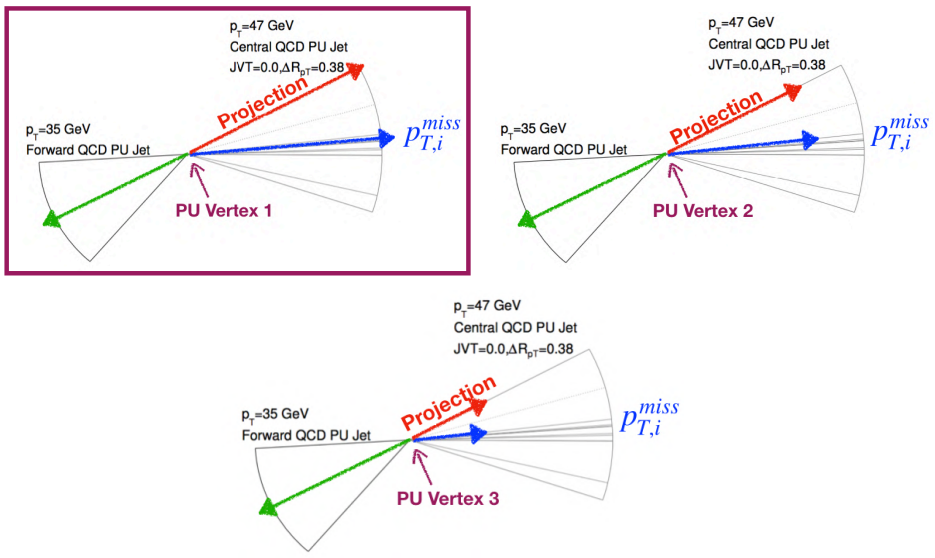

FIGURE 5.6: Schematic example of the fJVT algorithm

dataset, the fJVT discriminant has been trained using a simulated dijet MC sample, in a leading truth jet p_{T} range of 60 to 160 GeV, and validated using a simulated $Z(\rightarrow \mu^{+}\mu^{-})$ + jets MC sample.

It's also worth noting here that fJVT, by construction is designed to reject QCD pile-up jets. In this study, no further classification of the forward jets into QCD and stochastic jets, is performed. Therefore the algorithm is expected to be degraded by the presence of stochastic jets in the forward region. Stochastic forward jets can be efficiently removed by applying an extra requirement on the jet timing. Therefore, at analysis level the fJVT cut is usually accompanied by a requirement on the jet timing.

5.4 Results

5.4.1 fJVT discriminant with particle flow jets

The fJVT discriminant for forward jets is shown in Fig. 5.7 for different $p_{\mathrm{T}}^{\mathrm{jet}}$ bins. The fJVT value for pile-up jets tends to be smaller than those of hard-scatter jets, offering a powerful discriminant.

5.4.2 Performance

For a given fJVT cut value, where fJVT$<$ cut$_{\mathrm{fjvt}}$, the hard-scatter and pile-up efficiencies are defined as:

$$\varepsilon_{\mathrm{HS}} = \frac{\mathrm{N(jets_{HS}^{matched},\ \ with\ fJVT{<}\ cut_{fjvt})}}{\mathrm{N(jets_{HS}^{matched})}}\ , \tag{5.7}$$

and

$$\varepsilon_{\mathrm{PU}} = \frac{\mathrm{N(jets_{PU}^{matched},\ \ with\ fJVT{<}\ cut_{fjvt})}}{\mathrm{N(jets_{PU}^{matched})}}\ , \tag{5.8}$$

where N(jets$_{\mathrm{HS}}^{\mathrm{matched}}$) is the number of jets matched geometrically to truth jets coming from the hard-scatter vertex, and N(jets$_{\mathrm{PU}}^{\mathrm{matched}}$) is the number of jets that are not matched geometrically to truth jets and are therefore considered to be pile-up jets. The pile-up jet efficiency as a

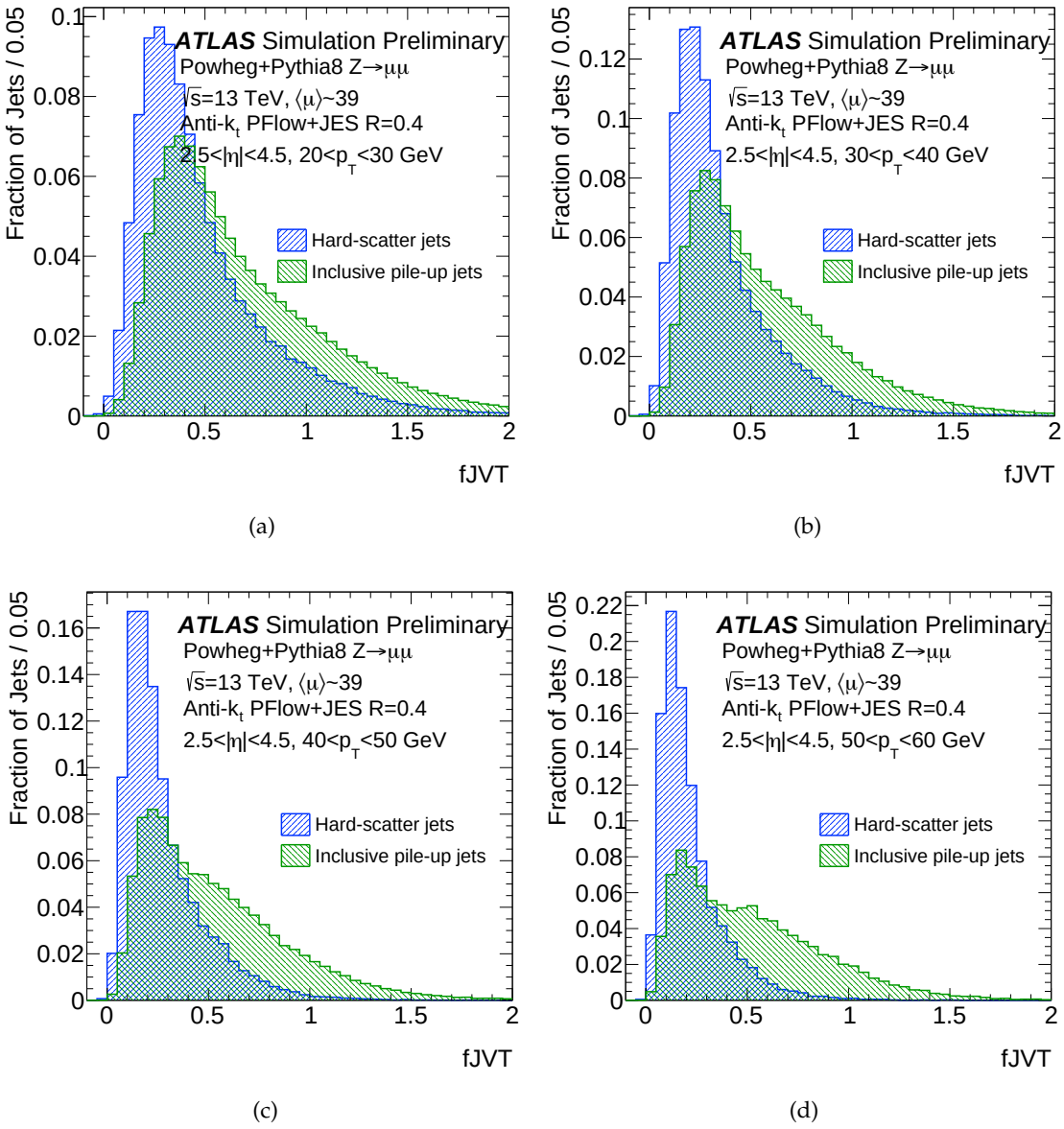

FIGURE 5.7: fJVT distributions for hard-scatter (blue) and pile-up (green) forward jets with $20 < p_{\mathrm{T}}^{\mathrm{jet}} < 30\,\mathrm{GeV}$ (a) , $30 < p_{\mathrm{T}}^{\mathrm{jet}} < 40\,\mathrm{GeV}$ (b) , $40 < p_{\mathrm{T}}^{\mathrm{jet}} < 50\,\mathrm{GeV}$ (c) and $50 < p_{\mathrm{T}}^{\mathrm{jet}} < 60\,\mathrm{GeV}$ (d).

function of the hard-scatter jet efficiency, while varying the fJVT cut value (fJVT$<$ cut$_{\text{fjvt}}$), is plotted in Fig. 5.8 for four p_{T} regions. The performance of the fJVT discriminant improves as p_{T} increases. For an fJVT cut value of 0.53 (0.72), hard-scatter efficiencies of 76% (87%) are achieved, yielding pile-up efficiencies of 49% (66%) for forward jets with 20 < p_{T} < 60 GeV.

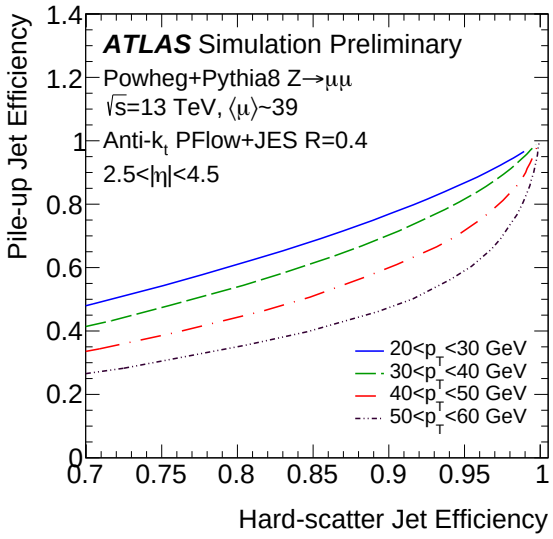

FIGURE 5.8: Efficiency for pile-up jets in simulated Z + jets events as a function of the efficiency for hard-scatter jets for different jet p_{T} ranges. For a standard value of hard-scatter jet efficiency the pile-up jet efficiency is improving with p_{T} since pile-up effects are less dominant in higher p_{T} bins.

The dependence of the hard-scatter and pile-up efficiencies on the forward jet p_{T} is shown in Fig. 5.9. As expected, the probability of mis-labelling a forward hard-scatter jet as pile-up is higher in the low p_{T} bins, yielding to lower hard-scatter jet efficiencies. In Fig. 5.10, the hard-scatter and pile-up jet efficiencies are plotted as a function of the number of primary vertices (N_{PV}) for two forward jet p_{T} regions. A dependency of the hard-scatter jet efficiency on the N_{PV} is observed as expected.

The pile-up efficiency shows also a dependance on the forward jet p_T. This can be attributed to the relative number of QCD and stochastic pile-up jets; stochastic pile-up jets are in general expected to be in low p_T bins. The algorithm is designed to assign a forward jet to a QCD pile-up vertex employing momentum conservation. For stochastic forward jets, the fJVT value is expected to be close to 0 (since a stochastic forward jet is not compatible with any pile-up vertex). Therefore, stochastic jets will survive the fJVT cut, leading to higher pile-up contamination in the low p_T bins.

The performance was also evaluated using the dijet sample, and for a fixed hard-scatter jet efficiency the background rejection was compatible within a relative 5%.

5.4.3 Algorithm timing optimisation

As described in Sec. 5.3, the first step of the fJVT algorithm is to reconstruct the jets for every pile-up vertex of the event. However this is found to be significantly CPU time-consuming. In order to improve the speed of the algorithm, several algorithm timing optimisation studies were performed. Pile-up vertices are ranked based on the $\sum p_{\text{T}}^2$ of the constituent tracks, starting from the higher value of $\sum p_{\text{T}}^2$. The most efficient way of improving the speed of the algorithm was found to be the jet reconstruction for only the first N vertices for each event, instead of all vertices, as these contain most of the pile-up activity. For N=10,

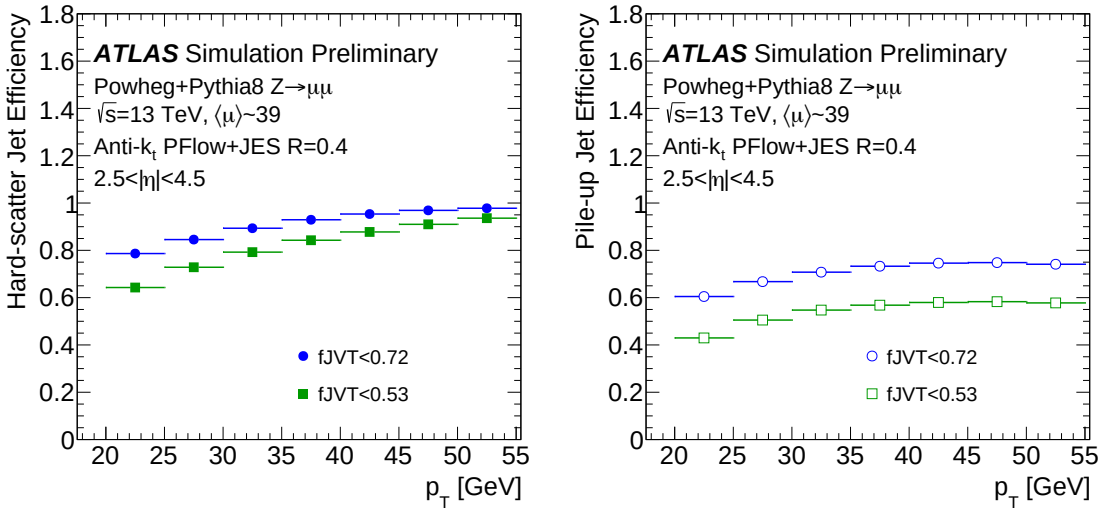

(a) (b)

FIGURE 5.9: Hard-scatter (a) and pile-up (b) jet efficiency as a function of forward jet p_{T} for simulated Z + jets events.

the CPU time is reduced by 50% compared to the baseline case, while the fJVT performance is not affected as shown in Fig. 5.11. Decreasing further the number of vertices has a clear impact on the performance of the algorithm, as it is also shown for N=5 in Fig. 5.11. For this reason, N=10 is chosen to be the optimal point. As a result, reconstructing the jets from the 10 first pile-up vertices of the event will be used in the future implementation of the particle flow fJVT in ATLAS.

5.4.4 Comparison with EMTopo fJVT

The current algorithm is compared to the fJVT algorithm built with topo-cluster jets (referred to as EMTopo), described in Ref. [71]. The comparison is made in a simulated dijet MC sample. For this purpose fJVT is estimated for three cases:

- fJVT PFlow: the forward PFlow jet is balanced with the missing transverse energy (MET) as estimated with PFlow jets
- fJVT EMTopo: the forward EMTopo jet is balanced with the MET as estimated with EMTopo jets
- MET of EMTopo jets: the forward PFlow jet is balanced with the missing transverse energy (MET) as estimated with EMTopo jets

The last estimation is added in order to see if any performance difference seen between the two algorithms is due to the different MET estimations between PFlow and EMTopo jets. The pile-up jet efficiency as a function of the hard-scatter jet efficiency, while varying the fJVT cut value, is plotted in Fig. 5.12 for four p_{T} regions. Overall the two algorithms show very similar performance.

The hard-scatter and pile-up efficiencies on the forward jet p_{T} is shown in Fig. 5.13 for an fJVT cut value of 0.53. The PFlow fJVT shows a better hard-scatter efficiency in the low p_{T} bins but with a slightly worse background rejection.The MET of EMTopo estimation closely

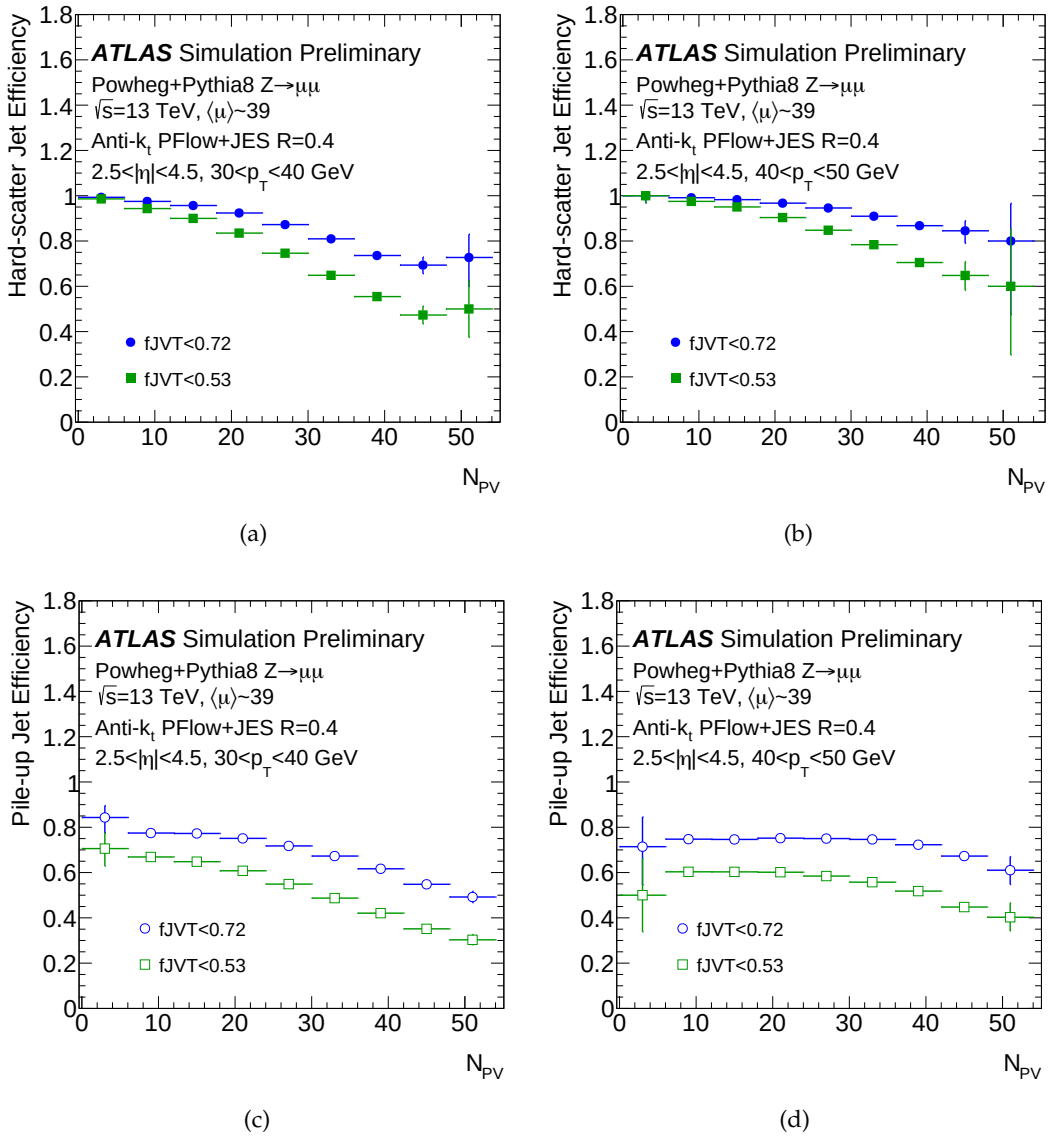

FIGURE 5.10: Efficiency in simulated Z+jets events as a function of N_{PV} for hard-scatter forward jets with $30\ \mathrm{GeV} < p_{\mathrm{T}} < 40\ \mathrm{GeV}$ (a), $40\ \mathrm{GeV} < p_{\mathrm{T}} < 50\ \mathrm{GeV}$ (b), and for pile-up forward jets with $30\ \mathrm{GeV} < p_{\mathrm{T}} < 40\ \mathrm{GeV}$ (c), and $40\ \mathrm{GeV} < p_{\mathrm{T}} < 50\ \mathrm{GeV}$ (d).

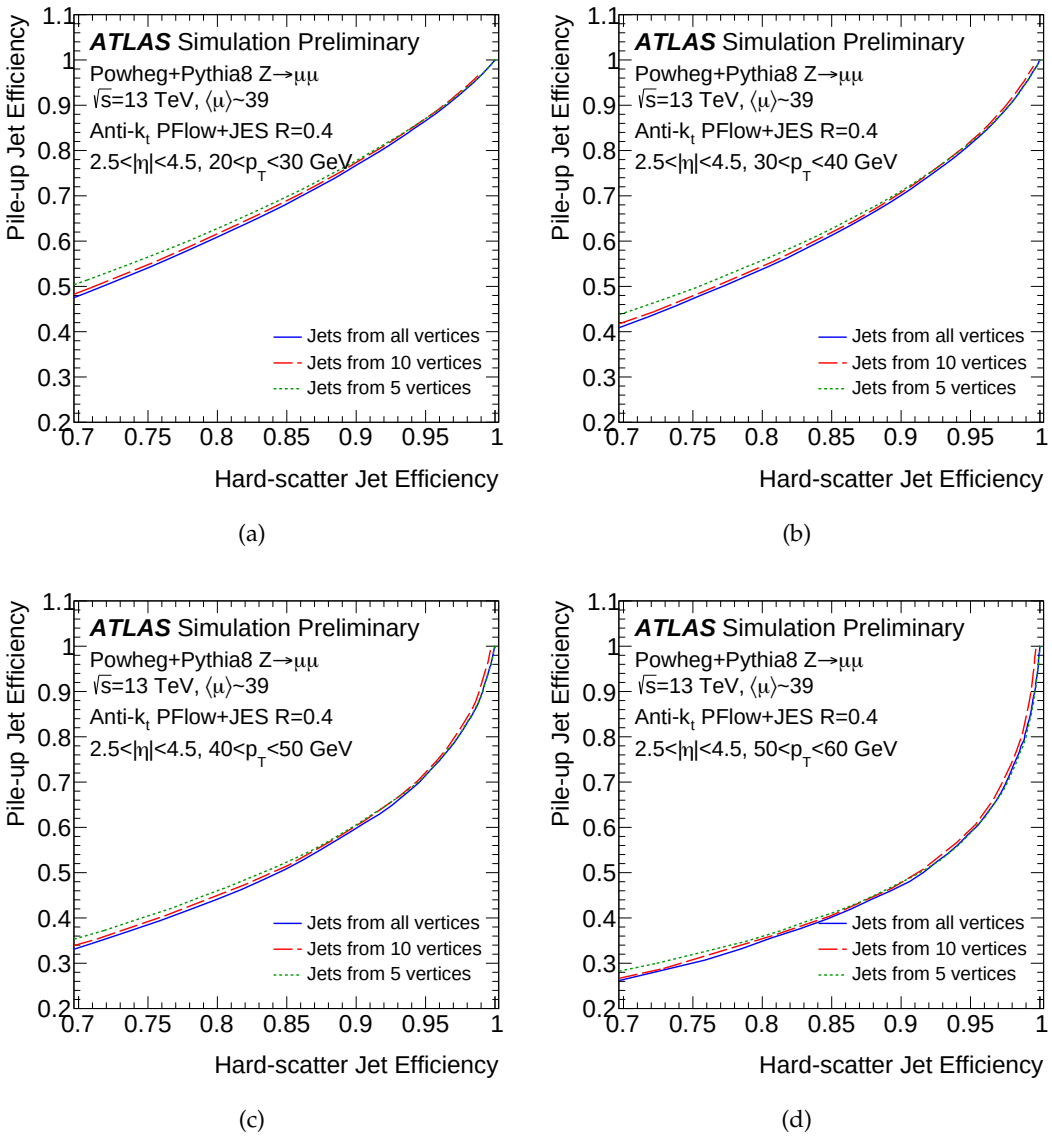

FIGURE 5.11: Efficiency for pile-up jets in Z + jets simulated events as a function of the efficiency for hard-scatter jets for forward jets with $20\text{ GeV} < p_{\text{T}} < 30\text{ GeV}$ (a), $30\text{ GeV} < p_{\text{T}} < 40\text{ GeV}$ (b), $40\text{ GeV} < p_{\text{T}} < 50\text{ GeV}$ (c) and $50\text{ GeV} < p_{\text{T}} < 60\text{ GeV}$. The baseline case, where all the vertices of the event are processed for the jet reconstruction, is compared to the case where: i) the first 10, and ii) the first 5 vertices of the event are processed.

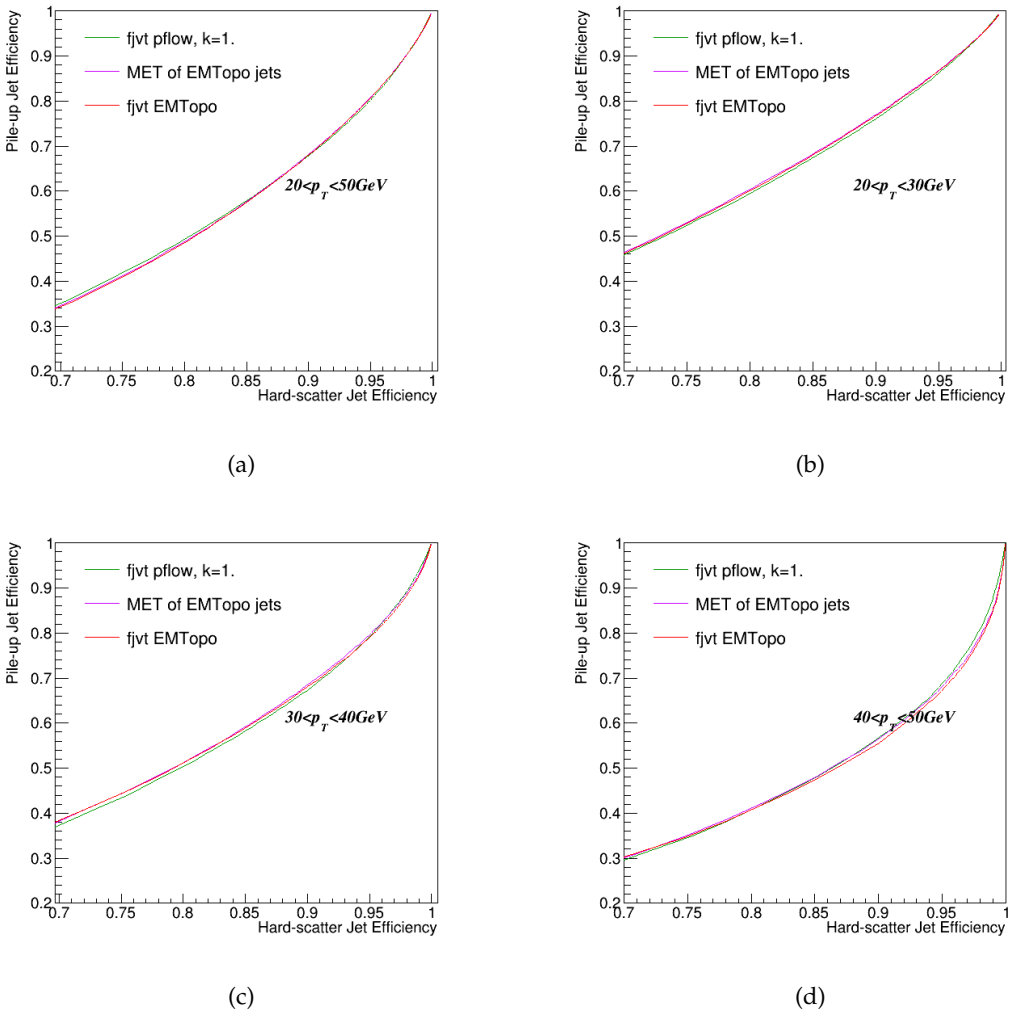

(a) (b)

(c) (d)

FIGURE 5.12: Performance comparison between the PFlow and EMTopo fJVT algorithms.

follows that of the fJVT EMTopo, indicating that the observed differences are due to the different MET estimations. As already discussed in 5.2.1, in the forward region, jets are exclusively built from topo-clusters. Therefore, a MET estimation using topo-clusters would normally better balance such jets.

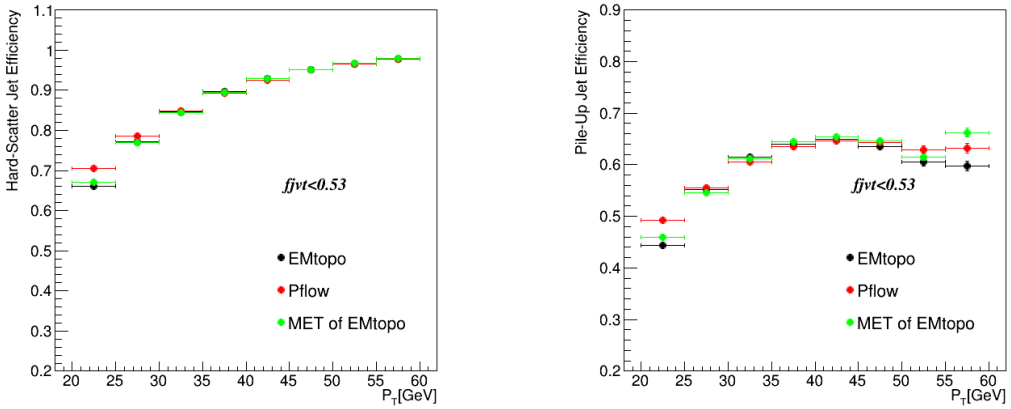

(a) (b)

FIGURE 5.13: Hard-scatter (a) and pile-up (b) jet efficiency as a function of forward jet p_{T} for simulated Z + jets events. A comparison between the PFlow and EMTopo fJVT algorithms is made here.

5.5 Calibration

The fJVT hard-scatter and pile-up efficiencies were evaluated in the previous section using simulated MC samples. However, such an evaluation can not be fully trusted. The MC generators are usually modelling the different processes with a certain accuracy which is not perfect and mis-modelling can occur. Moreover the pile-up is also known to be mis-modeled and corrections from data are usually necessary. In addition to these, mis-modeling might also appear due to the imperfect knowledge of the detector response which might affect the measurement of relevant for the discriminant objects, like jets. For this reason, the tagger performance is usually evaluated with actual data. In the case where discrepancies between the performance in data and MC are found, the second is corrected in order to match the performance in data. This is usually done by extracting dedicated correction factors from the data and MC comparison of some representative process. The correction factors are derived centrally and applied to the individual analyses.

For the fJVT discriminant, the calibration is performed by comparing data to Z+jets events [80]. In order to evaluate the tagger hard-scatter and pile-up efficiencies in data, pile-up and hard-scatter depleted regions, referred to as HS and PU control regions, respectively, are defined. This is can be achieved, for instance, by requiring a cut on $\Delta\phi(jet, Z)$. Jets from the hard-scatter vertex are typically expected to be recoiling against the Z boson, therefore peaking at a $\Delta\phi(jet, Z)$ of $\sim$3. On the other hand the $\Delta\phi(jet, Z)$ distribution is expected to be flat for pile-up jets. The contamination from pile-up in the HS control region, N_{PU}, is estimated from the PU control region and subtracted from the yield in the HS region. The hard-scatter efficiency in data is then estimated in the HS control region as follows:

$$\epsilon_{HS}^{data} = \frac{N_{data}^{pass} - N_{PU}^{pass}}{N_{data} - N_{PU}}$$

where N_{data}^{pass} is the number of data events passing the fJVT tagger requirement in the HS control region, N_{data} is the total of data events in that region and N_{PU}^{pass} is the number of pile-up jets, pre-estimated from data in the CR, that pass fJVT. The same estimation is done using the MC event yields, in order to evaluate the MC hard-scatter efficiency ϵ_{HS}^{MC}. Scale factors (SFs) are then derived to correct the MC with respect to data:

$$SF = \frac{\epsilon_{HS}^{data}}{\epsilon_{HS}^{MC}}$$

The SFs are derived in bins of p_{T} and μ.

The derivation of the efficiency SFs is done with a certain precision. A few systematic sources can influence this derivation considerably. Therefore, the impact of such systematic sources on the evaluated SFs is also estimated. Five systematic sources are considered for the fJVT SF derivation:

- Statistical uncertainties arising from the limited number of statistics. These are found to be really small in the low p_{T} regions and become much more important in the higher p_{T} regimes.
- MC modelling uncertainties; These are estimated by comparing the nominal `POWHEG+PYTHIA` sample SF estimation with an alternative SF estimation performed using a SHERPA Z + jets generated sample. The discrepancies between nominal and alternative estimations were found to be negligible.
- PU estimation uncertainty; A 10% uncertainty is considered in order to account for the PU mis-modelling.
- η-dependance uncertainty; It is found that scale factors estimated for jets reconstructed in the end-cap are slightly different from those for jets in the FCal. To account for these differences a conservative uncertainty band is defined as the envelope of nominal SF and SF estimated in these two regions.
- Year dependance uncertainty; a dependance of the SF derivation on the data taking period during Run2 was found. Therefore an uncertainty band is defined by taking the envelope of nominal SF and SFs derived for each data-taking period.

The fJVT performance in data is plotted for PFlow and EMTopo jets in Figure 5.14. The HS efficiency as a function of p_{T}, for $25 < \mu < 50$, is shown. The tool was calibrated for three different working points; loose, medium and tight. The PFlow fJVT shows a better performance in the low p_{T} bins. Though, the improvement comes with an overall larger uncertainty, especially for the tight working point.

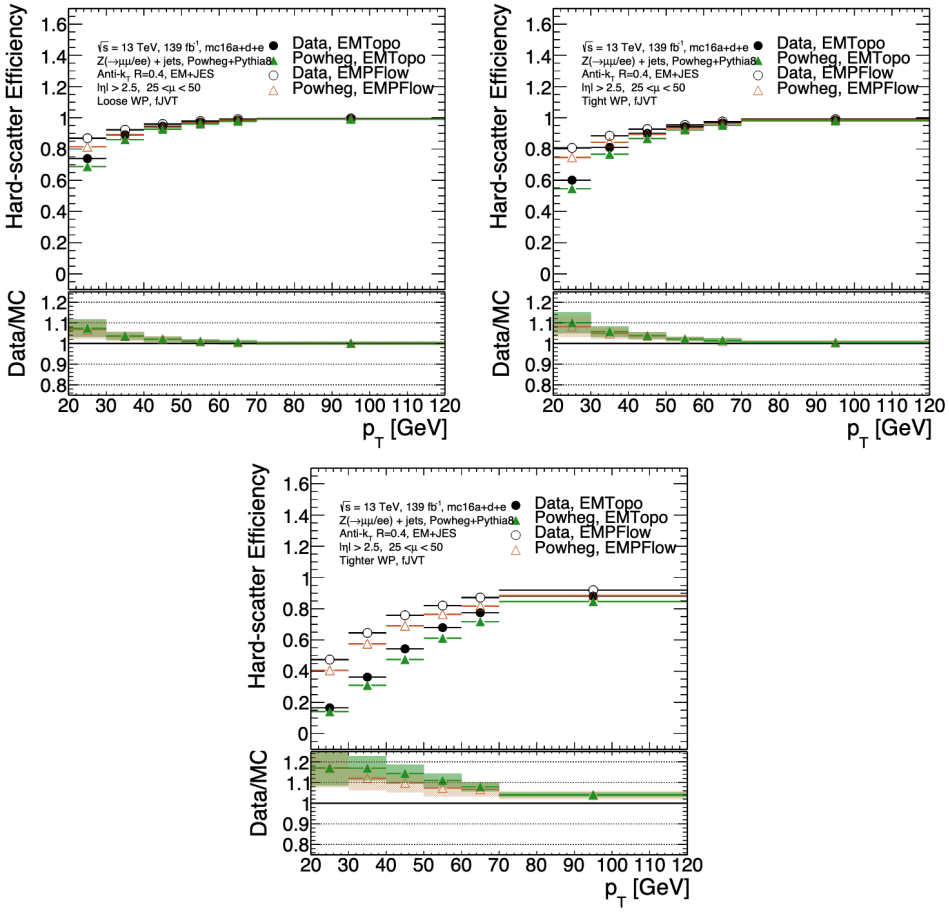

FIGURE 5.14: Hard-scatter jet efficiencies for PFlow and EMTopo jets for three fJVT working points: Loose (top left), Medium (top right) and Tight (bottom). The EMTopo results, in MC and data, are plotted with solid markers. The corresponding results for PFlow jets are shown with open markers. The derived SFs from calibration are plotted in the ratio plot with the corresponding uncertainty bands [80].

6. Search for electroweak diboson production in association with a high-mass dijet system in semileptonic final states

In this chapter, the Vector Boson Scattering (VBS) process in semileptonic final states is studied, using data collected by the ATLAS detector during 2015-2018. In the semileptonic VBS final states, one of the two bosons decays hadronically into a pair of quarks while the other decays leptonically. Depending on the leptonic decay of the boson, three analysis channels are considered; 0-lepton,1-lepton and 2-lepton. My involvement in this analysis is heavily focused on the 2-lepton channel, and it includes all steps to the signal strength measurement. First, an introduction to the analysis is presented in Section 6.1. Next a description of the samples and object reconstruction is given in Sections 6.2 and 6.3, respectively. The 2-lepton channel event selection and analysis regions are defined in Sections 6.4-6.5. Following, the background modeling is studied in Section 6.6. Finally, all the details related to the signal extraction in the 2-lepton channel are presented in Sections 6.7- 6.10. The studies presented in Sections 6.4- 6.10 correspond to personal contributions.

6.1 Introduction

Although EW $VVjj$ searches are in general challenging due to the very low production cross sections, they benefit from a very characteristic event topology. The EW $VVjj$ process is identified experimentally by the presence of two bosons (V= W, Z) and two jets in the opposite hemispheres with a large di-jet invariant mass (tagging jets). An illustration of a EW $VVjj$ event as it would be reconstructed in the detector is shown in Figure 6.2. The event is mainly identifiable thanks to the two tagging jets accompanying the VV scattering. Figure 6.2(a) shows a typical VBS process Feynman diagram. In Figures 6.2(b) and 6.1(c) representative Feynman diagrams of non-VBS electroweak (EW) and QCD induced processes that contribute to the same final state are shown. Due to the large interference, non-VBS EW processes cannot be separated from the VBS process in a gauge invariant way, therefore are considered as part of our signal definition. In the contrary, QCD induced processes where the interference is usually small, are separated from our signal definition and considered as part of our background samples.

In this analysis, semileptonic final states are studied, meaning that one of the two bosons described above, V_{had} , decays hadronically to a pair of $q\bar{q}$, while the other, V_{lep} , decays leptonically. The advantages of semileptonic final states, with respect to other fully leptonic searches, is the higher branching ratio, as well as, the exploitation of jet substructure techniques, for the W/Z identification, which allow high reconstruction efficiency in the high- p_{T} regimes, where there is higher sensitivity to anomalous quartic gauge couplings (aQGC). However, such final states usually suffer from an overall higher background contamination, mainly originating from W+jets, Z+jets and tt-bar processes.

Depending on the leptonic decay of the boson, the analysis is further split in three channels: 0-lepton, 1-lepton, 2-lepton. Charged leptons are considered electrons, muons and their neutral equivalent. In the 0-lepton channel the Z boson decays to a pair of neutrinos which is then reconstructed experimentally as missing transverse energy (MET). In the 1-lepton channel the W decay of the boson is reconstructed, thus we are looking for one lepton accompanied

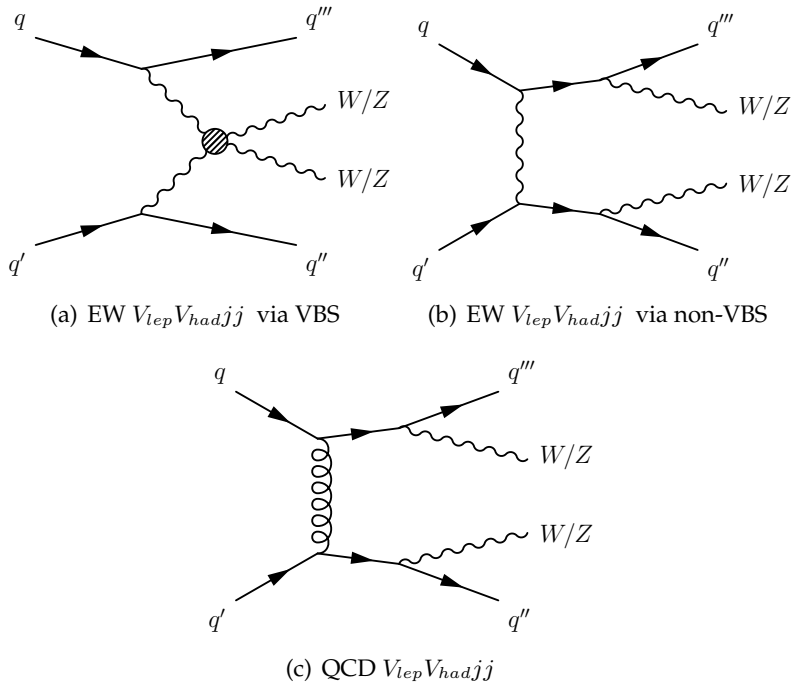

(a) EW $V_{lep}V_{had}jj$ via VBS (b) EW $V_{lep}V_{had}jj$ via non-VBS

(c) QCD $V_{lep}V_{had}jj$

FIGURE 6.1: Representative Feynman diagrams for (a) EW $V_{lep}V_{had}jj$ production via VBS, (b) EW $V_{lep}V_{had}jj$ production via non-VBS contribution, and (c) QCD $V_{lep}V_{had}jj$ production.

by MET. In the 2-lepton channel the boson decays to a pair of charged leptons, originating from a Z decay, and thus two leptons are required in the analysis. In all three channels, the event is always required to contain a hadronically decaying V_{had} candidate together with two jets (denoted by jj) to reconstruct the final $V_{lep}V_{had}jj$ state. The hadronic $W/Z \to q\bar{q}$ decay is reconstructed either as a pair of small-R jets, or as a single large-R jet . The last, intends to reconstruct events for which the W/Z boson has a large Lorentz boost, therefore its decay products are highly collimated in the direction of the parent particle. A schematic representation of the two reconstruction methods is shown in Figures 6.2. More details about the reconstruction of each category are given in Section 6.4.

In the following, we will focus on the 2-lepton semileptonic final state. In this case our EW signal definition contains contributions from $Z(\ell\ell)W(q\bar{q})jj$ and $Z(\ell\ell)Z(q\bar{q})jj$ diagrams only. A summary of the cross section values for all lepton multiplicities (0-,1- and 2-lepton) is shown in Table 6.1. The 2-lepton channel has the lowest EW signal cross-sections comparing to the 0- and 1-lepton channels. However, the background contamination is also much lower in the 2-lepton channel. The major background processes contributing to the 2-lepton final state are originating from Z + jets, single-top and tt-bar (collectively referred to as top events), as well as, QCD induced diboson events. Some of these processes are greatly suppressed through the analysis event selection. For example, diagrams of the form 6.1(c), will be suppressed by kinematic cuts on the tagging jet system. Moreover, diagrams containing a Wtb vertex, such as those shown in Figure 6.5, are all suppressed by requiring a b-veto for the tagging jets.

6.2 Data and Monte Carlo Simulation

6.2.1 Data

The data used in the analysis correspond to pp collisions at a center of mass energy of 13 TeV and were collected by the ATLAS detector during the full Run 2 period between 2015

TABLE 6.1: List of VBS cross sections in semileptonic final states.

Process	cross-section (pb)
$W(\ell\nu)W(q\bar{q})jj, b-veto$	1.9994
$W(\ell\nu)W(q\bar{q})jj, b-filter$	1.9777
$W(\ell\nu)Z(q\bar{q})jj$	0.2571
$Z(\nu\nu)W(q\bar{q})jj$	0.15532
$Z(\nu\nu)Z(q\bar{q})jj$	0.032238
$Z(\ell\ell)W(q\bar{q})jj$	0.045609
$Z(\ell\ell)Z(q\bar{q})jj$	0.0096553

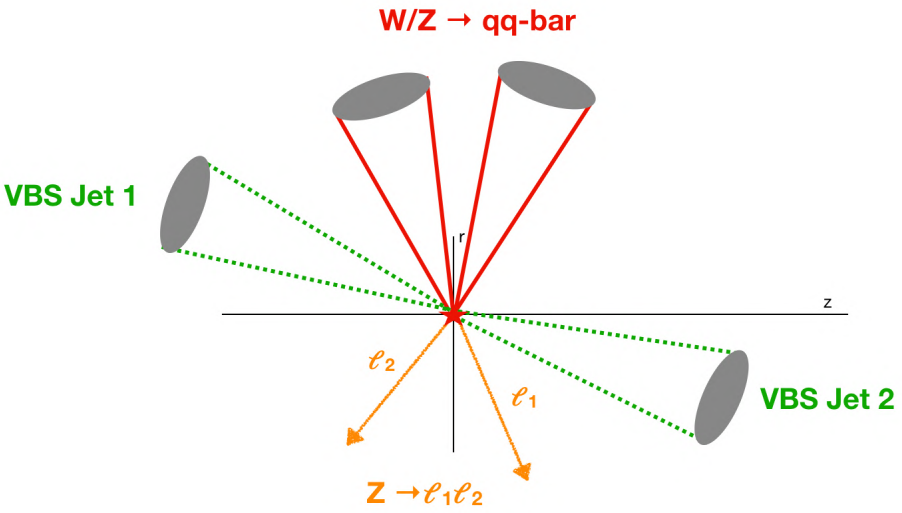

(a) Resolved reconstruction

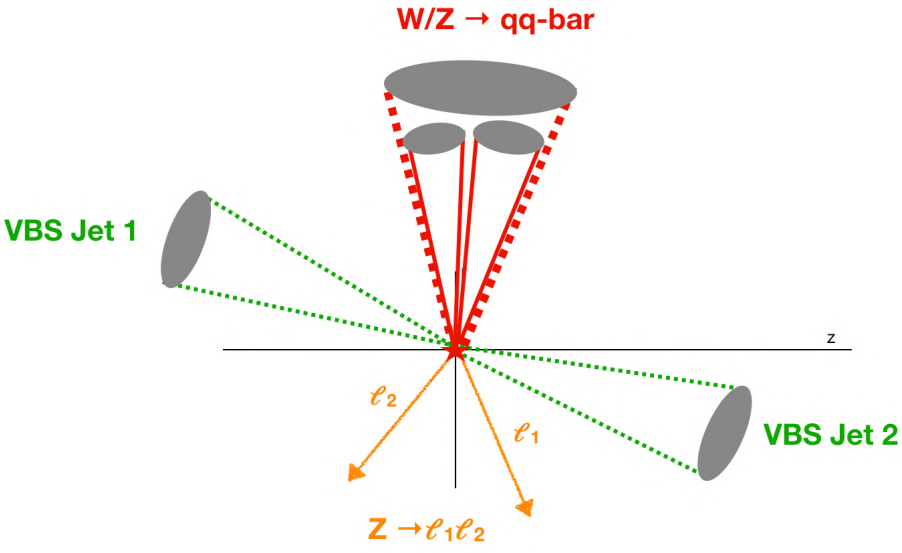

(b) Merged reconstruction

FIGURE 6.2: Schematic representation of a EW $WZjj$ event with $Z \to \ell\ell$ and $W \to q\bar{q}$. The hadronic decay of W is either reconstructed as a pair of small-R jets (resolved) or a single large-R jet (merged)

and 2018. The total integrated luminosity corresponding to this period is 139 fb^{-1} with an uncertainty of 1.7%. This reflects an increase of luminosity with respect to the previous round of the analysis [26] of almost a factor of 4.

6.2.2 Signal and Background Monte Carlo Simulation

Electroweak signal and background processes are modeled using Monte Carlo (MC) simulation. Simulated processes are essential for optimizing the analysis event selection, estimating the background contributions within our signal regions and developing multivariate discriminant techniques in order to enhance the analysis sensitivity to the target signal.

The main stages of event generation include : the calculation of the matrix element (at a given order) for the hard-process of interest, the generation of the process (at partonic level), the evaluation of parton shower effects on the hard process (e.g Initial State Radiation and other soft effects, underlying-event activity) and finally the hadronization of the parton configuration by string fragmentation. All simulated processes are normalized using the most precise and recent theoretical cross-section predictions at some order of QCD.

In order to take into account the detector geometry and reconstruction efficiency, the generated MC events are then processed through a detailed detector simulation based on GEANT4 . Activity coming from secondary collisions, happening within the same (or previous/next) bunch crossings (pile-up), is also considered, by overlaying additional generated inelastic pp collisions to the MC events. The MC samples are then reweighted to match the pileup conditions in the data.

Signal SM EW VV+jj processes

For the EW $V_{lep}V_{had}jj$ signal process, the MadGraph5_aMC@NLO v2.3.3 event generator is used for the $V_{lep}V_{had}jj$ generation while PYTHIA 8 is employed for the parton shower modeling and hadronization. The NNPDF30LO PDF set is used. The EW $V_{lep}V_{had}jj$ samples are generated at LO with two on-shell V bosons, with one V boson decaying leptonically ($Z \to \ell\ell$ with $\ell = e, \mu$), and the other V boson decaying hadronically. For the W boson, both W^+ and W^- are considered. Purely EW tree-level diagrams, $\mathcal{O}(\alpha_{\mathrm{EW}}^6\alpha_{\mathrm{S}}^0)$, including non-VBS EW diboson processes, are also considered in our signal generation. The EW $V_{lep}V_{had}jj$ signal diagrams are shown in Figure 6.3. Examples of the non-VBS electroweak diagrams are plotted in Figure 6.4.

Background processes

The most relevant background processes in the 2-lepton channel are the Z + jets, $t\bar{t}$, single top and diboson (WW, WZ, ZZ) productions. The Z + jets events are simulated using SHERPA 2.2.1, and considering up to two partons at NLO and up to four partons at LO for the matrix element calculation. The NNPDF3.0NNLO PDF set is used in association to authors tuning. QCD induced $V_{lep}V_{had}jj$ processes shown in Figure 6.5, which contain a mix of the strong and EW couplings, $\mathcal{O}(\alpha_{\mathrm{EW}}^4\alpha_{\mathrm{S}}^2)$, are part of the $t\bar{t}$, single top and diboson background samples. The diboson events are generated using the SHERPA 2.2.1 generator. The ttbar and single-top events are generated with the Powheg-Box [81] generator with the NNPDF3.0NLO PDF[82] sets in the matrix element calculation. For the parton shower modeling and hadronization PYTHIA 8 is employed.

6.3 Object Reconstruction

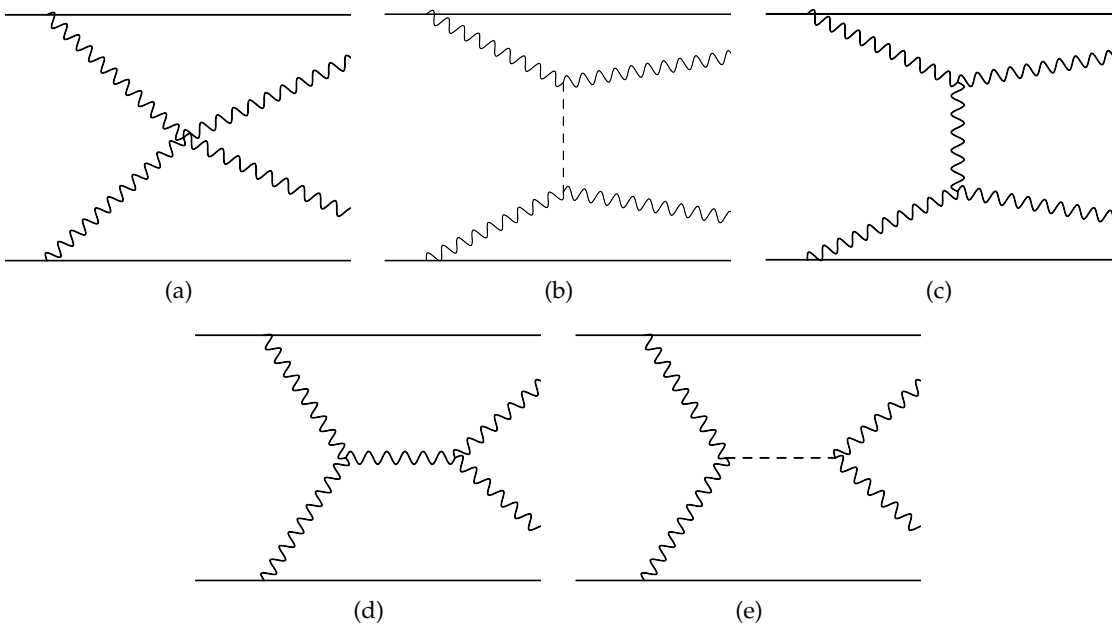

FIGURE 6.3: Examples of VBS diagrams that contribute to the signal. The dashed line represents the Higgs boson. The decays of the bosons are not shown.

6.3.1 Triggers

In order to select events that are interesting for our search out of the millions of events recorded in the detector, trigger requirements are necessary. The triggers applied depend on the channel and on the data taking period. The trigger selection is done using a logical OR of multiple single-electron or single-muon triggers. In the 2-lepton channel, at least one of the two leptons in the final state is required to pass either the single electron or the single muon trigger.

6.3.2 Leptons

Electrons and muons are used in the 2-lepton channel to reconstruct $Z \to \ell\ell$ decay. Electrons are required to have transverse energy $E_{\mathrm{T}} > 7$ GeV and pseudorapidity $|\eta| < 2.47$ while muons should satisfy: $p_{\mathrm{T}} > 7$ GeV and $|\eta| < 2.5$. Both electrons and muons are required to have a transverse impact parameter significance relative to the beam line ($|d_0/\sigma_{d_0}|$) smaller than 5 and 3, respectively, and a longitudinal impact parameter $|z_0 \times \sin\theta| < 0.5$ mm relative to the primary vertex. Furthermore, leptons should satisfy isolation criteria based on both track and calorimeter isolation variables. Calorimeter-based isolation variables are calculated by summing the energies of all positive-energy topological clusters, whose barycentres fall within a cone of radius $\Delta R = 0.2$ around the lepton direction [83]. The track-based isolation variables, are using the sum of transverse momentum of tracks around the lepton direction within a cone of p_{T}-dependent size. The p_{T}-dependent cone size is added in order to maintain high signal efficiencies in boosted topologies. Several isolation operating points are available [83]. In the 2-lepton channel, electrons and muons are required to be identified as "loose" and satisfy "loose" isolation criteria. This selection is expected to maintain a high signal efficiency in the high-p_{T} region, where the two lepton candidates are close to each other.

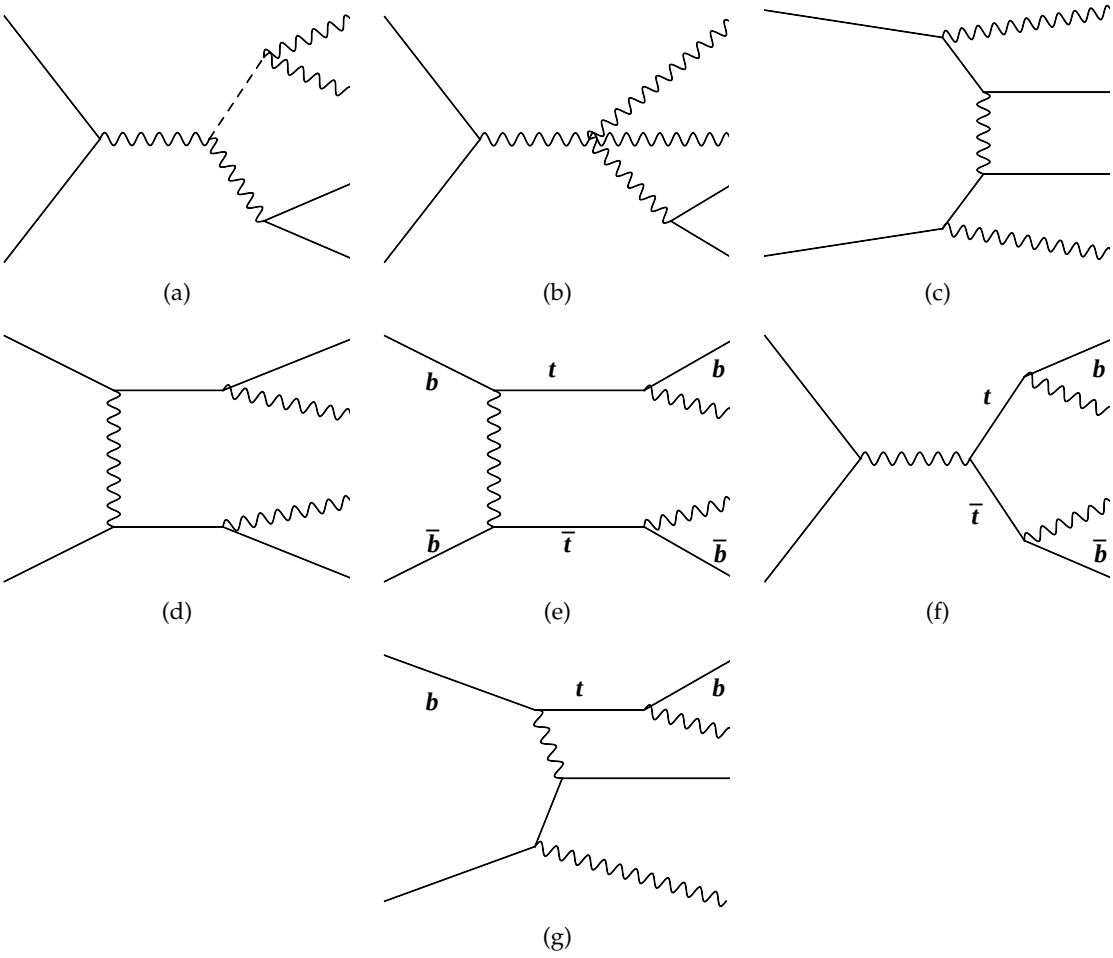

FIGURE 6.4: Examples of non-VBS $\mathcal{O}(\alpha_{EW}^6)$ diagrams that contribute to the signal. The decays of the bosons are not explicitly shown, but the counting of powers of α includes the boson decays.

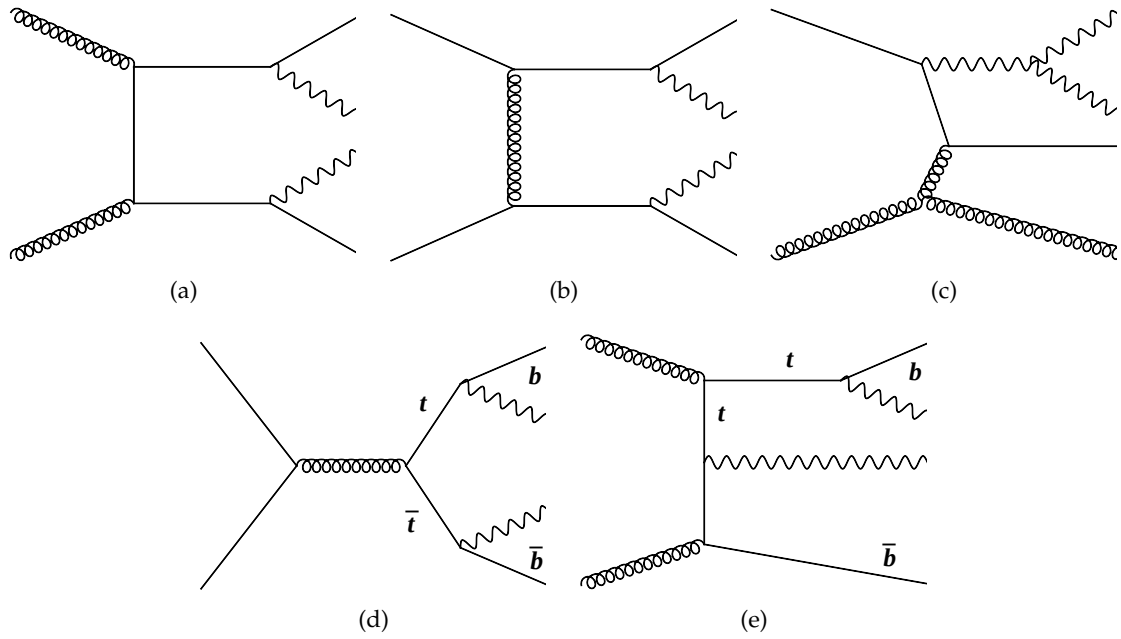

FIGURE 6.5: Examples of $\mathcal{O}(\alpha_{EW}^4\alpha_S^2)$ diagrams that lead to the VV+2parton final state. These are not included in the signal definition. The decays of the bosons are not explicitly shown, but the counting of powers of α includes the boson decays.

6.3.3 Jets

As discussed in 4.4, based on the reconstruction method, two jet categories are defined: small-R jets and large-R jets. Both categories are used in the analysis. A detailed description of the jet selection is given in the following subsections.

Small-R Jets

Small-R jets are used in the analysis to reconstruct the $W/Z \to qq$ decay at low-p_{T}, as well as, for the tagging jet selection. Small-R jets are reconstructed using the PFlow algorithm described in 4.4. Small-R jets within $|\eta| < 2.5$ (central jets) are required to have a $p_{\mathrm{T}} > 20$ GeV while jets with $|\eta| > 2.5$ (forward jets) should satisfy: $p_{\mathrm{T}} > 30$ GeV . In order to reassure that the selected jets are coming from the hard-scatter vertex of interest, the JVT algorithm, introduced in Section 5.1.2, is employed for jets with $p_{\mathrm{T}} < 60$ GeV and $|\eta| < 2.4$. The "tight" JVT working point is selected. For jets outside the tracking coverage the fJVT algorithm, discussed in 5.3, is employed. The "loose" fJVT working point is chosen.

Large-R Jets

Large-R jets are used in the analysis to reconstruct the $W/Z \to qq$ decay at high-p_{T} where the two jets originating from the decay are highly boosted. Large-R jets are required to have $p_{\mathrm{T}} > 200$ GeV and $|\eta| < 2.0$. In order to to classify a selected large-R jet as originating from a heavy W/Z decay as opposed to a light jet originating from gluons or quarks, a W/Z tagger is employed [84]. Two working points are provided; 50% and 80% flat signal efficiency, both used in this analysis to define signal regions with different purities. The tagger decision is based on the following three large-R jet related variables:

- the combined mass, reconstructed as the weighted sum of masses from calorimeter information and from mixed calorimeter and tracking information.
- the energy correlation function ratio D_2 defined as:

$$D_2 = E_{CF3}\left(\frac{E_{CF1}}{E_{CF2}}\right)^3 \tag{6.1}$$

where the energy correlation functions (E_{CF}) are defined as:

$$\begin{aligned} E_{CF1} &= \sum_i p_{T,i} \\ E_{CF2} &= \sum_{ij} p_{T,i}p_{T,j}\Delta R_{ij} \\ E_{CF3} &= \sum_{ijk} p_{T,i}p_{T,j}p_{T,k}\Delta R_{ij}\Delta R_{jk}\Delta R_{ki} \end{aligned} \tag{6.2}$$

where the sums are over the constituents i in the jet J such that the 1-point correlation function E_{CF1} is approximately the jet p_{T}, while the function E_{CF2} can be seen as the equivalent to the mass of a particle undergoing a two-body decay in collider coordinates. The D_2 has been shown to be very useful in identifying two-body structures within jets.

- the track multiplicity Ntrk, which is the number of tracks associated to the original ungroomed[1] jet. This variable was found to improve the background rejection for a fixed signal efficiency due to the rejection of jets seeded by gluons.

6.4 Event Selection

In this section the event selection is described, optimized in order to maximize the expected significance of the signal over background prediction. In order to reconstruct the $V_{lep}V_{had}jj$ final state a series of selections are applied. First, the leptonically decaying candidate V_{lep} is reconstructed as described in 6.4.1. Following, the two jets accompanying the $V_{lep}V_{had}$ decay (referred to as tagging jets) are selected in 6.4.2. Finally, the hadronic decay of the boson V_{had} is reconstructed as described in 6.4.3.

6.4.1 Leptonically decaying boson

The leptonic decay of the Z boson to either two electrons or muons is reconstructed using the objects defined in 6.3.2. Two same flavor loose-leptons with the leading (sub leading) lepton satisfying $p_{\mathrm{T}} > 28$ GeV ($p_{\mathrm{T}} > 20$ GeV) and an invariant mass of the lepton system ($m_{\ell\ell}$) close to the Z boson mass are requested. Depending on the lepton pair (ee, $\mu\mu$) different mass window requirements are applied; For electrons, a fixed $m_{\ell\ell}$ window $83 < m_{ee} < 99$ GeV is applied. In the case where the $\mu\mu$ system is reconstructed a $p_{\mathrm{T}}^{\mu\mu}$ dependent cut is required in order to recover for the degraded di-muon invariant mass resolution at high p_{T}:

$$(-0.0117 \times p_{\mathrm{T}}^{\mu\mu} + 85.63\ \mathrm{GeV}) < m_{\mu\mu} < (0.0185 \times p_{\mathrm{T}}^{\mu\mu} + 94\ \mathrm{GeV})$$

. In addition, muons are required to be within an $|\eta| < 2.5$ and to be of opposite sign. The opposite sign requirement is not requested for electrons which are more prone to misidentification[2].

[1] these are the original large-R jets (before the trimming procedure applied in order to remove effects from pile-up, the underlying event as well as soft and wide-angle radiation)

[2] due to the conversions of photons from bremsstrahlung

6.4.2 Tagging jets selection

The tagging jets reconstruction is a key element of the analysis since they help us separate the VBS process from the main background and other VV productions in LHC. Tagging jets are selected from the small-R jet collection described in 6.3.3 after removing jets that are b-tagged, as well as, those failing loose fJVT requirements. The not-b-tagged requirement is imposed in order to reduce contributions from non-VBS EW processes (especially the electroweak tt-bar production). The fJVT requirement is used to suppress pile-up contributions in the forward region. Finally the tagging jets are selected to be in the opposite hemispheres and have the highest di-jet invariant mass of the event. After the selection, they are additionally required to have a $p_{\mathrm{T}} > 30$ GeV and a dijet invariant mass $M_{jj}^{tag} > 400$ GeV. The M_{jj}^{tag} requirement is mainly performed in order to reduce contributions from QCD induced $V_{lep}V_{had}jj$ processes which are expected to carry different tagging jets kinematics. Moreover this cut further reduces contributions from other non-VBS diagrams like triboson (VVV) contributions where one of the boson decays hadronically, with a dijet invariant mass close to the W or Z peak.

6.4.3 Hadronically decaying boson

The hadronically decaying boson V_{had} is reconstructed either as a pair of small-R jets or a single large-R jet in the case where the two jets are highly boosted. Based on the V_{had} reconstruction technique, the selection is called either as resolved (reconstructed as a pair of small-R jets) or merged (reconstructed as a single large-R jet). In both cases, the V_{had} selection is performed after the tagging jets are selected.

More details about each selection are given in the following subsections.

Merged reconstruction

The large-R jet (J) candidate is selected from the large-R jet collection after removing those large-R jets overlapping with the tagging jets (require $\Delta R(J, j)$ >1.4). Next, the leading large-R jet of the event is selected as the signal jet ($sigJ$) candidate. The selected $sigJ$ is required to have a $p_{\mathrm{T}} > 200$ GeV, $|\eta| < 2.0$ and not overlap with the two leptons l_1 and l_2 of the event ($\Delta R(J, l_{1,2})$ >1.0). The last requirement prevents double counting of energy from leptons falling within the $sigJ$.

Furthermore, in order to select events coming from the W/Z hadronic decay, the boson tagging algorithm discussed in 6.3.3 is employed. Two different signal regions are reconstructed based on the working point requirement of the algorithm. Events for which the $sigJ$ candidate passes, either the W or Z, 50% working point tagger requirements are considered in the so-called high-purity (HP) signal region (SRVBS_HP) while events failing the 50% but passing the 80% working point requirements are included in the low-purity (LP) signal region (SRVBS_LP).

Resolved reconstruction

In the resolved selection the two jet candidates (signal jets) are selected from the small-R jet collection after tagging jets are removed.The two leading jets of the event are selected here as the signal jet candidates, in contrast with the first publication based on Run 1 data [26]. When background uncertainties are considered, this selection is proven to give better signal sensitivity with respect to the old signal jet selection, where the two jets with invariant mass closest to the W/Z mass were selected. More details are given in E. The selected leading signal jet is required to have a $p_{\mathrm{T}} > 40$ GeV and the invariant mass of the dijet system (M_{jj}^{sig}) should be compatible with the W/Z mass ($64 < M_{jj}^{sig} < 106$ GeV).

As discussed in Section 6.2, the EW top and VVV processes are included in our signal MC sample generation. Truth studies have shown that in particular the EW top production is still significant in our resolved regions after the full event selection is applied. In order to reduce this contribution, an additional "VBS enhancing" cut is introduced; First the top-quark is reconstructed by considering the system of signal jets and the additional third jet of the event which is closest to the top mass (172.76 GeV). The invariant mass of the 3-jet system (or topMass) is plotted in Figure 6.7(a), for the EW signal. The contribution of the EW top and VVV diagrams in the total yield, is obtained using truth particle information, and is plotted in red and green, respectively. A cut on the invariant mass of the 3-jet system is applied to reject the majority of EW top events; M_{jjj} at 220 GeV. The resolved reconstruction without the top mass cut applied is still considered in the analysis and is referred to as "Loose Resolved" selection. The selection with the top mass cut applied is mentioned as "Tight Resolved".

The VBS purity of the merged SRVBS_HP and SRVBS_LP regions, is also studied. The corresponding plots are shown in Figures 6.7(b) and 6.7(c). The merged signal regions are found to be already pure in VBS events.Therefore no additional cuts are introduced for these regions. The diagram composition of the merged and resolved regions is summarized in Table 6.6

	Loose Resolved SR	Tight Resolved SR	Merged HP SR	Merged LP SR
tX purity	0.46	0.10	0.15	0.20
VVV purity	0.03	0.02	0.05	0.05
VBS purity	0.51	0.88	0.80	0.75

FIGURE 6.6: Diagram composition of the EW signal in the resolved and merged signal regions.

TABLE 6.2: Summary of event selection for the merged regime in the 2-lepton channel.

Selection		SR		Z CR
		HP	LP	incl
$Z \to \ell\ell$	Number of Loose leptons	2		
	Same flavor	yes		
	Leading lepton p_{T}	> 27 GeV		
	Subleading lepton p_{T}	> 27 GeV		
	dilepton invariant mass	$83 < m_{ee} < 99$ GeV $(-0.0117 \times p_{\mathrm{T}}^{\mu\mu} + 85.63\ \mathrm{GeV}) < m_{\mu\mu} < (0.0185 \times p_{\mathrm{T}}^{\mu\mu} + 94\ \mathrm{GeV})$		
	Opposite sign	For $\mu\mu$ channel only		
VBS jets candidates	Leading Tag jet p_{T}	> 30 GeV		
	Subleading Tag jet p_{T}	> 30 GeV		
	m_{jj}	> 400GeV		
	$\eta_{\mathrm{tag},j_1} \cdot \eta_{\mathrm{tag},j_2}$	< 0		
$W/Z \to J$	Num of large-R jets	≥ 1		
	3-Var Tagger	pass50WP	pass80WP && !pass50WP	fail80WP

6.5 Analysis regions

The analysis signal regions (SRs) are classified as merged or resolved based on the hadronic reconstruction of the W/Z boson. The cuts applied in the merged and resolved SRs are summarized in Tables 6.2 and 6.3 respectively. In order to constrain the main background contribution within our signal regions, signal-depleted regions, called control regions (CR), are also defined. For the background estimation to be precise, control regions have to be defined in a similar way as the signal regions, such as the shape of the background , when moving from the control to the signal region, doesn't change. The dominant background contribution for the 2-lepton channel is the Z + jets production (90 %). Thus, Z + jets control regions are considered (CRVjet).

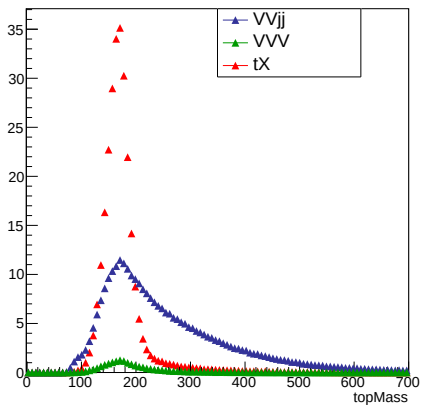

(a) Loose Resolved SR

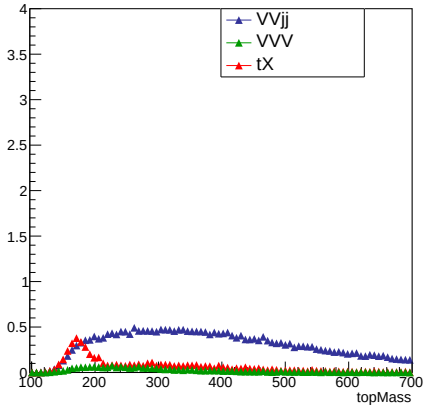

(b) Merged HP SR

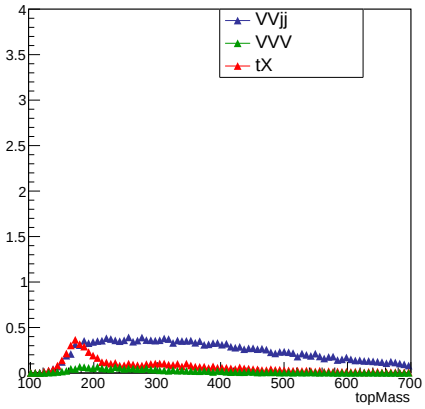

(c) Merged LP SR

FIGURE 6.7: Diagram composition of the EW signal, plotted for the reconstructed topMass, in the resolved and merged signal regions.

TABLE 6.3: Summary of event selection for the resolved regime in the 2-lepton channel.

Selection		SR	Z CR
$Z \to \ell\ell$	Number of Loose leptons	2	
	Same flavor	yes	
	Leading lepton p_{T}	> 27 GeV	
	Subleading lepton p_{T}	> 27 GeV	
	dilepton invariant mass	$83 < m_{ee} < 99$ GeV $(-0.0117 \times p_{\mathrm{T}}^{\mu\mu} + 85.63\ \mathrm{GeV}) < m_{\mu\mu} < (0.0185 \times p_{\mathrm{T}}^{\mu\mu} + 94\ \mathrm{GeV})$	
	Opposite sign	For $\mu\mu$ channel only	
VBS jets candidates	Leading Tag jet p_{T}	> 30 GeV	
	Subleading Tag jet p_{T}	> 30 GeV	
	m_{jj}	> 400GeV	
	$\eta_{\mathrm{tag},j_1} \cdot \eta_{\mathrm{tag},j_2}$	< 0	
$W/Z \to jj$	Num of signal small-R jets	2	
	Leading signal jet p_{T}	> 40 GeV	
	Subleading signal jet p_{T}	> 20 GeV	
	$Z \to q\bar{q}$ and $W \to q\bar{q}$	$64 < m_{jj} < 106$GeV	$50 < m_{jj} < 64\,GeV$ or $m_{jj} > 106$
VBS enhancing	m_{jjj}	> 220 GeV	

A single merged Z+jets control region is defined. Events in the merged CRVjet are required to pass all the common cuts of the HP/LP SRs but fail any of the W/Z tagger requirements of the 80% working point. In the resolved regime, the CRVjet events are selected by reversing the M_{jj}^{sig} mass window cut; events should pass all cuts of the resolved signal region except for M_{jj}^{sig} , which should satisfy: $50 < M_{jj}^{sig} < 64$ GeV or $M_{jj}^{sig} > 106$ GeV.

Events can satisfy the requirements of more than one of the regions described above. However, an event should be included to a single region only. The event classification to the different regions is happening following the order shown in Figure6.8. An event is first examined to pass any of the signal region definitions. If the event fails to be classified as a signal event, is then tested for the control regions. In all cases, priority is given to the merged selection which offers a better background rejection comparing to the resolved selection.

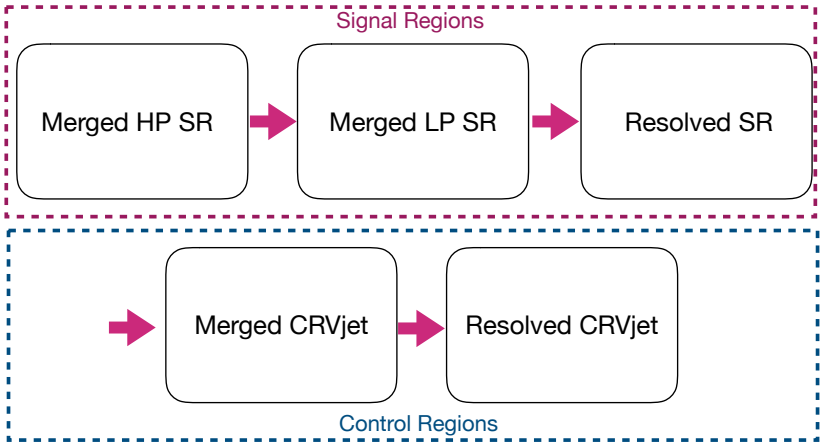

FIGURE 6.8: The event categorization to regions.

6.6 Background modeling

The modeling of the dominant background for the 2-lepton channel, Z+jets, is studied in this section. In Figure 6.9 the M_{jj}^{tag} distributions for the merged and resolved control regions

are plotted. Large discrepancies with respect to data are observed in both cases. Similar discrepancies have been reported in the first publication based on Run 1 data [26]. This effect is believed to be due a combination of the shower activity as well as the scale choice for NLO real emissions in the sherpa samples. In order to account for this mis-modeling, a reweighting for the Z + jets MC is derived. Two reweighting functions are obtained separately for the merged and resolved regimes. The reweighting functions are derived in the control regions and are used to apply corrections in the signal regions. A simple linear fit to the M_{jj}^{tag} distribution is performed. The fit function is defined as follows :

$$R = p_0 * M_{jj}^{tag} + p_1$$

, where $R = data/MC$. Since the correction functions are derived for the Z + jets MC only, all the non Z + jets MC events are first subtracted from data. In Figure 6.10 and 6.11 fit results for the combined and individual MC16a,d and e periods are plotted for the merged and resolved regions, respectively. Some dependance on the MC period is noticed especially in the resolved regime. However, the gain on the final re-weighted distribution from using a per period M_{jj}^{tag} reweighting is found to be small and therefore fit results from the combined period are used.

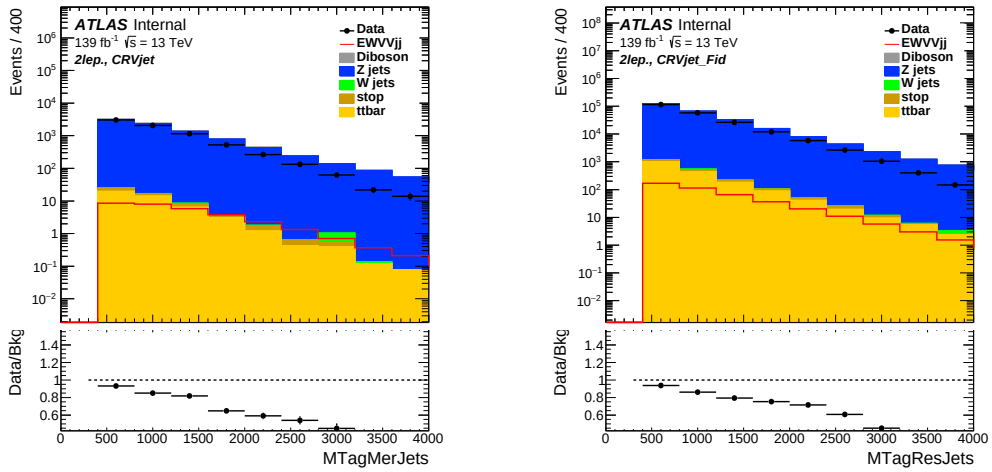

(a) (b)

FIGURE 6.9: M_{jj}^{tag} distributions for the merged (a) and resolved (b) control regions in the 2-lepton channel.

Parameter	Merged CRVjet	Resolved CRVjet
p_0 (slope) [GeV^{-1}]	$(-23.8 \pm 2.5)e^{-5}$	$(-17.5 \pm 0.5)e^{-5}$
p_1 (constant)	1.298 ± 0.031	1.187 ± 0.005

TABLE 6.4: Fitted reweighting parameters for the merged and resolved regions.

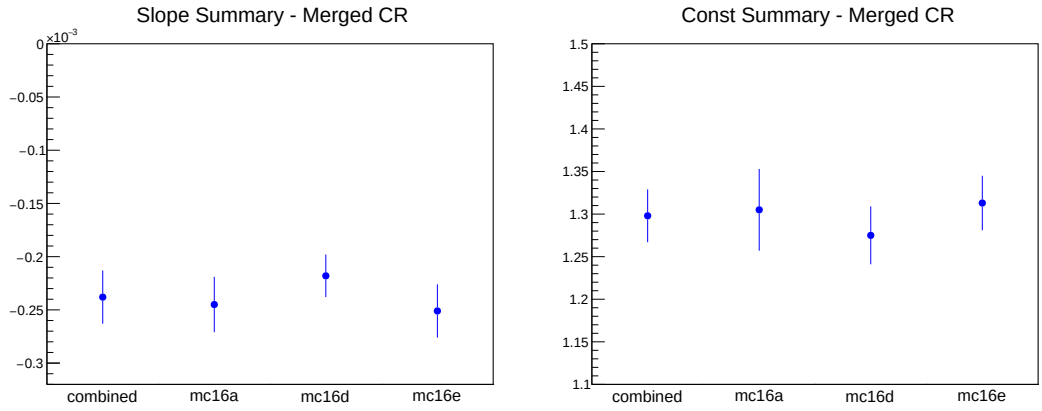

(a) (b)

FIGURE 6.10: Fit summary results for the merged regime in the 2-Lepton Channel

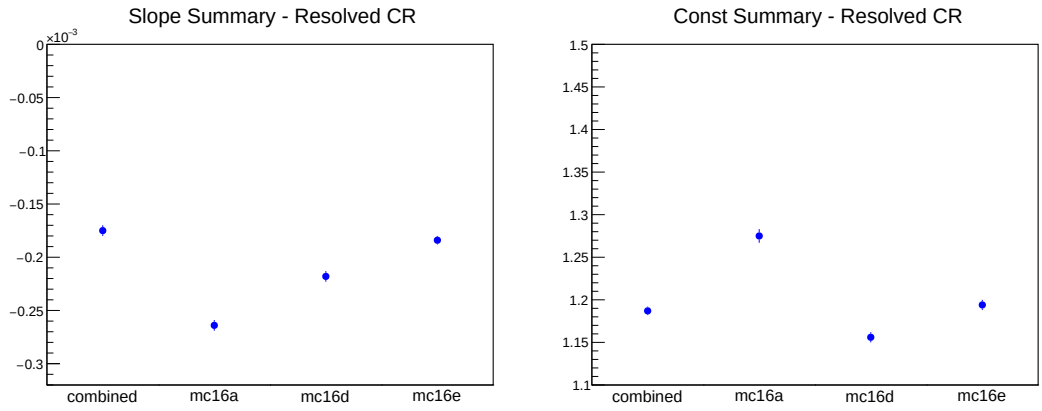

(a) (b)

FIGURE 6.11: Fit summary results for the resolved regime in the 2-Lepton Channel

In Figure 6.12, the fitted slopes as a function of M_{jj}^{tag} for the merged and resolved control regions are shown for the combined MC16a,d and e periods. All distributions are first normalized, thus the derived correction functions account only for shape differences between Z+jets MC and data. Differences coming from normalization will be considered later in the final fit model. The fitted parameters for the merged and resolved regimes are summarized in Table 6.4.

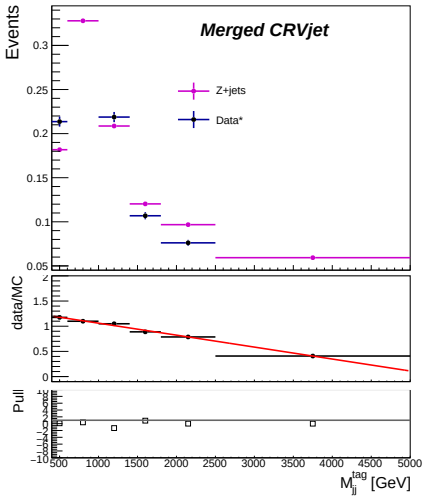

(a)

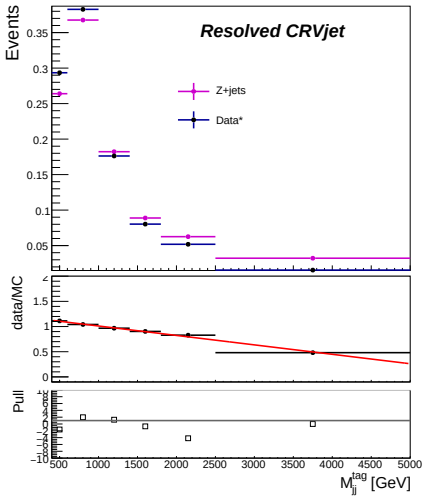

(b)

FIGURE 6.12: M_{jj}^{tag} reweighting for the merged (a) and resolved (b) regimes. Distributions are normalized and a re-binning has been performed in order for the statistical uncertainty of each bin to be less than 5%. A linear fit is performed to the data/MC ratio. The pull from the fit for each bin is also computed and plotted.

The modeling of various kinematic variables, after re-weighting is performed, is plotted in Figure 6.13 and Figure 6.14 for the merged and resolved control regions, respectively. The Data/Bgd ratios are overall flat, indicating a successful re-weighting.

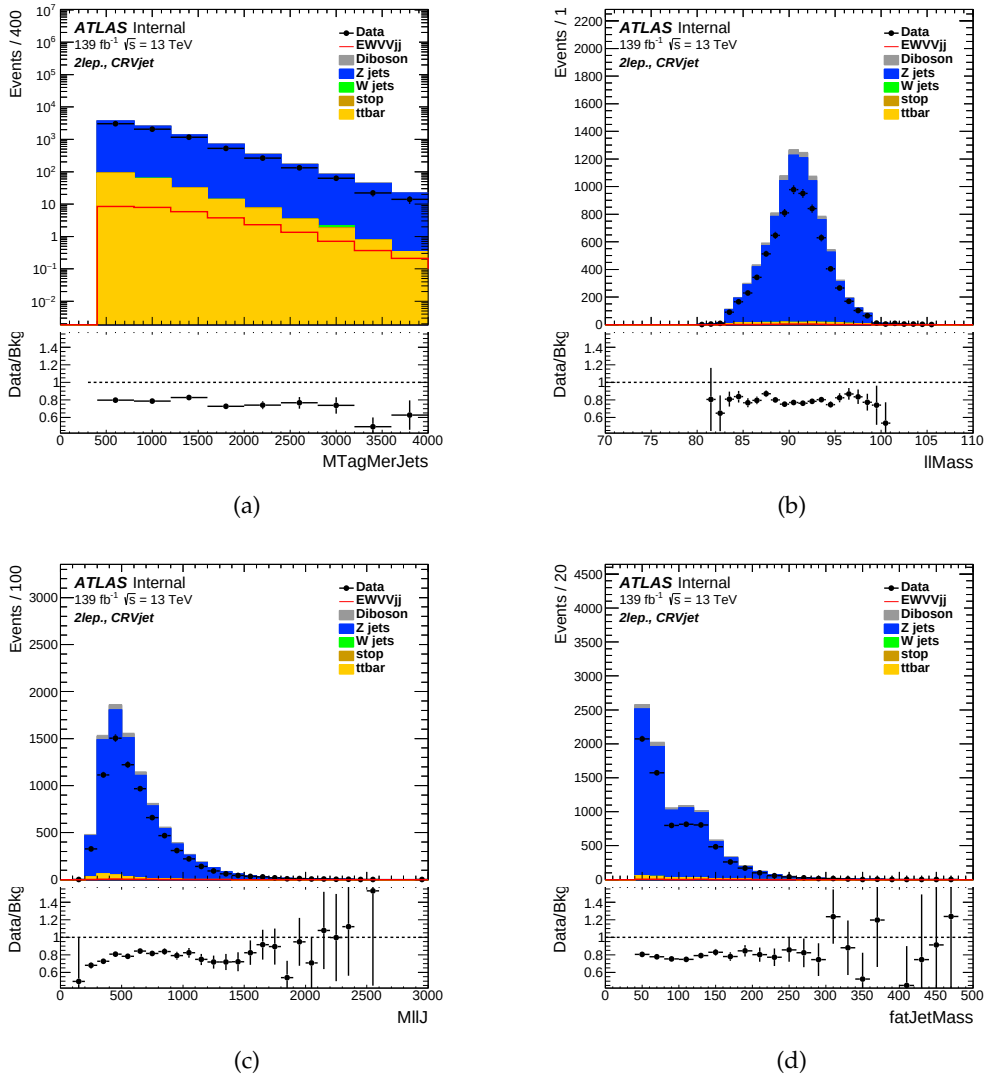

FIGURE 6.13: Various kinematic variables in the Z+jets merged CR in the 2-lepton channel analysis.

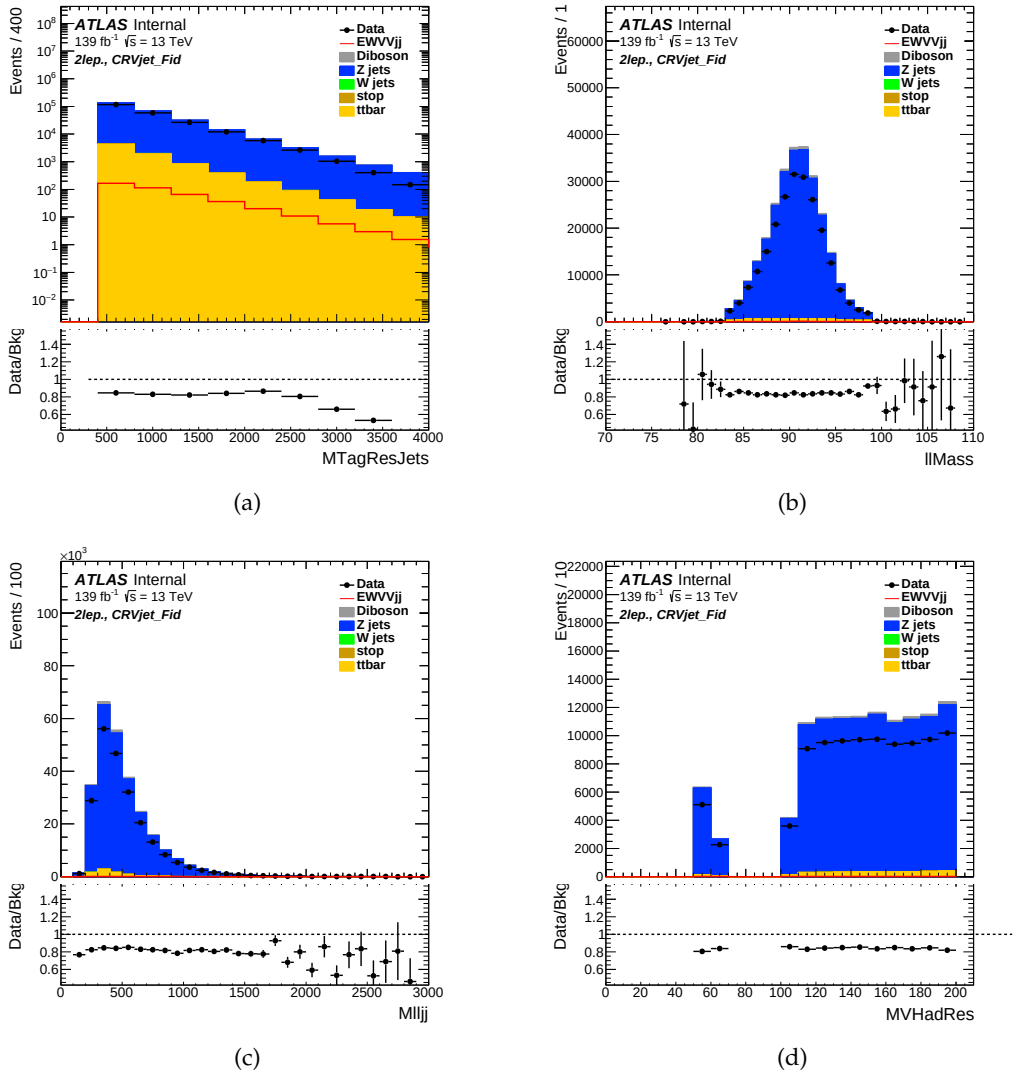

FIGURE 6.14: Various kinematic variables in the Z+jets resolved CR in the 2-lepton channel analysis.

6.7 Multivariate analysis

In order to improve the sensitivity of the analysis to the target signal, a multivariate technique is used. Goal of the multivariate algorithm is to increase as much as possible the separation between signal and background. In this analysis, the XGBoost (eXtreme Gradient Boosting) classifier is used [85]. XGBoost is a supervised learning algorithm which employs gradient tree boosting in order to perform classification. Gradient Boosted Decision Trees (BDT) are widely used in machine learning and have shown remarkable results on many classification problems [85].

6.7.1 k-Fold cross validation

In order to take advantage of the full set of simulated events and evaluate the performance in an unbiased way, the k-fold cross validation method is used [86]. In this method the dataset is split in k equally sized parts (or folds) as shown in Figure 6.15. The algorithm is then trained and validated k times. In each iteration k-1 folds are used for training and the rest for validation. This way the entire dataset is used both for training and validation.

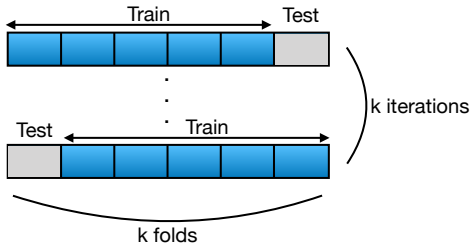

FIGURE 6.15: Schematic view of k-fold cross validation method.

In this analysis the k-fold cross validation method, with k=5, is used. The choice of number of folds is motivated by the fraction of events used each time for training. When k=5, the largest fraction of the dataset (80%) is used (during each iteration) for training, leading to a better learning performance. This is especially important for the merged regime where the statistics is limited.

The events are distributed in the different folds based on the remainder of the event number (eventN) division by five as shown in Table 6.5. After the training, the performance for each fold is evaluated using the test dataset. Finally the test datasets of all folds are combined together in order to evaluate the final performance.

Separate BDT trainings are performed for the resolved and merged regimes. Events from the corresponding signal regions are used for the BDT trainings.

Fold #	Events for training	Events for testing
Fold 0	(eventN % 5) $\in [0, 3]$	(eventN % 5) = 4
Fold 1	(eventN % 5) $\in [1, 4]$	(eventN % 5) = 0
Fold 2	(eventN % 5) $= 0, 2, 3, 4$	(eventN % 5) = 1
Fold 3	(eventN % 5) $= 0, 1, 3, 4$	(eventN % 5) = 2
Fold 4	(eventN % 5) $= 0, 1, 2, 4$	(eventN % 5) = 3

TABLE 6.5: Event categorization into folds.

6.7.2 Feature Engineering

Depending on the region, a set of different features are used as inputs for the BDT training . The choice of variables depend on the separation achieved between signal and background. All possible variables are initially examined and used as inputs for the BDT training. Features that are not important and don't contribute to the training process will be eliminated later on Section 6.7.5.

Resolved regime

Inputs used for the resolved regime training can be grouped into the following categories:

- Variables related to the signal jets and di-lepton system (denoted as $lljj$ in plots).
- Variables related to the entire system of signal jets, di-lepton system and tagging jets (denoted as fullSystem in plots).
- Variables associated to the signal jets.
- Features linked to the tagging jets.
- Other variables designed to take into account the geometry of the event. Such variables are:
  - The Zeppenfeld variable defined as:

$$Zepp = |\eta_{obj} - \frac{(\eta_{\text{tag},j_1} + \eta_{\text{tag},j_2})}{2}| \tag{6.3}$$

    , where η_{obj} is the pseudorapidity of the leading small-R jet from the remaining small-R jet collection (after removing the tagging and signal jets). The corresponding variable is denoted as ZeppRes in the plots. Due to the suppressed hadronic activity in VBS events (no color flow between the interacting partons) the ZeppRes tends to take larger values for signal than background events. Alternative definitions of the Zeppenfeld variable are also considered; by replacing η_{obj} with the pseudo-rapidity of the $V_{lep}V_{had}$, V_{had} or V_{lep} candidate. The corresponding Zeppenfeld variables in this case, denoted as ZeppZV, ZeppV and ZeppZ, take smaller values for signal than background events.
  - The centrality defined as :

$$Centrality = min(\Delta\eta_-, \Delta\eta_+) \tag{6.4}$$

    where

$$\Delta\eta_- = min(\eta_{V_{lep}}, \eta_{V_{had}}) - min(\eta_{\text{tag},j_1}, \eta_{\text{tag},j_2})$$

    and

$$\Delta\eta_+ = max(\eta_{\text{tag},j_1}, \eta_{\text{tag},j_2}) - max(\eta_{V_{lep}}, \eta_{V_{had}})$$

    The centrality measures the position of the emitted bosons with respect to the tagging jets. In the case of VBS events, the bosons are expected to be produced centrally and be accompanied by two jets with a large pseudo-rapidity gap. Thanks to this characteristic topology, VBS events tend to have a more positive centrality value with respect to background events. It is worth noting here, that the centrality definition is very similar to the alternative Zeppenfeld variable definitions described above. Both types of variables are expected to give a very similar description of the event and are usually highly correlated.

Modeling plots for all the inputs described above, in the tight resolved SR[3], are shown in Appendix A. The EW signal is compared to the irreducible background. Since, the major background contributions are treated as floating normalizations in our fit model, only shape effects matter. Therefore, all distributions are shown after being normalized. The modeling plots for the final BDT features, after the studies presented in section 6.7.5, are shown in Figure 6.16. A few variables, mostly related to jet substructure (e.g., NtrkSignalJet1), show some discrepancies between data and MC. However, it is verified that the final BDT score distributions show a good agreement between data and MC in the SR[4].

Merged regime

Similarly to the resolved regime, inputs for the merged HP and LP regions can be grouped into the following categories:

- Variables related to the $sigJ$ an di-lepton system (denoted as llJ).
- Variables related to the entire system of $sigJ$, di-lepton and tagging jets (denoted as fullSystem in plots).
- Variables associated to the $sigJ$ (identified as fatJet in plots).
- Tagging jet related variables.
- The zeppenfeld and centrality variables defined as in equations 6.3 and 6.4 after replacing the signal jets with the large-R jet signal candidate.

The modeling plots for all the features described above, are shown in Appendix A. The modeling distributions for the final set of BDT features, after the studies presented in section 6.7.5, are shown in Figures 6.17 and 6.18, for the Merged HP and LP SRs, respectively. In general, a flat data to MC ratio is noticed for the majority of features, with a few discrepancies. Similarly to the resolved regime, a data over MC comparison is made for the final BDT score distributions in order to verify that the agreement is good.

To quantify the discrimination power of each feature, the binned discovery significance is computed for all distributions, using the following definition [87]:

$$Z = \sqrt{\sum_{i=0}^{N_{bins}} 2\big[(s_i+b_i)ln(\frac{(s_i+b_i)(b_i+\sigma_{b_i}^2)}{b_i^2+(s_i+b_i)\sigma_{b_i}^2}) - \frac{b_i^2}{\sigma_{b_i}^2}ln(1+\frac{\sigma_{b_i}^2 s_i}{b_i(b_i+\sigma_{b_i}^2)})\big]} \tag{6.5}$$

where s_i and b_i are the corresponding signal and background events in bin i and the sum runs over all the bins of the distribution. In order to take into account background uncertainties, a fixed 10% uncertainty is considered for each bin of the distribution ($\sigma_{b_i} = 0.10 b_i$). Summary plots with the computed significance values for the merged HP, merged LP, and resolved SR related features are shown in Figures 6.19- 6.20. The tagging jet related features, offer the best discrimination power in all three regions. It is worth noting here, that for the majority of features, the merged HP SR shows a much better significance. Even though this region is poor in statistics, comparing to the resolved SR, it offers a powerful background rejection, thanks to the W/Z tagger algorithm employed for the V_{had} selection.

[3]The modelling for all distributions was first checked in the CRVjet, before the SR unblinding.
[4]This is verified in the left bins of the BDT score which are less sensitive to the EW signal.

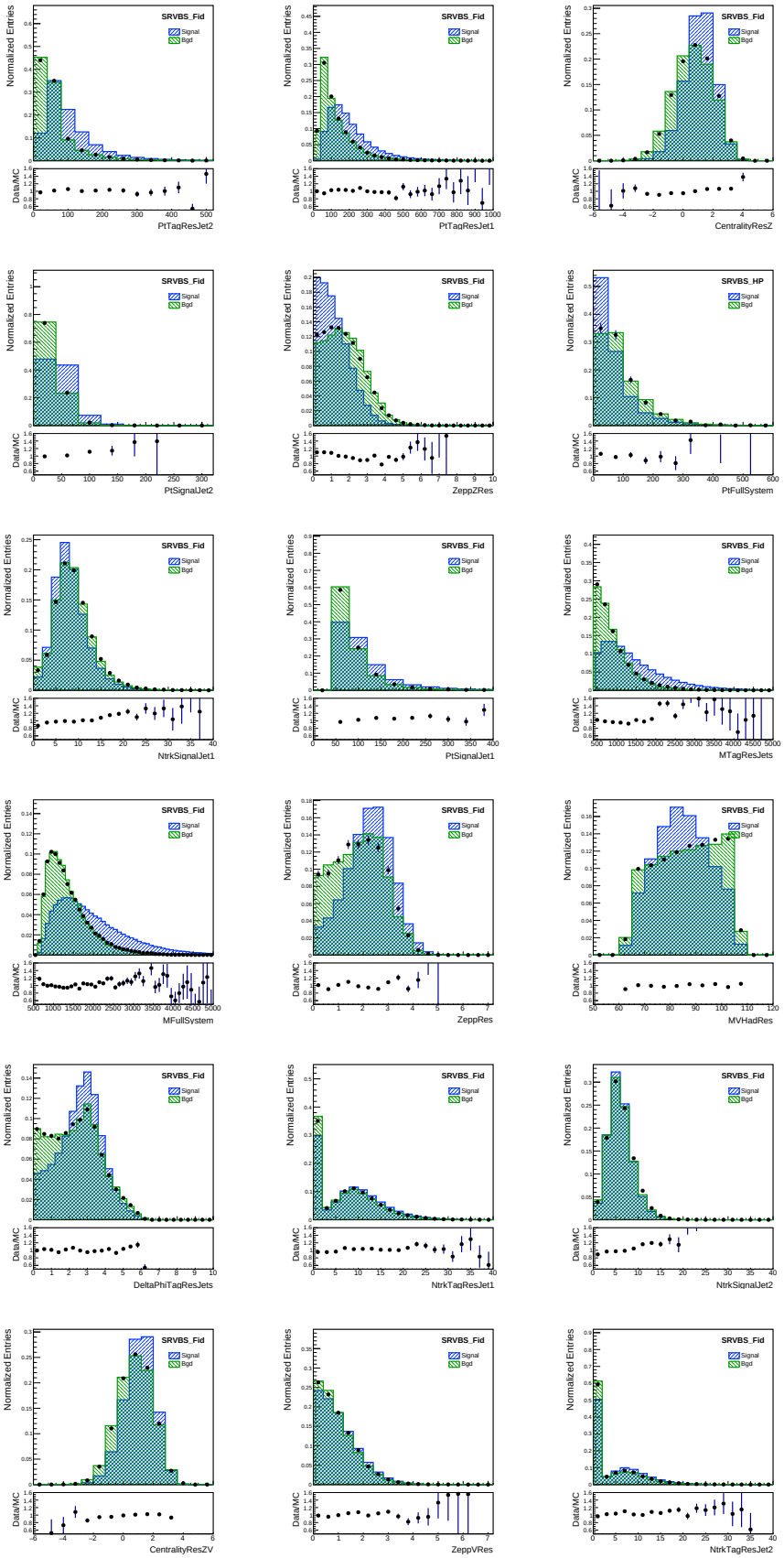

FIGURE 6.16: Final set of features used for the BDT training in the resolved SR.

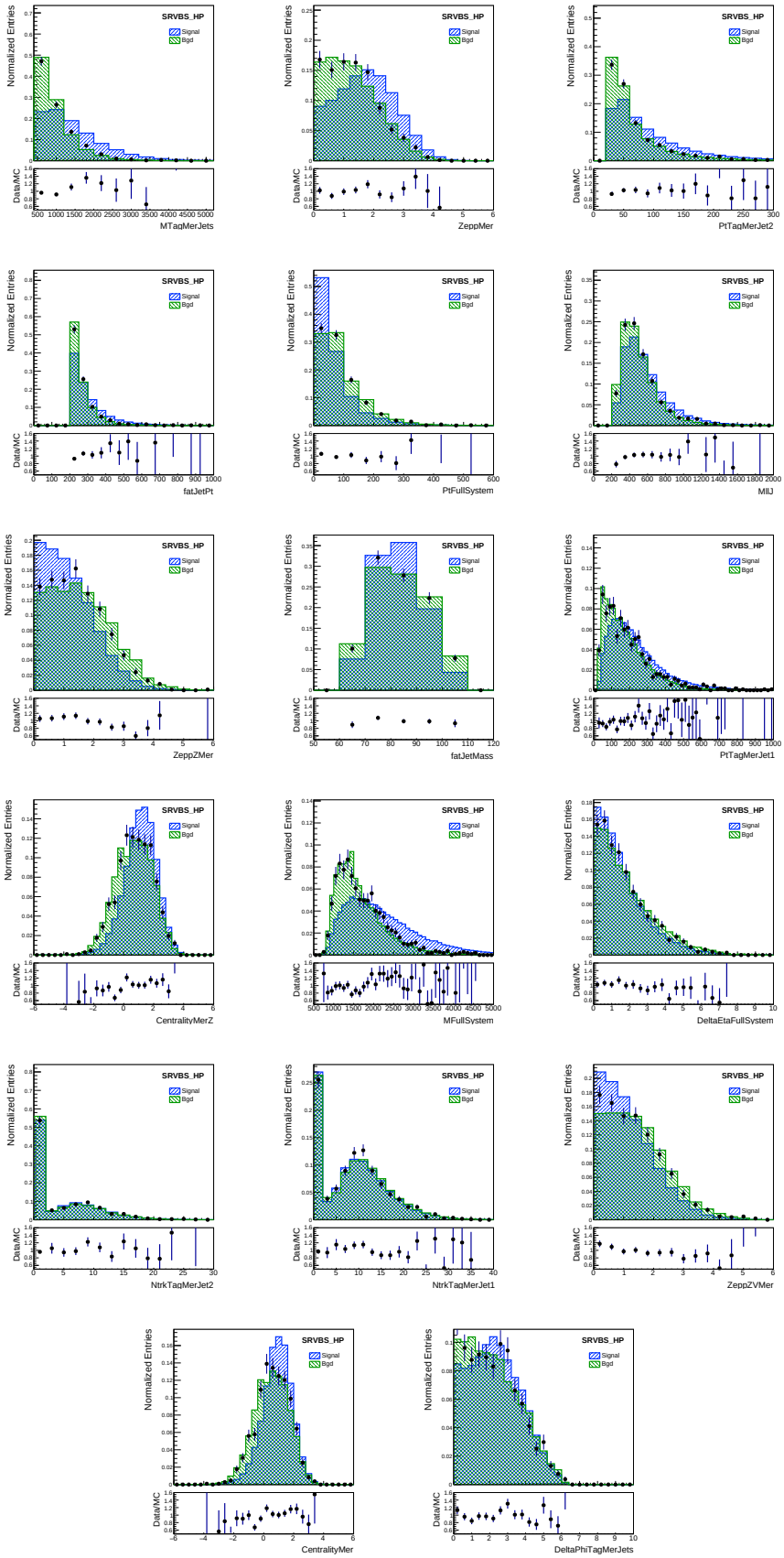

FIGURE 6.17: Final set of features used for the BDT training in the merged HP SR.

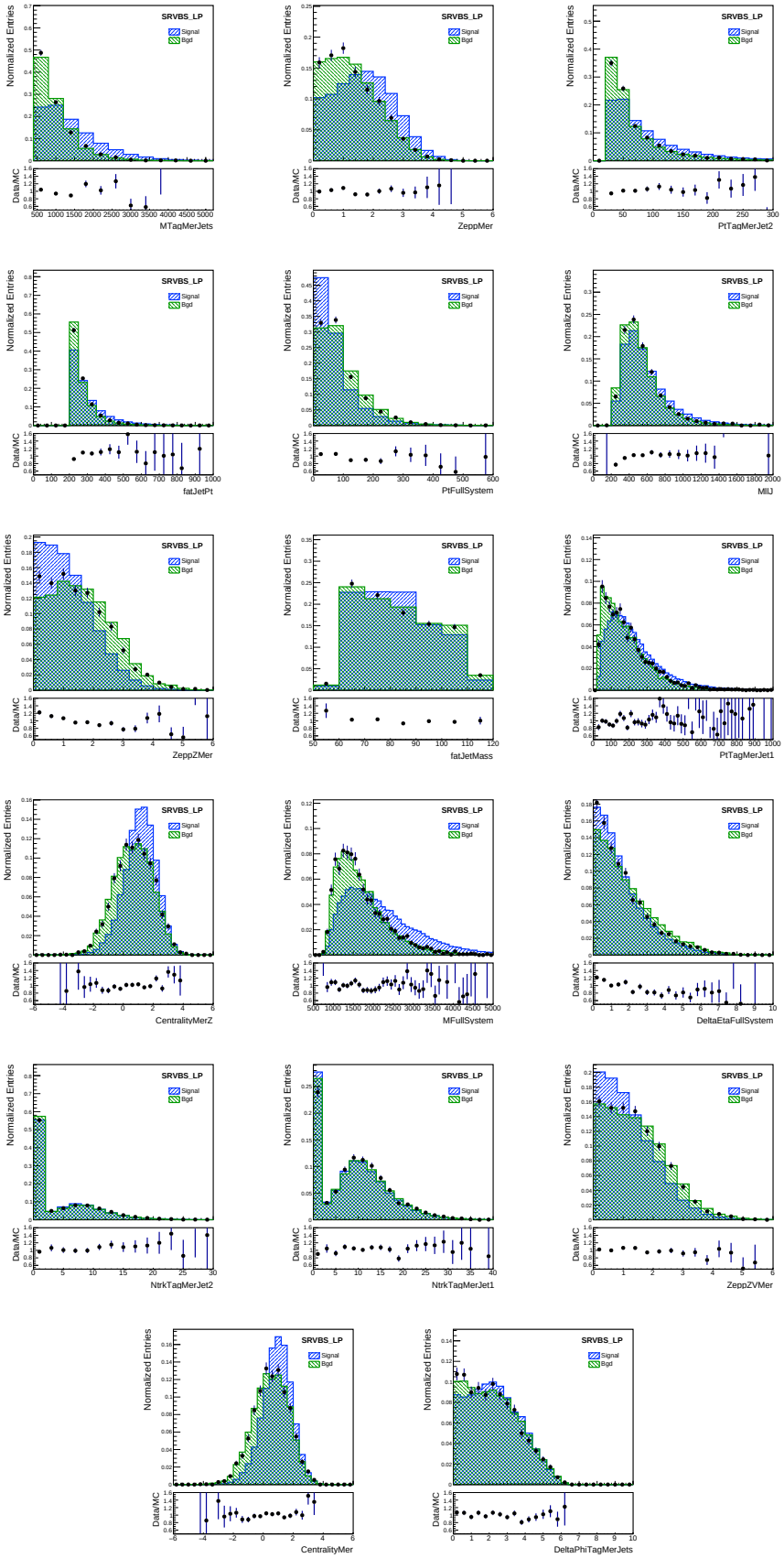

FIGURE 6.18: Final set of features used for the BDT training in the merged LP SR.

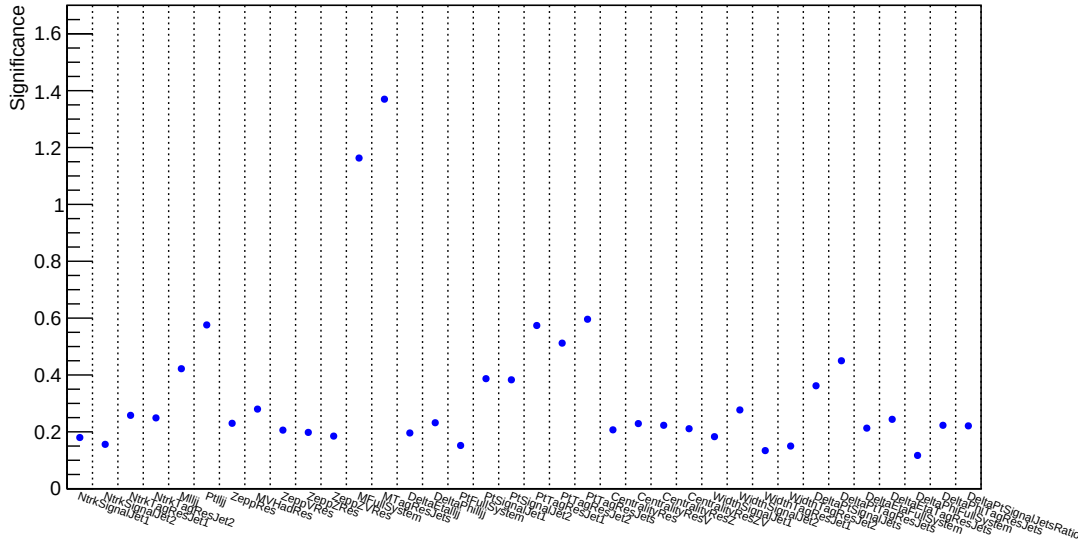

FIGURE 6.19: Significance values for features in the resolved SR.

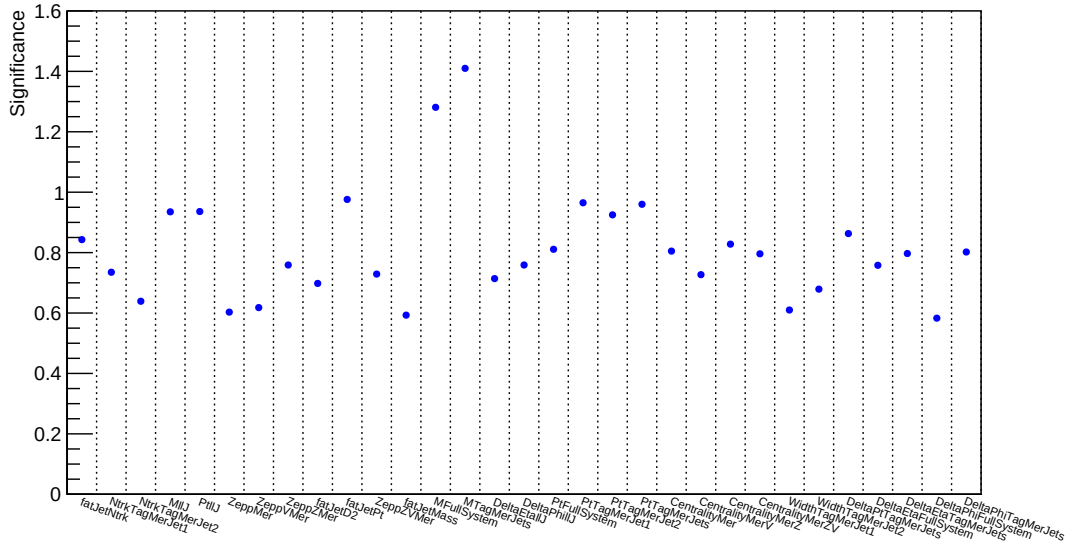

FIGURE 6.20: Significance values for features in the merged HP SR.

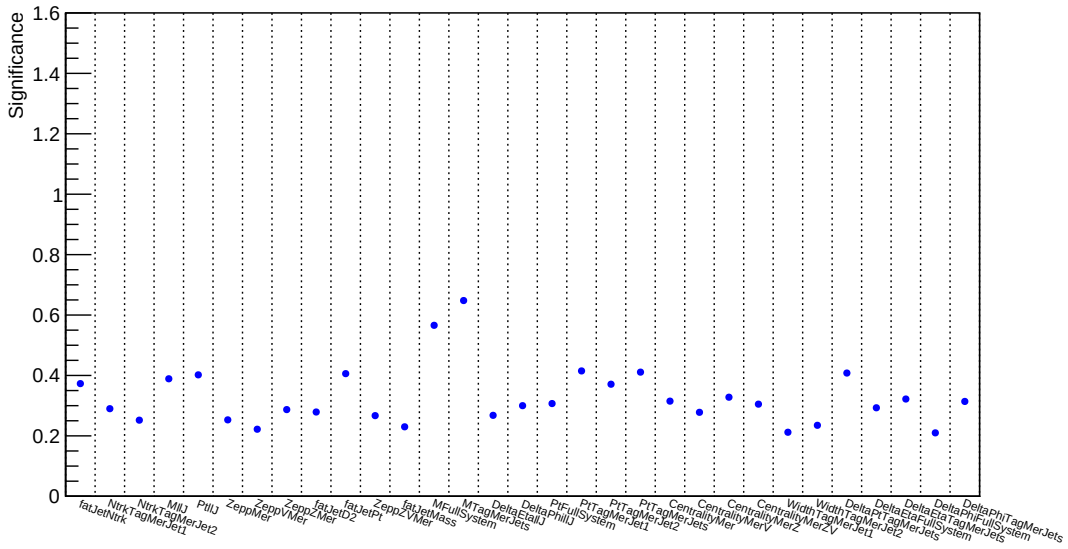

FIGURE 6.21: Significance values for features in the merged LP SR.

6.7.3 BDT training

Merged training

The merged SRs have in general poor statistics, which might affect the learning procedure during training. In order to improve the training statistics, two different types of training are tested for the merged HP/LP regimes:

- Type A: Training in an inclusive merged SR which is formed from the combination of the HP and LP signal regions.
- Type B: Training in the individual HP and LP signal regions.

The k-fold cross validation with k=5, as described in 6.7.1, is used for both types of training. The output model performance is then evaluated in the corresponding HP and LP signal regions. The train and test BDT score distributions in the five folds, and for the two types of training, are shown in Appendix B. A good test-train agreement is observed in all the folds. Next, the test datasets from all folds are combined together, for the final performance evaluation. In Figures 6.22(a) and 6.22(b), a comparison of the two types of training for the combined distributions, is shown for the merged HP and LP SRs, respectively. The corresponding significance values are summarized in Tables 6.6 and 6.7. A ∼10% better performance is achieved when training in the individual HP and LP signal regions. Therefore, the type B training is selected. The performance difference between the two types of training, can be attributed to shape differences between the large-R jet related variables in the merged HP and LP SRs A.

Training	Z ($\sigma_{b_i} = 0$)	Z ($\sigma_{b_i} = 0.10 b_i$)
Type A	3.86	2.80
Type B	4.13	3.14

TABLE 6.6: Significance summary table for merged HP.

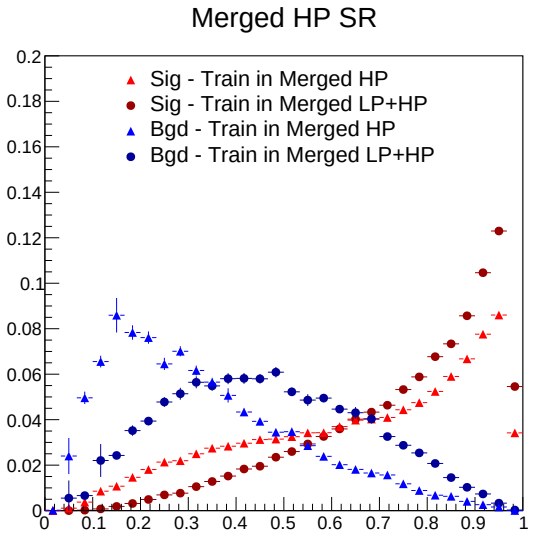

(a)

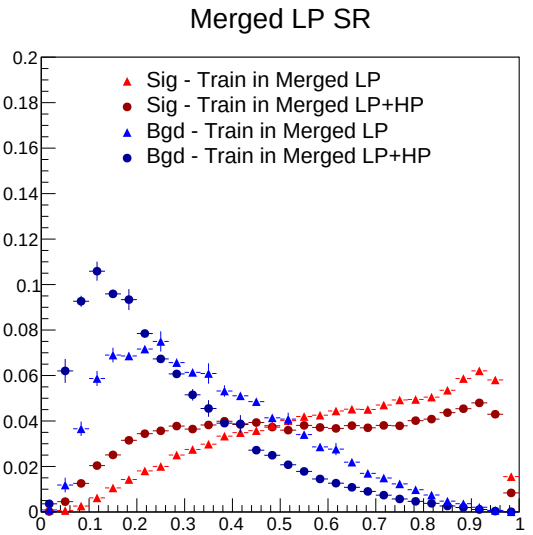

(b)

FIGURE 6.22: Final BDT scores after combining the test datasets from all folds for the merged HP (a) and LP (b) regions. Circular markers correspond to cases where the BDTs were trained in the inclusive Merged SR while triangles to trainings in the individual HP or LP SR.

Training	Z ($\sigma_{b_i} = 0$)	Z ($\sigma_{b_i} = 0.10 b_i$)
Type A	1.63	1.50
Type B	1.66	1.41

TABLE 6.7: Significance summary table for merged LP.

Resolved training

The resolved SR is classified as "Tight" or "Loose" based on the criteria discussed in 6.4.3. The tight resolved SR being more pure in VBS events is the region we are mostly interested about. Two types of training are examined:

- Type C: Training in the loose resolved SR and evaluating performance in the tight region.
- Type D: Training and testing in the tight resolved SR.

Similarly to the merged regime, the k-fold cross validation with k=5 is employed for both types of training. The training results are shown in Figures B.5-B.6. A comparison of the two methods for the final BDT scores, after combining the test datasets from all folds, is plotted in Figure **??**. The corresponding significance values are summarized in Table 6.8. Training in the loose resolved SR is found to give a better performance thanks to the higher statistics available for training.

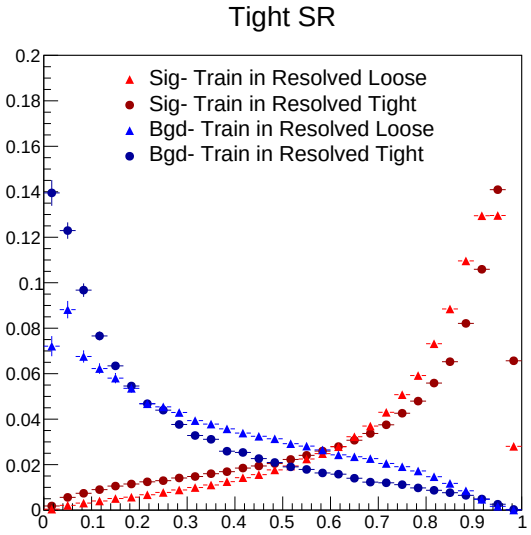

FIGURE 6.23: Final BDT scores after combining the test datasets from all folds for the tight resolved SR. Circular markers correspond to cases where the BDTs were trained in the tight resolved SR while triangles to trainings in the loose resolved SR.

Training	Z ($\sigma_{b_i} = 0$)	Z ($\sigma_{b_i} = 0.10 b_i$)
Type C	4.35	2.27
Type D	4.24	1.86

TABLE 6.8: Significance summary table for resolved SR.

6.7.4 Feature Importance

The feature importance for the model predictions is measured using the so-called SHAP (SHapley Additive exPlanation) values as proposed in [88]. The goal of SHAP is to explain the model prediction for an event by estimating how much each feature contributes to the final decision. What SHAP is actually doing is computing Shapley values from coalitional game theory. In this approach, the feature values for an event act as players in a coalition and

Shapley values give an estimate of the contribution of each player (or feature value) to the resulting collective payoff (or prediction).

A single fold from each signal region (merged HP, LP or tight resolved) is used for the feature importance study. In Figure 6.24 a comparison of the BDT shapes in the different folds is plotted for the three signal regions. Since the BDTs in each fold, are trained using the same set of hyperparameters, they can be considered equivalent.

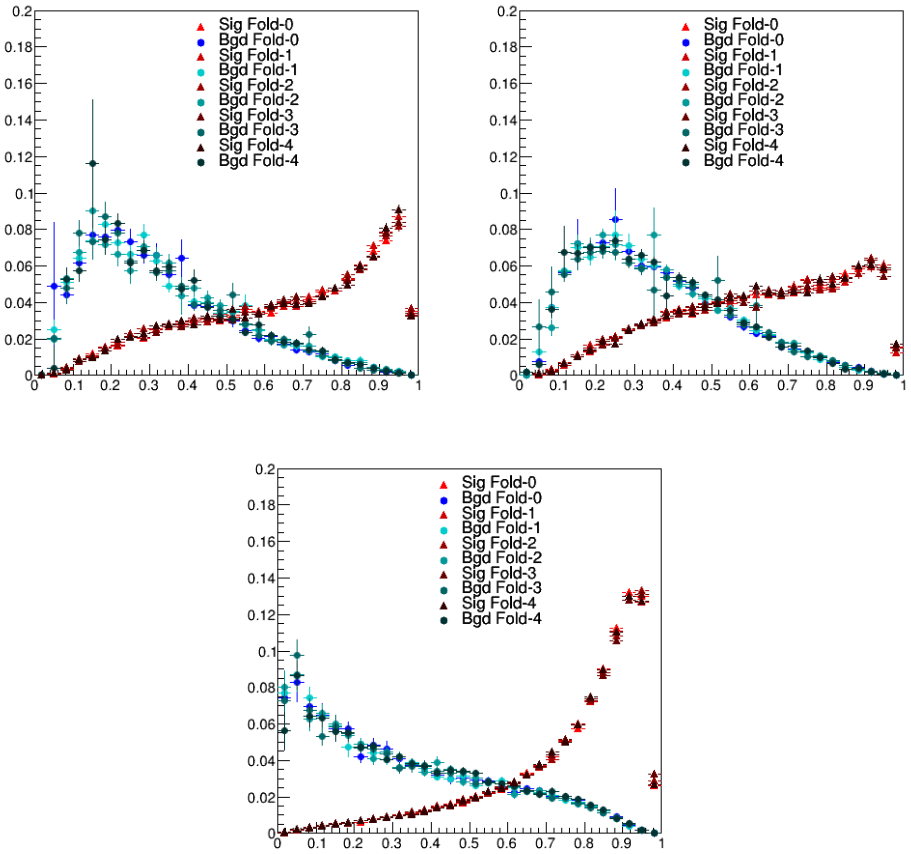

FIGURE 6.24: Folds comparison for the merged HP (a), merged LP (b) and tight resolved (c) signal regions

The SHAP summary plots for the BDT in fold-0 of the merged HP, LP and tight resolved SRs are plotted in Figures 6.25-6.27. In the density scatter plots in the left, SHAP values are plotted, in order to give an estimation of the impact of each feature on the final prediction for each event. Features are sorted by the sum of the SHAP value magnitudes across all events. The color in these plots shows the feature value (red high, blue low). As expected the HP and LP SRs show a very similar feature ranking. The MTagMerJets (mass of the tagging jets) is ranked as the most important feature as it affects a big number of predictions. In the resolved regime the p_{T} of the tagging jets are ranked as the most important variables. Although other features (like the WidthSignalJet2) affected bigger number of predictions, the p_{T} of the tagging jets had a larger impact on the final model output. The mean absolute SHAP values for each feature, are also shown in the right side of these plots.

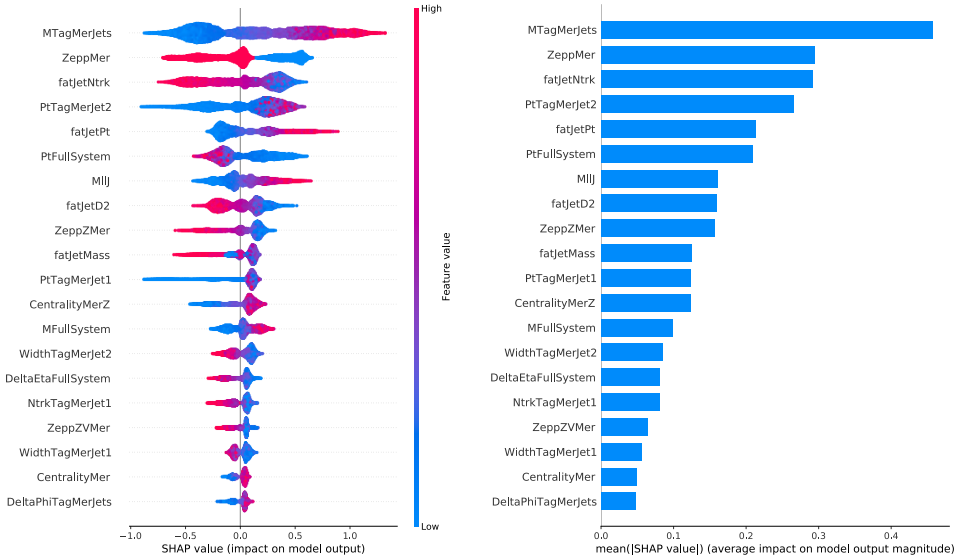

FIGURE 6.25: SHAP summary plots for the BDT trained in fold-0 of the merged HP SR.

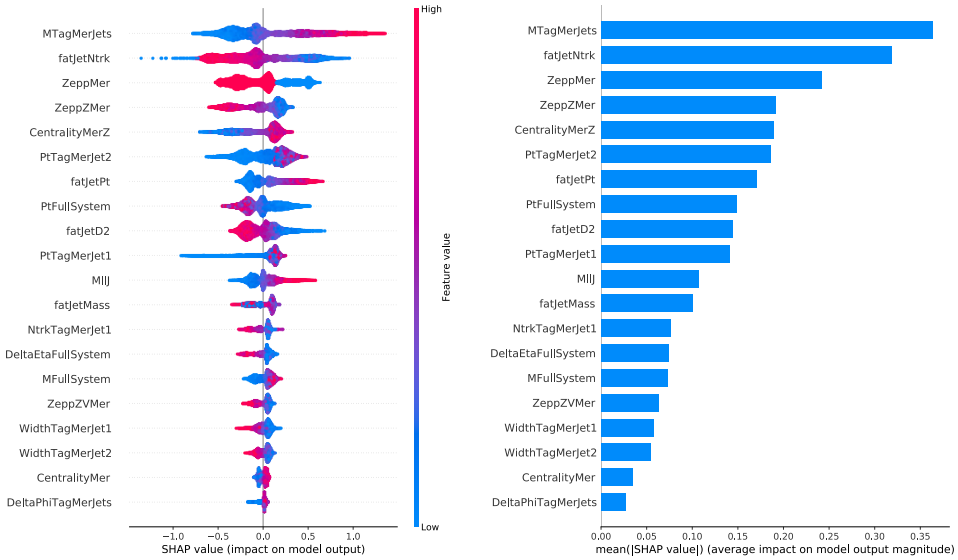

FIGURE 6.26: SHAP summary plots for the BDT trained in fold-0 of the merged LP SR.

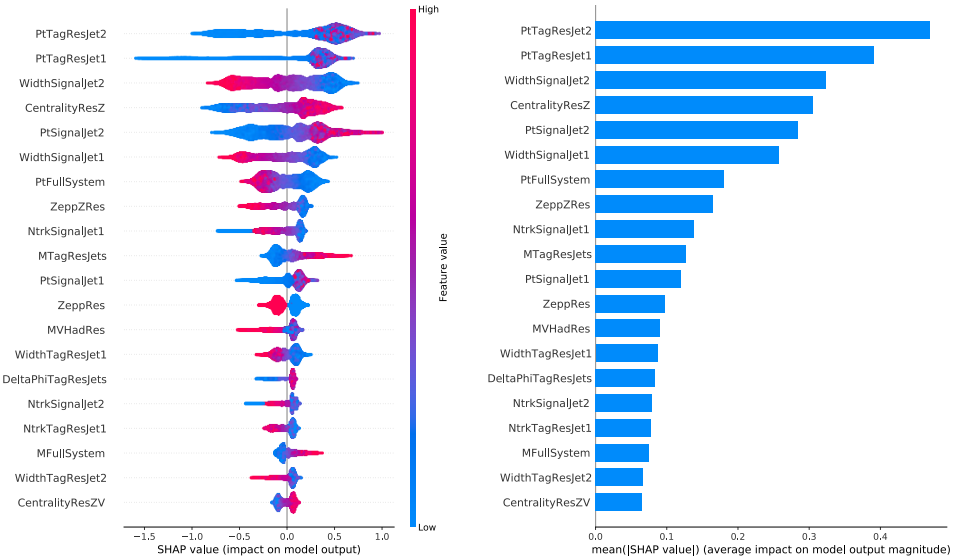

FIGURE 6.27: SHAP summary plots for the BDT trained in fold-0 of the tight resolved SR.

6.7.5 Feature Elimination

In order to keep the models as simple as possible, a backward feature elimination (FE) is performed. In this, features are eliminated one by one based on a SHAP threshold value. In each step features with a mean absolute SHAP value smaller than the current threshold are eliminated, the BDT is re-trained and the performance drop, in terms of significance, is estimated using the test data of a single fold. For the significance estimation the formula of equation 6.5 is used, assuming no background uncertainty.

In Figures 6.28 - 6.30 the significance drop as a function of the mean absolute SHAP threshold value is plotted for the merged HP, LP and resolved SRs respectively. Due to the poor statistics available, large fluctuations are observed in the significance drop estimation of the merged HP SR. For the final discriminant features with SHAP values greater than 0.041 for the merged HP, 0.024 for the merged LP and 0.058 for the resolved region are selected. These numbers correspond to a selection of 20 features per region.

After the feature elimination is performed, the BDTs are re-trained using the new set of features. The updated BDT scores are then compared to the original ones, before any feature elimination, as shown in Figure 6.31. The shapes after FE are represented by solid lines, while dashed lines are used for the original shapes. In the merged regimes the BDT shapes appear unaffected after the FE, while small differences are noticed in the resolved regime. Such small differences were expected given the selected SHAP threshold value. The corresponding drop in significance was found to be less than 5%.

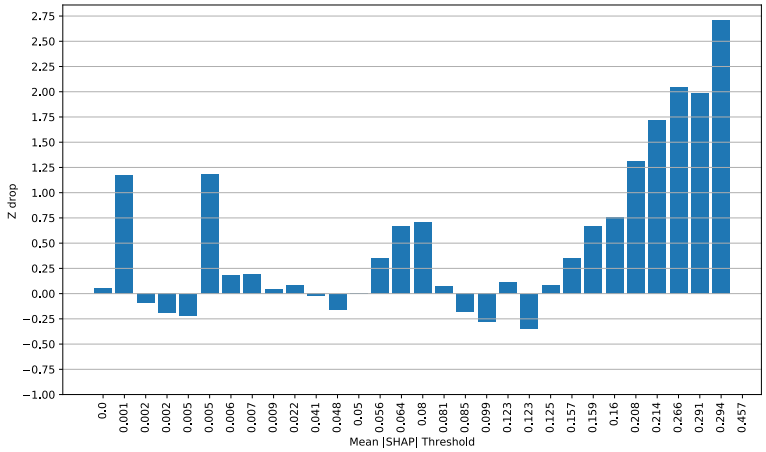

FIGURE 6.28: Backward feature elimination for merged HP SR

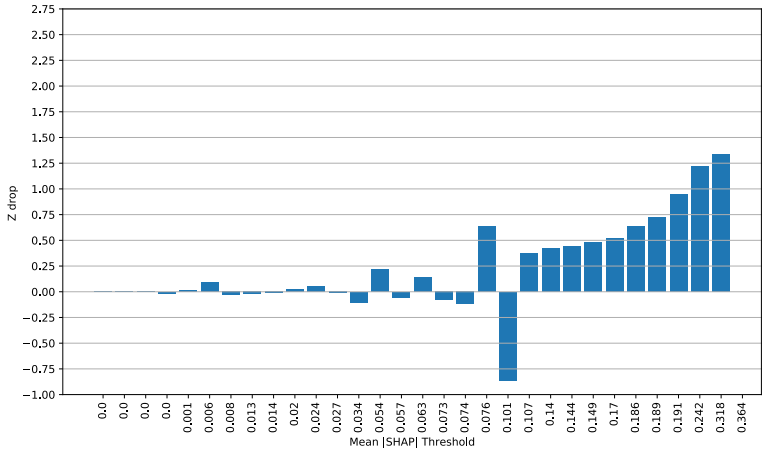

FIGURE 6.29: Backward feature elimination for merged LP SR

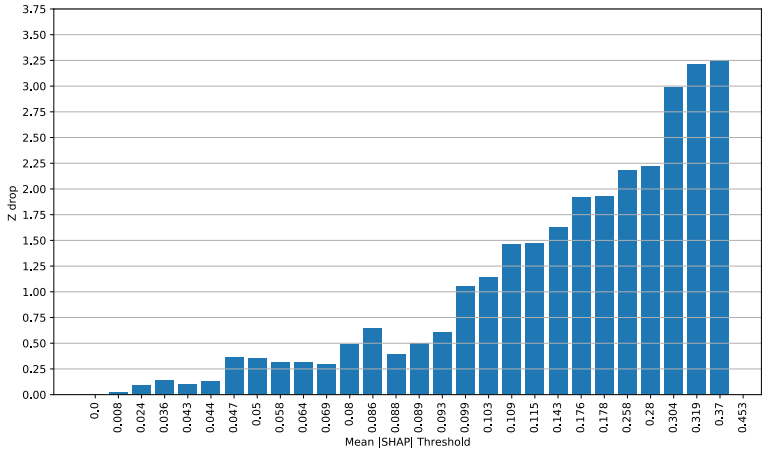

FIGURE 6.30: Backward feature elimination for resolved SR

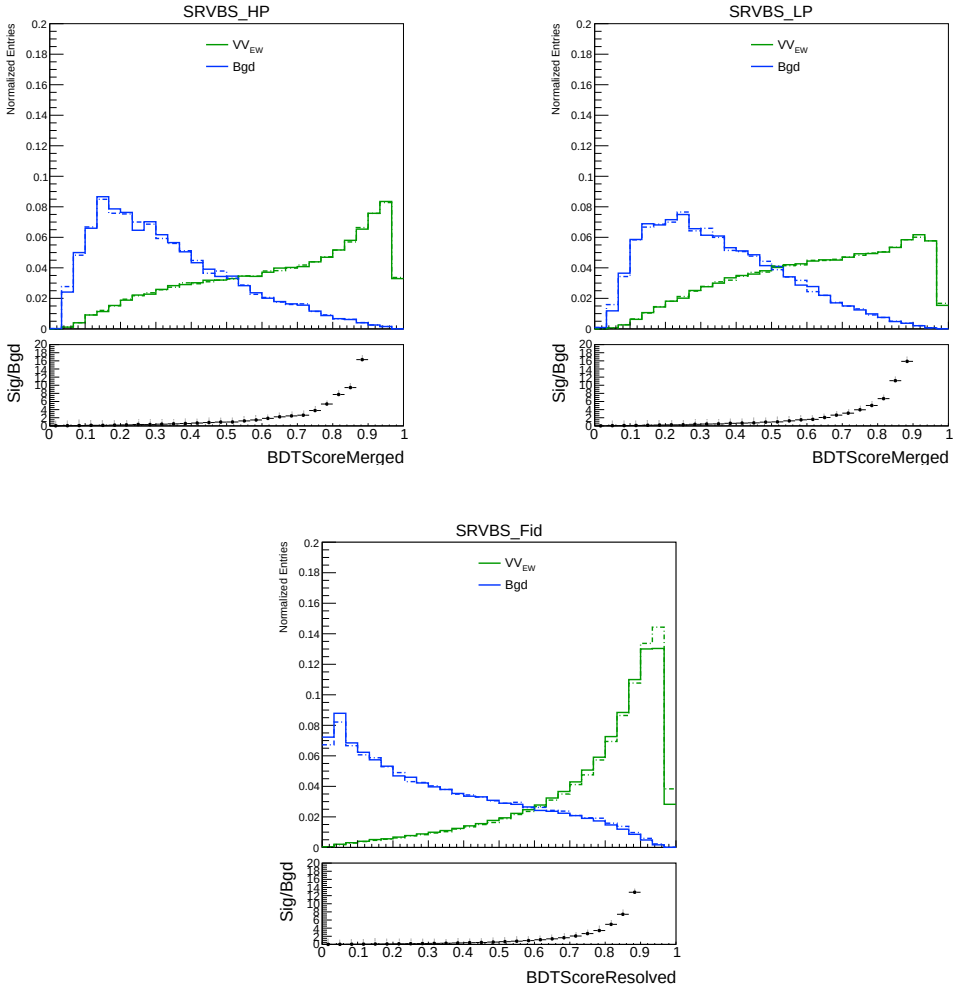

FIGURE 6.31: BDT shape before (dashed line) and after (solid line) feature elimination for the merged HP (a), LP (b) and resolved SR (c).

Feature Elimination based on modeling uncertainties

The modeling uncertainties are found to have large effects on the shape of the BDT scores, especially in the HP SR, as discussed in Section 6.8.2. In order to understand which features are responsible for this difference in modeling, the significance for all variables used by the BDT is estimated using the formula of equation 6.5 for the following cases:

- Assuming no uncertainty on the background for all bins ($\sigma_{b_i} = 0$)
- Considering the modeling differences as the uncertainty per bin ($\sigma_{b_i} = b_{i,MadG} - b_{i,Sherpa}$)
- Assuming 10% uncertainty on the background for all bins $\sigma_{b_i} = 0.10 b_i$)

In Figure 6.32 the significance summary table is shown for features in the merged HP SR. The binning used for the significance calculation of these features corresponds to that of Figures A.5-A.8. In the summary table features are sorted based on the significance drop when considering no background uncertainties and modeling uncertainties for the significance calculation. The largest drop in significance is seen in the Zeppenfeld variable (ZeppMer). This variable uses the extra jets of the event to describe the color flow between the tagging jets. It is known that the number of jets between Sherpa and MadGraph is mis-modeled.

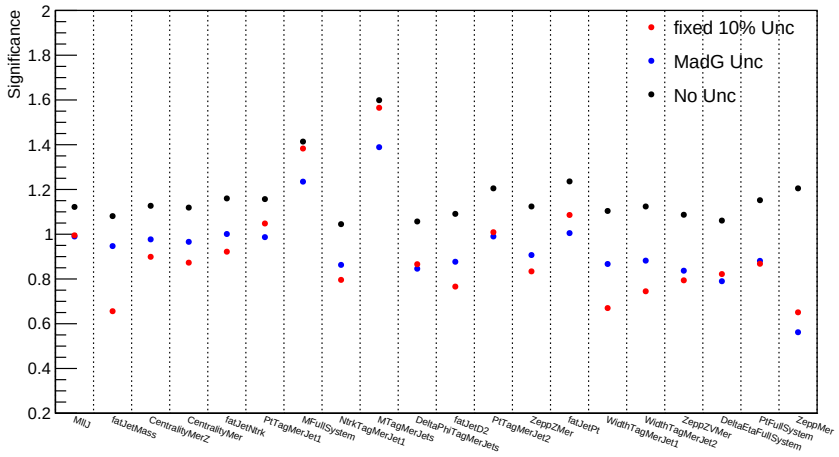

FIGURE 6.32: Significance values for features used by the BDT in the merged HP SR. The significance is estimated using three different background uncertainty hypothesis; no uncertainty (in black), fixed 10% uncertainty for all bins (in red), considering modeling differences as the uncertainty per bin (in blue)

Bad modeled features used during training, can result in high uncertainties on the output discriminant. The price we pay in terms of larger uncertainty has to be compared with the gain we have in terms of discrimination power between signal and background. In order to quantify this trade-off, the following test is performed in the HP SR:

- The BDT is trained with N features and the initial significance Z_N is estimated.
- The BDT is re-trained N times, eliminating each time 1 feature (N-1 features used during each training). The significance Z_{N-1} of the output BDT score for each training is recorded.

- The relative significance drop for each training is estimated as: $Z_{drop} = \frac{Z_N - Z_{N-1}}{Z_N} \times 100$

The significance calculation in each step is done using equation 6.5 and by considering the modeling uncertainties. The Z_{drop} on the final BDT score for each of the eliminated features is plotted in Figure 6.33. The relative drop after eliminating the Zeppenfeld variable is around 13%. Even though this variable has large modeling uncertainties, by removing it from the training the loss we have in terms of discrimination power is higher. A few variables have a negative relative drop, indicating that by removing them from the training the expected significance would improve. However the expected improvements would be less than 5%.

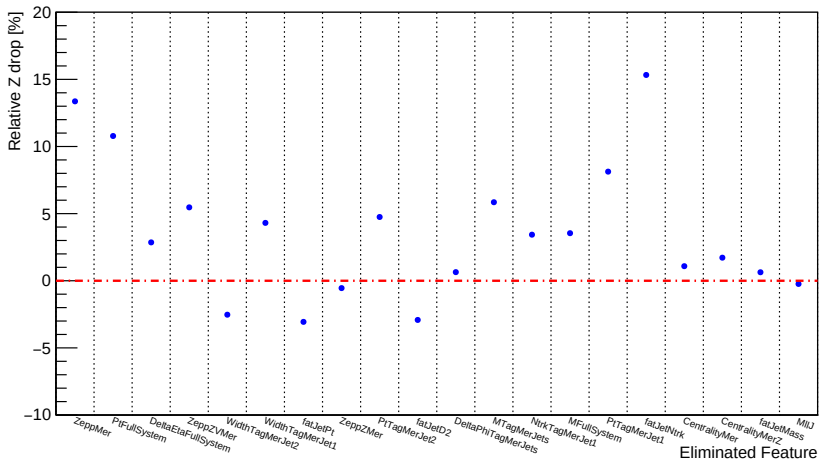

FIGURE 6.33: Relative significance drop on the output BDT score as a function of the eliminated feature. The significance values are estimated by considering the modeling uncertainties in the calculation

Feature Elimination of JSS variables

The models described in the previous sections use as inputs jet substructure (JSS) variables, like the Ntrk and D2 for the large-R jet and width for the small-R jets. However, not dedicated uncertainties are currently available for this type of variables. Therefore the BDT models are re-trained and the performance is re-evaluated after removing them. The BDT shape comparison before and after removing the JSS variables is plotted in Figure **??**.

The expected significances before and after the feature elimination are summarized in Table 6.9. An important significance drop is observed for all three regions. This is expected since substructure variables, are in general powerful quark-gluon discriminants, and are ranked quite high in the feature importance plots of Section 6.7.4.

6.7.6 BDT Final Models and Performance

The final set of features, that are used as inputs for the BDT training, are summarized in Tables 6.11 and 6.12, for the merged and resolved regimes respectively. Features are selected based on studies presented on sections 6.7.5- 6.7.5. In the resolved regime the training in the loose signal region, without the M_{top} cut applied is used, since it was found to have a better performance 6.7.3. In the merged regime, independent trainings in the HP and LP signal regions are performed. For all cases the VBS tagging jets invariant mass,M_{jj}^{tag}, reweighting was applied for Z +jets, as described in Section 6.6. Moreover, the models were trained with no fJVT cut applied for the tagging jet selection as it was introduced in the last stage of the

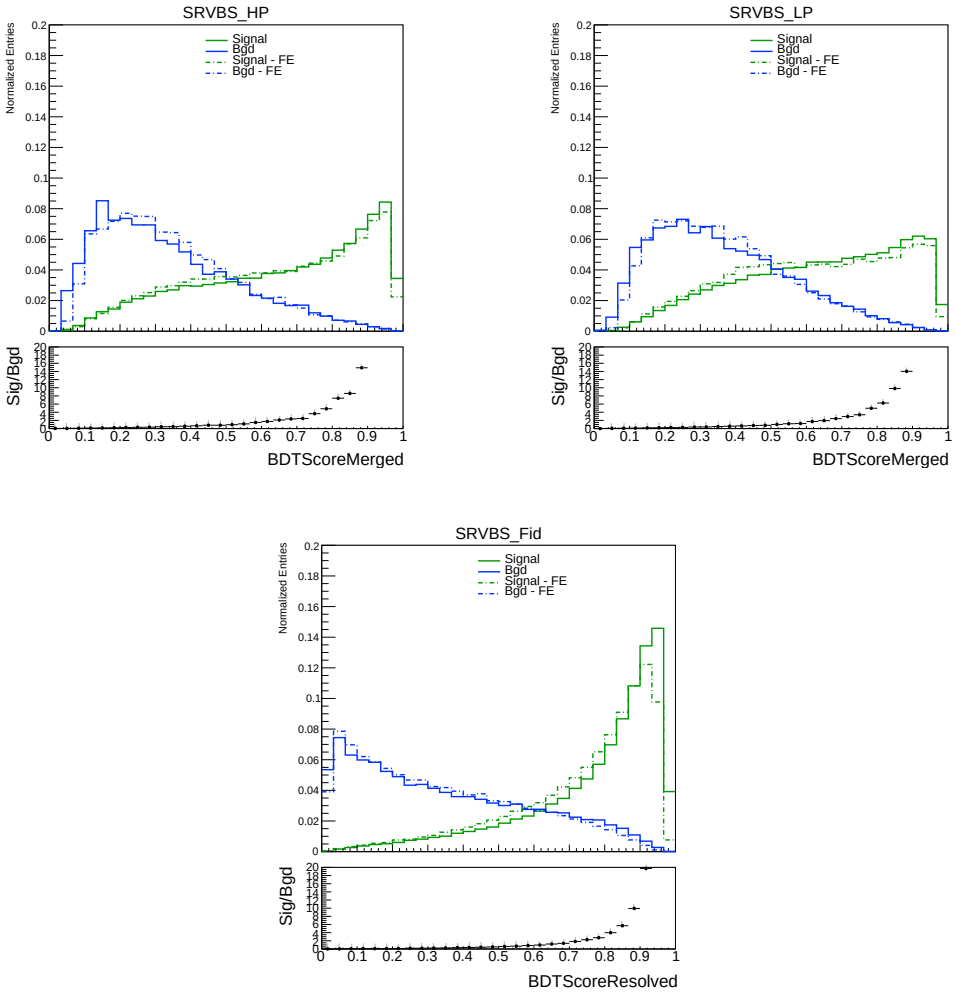

FIGURE 6.34: BDT shape before (solid line) and after (dashed line) JSS feature elimination for the merged HP (a), LP (b) and resolved SR (c).

TABLE 6.9: Expected significances in the Merged and Resolved SRs before and after the JSS feature elimination

	region	Significance
w/ JSS	Merged HP SR	3.50
	Merged LP SR	1.55
	Resolved SR	4.06
w/o JSS	Merged HP SR	3.0
	Merged LP SR	1.39
	Resolved SR	3.69
Relative Drop [%]	Merged HP SR	14%
	Merged LP SR	10%
	Resolved SR	9%

analysis. The performance improvement introduced by fJVT, when included in the training was studied and it was found to be less than 5%.

The k-fold method as described in 6.7.1 is applied in all regions, with the same hyper parameter settings used for all folds. The weighted events are used during training since it was found to give a better performance comparing to training without event weights. Events of each fold receive an extra weight during training in order for the total signal and background yields to be equal. As shown in [89], this best approaches the likelihood ratio of signal versus background hypothesis, which is the most optimal discriminant. In Table 6.10 the total yields as well as the raw statistics used during training are shown. Comparison of the test and training BDT response distributions after combining all folds is shown in Figure **??**. A good agreement between the test and train distributions is noticed, indicating no over-training. The expected significances per region and after combining all regions are summarized in Table 6.13. The significance is estimated using equation 6.5, assuming no background uncertainties and for two different binnings of the BDT score. It is worth noting that the significance values reported are estimated after the M_{jj}^{tag} reweighting is applied. Since the corrections derived account only for the shape differences between the Z+jets MC and data, while normalization differences will be corrected later in the fit, the significance values reported here are expected to be lower than in actual data.

TABLE 6.10: Raw events and yields for the 2-lepton channel in the different SRs considered in the analysis.

process	Merged HP SR		Merged LP SR		Resolved (Tight) SR	
	events	yields	events	yields	events	yields
Z + jets	46041.0	1246.221	147833.0	3547.161	703628.0	37307.512
W + jets	9.0	0.602	28.0	1.664	146.0	16.645
$SMdiboson$	7335	117.175	8733	159.205	43264	669.575
$t\bar{t}, single-top$	876	35.697	2217	84.802	24361.0	920.546
$EWVV + jj$	122656.0	37.660	82303.0	30.906	512112.0	177.276

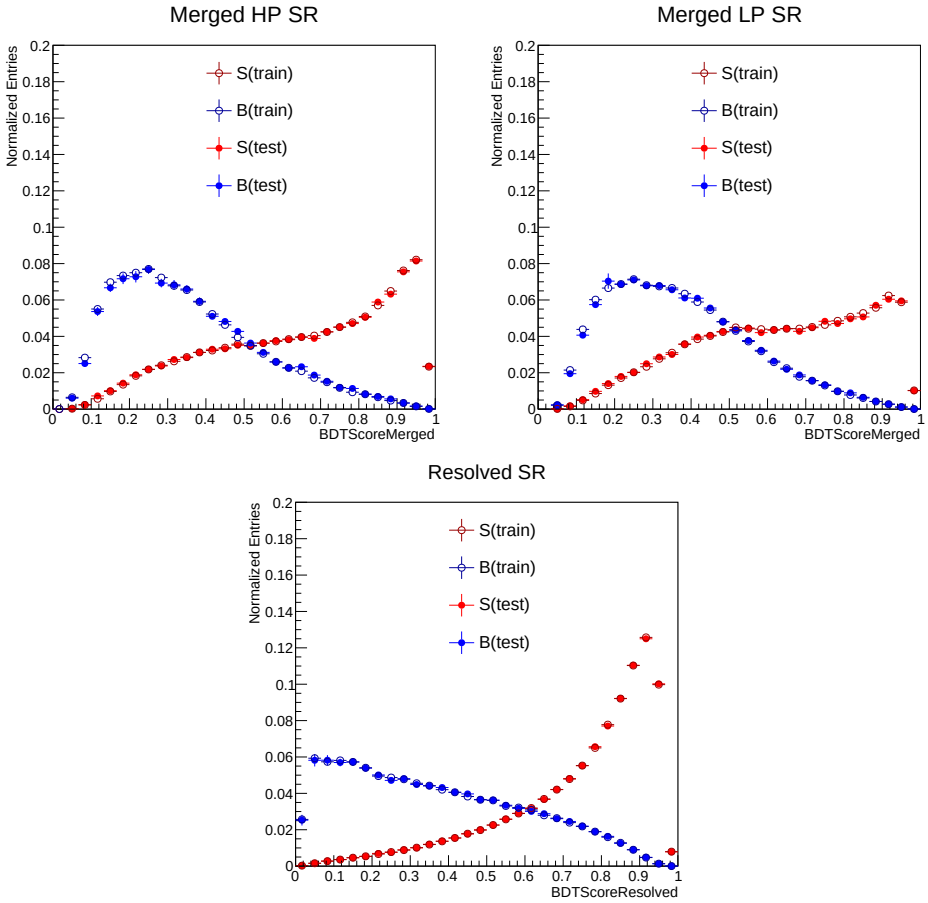

FIGURE 6.35: Comparison of test and training BDT response distributions in 2-lepton channel, for the merged HP (a), LP (b) and resolved (c) regimes.

Inputs - Merged training
DeltaPhiTagMerJets
CentralityMer
ZeppZVMer
NtrkTagMerJet1
NtrkTagMerJet2
DeltaEtaFullSystem
MFullSystem
CentralityMerZ
PtTagMerJet1
fatJetMass
ZeppZMer
MllJ
PtFullSystem
fatJetPt
PtTagMerJet2
ZeppMer
MTagMerJets

TABLE 6.11: Summary of the input variables for the BDT training in the merged regime in 2-lepton channel.

Inputs - Resolved training
CentralityResZV
NtrkSignalJet2
NtrkTagResJet1
DeltaPhiTagResJets
MVHadRes
ZeppRes
MFullSystem
MTagResJets
PtSignalJet1
NtrkSignalJet1
PtFullSystem
ZeppZRes
PtSignalJet2
CentralityResZ
PtTagResJet1
PtTagResJet2
NtrkTagResJet2
ZeppVRes

TABLE 6.12: Summary of the input variables for the BDT training in the resolved regime in 2-lepton channel.

TABLE 6.13: Expected significances in the three SRs of the 2-lepton channel for two different binnings of the BDT score.

region	30 bins	10 bins
Resolved Tight SR	3.691	3.178
Merged HP SR	2.993	2.755
Merged LP SR	1.390	1.258
Combined regions	4.952	4.390

6.8 Systematic uncertainties

The largest source of uncertainty in the analysis, is the statistical uncertainty, mainly due to the very low cross section of the target EW VBS signal but also due to the restrictive event selection applied in order to enhance separation with the background. The next major sources can be classified in two categories; the experimental systematic uncertainties, mostly accounting for uncertainties on the reconstruction and calibration of all physics objects, and the theory uncertainties accounting for theoretical assumptions within the simulated signal and background processes. The two categories are discussed in more detail in the next subsections.

6.8.1 Experimental uncertainties

Uncertainties considered in this category are:

- **Luminosity:** The uncertainty on the integrated luminosity for the 2015+2016 dataset is 2.1%, and 2.4% for the 2017 dataset. The uncertainty for the 2018 data alone is 2.0%, and the uncertainty for the combined run-2 dataset (2015-2018) is 1.7% [90].
- **Pile-up Reweighting:** To account for the mis-modelling of the pileup overlay applied to MC samples, the MC events are weighted so that the MC average number of interactions per bunch crossing (μ) distribution matches that of the data. Before calculating the pileup weights, the data are scaled by a factor of $1/1.03$. The scaling is performed in order to correct for the difference in the distribution of vertex multiplicity used to produce the MC samples to that distribution measured for the actual data for a given μ. The pile-up reweighting uncertainty is then estimated by changing the scaling to $1/1.0$ or to $1/1.18$ to get the up and down variations respectively.
- **Leptons:** The lepton related uncertainties arise from the reconstruction and identification of both electrons and muons, in addition to the calibration of the energy scale and resolution. A summary of these uncertainties is presented in Table 6.14.
- **Small-R Jet:** This category includes uncertainties on the jet energy energy scale (JES) and jet energy resolution (JER) calibration. The JES and JER are measured in situ by calculating the response between MC and data in various bins of kinematic phase space. Several primary sources of JES uncertainties are considered and are detailed in 4.4.1. The main sources of JER uncertainties arise from data to MC comparisons performed to account for differences in JER between MC and data, the noise term evaluation in zero bias data, as well as in situ dijet p_{T} balance asymmetry corrections [65]. The JES and JER uncertainties are broken into 30 and 13 components, respectively, and are summarized in Table 6.15. Uncertainties on the efficiencies of the pile-up jet and flavour-tagging tools used in the analysis are also considered.
- **Large-R Jet:** Similarly to the small-R jet, uncertainties on the JES and JER calibration of large-R jets are considered. They are summarized in Table 6.16
- **W/Z-tagger uncertainties:** In order to correct the boson tagger efficiency in MC to match that in data, scale factors are introduced [84]. Scale factors (SFs) are derived for signal-like jets [5] from data using tt-bar events, while for background jets are extracted from γ+jet and multijet events. A number of sources of systematic uncertainties are considered in the scale factor derivation; these include both theoritical assumptions in the MC samples used for the SF determination, as well as, reconstruction and calibration uncertainties of the physics objects . All sources of uncertainty are propagated to the scale

[5] a reconstructed jet is labelled as signal-like if the associated truth jet is consistent with a W/Z boson decay

factors. The total uncertainty of the scale factor is obtained by adding in quadrature the individual scale factor variance for all uncertainty sources. In Figure 6.36 a breakdown of the boson tagger related uncertainties is plotted as a function of the mass of the tagging jets for Z+jets background in the 2-lepton channel. The systematic source with the largest impact is the γ+jet modeling uncertainty, affecting mostly the HP signal region. As shown in Ref. [84] this uncertainty is found to have large effects especially for the 50% working point W/Z tagger. In the merged CR the major systematic source is related to the efficiency uncertainty of the 80% tagger working point while in the LP SR major systematics sources (still less than 5%) are related to the γ+jets modeling and the efficiency uncertainty of the 50% tagger working point. The fact that the efficiency uncertainty of the 50% tagger working point is relevant in the LP SR is not surprising given the SF calculation in this region (Appendix C).

TABLE 6.14: Qualitative summary of the lepton-related systematic uncertainties included in the analysis.

Source	Description	Analysis Name	Notes
Electrons	Energy scale	EG_SCALE_ALL	
Electrons	Energy resolution	EG_RESOLUTION_ALL	
Electrons	Trigger	EL_EFF_Trigger_TOTAL_1NPCOR_PLUS_UNCOR	
Electrons	ID efficiency SF	EL_EFF_ID_TOTAL_1NPCOR_PLUS_UNCOR	
Electrons	Isolation efficiency SF	EL_EFF_Iso_TOTAL_1NPCOR_PLUS_UNCOR	
Electrons	Reconstruction efficiency SF	EL_EFF_Reco_TOTAL_1NPCOR_PLUS_UNCOR	
Muons	p_{T} scale	MUONS_SCALE	
Muons	p_{T} scale (charge dependent)	MUON_SAGITTA_RHO	
Muons	p_{T} scale (charge dependent)	MUON_SAGITTA_RESBIAS	
Muons	p_{T} resolution MS	MUONS_MS	
Muons	p_{T} resolution ID	MUONS_ID	
Muons	Isolation efficiency SF	MUON_ISO_SYS	
Muons	Isolation efficiency SF	MUON_ISO_STAT	
Muons	Muon reco & ID efficiency SF	MUONS_EFF_STAT	
Muons	Muon reco & ID efficiency SF	MUONS_EFF_STAT_LOWPT	
Muons	Muon reco & ID efficiency SF	MUONS_EFF_SYST	
Muons	Muon reco & ID efficiency SF	MUONS_EFF_SYST_LOWPT	
Muons	Track-to-vertex association efficiency SF	MUON_TTVA_SYS	
Muons	Track-to-vertex association efficiency SF	MUON_TTVA_STAT	
MET	Soft term	MET_SoftTrk_ResoPerp	
MET	Soft term	MET_SoftTrk_ResoPara	
MET	Soft term	MET_SoftTrk_Scale	

TABLE 6.15: Qualitative summary of the small-R jet systematic uncertainties included in this analysis.

Source	Description	Analysis Name	Notes
Small-R Jets	JES category reduction	JET_BJES_Response	
Small-R Jets	JES category reduction	JET_EffectiveNP_Detector1	
Small-R Jets	JES category reduction	JET_EffectiveNP_Detector2	
Small-R Jets	JES category reduction	JET_EffectiveNP_Mixed1	
Small-R Jets	JES category reduction	JET_EffectiveNP_Mixed2	
Small-R Jets	JES category reduction	JET_EffectiveNP_Mixed3	
Small-R Jets	JES category reduction	JET_EffectiveNP_Modelling1	
Small-R Jets	JES category reduction	JET_EffectiveNP_Modelling2	
Small-R Jets	JES category reduction	JET_EffectiveNP_Modelling3	
Small-R Jets	JES category reduction	JET_EffectiveNP_Modelling4	
Small-R Jets	JES category reduction	JET_EffectiveNP_Statistical1	
Small-R Jets	JES category reduction	JET_EffectiveNP_Statistical2	
Small-R Jets	JES category reduction	JET_EffectiveNP_Statistical3	
Small-R Jets	JES category reduction	JET_EffectiveNP_Statistical4	
Small-R Jets	JES category reduction	JET_EffectiveNP_Statistical5	
Small-R Jets	JES category reduction	JET_EffectiveNP_Statistical6	
Small-R Jets	JES category reduction	JET_Flavor_Composition	
Small-R Jets	JES category reduction	JET_Flavor_Response	
Small-R Jets	JES category reduction	JET_Pileup_OffsetMu	
Small-R Jets	JES category reduction	JET_Pileup_OffsetNPV	
Small-R Jets	JES category reduction	JET_Pileup_PtTerm	
Small-R Jets	JES category reduction	JET_Pileup_RhoTopology	
Small-R Jets	JES category reduction	JET_PunchThrough_MC16	
Small-R Jets	JES category reduction	JET_SingleParticle_HighPt	
Small-R Jets	JES category reduction	JET_EtaIntercalibration_TotalStat	
Small-R Jets	JES category reduction	JET_EtaIntercalibration_Modelling	
Small-R Jets	JES category reduction	JET_EtaIntercalibration_NonClosure_highE	
Small-R Jets	JES category reduction	JET_EtaIntercalibration_NonClosure_negEta	
Small-R Jets	JES category reduction	JET_EtaIntercalibration_NonClosure_posEta	
Small-R Jets	JER	JET_JERMC_DataVsMC_MC16	
Small-R Jets	JER	JET_JERMC_EffectiveNP_1	
Small-R Jets	JER	JET_JERMC_EffectiveNP_2	
Small-R Jets	JER	JET_JERMC_EffectiveNP_3	
Small-R Jets	JER	JET_JERMC_EffectiveNP_4	
Small-R Jets	JER	JET_JERMC_EffectiveNP_5	
Small-R Jets	JER	JET_JERMC_EffectiveNP_6	
Small-R Jets	JER	JET_JERMC_EffectiveNP_7	
Small-R Jets	JER	JET_JERMC_EffectiveNP_8	
Small-R Jets	JER	JET_JERMC_EffectiveNP_9	
Small-R Jets	JER	JET_JERMC_EffectiveNP_10	
Small-R Jets	JER	JET_JERMC_EffectiveNP_11	
Small-R Jets	JER	JET_JERMC_EffectiveNP_12restTerm	

TABLE 6.16: Qualitative summary of the large-R jet systematic uncertainties included in this analysis.

Source	Description	Analysis Name	Notes
Large-R Jets	JES category reduction	FATJET_CR_JET_CombMass_Baseline	
Large-R Jets	JES category reduction	FATJET_CR_JET_CombMass_Modelling	
Large-R Jets	JES category reduction	FATJET_CR_JET_CombMass_TotalStat	
Large-R Jets	JES category reduction	FATJET_CR_JET_CombMass_Tracking1	
Large-R Jets	JES category reduction	FATJET_CR_JET_CombMass_Tracking2	
Large-R Jets	JES category reduction	FATJET_CR_JET_CombMass_Tracking3	
Large-R Jets	JES category reduction	FATJET_CR_JET_EffectiveNP_R10_Detector1	
Large-R Jets	JES category reduction	FATJET_CR_JET_EffectiveNP_R10_Detector2	
Large-R Jets	JES category reduction	FATJET_CR_JET_EffectiveNP_R10_Mixed1	
Large-R Jets	JES category reduction	FATJET_CR_JET_EffectiveNP_R10_Mixed2	
Large-R Jets	JES category reduction	FATJET_CR_JET_EffectiveNP_R10_Mixed3	
Large-R Jets	JES category reduction	FATJET_CR_JET_EffectiveNP_R10_Mixed4	
Large-R Jets	JES category reduction	FATJET_CR_JET_EffectiveNP_R10_Modelling1	
Large-R Jets	JES category reduction	FATJET_CR_JET_EffectiveNP_R10_Modelling2	
Large-R Jets	JES category reduction	FATJET_CR_JET_EffectiveNP_R10_Modelling3	
Large-R Jets	JES category reduction	FATJET_CR_JET_EffectiveNP_R10_Modelling4	
Large-R Jets	JES category reduction	FATJET_CR_JET_EffectiveNP_R10_Statistical1	
Large-R Jets	JES category reduction	FATJET_CR_JET_EffectiveNP_R10_Statistical2	
Large-R Jets	JES category reduction	FATJET_CR_JET_EffectiveNP_R10_Statistical3	
Large-R Jets	JES category reduction	FATJET_CR_JET_EffectiveNP_R10_Statistical4	
Large-R Jets	JES category reduction	FATJET_CR_JET_EffectiveNP_R10_Statistical5	
Large-R Jets	JES category reduction	FATJET_CR_JET_EffectiveNP_R10_Statistical6	
Large-R Jets	JES category reduction	FATJET_CR_JET_EtaIntercalibration_Modelling	
Large-R Jets	JES category reduction	FATJET_CR_JET_EtaIntercalibration_NonClosure_2018data	
Large-R Jets	JES category reduction	FATJET_CR_JET_EtaIntercalibration_R10_TotalStat	
Large-R Jets	JES category reduction	FATJET_CR_JET_Flavor_Composition	
Large-R Jets	JES category reduction	FATJET_CR_JET_Flavor_Response	
Large-R Jets	JES category reduction	FATJET_CR_JET_LargeR_TopologyUncertainty_V	
Large-R Jets	JES category reduction	FATJET_CR_JET_LargeR_TopologyUncertainty_top	
Large-R Jets	JES category reduction	FATJET_CR_JET_SingleParticle_HighPt	
Large-R Jets	Mass resolution	FATJET_JMR	
Large-R Jets	JER	FATJET_JER	

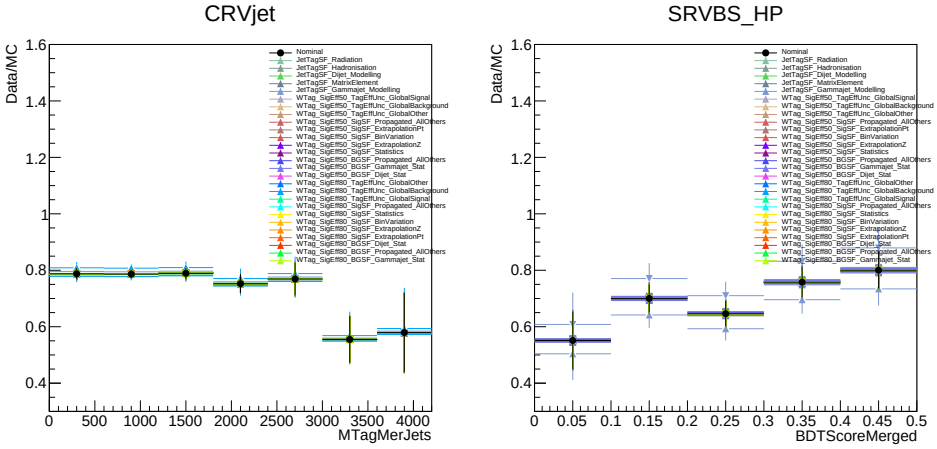

(a) Merged CR (b) Merged HP SR

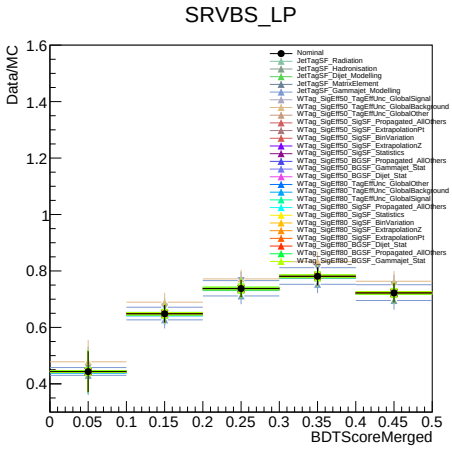

(c) Merged LP SR

FIGURE 6.36: Data/MC ratio as a function of the BDT score distribution in the SRs and the M_{jj}^{tag} in the CR. All Boson Tagger SF related uncertainties are plotted.

6.8.2 Theory uncertainties

Three types of theory uncertainties are considered:

- **Modeling uncertainties:** Uncertainties on the modeling of background processes are estimated by comparing the nominal samples to alternative ones. The shape difference between the nominal Sherpa and alternative MadGraph+Pythia predictions is used to estimate the model uncertainty for the Z + jets template. In order to reassure that uncertainties arising from the generator comparison do not double-count differences in the mass of the tagging jets shape (already accounted in the M_{jj}^{tag} re-weighting uncertainties discussed below) the MadGraph+Pythia samples are re-weighted using a similar procedure to what is described in 6.6. The difference between the two predictions is symmetrized and used to define an uncertainty band around the Z + jets background in the fit. Modeling uncertainties on the QCD $V_{lep}V_{had}jj$ MC simulation are also considered by performing a similar comparison of our nominal Sherpa to alternative MadGraph+Pythia samples. Finally, a comparison of our nominal tt-bar simulation generated with Powheg+ PYTHIA 8 to the alternative Powheg+Herwig one is made, to estimate a modeling uncertainty for the tt-bar template.

  As described in section 6.6, a re-weighting is applied to the Z + jets MC prediction as a function of M_{jj}^{tag} . A re-weighting systematic uncertainty for Z + jets events is considered, by taking the difference of their respective distributions before and after applying the re-weighting. In Figure 6.52 the impact of the re-weighting uncertainty on the final discriminant and M_{jj}^{tag} distributions is plotted

- **PDF uncertainties:** Parton Distribution Functions (PDFs) are essential input to the MC event generation. Since they can't obtained directly from perturbative QCD, PDFs are usually obtained from fits to experimental data (Section 2.3). Therefore, the major PDF uncertainties are experimental ones; arising from the fitting procedure, the parameterization of the PDF set and the input data. Two types of uncertainties are considered in order to account for these: internal uncertainties related to the PDF choice and those arising from differences between our nominal and other PDF sets [6]. Both of uncertainties are computed using the built-in weights of our MC samples.

  For the internal uncertainties the 100 MC replicas of the NNPDF [91] set are used. These replicas are usually obtained by allowing the individual data points to fluctuate randomly by amounts determined by the size of the data uncertainties. The standard deviation of the mean value of the 100 MC replicas per distribution bin is considered as the pdf uncertainty $\delta^{PDF}\sigma$ for that bin. An uncertainty on the strong coupling constant value α_s, is also considered, since α_s affects the cross-section estimation. Although the running of the strong coupling constant α_s is predicted theoretically, its actual value is determined experimentally and is usually quoted at the mass the Z boson. The extrapolation of α_s to the process energy scale is usually done through the so-called renormalization group equation (RGE), which is estimated at a given order in perturbation theory. Therefore, there are two main sources of uncertainty: experimental errors in estimation of α_s, as well as, missing higher orders in RGE. The α_s uncertainty is usually estimated by using the same PDF set evaluated with two different α_s values. The uncertainty in α_s is then given by:

$$\delta^{\alpha_s}\sigma = \frac{\sigma(\alpha_s^{down}) - \sigma(\alpha_s^{up})}{2}$$

[6] referred to as external uncertainties

The combined NNPDF and α_s uncertainty is then evaluated per histogram bin as follows:

$$\delta^{\alpha_s+PDF}\sigma = \sqrt{(\delta^{PDF}\sigma)^2 + (\delta^{\alpha_s}\sigma)^2}$$

Internal PDF uncertainties are estimated both for the EW signal and Z + jets background processes.

For the external PDF uncertainties a comparison of our nominal distributions with alternative PDF sets is made. The uncertainty is evaluated by taking an envelope of all of the alternative pdf sets per histogram bin. If no down variation results from the envelope, the up variation is symmetrized, to form an uncertainty band around the nominal. External PDF uncertainties are currently considered only for the Z + jets simulation [7]. However, the effects of such uncertainties are expected to be rather small.

- **QCD scale uncertainties:** Uncertainties due to missing higher order corrections, are estimated by varying the renormalisation (μ_r) and factorisation (μ_f) scales (Section 2.3). The following pairwise variations are considered:

$$\{\mu_r, \mu_r\} \times \{0.5, 0.5\}, \{1, 0.5\}, \{0.5, 1\}, \{1, 1\}, \{2, 1\}, \{1, 2\}, \{2, 2\}$$

. The uncertainties are combined by taking an envelope of all the uncertainties per histogram bin. QCD scale uncertainties are estimated for both the EW signal and Z + jets background process.

The impact of the PDF and QCD scale uncertainties on the distributions considered in the fit is shown in Figure 6.37 and 6.38 for the EW signal and Z + jets predictions, respectively. Shape-only effects are plotted for the Z + jets template, since normalization effects are estimated from data. The QCD scale uncertainty is found to have an up to 15% effect on the Z + jets process, mostly affecting the resolved signal and control regions, while be negligible in the merged regime. The impact on the EW signal, is found to be up to 10%, mostly affecting the right-most bins of all distributions, in both the merged and resolved regions. The PDF uncertainties are in general found to have a much smaller impact, on both the EW signal and Z + jets process, for all regions.

The shape effect of the modeling uncertainties on the Z + jets process, is plotted in Figure 6.39, for the different analysis regions. The modeling uncertainty is found to have very large impact on the BDT distribution of the merged HP SR, as well as, on the M_{jj}^{tag} distributions of both the merged and resolved regions. As discussed in Section 6.7.5, the large discrepancy seen in the BDT score, is mainly due to the Zeppenfeld variable used during the BDT training. As it will be shown later in Section 6.10.4, such large uncertainties get constrained in the fit.

[7] due to missing built-in weights in our signal and rest of MC samples

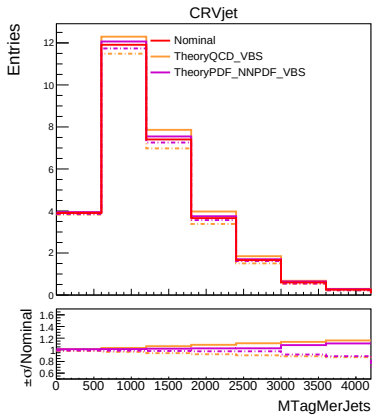

(a) Merged CR

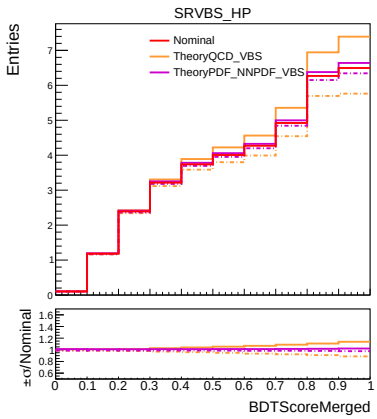

(b) Merged HP SR

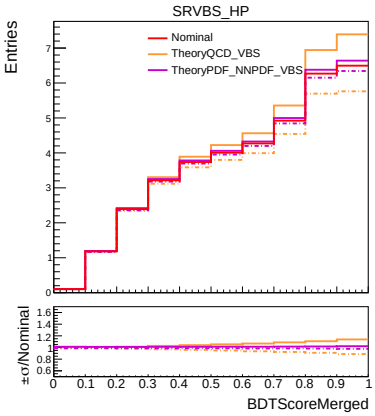

(c) Merged LP SR

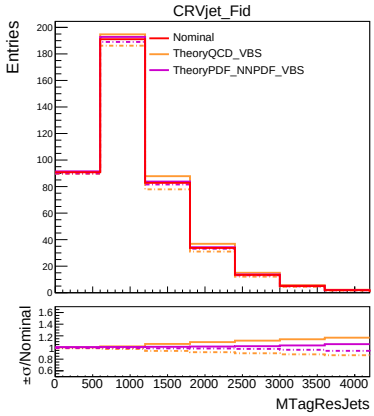

(d) Resolved CR

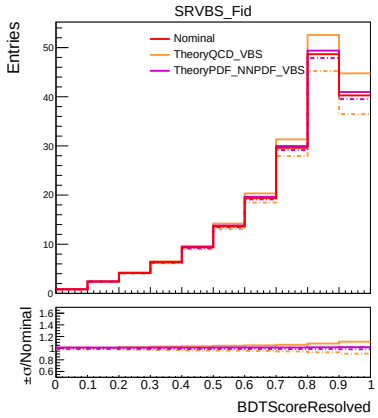

(e) Resolved SR

FIGURE 6.37: Impact of theory uncertainties on the EW signal template for the distributions considered in the fit.

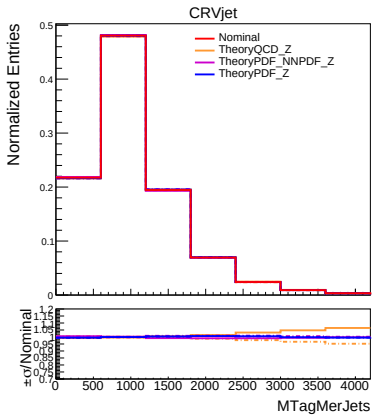

(a) Merged CR

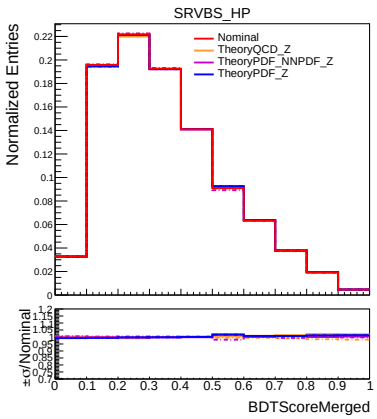

(b) Merged HP SR

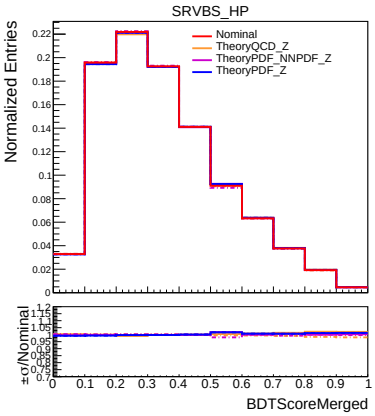

(c) Merged LP SR

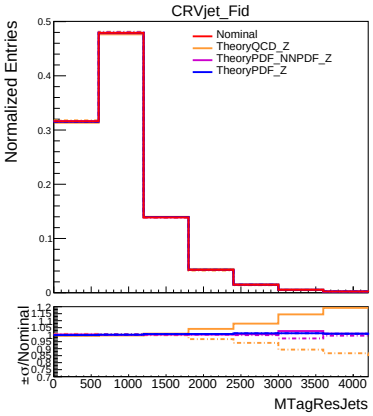

(d) Resolved CR

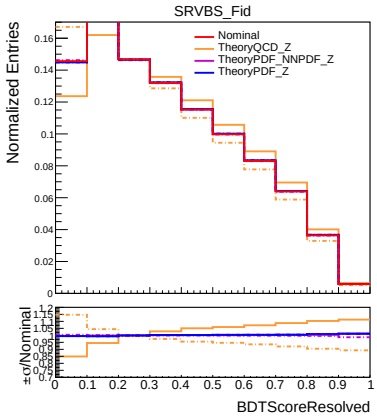

(e) Resolved SR

FIGURE 6.38: Impact of theory uncertainties on the Z + jets template for the distributions considered in the fit.

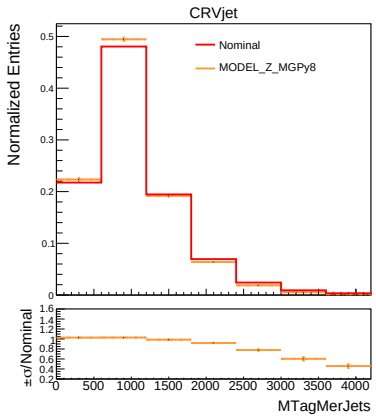

(a) Merged CR

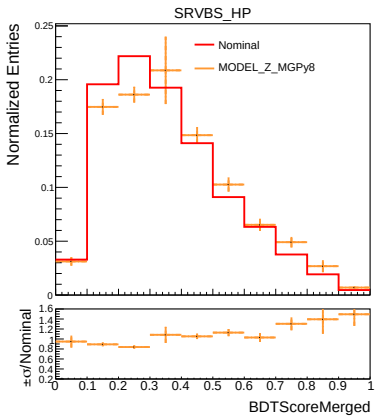

(b) Merged HP SR

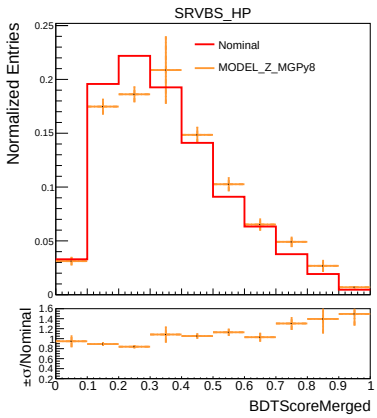

(c) Merged LP SR

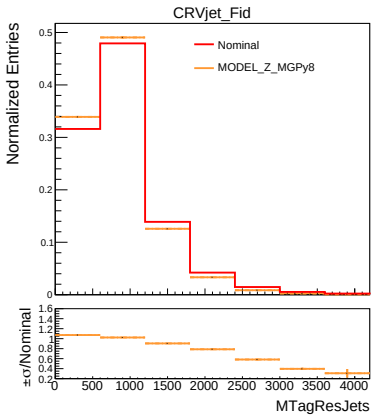

(d) Resolved CR

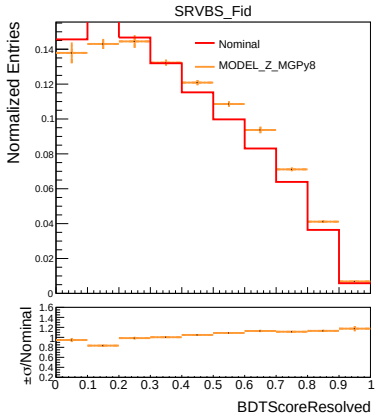

(e) Resolved SR

FIGURE 6.39: Impact of modeling uncertainties on the Z + jets template for the distributions considered in the fit.

6.9 Statistical Interpretation

6.9.1 Likelihood function definition

A binned maximum likelihood fit is performed in order to extract the signal strength μ. The binned likelihood fit function is written as:

$$\mathscr{L}\left(N, \tilde{\theta}|\mu, \theta\right) = P\left(\mu|\mu s + b\right) \cdot p\left(\tilde{\theta}|\theta\right) \tag{6.6}$$

where P is the product of Poisson probability terms over all the histogram bins:

$$P\left(\mu|\mu s + b\right) = \prod_{i=1}^{N_{bins}} \frac{(\mu s_i(\theta) + b_i(\theta))^{N_i}}{N_i!} e^{-(\mu s_i(\theta) + b_i(\theta))} \tag{6.7}$$

with μs_i, b_i being the expected number of signal and background events in bin i, respectively, and N_i is the number of observed events in that bin. The θ represents all the theory and experimental uncertainties considered in the analysis. The second term of equation G.1, $p(\tilde{\theta}|\theta)$, usually referred to as a prior, is added to represent our knowledge about the systematic effects. Assuming not correlated uncertainties this term is given by the product of all single uncertainty priors; $p\left(\tilde{\theta}|\theta\right) = \prod_j p_j\left(\tilde{\theta_j}|\theta_j\right)$ where j is running over all uncertainties and θ_j is the nuisance parameter associated to the source of systematic uncertainty j. Each of the terms represents the probability of the uncertainty to have a true value equal to θ_j given the best estimate $\tilde{\theta_j}$ obtained from an auxiliary measurement. In our analysis priors are considered to be gaussian distributed and θ_j is scaled so that $\theta_j = 0$ corresponds to the nominal expectation while $\theta_j = \pm 1$ correspond to the $\pm 1\sigma$ variations of the systematic source. This parametrization is convenient in order to easily spot constrained nuisance parameters that might be problematic (discussed more in 6.10.4). Parameters treated as floating normalizations in the fit are not assigned priors. Such normalizations factors are added for example in the case of the Z + jets background in order to derive a data-driven estimate for its contribution.

The fit result is obtained by maximizing the likelihood function of equation G.1 with respect to all the parameters. A likelihood function in the form of Equation G.1 is very often referred to as a profile likelihood. In order to test the compatibility of the fit result with respect to a hypothesized value of μ, the profile likelihood ratio is defined:

$$\lambda(\mu) = \frac{L(\mu, \hat{\hat{\theta}})}{L(\hat{\mu}, \hat{\theta})} \tag{6.8}$$

where $\hat{\hat{\theta}}$ is the best fit values that maximizes L for a certain value of μ, while $\hat{\mu}$ and $\hat{\theta}$ are the maximum likelihood estimators of equation G.1. A test statistic is then constructed:

$$t_\mu = -2ln\lambda(\mu). \tag{6.9}$$

where higher values of t_μ correspond to increasing incompatibility between the data and the hypothesis under test. The significance Z of the measurement is estimated by looking at the value of the function for the background only hypothesis, corresponding to $\mu = 0$. Its value is computed as:

$$Z = \sqrt{2t_{\mu=0}} \tag{6.10}$$

6.9.2 Monte Carlo statistical uncertainty implementation

Due to the limited statistics of our Monte Carlo simulations the histograms used to describe our background and signal contributions are not always the best description of the real distribution. Instead they are an estimate of the actual distribution with some statistical uncertainty. In order to account for the MC statistical uncertainties, extra nuisance parameters per bin (referred to as gammas) are added in the likelihood of Equation G.1. Each of the gammas is associated to the total Monte Carlo estimate and the total statistical uncertainty of a specific histogram bin i. When treating the MC estimate as an auxiliary measurement, a poisson distribution is expected. Therefore, poisson priors are assigned to gamma parameters. Conventionally, gammas are parametrized such as their nominal expectation corresponds to 1 and their up/down variations correspond to $1 \pm \sigma$, where sigma is the relative MC statistical uncertainty of the bin i.

6.9.3 Pulls and constraints of NPs

An important advantage of using a profile likelihood fit is that additional information on the systematic uncertainty sources considered, can be revealed from the fit to data. Therefore, NPs in the fit model, can be "pulled" from their initial central values as well as get constrained. The term "constrained" refers to a reduction of their intial uncertainty value. Constraints of certain NPs can appear especially for systematic sources that the analysis is sensitive on. Such examples are the JER JET_Flavor_Composition and JET_Flavor_Response uncertainties which account for the difference in response between quark and gluon initiated jets. These uncertainties are usually estimated following a conservative approach; a 50% gluon fraction with a 100% uncertainty and they are jet p_{T} and η dependent. Since our analysis phase space is sensitive in such uncertainties, they are expected to get constrained in the fit. However, many times fake constraints or over-constraints might also appear, due to a bad modeling of the systematic uncertainty or missing degrees of freedom in the fit model. Since a constrained NP would indicate that the propagated uncertainty of the corresponding systematic source to the parameter of interest μ is also reduced, constrained NPs are studied carefully in order to re-assure that the constraints are genuine.

6.9.4 Smoothing of uncertainties

Systematic uncertainties can be subject to statistical fluctuations due to the limited number of MC events. In order to remove such fluctuations that might create spurious effects in the fit a smoothing procedure is applied. First systematics templates are built as the ratios of varied to nominal MC templates. A kernel smoother is then employed in order to perform the smoothing. The kernel smoothing proceeds by generating for each histogram bin a new value that is some function of the original value at that point and the surrounding bins. The chosen function in our case is a gaussian curve. An example of the smoothing result is plotted in Figure 6.40 for the QCD diboson modelling uncertainty in the 2-lepton channel.

6.9.5 Pruning of uncertainties

Uncertainties with a negligible impact on the final result are neglected. The pruning procedure is applied as follows:

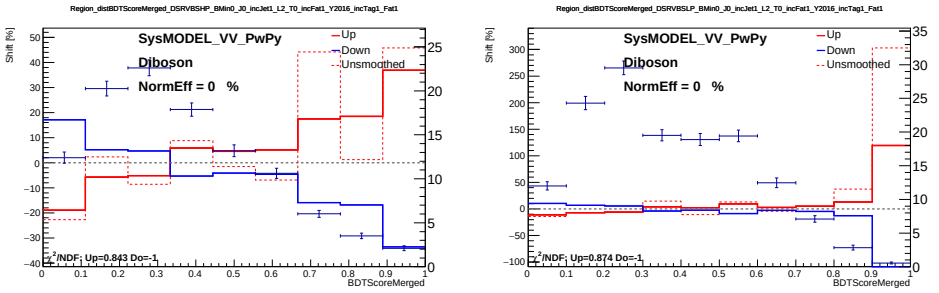

(a) Merged HP SR

(b) Merged LP SR

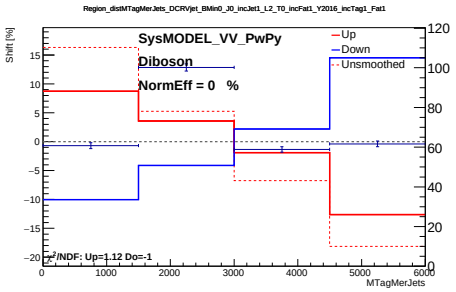

(c) Merged CR

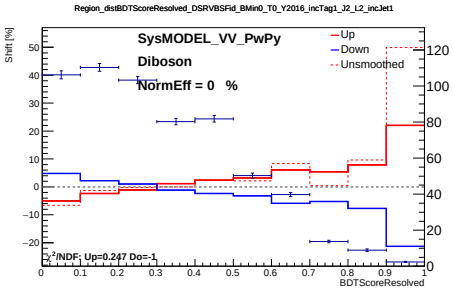

(d) Resolved SR

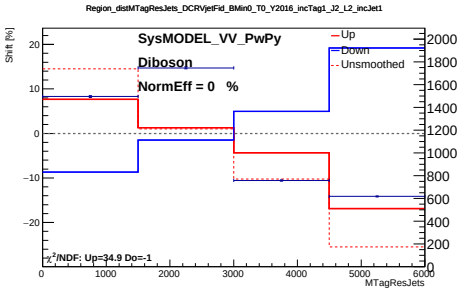

(e) Resolved CR

FIGURE 6.40: Example of smoothing of the jet flavor composition variation in the 2-lepton channel

- Normalization uncertainties with a less than 1% effect or same sign effects (relative variation being positive/negative for both the up and down uncertainty) are pruned away.
- Shape uncertainties with less than 1% effect for all bins of the distribution (after the overall normalization is removed) or missing one of the up and down variations are pruned away.

In order to re-assure that the value of the pruning threshold doesn't change the final result, fits with no pruning threshold on Asimov datasets are performed and the significances before and after pruning are compared. The effect on the final significance when considering a pruning threshold of 1% is found to be negligible.

6.9.6 Fit strategy

Fits on the Asimov dataset are used to validate the systematic model independently from the data. The Asimov dataset is an artificial dataset obtained from replacing the real data with Monte Carlo simulations. By definition, when it is used to evaluate the parameter estimators, the input values are obtained. Therefore, no pulls are expected from fits to the Asimov dataset. However, constraints of NPs are still expected since the Asimov dataset carries the luminosity of data.

A simultaneous fit to the merged and resolved signal and control regions is performed. In the signal regions the BDT score is fitted, while in the CRs the M_{jj}^{tag} distribution is used instead, in order to better constrain the M_{jj}^{tag} re-weighting uncertainty. In all cases, individual fits to the merged and resolved regimes are also performed for testing purposes. Fits are classified as "unconditional" or "conditional" based on if the signal strength μ is fitted or fixed to a predefined value. In the case of unconditional fits, μ is fitted.

As mentioned in 6.9.1, all the systematic uncertainties enter the profile likelihood fit as nuisance parameters (NPs) which are either treated as floating parameters or parameters with priors. For the most significant backgrounds, those which the analysis is designed to constrain, floating normalization parameters are assigned to their contribution. Such a contribution is, in the 2-lepton channel, the Z+jets background. Small background contributions, that have little impact on the signal strength measurement, are treated as NPs with a prior. Such background are the tt-bar production, which is assigned a 30% prior. The QCD diboson production is also treated with a prior. The prior values are estimated by comparing the nominal MC yields to yields obtained from an alternative sample. Different prior values are used for the merged and resolved regimes. A 50% prior is assigned to the diboson contribution in the merged region, while in the resolved regime a 30% prior is used. It is worth noting here that, the QCD diboson production is found to be highly anti-correlated with the EW signal production. Normally, the QCD diboson contribution should be constrained in a data-driven way. However, due to the lack of a dedicated control region, it is currently treated with a prior. Theory uncertainties, associated to background samples whose contributions are left floating in the fit, are treated as shape only uncertainties. Theory uncertainties affecting the EW signal predictions are allowed to have both a normalization and shape effect for the signal strength measurement.

6.10 Results

This section describes the results of the analysis, in the resolved, merged and combined regions. For each case, the following fits are performed:

- **Step 1**: Unconditional fits to Asimov data in the full range of the BDT score. This gives a first validation of the model and an idea of the expected constraints. Moreover, the expected significance of the measurement is estimated.
- **Step 2**: Unconditional fits to observed data in the left bins of the BDT score (background-only fit). The sensitive bins of the BDT score, those being the right-most bins containing 70% of the total signal integral, are blinded, in order to verify that our background description is meaningful in data in the absence of signal. Similar fits to Asimov data are also performed for validation.
- **Step 3**: After the model is validated; the NPs constraints and pulls are well understood, constraints and correlations in data are not significantly different from those to the Asimov fits, the right bins of the BDT score are included in the fit. Unconditional fits to observed data in the full range of the BDT score are performed. The signal strength μ is extracted and the observed significance is estimated.

The observed data used in steps 2-3 correspond to the full Run-2 dataset of 139fb^{-1}. In the following sub-sections, fit results for steps 1 and 3 are discussed. The model inspection, described in step 2, is given in Appendix F.

6.10.1 Resolved-only fit

In Figure 6.41, the nuisance parameter pulls and constraints for fits to Asimov and observed data in the resolved-only region are shown. The NPs in the right most part of the pull plots (centered at 1), correspond to the gamma parameters discussed in 6.9.2. The correlation coefficients between the NPs for the two types of fits are summarized in Figure 6.42. Only the largest correlations are plotted. Similar correlations between data and Asimov fits are observed. The signal strength is found to be highly (anti-)correlated with the theory and modelling uncertainties assigned to the Z + jets prediction.

The pre-fit and post-fit M_{jj}^{tag} and BDT score distributions are summarized in Figure 6.43. The large pre-fit uncertainties, mainly originating from the M_{jj}^{tag} re-weighting and Z + jets modeling uncertainties, are highly constrained, thanks to the large statistical power of the resolved CR. The measured signal strength in the resolved-only fit is:

$$\mu_{Res} = 0.77^{+0.45}_{-0.42} = 0.77^{+0.28}_{-0.27}(\text{Stat})^{+0.35}_{-0.31}(\text{Syst})$$

The observed significance of the measurement is estimated at 1.90σ. In order to correctly estimate the expected significance, a post-fit Asimov dataset is constructed. This is done by replacing the nuisance parameter values of the Asimov dataset with those obtained from a conditional $\mu = 1$ fit to the observed data. This step is necessary since our initial Asimov dataset (pre-fit Asimov) assumes a much larger background contribution (it can be seen from the pre-fit plots that the data/MC ratios are centered around 0.80). This larger background contribution, which is more less constant over all bins, would lead to a lower expected significance in comparison with the observed significance, where the normalization of the background is corrected to match the observed data. The expected significance obtained from the post-fit Asimov fit is estimated at 2.51σ.

6.10.2 Merged-only fit

The corresponding pulls and correlation plots for the merged-only fit are shown in Figures 6.44 and 6.45, respectively. Similarly to the resolved, significant correlations between the

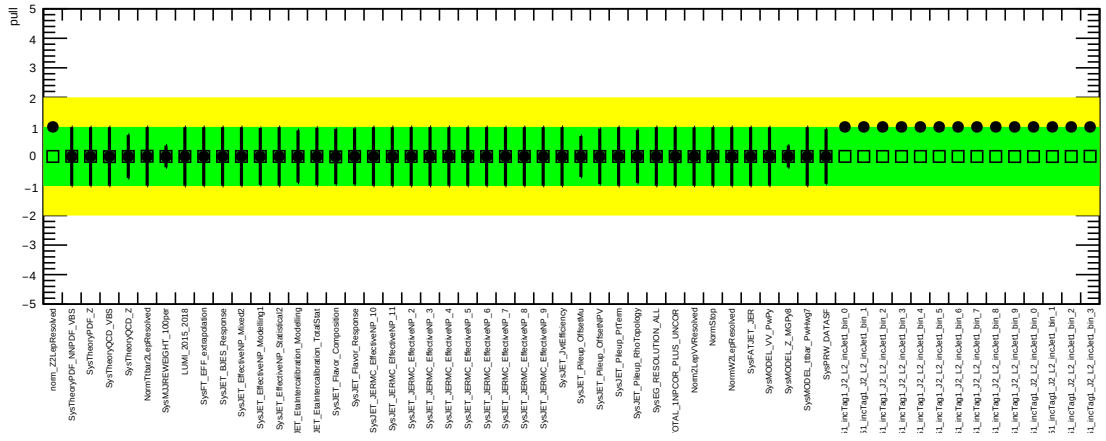

(a) Resolved-only Asimov fit

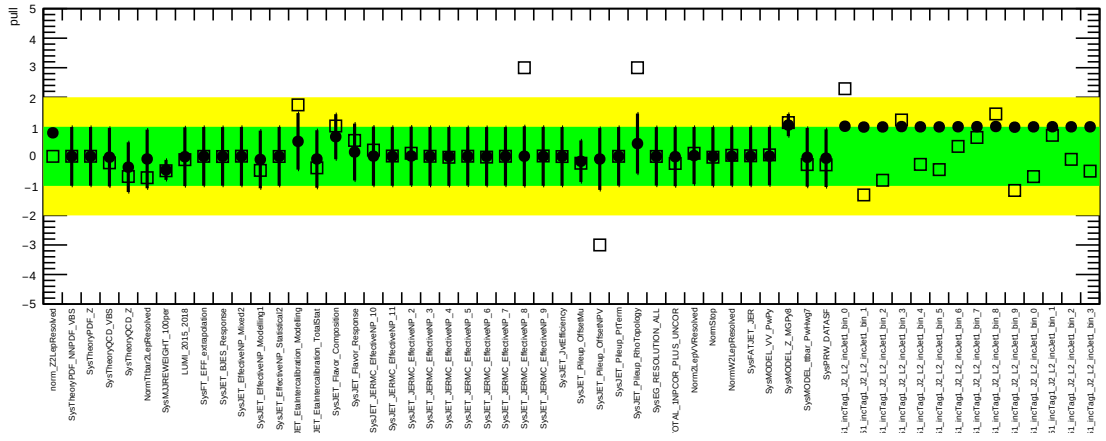

(b) Resolved-only Data fit

FIGURE 6.41: Nuisance parameter pulls for fits to Asimov and observed data in the resolved-only region. Simultaneous fits are performed in the full range of the BDT score in the SR and the M_{jj}^{tag} distribution in the CR. The data correspond to an integrated luminosity of $139 fb^{-1}$.

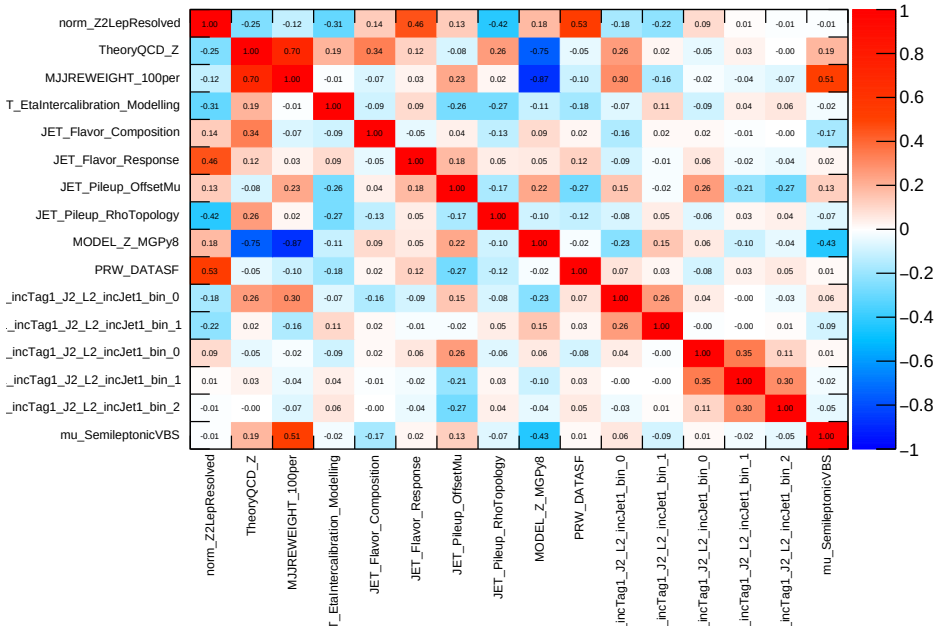

(a) Resolved-only Asimov fit

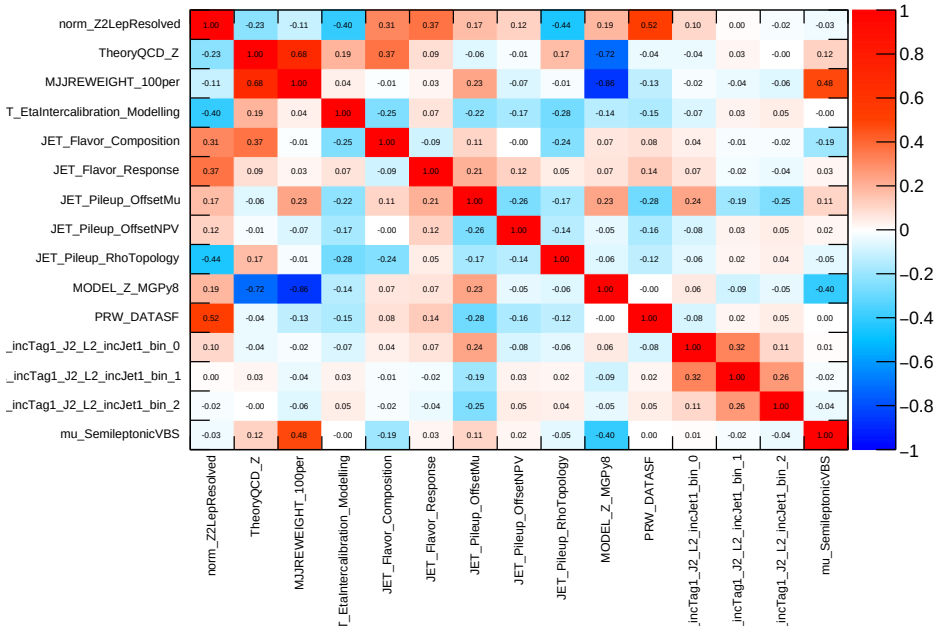

(b) Resolved-only Data fit

FIGURE 6.42: Correlation matrices for fits performed to Asimov and observed data in the resolved region. The data correspond to an integrated luminosity of $139 fb^{-1}$.

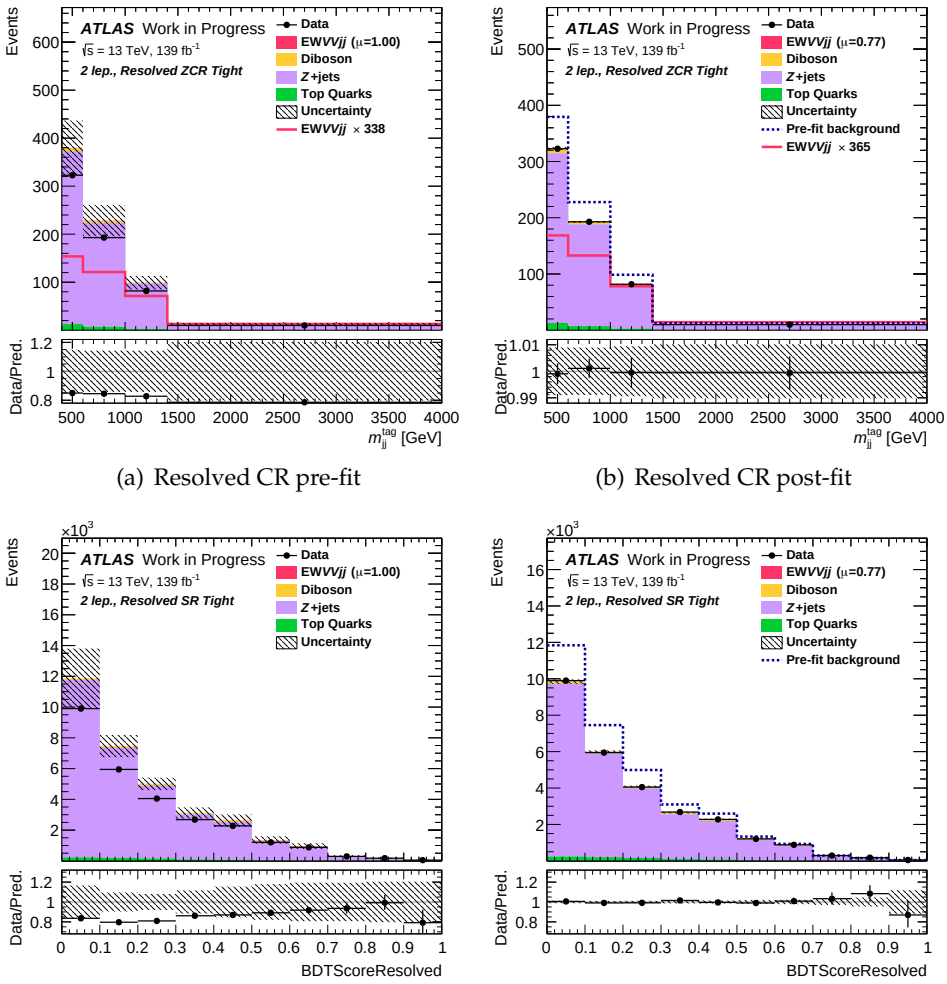

(a) Resolved CR pre-fit

(b) Resolved CR post-fit

(c) Resolved SR pre-fit

(d) Resolved SR post-fit

FIGURE 6.43: Pre-fit and post-fit distributions for the resolved-only fit in the 2-lepton channel. The data correspond to an integrated luminosity of $139 fb^{-1}$.

signal strength and the background modelling uncertainties are observed. Large correlations that appear only in the data fit but not in Asimov, are due to the selected threshold for plotting. Pre-fit and post-fit M_{jj}^{tag} and BDT score distributions are presented in Figure 6.46. The fitted signal strength in the merged-only fit is:

$$\mu_{Mer} = 2.23^{+0.76}_{-0.63} = 2.23^{+0.42}_{-0.40}(\text{Stat})^{+0.63}_{-0.49}(\text{Syst})$$

. The observed significance of the measurement is 4.39σ. The expected significance of the same measurement, obtained using the post-fit Asimov dataset discussed above, is 2.19σ.

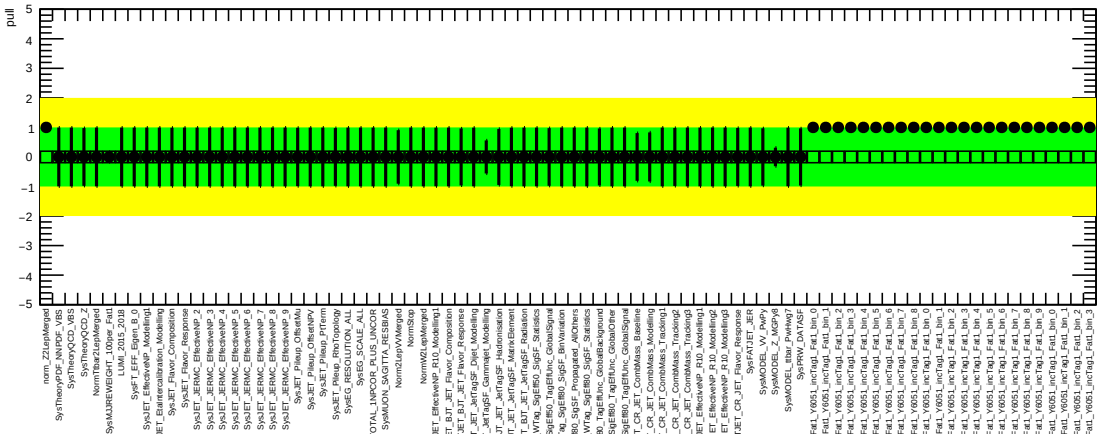

(a) Merged-only Asimov fit

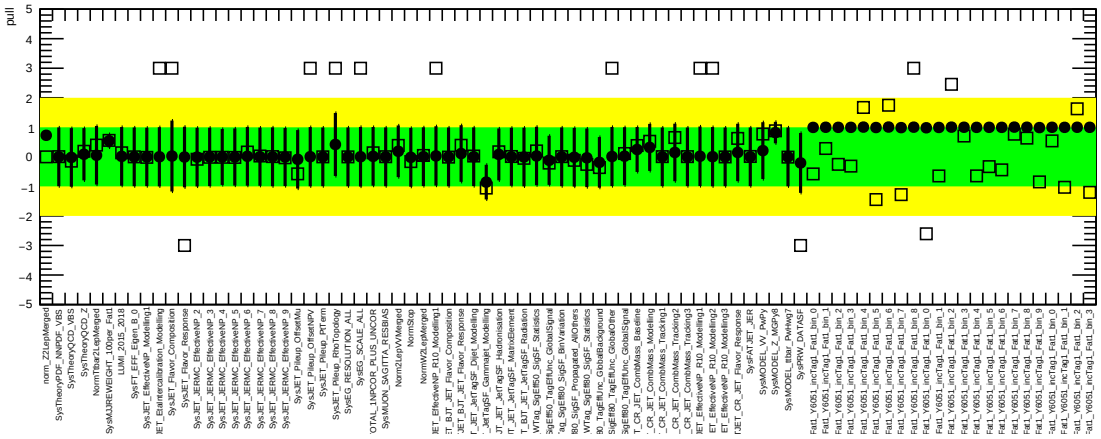

(b) Merged-only Data fit

FIGURE 6.44: Nuisance parameter pulls for fits to Asimov and observed data in the merged-only region. Simultaneous fits are performed in the full range of the BDT score in the HP and LP SRs and the M_{jj}^{tag} distribution in the CR.

6.10.3 Combined fit

In the combined fit, a simultaneous fit is performed in the merged and resolved analysis regions and the signal strength μ is evaluated. The nuisance parameter pulls and constraints are plotted in Figure 6.47. The gamma parameters (Section 6.9.2) are removed from plotting here, for better visibility of the results. The largest correlations arising between the NPs and the signal strength are shown in Figure 6.48. Separate normalization factors are used to constrain the Z + jets background normalization in the merged and resolved SRs. These constraints are coming from the merged and resolved CRs, respectively. Alternatively, a single

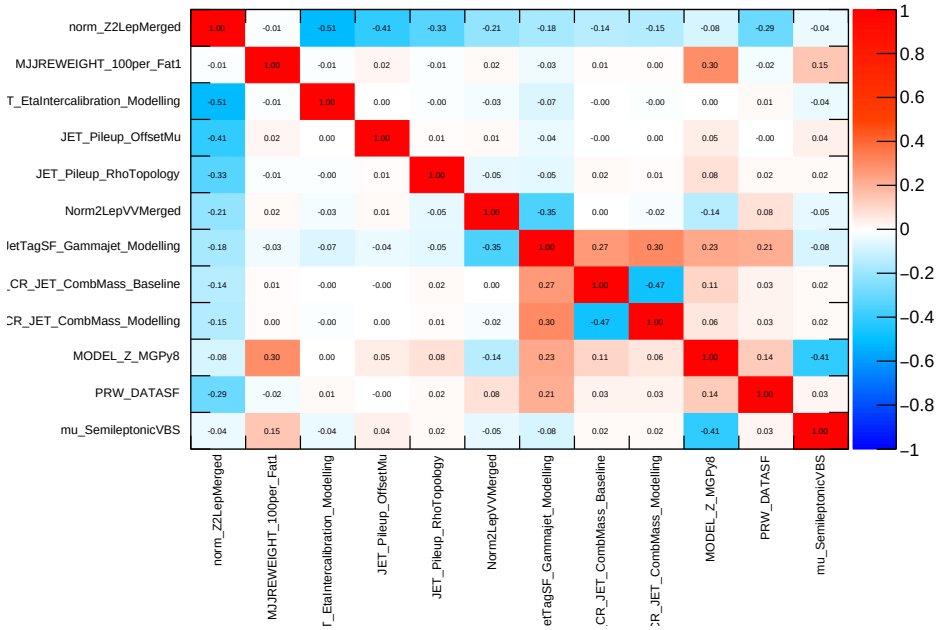

(a) Merged-only Asimov fit

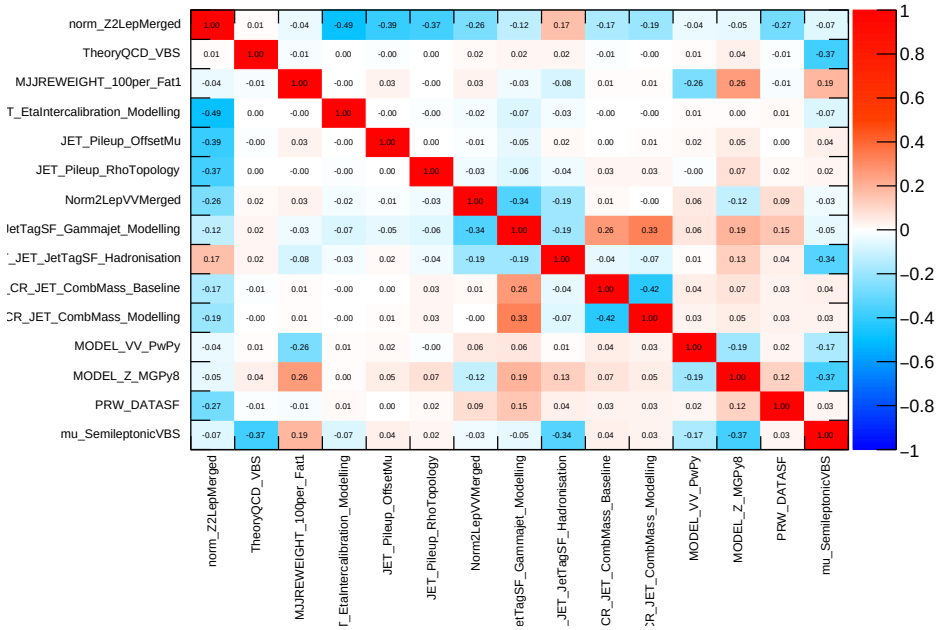

(b) Merged-only Data fit

FIGURE 6.45: Correlation matrices for fits performed to Asimov and observed data in the merged region.

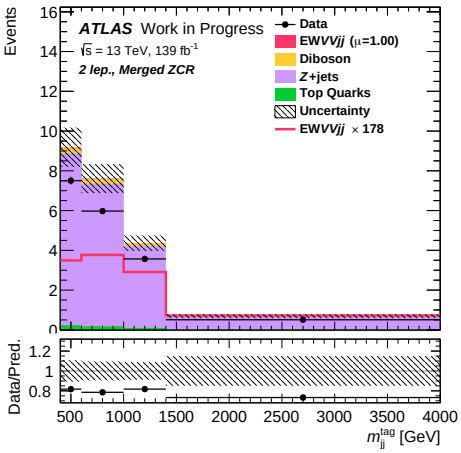

(a) Merged CR pre-fit

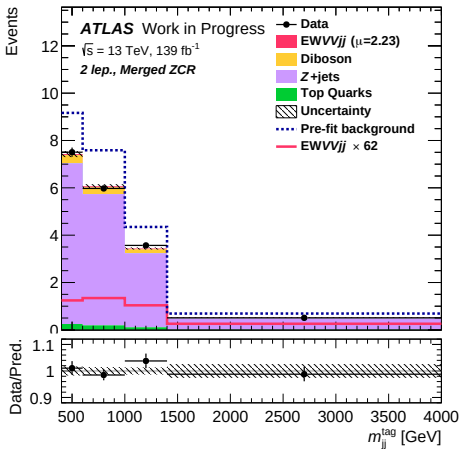

(b) Merged CR post-fit

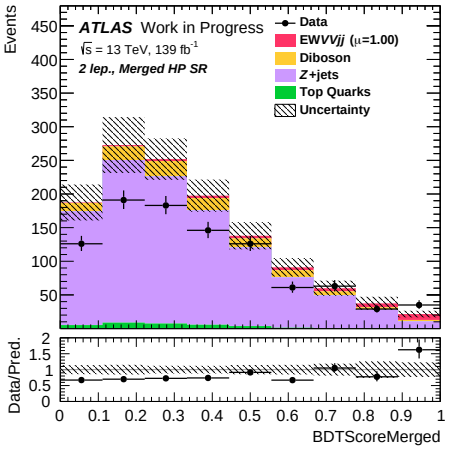

(c) Merged HP SR pre-fit

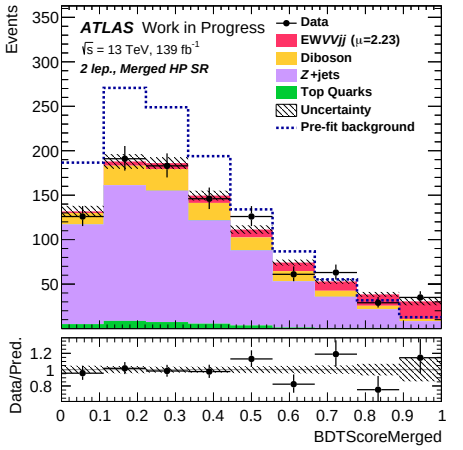

(d) Merged HP SR post-fit

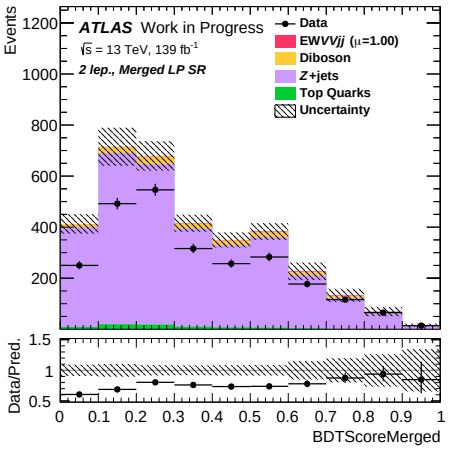

(e) Merged LP SR pre-fit

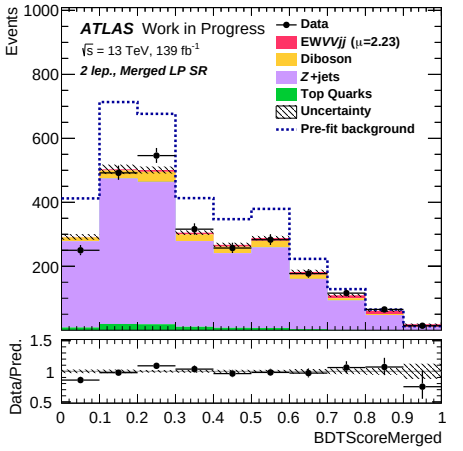

(f) Merged LP SR post-fit

FIGURE 6.46: Pre-fit and post-fit distributions for the merged-only fit in the 2-lepton channel. The data correspond to an integrated luminosity of $139 fb^{-1}$.

CR, e.g the resolved one, could be used in order to constrain the Z + jets normalization in both regions (with some additional extrapolation uncertainties implemented to account for the different acceptance of the two regions). However, the merged and resolved signal regions are dominated by different uncertainties, i.e in the merged the large-R jet and W/Z tagger related uncertainties, while in resolved the small-R jet related uncertainties are dominating, therefore separate CRs are needed to constraint such uncertainties. Systematic uncertainties that are relevant for all regions, are in general treated in a correlated way, with the exception of those which are pulled in different directions in the pull plots of the individual region fits, discussed previously. In such cases, the corresponding uncertainty is treated in an un-correlated way between the merged and resolved regimes. Such an example is the MJJREWEIGHT_Sherpa221 uncertainty which is pulled in opposite directions in the resolved-only and merged-only fits, as shown in Figures 6.41 and 6.44. A discussion about the pulls and constraints seen, is given in 6.10.4.

The estimated signal strength in the combined fit is:

$$\mu = 1.29^{+0.38}_{-0.34} = 1.29^{+0.23}_{-0.22}(\text{Stat})^{+0.31}_{-0.27}(\text{Syst})$$

The corresponding observed significance is 4.15σ, indicating a strong evidence of the EW $VVjj$ signal in the semileptonic final state with 2 leptons. The expected significance obtained with the post-fit Asimov dataset is estimated at 3.34σ. The post-fit M_{jj}^{tag} and BDT score distributions are summarized in Figure 6.49. In order to validate that our results can sufficiently describe other distributions than the BDT scores, the fit results are applied to the mass of the full system (MFullSystem) in the SRs. The corresponding pre-fit and post-fit plots are summarized in Figure 6.50.

Impact of fJVT on final results

The fJVT algorithm, described in Chapter 5, is applied during the tagging jet selection, in order to remove forward jets that most likely originate from pile-up interaction vertices. In order to quantify the impact of the algorithm on the final result, the fit is repeated and the significance is re-evaluated after removing fJVT. The newly estimated signal strength value is:

$$\mu = 1.42^{+0.42}_{-0.39} = 1.42^{+0.24}_{-0.23}(\text{Stat})^{+0.35}_{-0.31}(\text{Syst})$$

The result corresponds to an observed significance of 3.99σ, while the expected significance is estimated at 3.10σ. These values correspond to a $\sim 4\%$ drop in the observed significance and a $\sim 7\%$ drop in the expected significance. In general, fJVT is found to improve the background rejection in the right-most BDT bins of both the merged and resolved regions. However, these improvements are rather small, therefore its final impact on the results is also not significant. This can be partially attributed to the $p_{\text{T}} > 30$ GeV cuts applied to forward jets, which removes the large majority of pile-up jets expected at $20 < p_{\text{T}} < 30$ GeV.

6.10.4 Nuisance parameter pulls and constraints

A few nuisance parameters are highly constrained from the fit, especially the following ones:

- The Model_Z_MGPy8 and Theory_QCD_Z, which are the modeling and QCD-scale theory uncertainties associated to the Z + jets prediction, respectively. As shown in Section 6.8.2, such uncertainties are found to have large effects on the right most bins of our

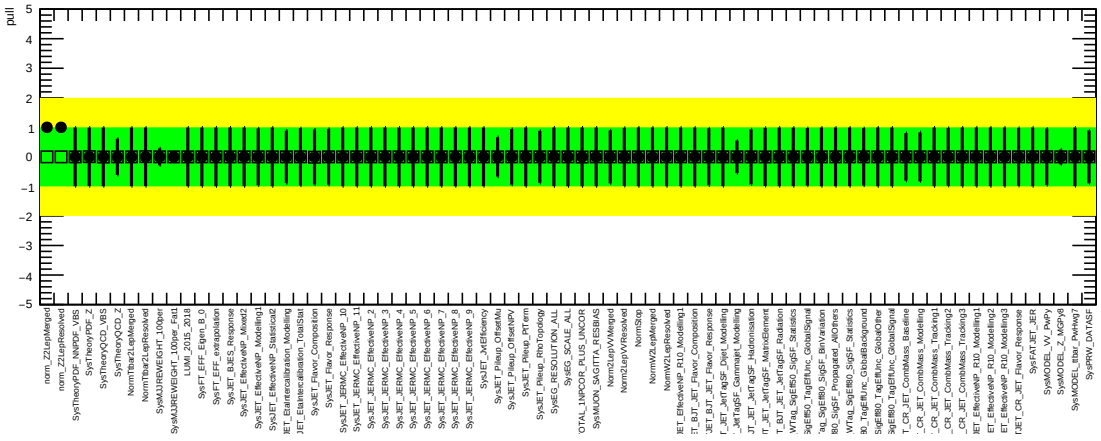

(a) Combined Asimov fit

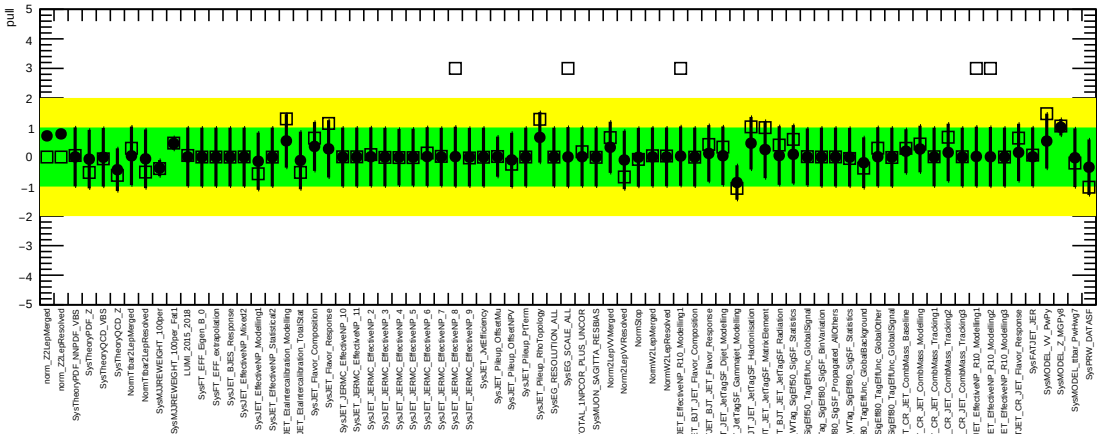

(b) Combined Data fit

FIGURE 6.47: Nuisance parameter pulls for fits performed to Asimov and observed data. The merged and resolved regions are fitted simultaneously.

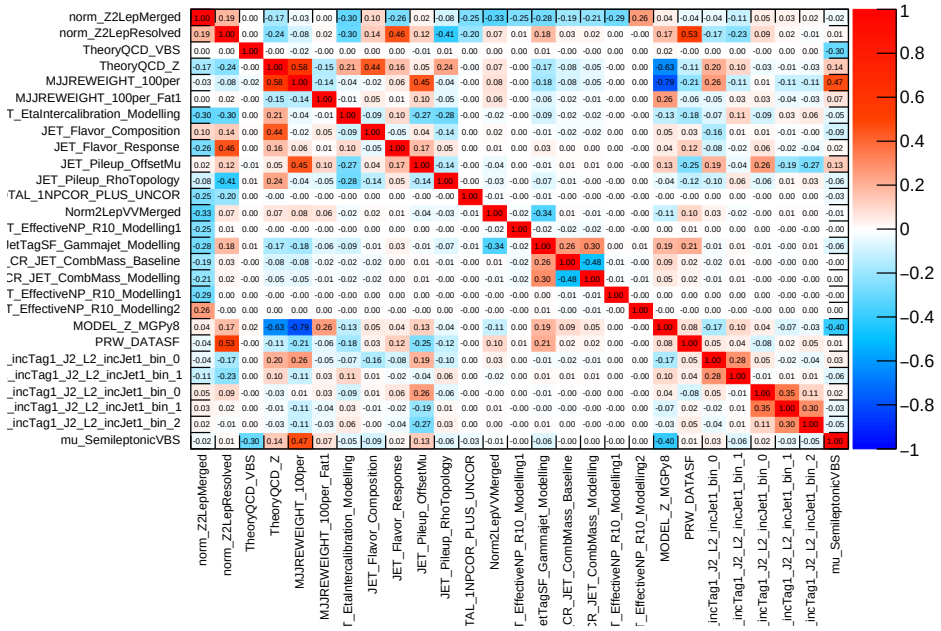

(a) Combined Asimov fit

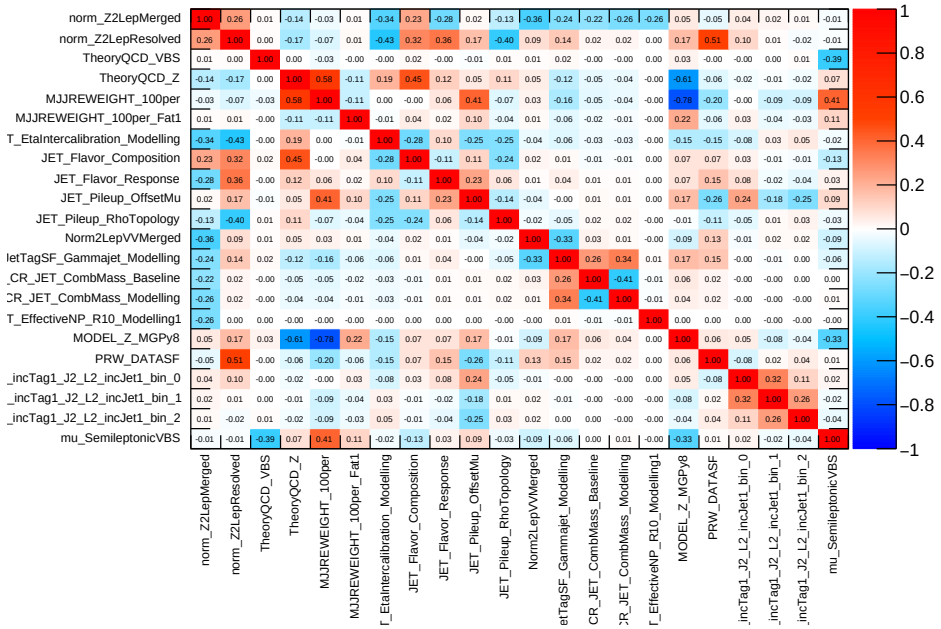

(b) Combined Data fit

FIGURE 6.48: Correlation matrices for fits performed to Asimov and observed data. The merged and resolved regions are fitted simultaneously. The data correspond to an integrated luminosity of $139 fb^{-1}$.

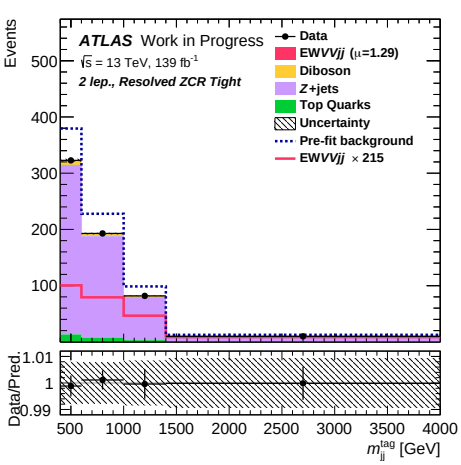

(a) Resolved CR post-fit

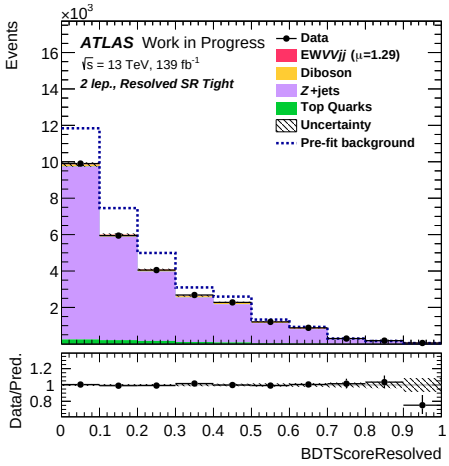

(b) Resolved SR post-fit

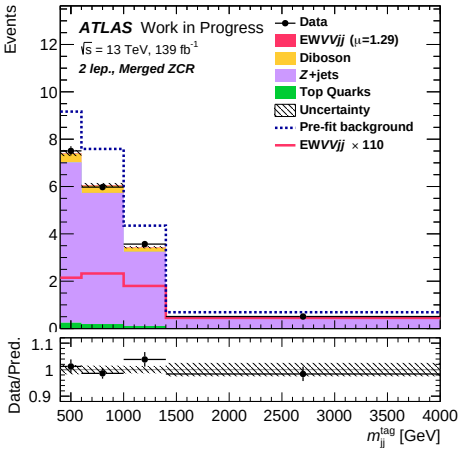

(c) Merged CR post-fit

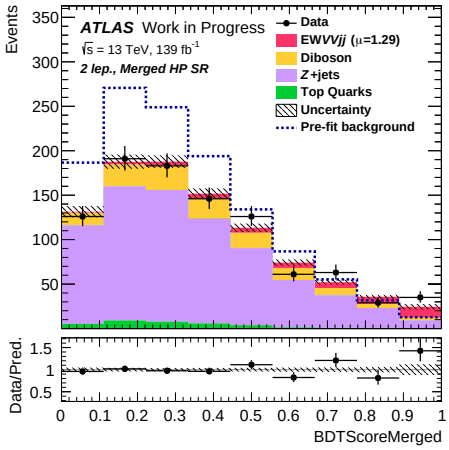

(d) Merged HP SR post-fit

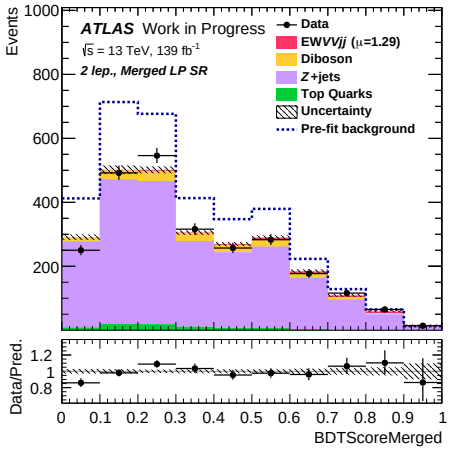

(e) Merged LP SR post-fit

FIGURE 6.49: Post-fit distributions for the combined fit in the 2-lepton channel. The data correspond to an integrated luminosity of $139 fb^{-1}$.

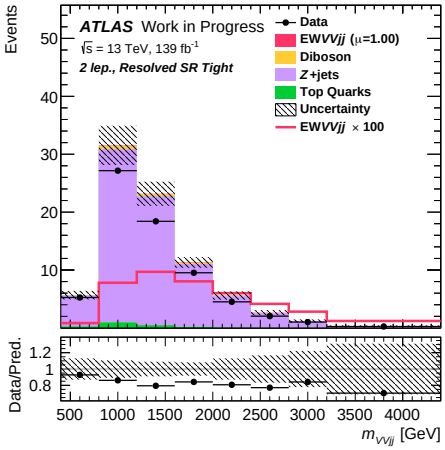

(a) Resolved SR pre-fit

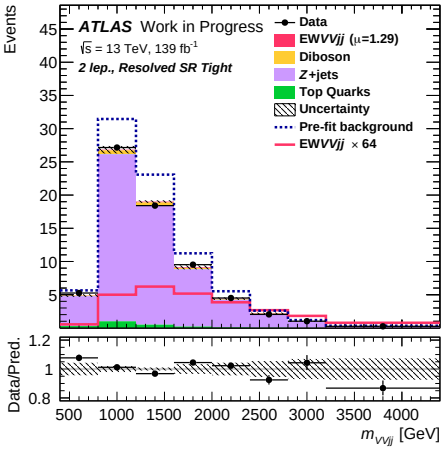

(b) Resolved SR post-fit

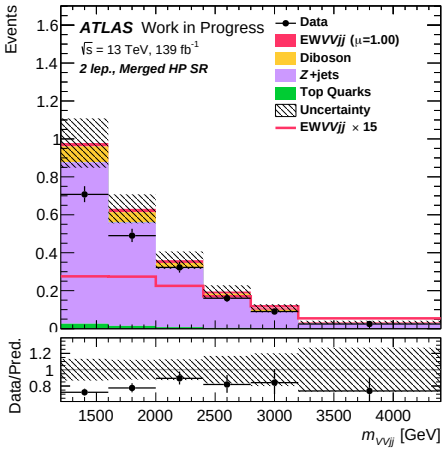

(c) Merged HP SR pre-fit

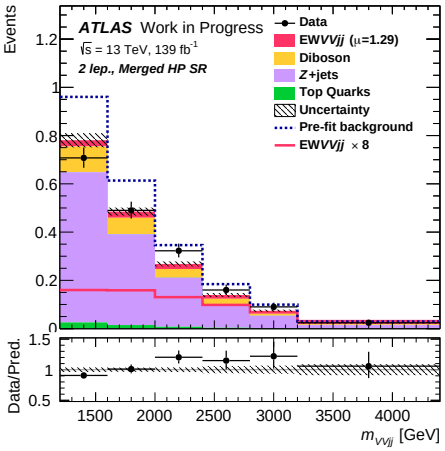

(d) Merged HP SR post-fit

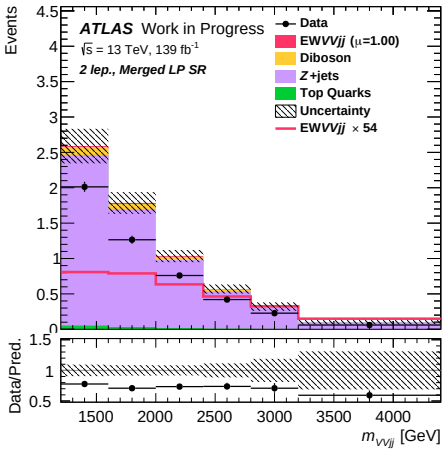

(e) Merged LP SR pre-fit

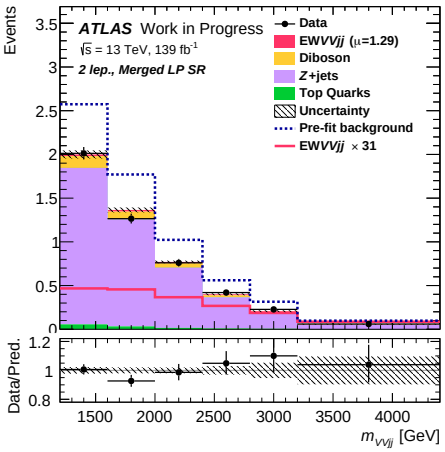

(f) Merged LP SR post-fit

FIGURE 6.50: Pre-fit and post-fit distributions of the MFullSystem in the analysis SRs. The fit results from the combined fit to the BDT scores, are applied to the post-fit distributions. The data correspond to an integrated luminosity of $139 fb^{-1}$.

SR and CR distributions. Since, theory uncertainties are treated in a correlated way between the regions, strong constraints originating from regions with the large statistical power, such as the control regions, are expected.

- The MJJREWEIGHT_Sherpa221_100per and MJJREWEIGHT_Sherpa221_100per_Fat1, which are the M_{jj}^{tag} reweighting uncertainties associated to the resolved and merged regions, respectively. The shape effects of these uncertainties on the distributions considered in the fit, are plotted in Figure 6.52. Their impact on both the merged and resolved distributions is found to be large (up to 30% in some cases). Given the large statistical power of the CRs, such large uncertainties are expected to be highly constrained.

- The small-R jet related JES uncertainties such as: JET_EtaIntercalibration_Modelling, JET_Pileup_OffsetMu, JET_Pileup_RhoTopology, JET_Flavor_Composition and JET_Flavor_Response. The JES uncertainties affect significantly many of the input variables used in the BDT training, therefore the final BDT score. Especially the JET_Flavor_Composition and JET_Flavor_Response uncertainties are generated in a very conservative approach, therefore are expected to have large effects in some bins. Thus, constraints of such NPs are also expected. The majority of these constraints are driven through the resolved CR.

- The JetTagSF_Gammajet_Modelling, which is the uncertainty related to the modelling of the γ+jet process, which is used by the W/Z tagger to derive scale factors for the background jets (explained in section 6.8). The effect of this uncertainty on the distributions considered in the fit is plotted in Figure 6.51. It is found to have large normalization impact on the HP SR, while be less important in the rest of merged regions. Since the uncertainty is treated in a correlated way among the regions it gets constrained from the merged CR.

- The PRW_DATASF, which is the pile-up reweighting uncertainty. This systematic uncertainty, also constrained in the previous round of the analysis, is found to have large shape effects on the quark-gluon tagging variables, such as the track multiplicity (Ntrk).

- The Norm2LepVVMerged which is the uncertainty associated to the diboson normalization in the merged regime. A conservative 50% prior is used, therefore the uncertainty gets constrained.

In general, over-constraints of NPs, indicate that the propagated uncertainty from the corresponding uncertainty source to the parameter of interest μ, is reduced. Such large constraints are usually unproblematic, from a statistical point of view, and convenient, from an analysis point of view, since they increase the analysis sensitivity to the target signal. However, at the same time such large constraints indicate that the analysis phase space is quite sensitive to the uncertainty source, and therefore to the parametric degrees of freedom associated to it. In the case of experimental uncertainties, such as the JES and JER uncertainties, their parametric form is known, since these uncertainties are derived from a previous measurement on data. Constraints on such uncertainties can more easily be justified and understood from a physics point of view. However, in the case of theory and modelling uncertainties, which can not be directly estimated from data, and therefore neither their true distribution nor their parametric form is known, it is un-clear how many degrees of freedom are needed in order to capture correctly their effects. As described in 6.8.2, such uncertainties are usually estimated by taking the difference between the nominal prediction and alternative predictions made with an alternative generator (2-point sytematics) and a signle NP is usually assigned to them. The fact that such uncertainties are described by a single NP and a gaussian prior is used, is just an assumption and can not be easily justified from a physics point of view.

Highly constrained NPs are usually expected to get pulled during the fit. As discussed above, constrained NPs correspond to uncertainties to which the analysis is sensitive on. Therefore, the data fit might decide on a better estimate for their central value than the initial one assumed. However, in some cases pulls may arise because of missing degrees of freedom. Such an example in our case is the JetTagSF_Gammajet_Modelling, which is pulled in order to absorb the differences in the Z + jets normalization between the merged signal and control region. Such pulls are usually fixable by considering additional normalization uncertainties which account for the different acceptance between regions.

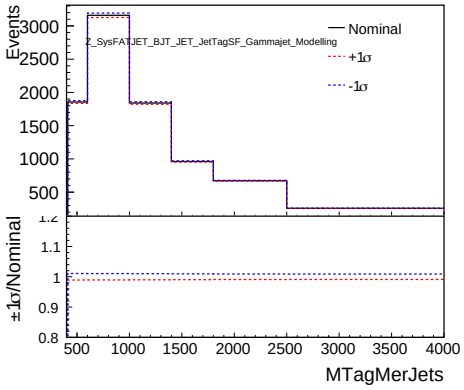

(a) Merged CR

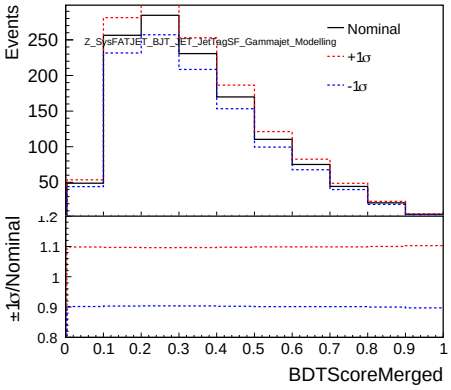

(b) Merged HP SR

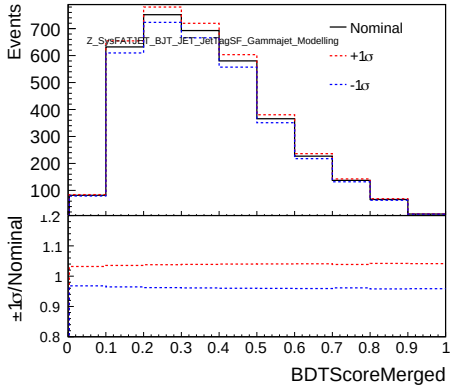

(c) Merged LP SR

FIGURE 6.51: Z + jets FATJET_BJT_JET_JetTagSF_Gammajet_Modelling uncertainty in the 2-lepton channel.

6.10.5 Ranking and breakdown of systematic uncertainties

In order to quantify the impact of each nuisance parameter on the signal strength measurement, a ranking of systematics is performed. First, a fit is performed and the NPs are fixed to their best fit estimates. Next, the fit is repeated, after fixing a single NP to its up (down) uncertainty value, and the new value of μ is recorded. The procedure is repeated for all NPs and the difference between the new estimate of μ and nominal value, is considered as the impact of the individual nuisance parameter on the measurement.

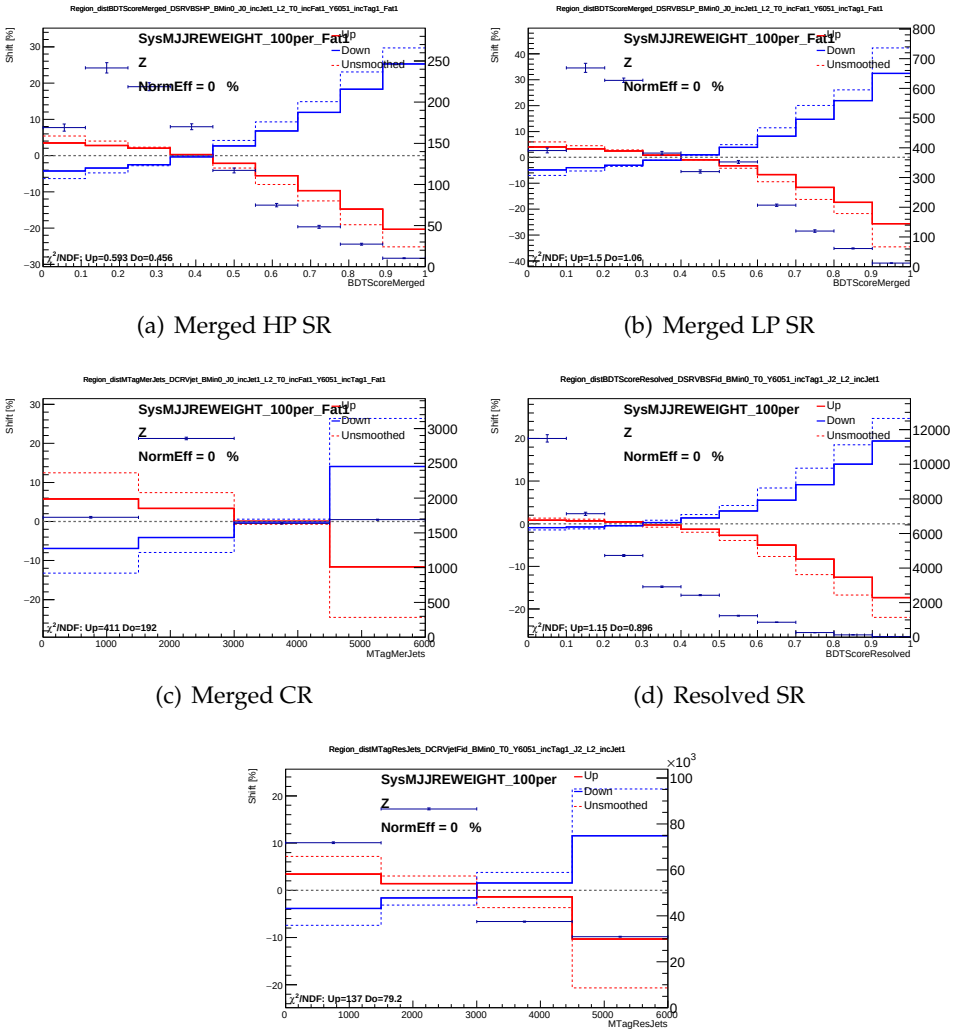

(a) Merged HP SR (b) Merged LP SR

(c) Merged CR (d) Resolved SR

(e) Resolved CR

FIGURE 6.52: Effect of the MJJREWEIGHT_Sherpa221 uncertainty in the various distributions used in the combined fit.

The nuisance parameter rankings for the combined fit to the Asimov dataset and to the observed data are summarized in Figure 6.53. Only the 15 highest ranked parameters are shown, not including nuisance parameters describing the uncertainty due to the size of the simulated samples (gamma parameters). Similar rankings are observed in both cases. The largest impact on the signal strength measurement is given by the MJJREWEIGHT uncertainty related to the Z + jets background. This is not surprising, since a conservative approach is chosen for the estimation of this uncertainty. The next major systematics are the QCD scale uncertainty related to the EW signal and the Z + jets background modelling uncertainty. As discussed in 6.8.2, these uncertainties are found to have a rather large impact on the sensitive bins of the BDT scores, in both merged and resolved SRs. In particular, the theory uncertainties related to the EW signal, are expected to be significant, since such uncertainties can not get constrained during the fit process. Significant impact on the signal strength has also the diboson background modelling uncertainty. The diboson production, containing the majority of the QCD induced VV diagrams, has a similar shape to the EW VV signal. Therefore, the modelling of this background is expected to be ranked high.

The above method gives an estimation of which systematic sources are the most important ones, by measuring their effect on the signal strength value. In order to answer a slightly different question; i.e., what is the contribution of a certain set of systematic uncertainties on the total μ uncertainty, a breakdown of systematic uncertainties is performed. During this procedure, the examined set of systematic uncertainties is removed from the model and the fit is repeated. The new, reduced uncertainty on μ is recorded and is then subtracted quadratically from the total uncertainty, in order to give an estimation of the impact of the examined set on the total μ uncertainty. The breakdown of systematic uncertainties, showing the contributions of different sources of uncertainties to the measured μ uncertainty, for fits to observed data (obs) and to the expectation from simulation (exp), are presented in Table 6.17. Results are shown for both the combined and individual resolved and merged region fits. The quadratic sum of the different contributions might be different from the total uncertainty because of correlations between the nuisance parameters. As shown, the largest impact on the μ uncertainty originates from systematic uncertainties. More specifically, the MJJREWEIGHT , background modelling and theory uncertainties are found to have the largest contributions. The statistical uncertainty, although smaller, is still comparable to that from systematic uncertainties and has a significant impact on the final μ uncertainty.

6.10.6 Results with 35.5fb^{-1}

In order to make a comparison with the results of the first publication based on Run 1 data [26], the fit is repeated, using only the data recorded in 2015 and 2016. The data correspond to an integrated luminosity of 35.5fb^{-1}. The uncertainty on the integrated luminosity is updated correspondingly to that of the 2015+2016 dataset (2.1%). A combined fit to the merged and resolved regions is performed. The "Loose Resolved" region (Section 6.4.3) is fitted, in order to make a fair comparison with the first publication.

The pull and correlation plots for fits to Asimov (constructed with mc16a MC samples) and to observed data, are summarized in Figures 6.54 and 6.55, respectively. The fitted signal strength is:

$$\mu = 1.95^{+0.61}_{-0.57} = 1.95^{+0.37}_{-0.36}(\text{Stat})^{+0.49}_{-0.45}(\text{Syst})$$

. The observed significance is estimated at 3.7σ. The corresponding expected significance is 1.96σ. The post-fit M_{jj}^{tag} and BDT score distributions are summarized in Figure 6.56.

TABLE 6.17: Breakdown of uncertainties for the combined, resolved and merged region fits, performed to the observed data (obs) and to the Asimov dataset (exp).

Uncertainty source	Combined		Resolved-only		Merged-only	
	σ_μ(exp)	σ_μ(obs)	σ_μ(exp)	σ_μ(obs)	σ_μ(exp)	σ_μ(obs)
Total	0.364	0.363	0.456	0.434	0.576	0.694
Statistical	0.231	0.222	0.290	0.279	0.384	0.408
Systematic	0.281	0.287	0.352	0.333	0.429	0.561
Normalizations						
All normalizations	0.017	0.041	0.021	0.028	0.045	0.063
Floating normalizations	0.009	0.010	0.011	0.024	0.025	0.049
Experimental Uncertainties						
Jets	0.089	0.087	0.09	0.105	0.207	0.330
Leptons	0.012	0.017	0.012	0.011	0.014	0.029
Luminosity	0.017	0.024	0.018	0.014	0.018	0.039
MJJREWEIGHT Uncertainty	0.179	0.158	0.228	0.200	0.088	0.134
Background Modelling Uncertainties						
Total	0.171	0.160	0.22	0.191	0.271	0.309
Z+jets Modelling	0.153	0.125	0.215	0.185	0.236	0.259
VV Modelling	0.051	0.076	0.036	0.037	0.095	0.119
ttbar Modelling	0.005	0.004	0.004	0.008	0.003	0.002
Theory Uncertainties						
Total	0.121	0.145	0.142	0.103	0.117	0.261
Theory QCD Z+jets	0.052	0.027	0.095	0.050	0.002	0.008
Theory QCD Signal	0.108	0.14	0.105	0.086	0.115	0.259
MC statistical	0.096	0.082	0.143	0.133	0.099	0.087

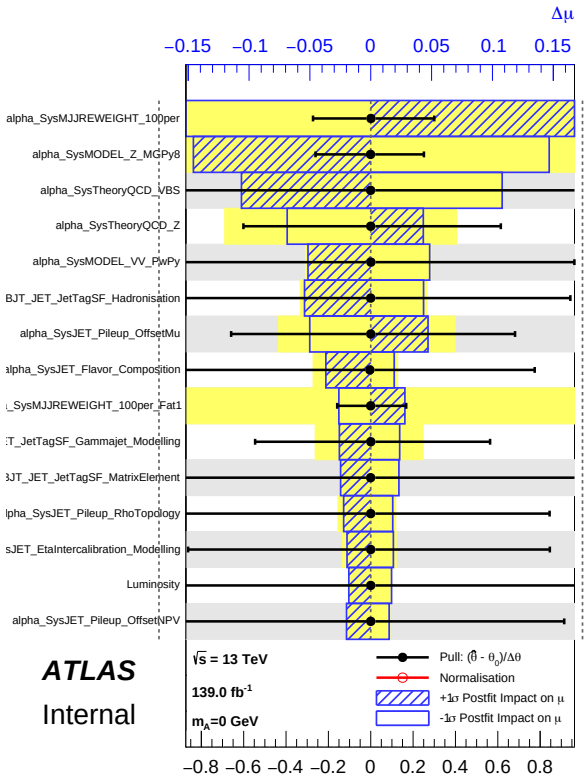

(a) Combined Asimov fit

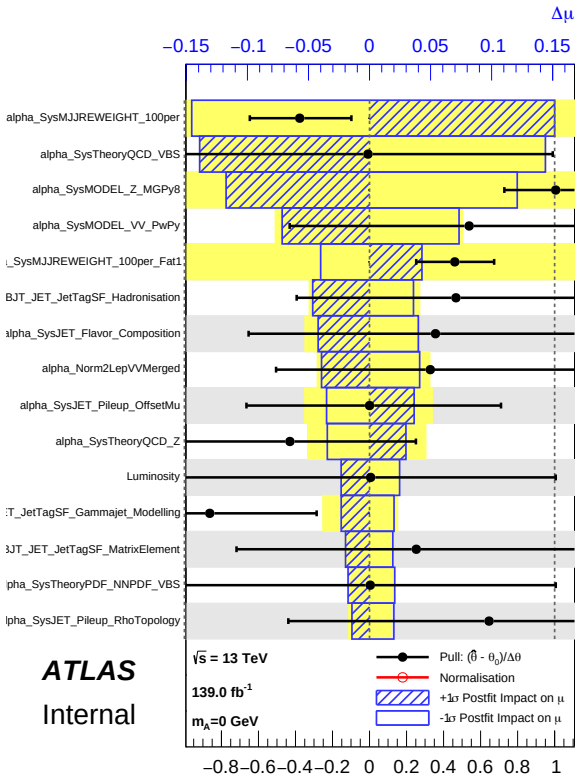

(b) Combined Data fit

FIGURE 6.53: Nuisance parameter ranking for the combined fit with Asimov data (a) and observed data (b). The data correspond to an integrated luminosity of $139 fb^{-1}$.

The signal strength parameter for the 2-lepton channel as estimated in [26] is:

$$\mu = 1.97^{+0.83}_{-0.77} = 1.97^{+0.50}_{-0.35}(\text{Stat})^{+0.65}_{-0.59}(\text{Syst})$$

. The observed and expected significance of the signal strength measurement was 2.07 and 1.34, respectively. The current analysis results correspond to a ∼46% better expected significance and a ∼78% improvement in observed significance. The large improvements can be attributed to a few parameters:

- The more precise estimation of the JES/JER uncertainties using the full Run2 dataset.
- The improved discrimination power of the BDT discriminant. The new BDT discriminant uses an updated set of features, as well as, different training methods. The k-fold validation, with k=5, is employed where 80% of the data is used each time for training. The old BDT discriminant was trained using 50% of the dataset. More importantly, the current BDT is trained exploiting the full Run2 dataset.
- The updated event selection and jet reconstruction. The PFlow algorithm is employed for the small-R jet reconstruction, in contrary with the previous round, where EMTopo jets were used.
- The updated W/Z tagger. In the previous results, a 2-variable W/Z tagger was used (based on the mass and substructure D2 requirements). In the current round the track multiplicity is added in order to improve the performance. Moreover, a new, more precise technique is used for the calibration and the uncertainty evaluation of the tool.

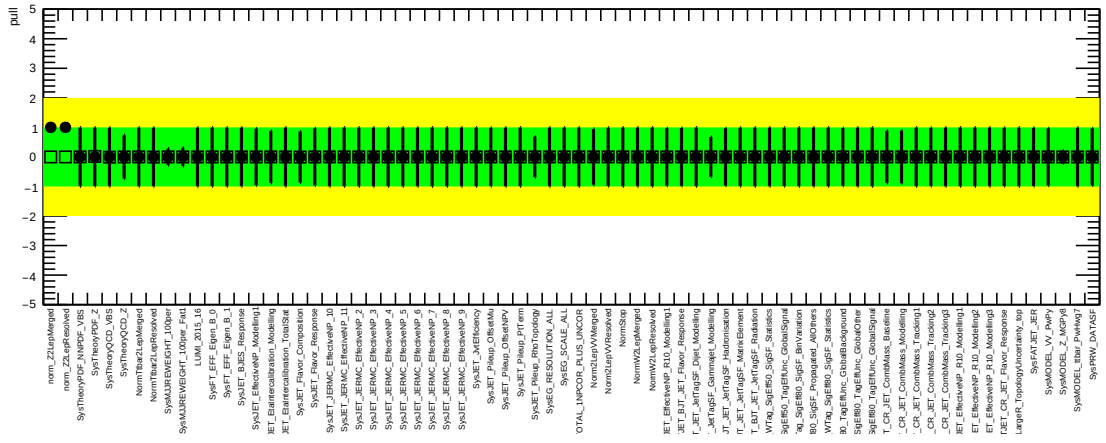

(a) Combined Asimov fit

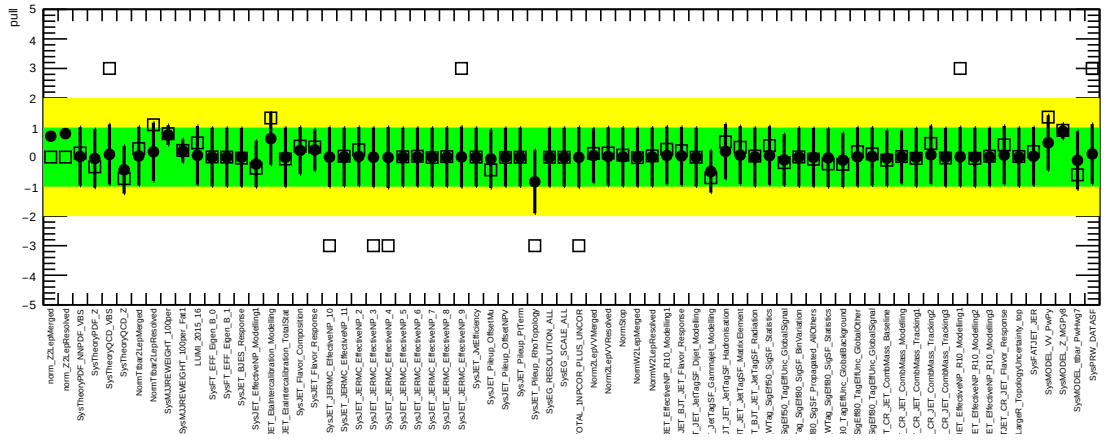

(b) Combined Data fit

FIGURE 6.54: Nuisance parameter pulls for fits performed to Asimov and observed data. The merged and resolved regions are fitted simultaneously. The data correspond to an integrated luminosity of $35.5 fb^{-1}$.

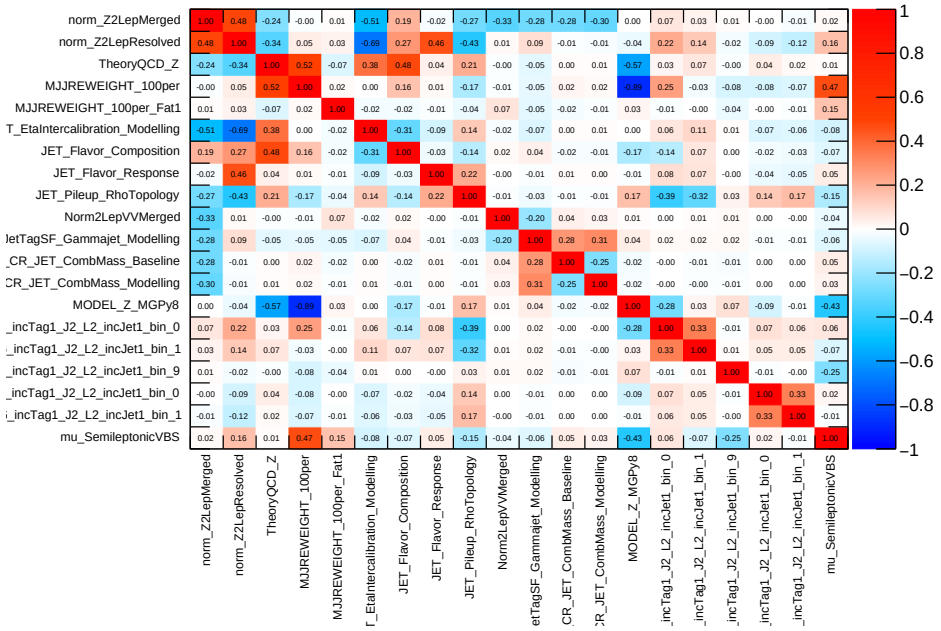

(a) Combined Asimov fit

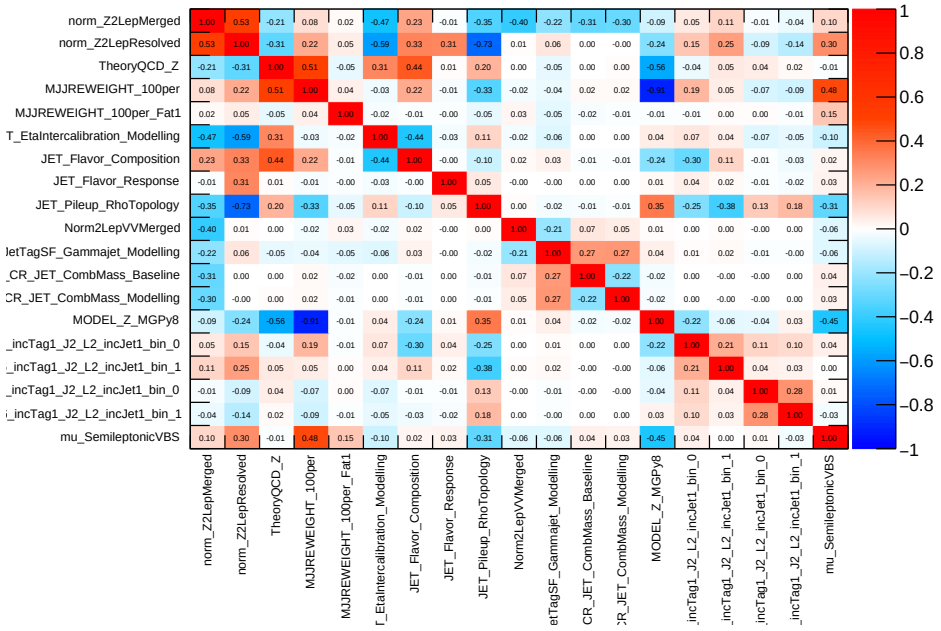

(b) Combined Data fit

FIGURE 6.55: Correlation matrices for fits performed to Asimov and observed data. The merged and resolved regions are fitted simultaneously. The data correspond to an integrated luminosity of $35.5 fb^{-1}$.

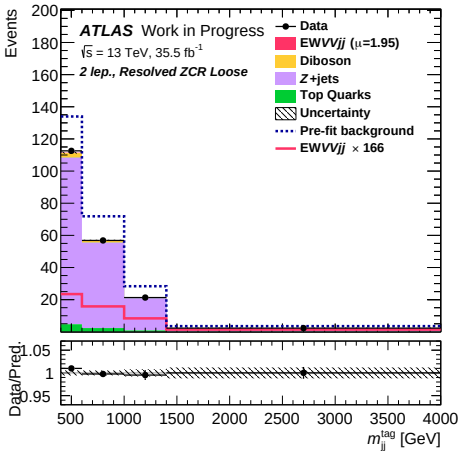

(a) Resolved CR post-fit

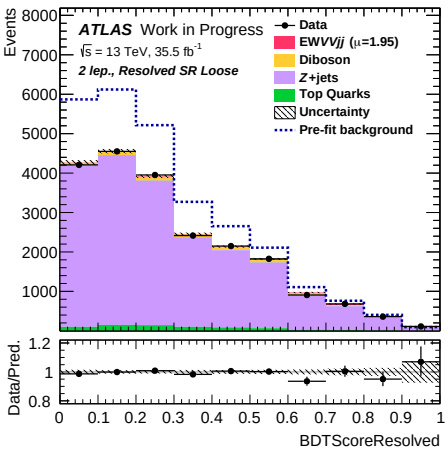

(b) Resolved SR post-fit

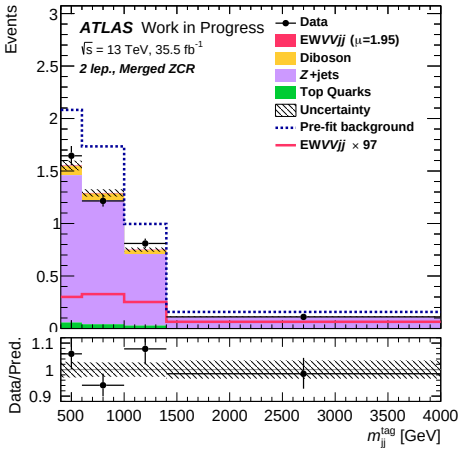

(c) Merged CR post-fit

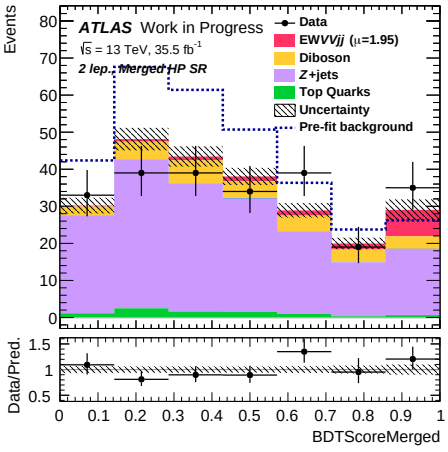

(d) Merged HP SR post-fit

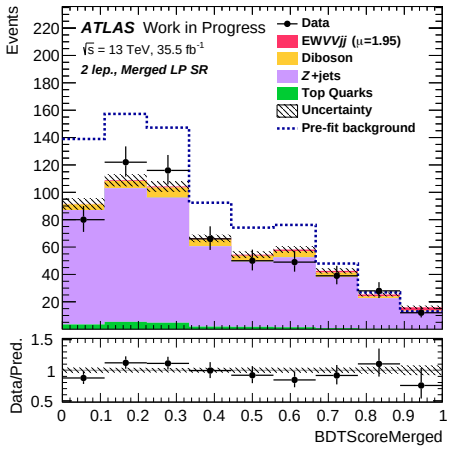

(e) Merged LP SR post-fit

FIGURE 6.56: Post-fit distributions for the combined fit with $35.5 fb^{-1}$ data.

6.11 Conclusions and prospects

The VBS semileptonic final state with 2-leptons has been studied. A measurement of the signal strength was performed, exploiting the full Run2 dataset of the ATLAS detector, which corresponds to an integrated luminosity of $139 fb^{-1}$. The signal strength is measured to be:

$$\mu = 1.29^{+0.38}_{-0.34} = 1.29^{+0.23}_{-0.22}(\text{Stat})^{+0.31}_{-0.27}(\text{Syst})$$

which is compatible with the SM prediction within uncertainties. The background only hypothesis is rejected with a significance of 4.15σ, indicating a strong evidence of the EW $VVjj$ signal in the semileptonic final state with 2 leptons. The expected significance obtained with the post-fit Asimov dataset is estimated at 3.34σ. A comparison of the analysis result with that of the previous publication based on Run 1 data [26], was also performed. For this purpose the fit is repeated after considering only the data recorded in 2015 and 2016, which correspond to an integrated luminosity of $35.5 fb^{-1}$. When comparing to the 2-lepton channel results of the previous round, the current analysis results in a ∼46% improvement in terms of expected significance and a ∼78% improvement in the observed significance. However, it should be noted that certain theory uncertainties related to the EW signal are not currently considered in this measurement. Such uncertainties are the EW signal modelling, as well as, the interference between the EW-$V_{lep}V_{had}jj$ and QCD-$V_{lep}V_{had}jj$ processes. Since the last two are modeled separately, their interference which is of the order $\mathcal{O}(\alpha^5_{\text{EW}}\alpha_{\text{S}})$ is not included. This is usually generated independently and is included as an additional uncertainty affecting both the normalization and the shape of the EW-$V_{lep}V_{had}jj$ signal kinematic distributions. In the previous round, the largest impact of these uncertainties on the signal prediction was found to be up to 5% and 10%, respectively. However, such uncertainties are not expected to affect the significance estimation, in which the likelihood of the background only hypothesis is tested.

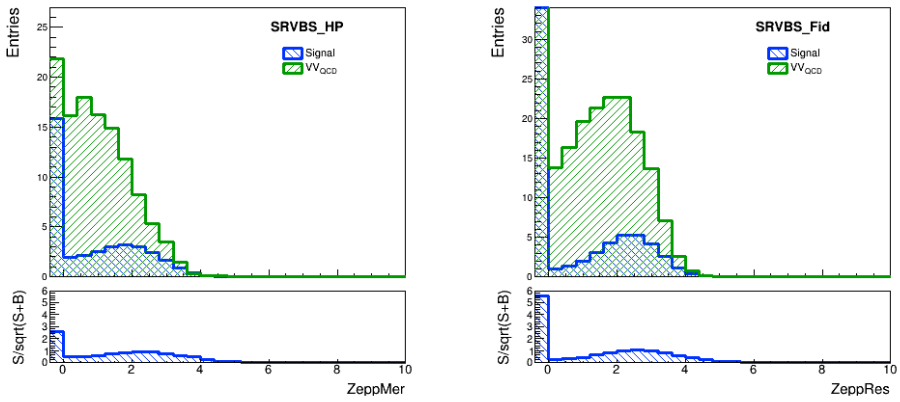

(a) Merged HP SR (b) Resolved SR

FIGURE 6.57: The Zeppenfeld variable in the Merged HP and Resolved SRs.

As already mentioned, the EW and QCD $V_{lep}V_{had}jj$ processes are treated separately in this analysis. The majority of QCD diboson events are suppressed thanks to the analysis selection cuts. Although, the surviving diboson events are much limited in number comparing to other background contributions, they have a very similar shape to the EW signal. As discussed in 6.9.6, the QCD diboson background is currently constrained with a prior. Normally its contribution should be estimated in a data driven way. This would require the construction of a dedicated CR. Such a CR could be constructed in the future by exploiting the increased

hadronic activity in QCD diboson events. In Figure 6.57 , the Zeppenfeld variable is plotted in the resolved and merged SRs for EW signal and QCD diboson events. The significance per bin is approximated as $S/\sqrt{S+B}$. The first bin corresponds to events with no extra jet. In the case of EW signal events no color flow between the interacting partons is expected, therefore events with no extra jets are more signal like. A requirement on the extra jets of the event could therefore be used in order to define a QCD CR within the SR.

The quark-gluon discrimination is also of paramount importance in this analysis, especially for the VBS tagging jet selection. Although no explicit quark-gluon discrimination tool is employed, quark-gluon discriminative variables, such the track multiplicity of jets, are used during the BDT training. Such variables are available only in the central regions of the detector, where the tracker information is available. However, tagging jets are expected in the most forward detector region, highlighting the necessity of a forward quark-gluon discriminant. This is also highlighted by the feature elimination described in 6.7.5. When variables which are sensitive to quark-gluon discrimination in the forward region, such as the width of small-R jets, are eliminated from the BDT, a significant performance drop is observed. In the future when the tracker will extend to a higher pseudorapidity range, VBS topologies will greatly benefit from the quark-gluon discrimination in the forward region.

Within the ATLAS collaboration two other final semileptonic channels (0- and 1-lepton) are converging their analyses and will be un-blided soon. The goal is to perform a combination of the 3 channels, similarly to [26].

7. The ATLAS pixel detector

This chapter presents a description of the ATLAS inner tracker pixel detector modules. As introduced in 3.4.1, the pixel detector consists of five flat barrel layers and multiple inclined or vertical ring-shaped end-cap disks. A schematic view of the pixel detector layout is shown in Figure 7.1. Two different silicon based detector technologies are considered for these layers; planar-pixel sensors and 3D-pixel sensors.

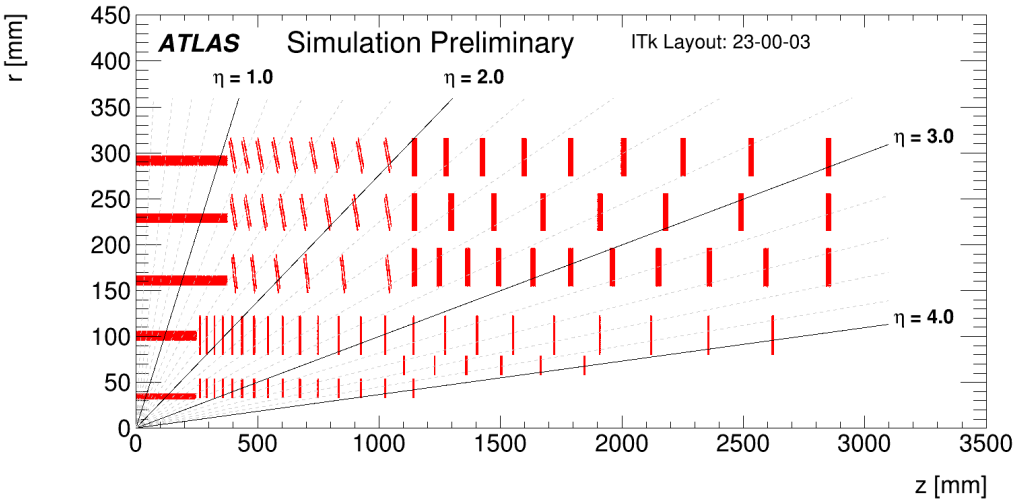

FIGURE 7.1: Schematic view of the pixel detector.

7.1 Semiconductor detectors overview

Semiconductor diode detectors are extensively used in High Energy Physics experiments, with silicon being the most common semiconductor material used. The main advantage in adopting such a detector technology relies on the compact size of silicon sensors, allowing to reach a high detector granularity - with a good energy resolution[1] and at the same time relatively fast timing characteristics. However, the material budget and cost of silicon-based detectors is significantly higher when compared to other detector technologies, such as gaseous detectors. Therefore, silicon detectors are usually placed as close to the interaction point as possible; in order to benefit from the high granularity and tracking resolution in the dense hit environment, while other types of detector technologies are usually employed to cover less dense areas far from the interaction point. A typical semiconductor sensor consists of a p-n junction briefly introduced in 7.1.1.

7.1.1 The p-n junction

Charged particles crossing a silicon layer generate electron-hole pairs [2]. The created electrons or holes can then be used in order to detect the passing particle. Immediate recombination of the charge carriers must, therefore, be prevented . Moreover the silicon bulk should be empty of free charge carriers inducing fake signals. Both conditions are achieved at the

[1] the low deposited energy needed for an electron-hole pair to be created allows for incremental pair production per small energy deposition steps

[2] on average 1 electron-hole pair per 3.6 eV of energy deposited

interface of an n-doped and p-doped semiconductor, known as p-n junction. Due to the doping of the silicon crystal, there are large numbers of mobile electrons on the n-type side, but very few mobile electrons on the p-type side. Thus when the n-type and the p-type materials are brought together, electrons from the n-type side start to diffuse into the p-type side, leaving behind positively charged ions. In a similar way holes in the p-type side start to diffuse across into the n-type side, leaving near the interface between the n and p regions, negatively charged ions. These fixed ions set up an electric field right at the junction between the n-type and p-type material. This intristic electric field causes some of the electrons and holes to flow in the opposite direction to the flow caused by diffusion. As soon as an equilibrium is reached,

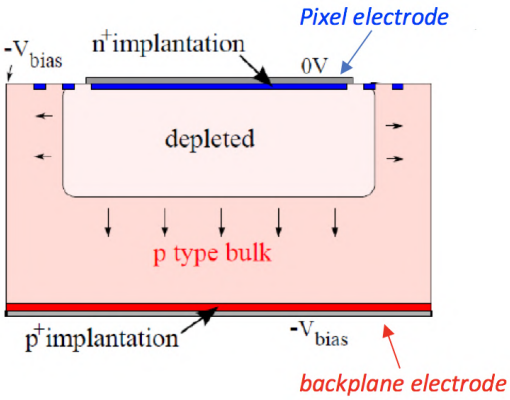

FIGURE 7.2: Cross section of a p-bulk planar silicon sensor [92].

a stable region is created on a p-n junction which is free of charge carriers and is called the depletion zone. The depletion zone can become wider by applying an external voltage, with reverse bias, enlarging this way the active volume of the detector and the resistivity of the material. This way the e-h pairs, created by a penetrating ionising particle in the active volume of the detector, will drift, due to the electric field, inducing a signal on the signal electrodes.

7.2 Pixel sensors for ITk

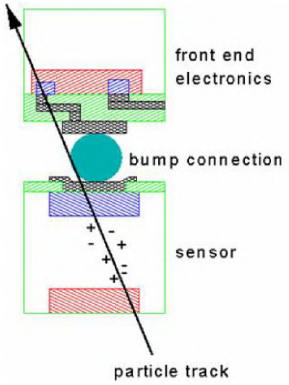

FIGURE 7.3: hybrid pixel readout channel [92].

The formation of the p-n junction in a silicon sensor depends on the types of the pixel electrode, bulk and backplane electrode. For the outer layers of ITk, planar n-in-p sensors are considered. An example of such a sensor is shown in Figure 7.2; In a n-in-p type of sensor a p type bulk is used with the pixel electrode being highly n-doped while the backplane is highly p-doped. The depletion region starts from the n+ pixel electrode and grows towards the backplane as a function of the applied reverse bias voltage. Electrons are collected in the

n+ pixel electrodes, while holes drift to the backplane. The backplane electrode is connected via an ohmic contact, realized by a highly p-doped implant and an aluminization, to the HV in order to avoid HV break down after the sensor is fully depleted. The pixel electrode is connected to a front-end read-out chip for further processing of the signal using a high density connection technique called bump-bonding as shown in Figure 7.3. This type of sensors are usually referred to as hybrid, while detectors where the read-out circuitry is included as part of the sensor design are called monolithic. Monolithic sensors have promising potential cost-reductions and manufacturing simplifications but they do not yet demonstrate the level of radiation hardness as a hybrid pixel sensor. For this reason hybrid only sensors are considered for the ATLAS pixel detector.

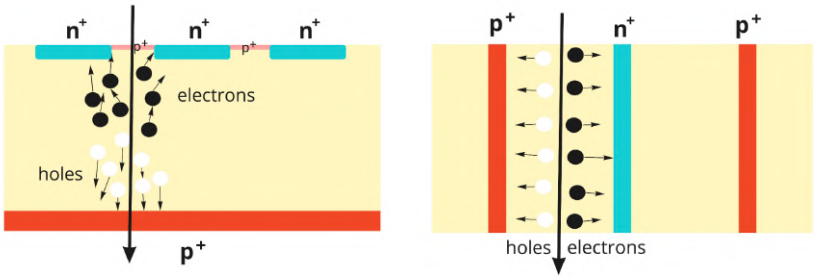

FIGURE 7.4: Schematic view of planar and 3D pixel sensors [93].

In the innermost part of ITk 3D silicon sensors are chosen. A schematic view of planar and 3D silicon sensors is shown in Figure 7.4. The main difference between the two detector technologies is found on the orientation of the charge collecting electrodes. In the case of planar sensors these are oriented parallel to the sensor surface while in 3D sensors they penetrate perpendicularly through the surface. The main advantage of a 3D sensor is the high charge collection efficiency despite crystal defects caused by radiation, while the biggest disadvantage is the advanced and expensive fabrication techniques need to be used for production. For these reasons, 3D sensors are selected for the innermost part of ITk while the outer layers, where the radiation level is lower, are based on planar sensors.

7.3 Leakage current

When the sensors are reversely biased small leakage currents usually arise. Such currents are created by the thermally produced electron-hole pairs in the silicon. The leakage current depends on the volume V and the temperature dependent density $n_i(T)$ of charge carriers with charge e in the silicon;

$$I_{leak} = \frac{en_i(T)V}{2\tau} \tag{7.1}$$

where τ is the life time for recombination of the charge carriers, which leads to a decrement of the leakage current. The charge carrier density in the above equation can be estimated using the Fermi-Dirac statistics, resulting in:

$$I_{leak} =\propto T^{\frac{3}{2}} \cdot e^{-\frac{E_G}{2k_B T}} \tag{7.2}$$

where E_G is the energy gap that separates the conduction band from the valence band in the semiconductor and k_B is the Boltzmann constant. As shown from equation 7.2 the leakage current is highly temperature dependent, with an increment in temperature of about 7°C leading to double amount of leakage current.

The leakage current is considered as a source of noise, since it doesn't reflect any real

incoming particle interacting with the lattice. The influence of this contribution is usually negligible when considering un-irradiated silicon sensors. However, as explained in 7.4, radiation damages can cause a large increment of the leakage current. In this case the leakage current can become a significant noise source.

Equations 7.1 and 7.2 are defined for a given bias voltage. For a certain value of the bias voltage an uncontrolled avalanche may start, rising drastically the current and leading to the breakdown of the sensor. The bias voltage at which this phenomenon is observed is called the break-down voltage. The operational bias voltage is usually chosen carefully to be far from the break-down voltage and at the same time be sufficient to cause full depletion of the sensor.

7.4 Radiation damage

The sensor properties may change when non-ionizing interactions of traversing particles with the silicon atoms occur. The majority of such changes cause degradation of the sensor performance. In the case where the incoming particle has significant energy to displace a silicon atom in between the regular lattice locations an interstitial defect is formed. The hole left in the lattice is called a vacancy. A vacancy and a neighboring interstitial site in interaction, form what is called a Frenkel defect pair. Interstitial, vacancies and Frenkel defects are referred to as point defects. In the case where enough energy was transferred, the recoiled atom might produce further damage and cluster defects (a combination of multiple point defects) are formed. Defects with energy levels close to the middle of the band gap act as generation centers increasing the amount of thermally generated charge carriers, consequently influencing the leakage current. The increased leakage current constitutes noise for the readout electronics but more importantly can cause a thermal runaway. The last effect consists of the irradiated sensor heating up from resistive heating due to the increased leakage current. Other macroscopic consequences of radiation on the silicon sensor are the change of the effective doping concentration as well as the reduced charge collection; the displacement of atoms from the lattice structure decreases the effective concentration of donors N_D and at the same time the fact that these damages act as acceptors increase the acceptor concentration N_A. The effective doping concentration $Neff = N_D - N_A$, which is positive for n-type silicon, will change sign after a significant radiation damage, causing type inversion from n-type to p-type silicon. For this reason n-type silicon sensors are usually considered as less radiation hard. Moreover, changes in the effective space charge concentration affect the bias voltage needed for full depletion. The depletion voltage increases with irradiation, leading to larger power dissipation. Finally, the radiation-induced defects are able to capture the charge carriers that are drifting to the signal electrodes, causing a reduced charge collection efficiency.

The radiation damages described above depend on the incoming particles. Therefore, it is necessary to scale the radiation damage caused by Non-Ionizing Energy Loss (NIEL) to a standard irradiation in order to compare the damage caused by different particles. The usual scaling used is the damage caused by a fluence of 1 MeV neutrons.

7.4.1 Annealing

An interesting phenomenon observed after irradiation is the so-called annealing. This mainly describes the repair of lattice defects caused by irradiation, with the rate of the healing being highly temperature dependent. This type of annealing is usually referred to as "beneficial" annealing and has typically a short time scale. A second type of an annealing effect is the "reverse" annealing; this actually causes the damage to increase and has a much longer time

scale. The annealing occurs faster at higher temperatures while it can be paused at low temperatures. Therefore, irradiated sensors are usually operated at low temperatures (of about 40C) in order to avoid reverse annealing.

7.5 ITk module specifications

In order to maintain its excellent performance during the HL-LHC upgrade already introduced in 3, the ITk requires [94]:

- efficiency in the innermost layer with particle fluence up to $1.3 \times 10^{16} n_{eq}/cm^2$ and 900 Mrad for the pixel detector and up to $1.6 \times 10^{15} n_{eq}/cm^2$ and 66 Mrad for the strip detector.
- thin sensors of 100-150 μm as low material budget would reduce multiple scattering and energy losses, improving the tracking performance
- fast and reliable readout electronics to cope with high pile-up of 200 collisions per bunch crossing.
- high hit efficiency of 97% after irradiation.
- high granularity with excellent vertex and track position resolution to deal with the high particle rates and pile-up.

The baseline module concept for the ITk pixel detector is the hybrid pixel detector discussed above, in which modules are composed of a sensor and the front-end chip bump-bonded to each other on a pixel level. In addition to this, a flex PCB hybrid glued to the back face of the silicon sensor and wire bonded to the modules is used in order to route all the connections[3] to the front-end chips and the sensor [94]. Two main types of hybrid modules are considered: the triplet modules, which correspond to three front-end chips bump bonded to a single 2×2 cm^2 sensor, and the quad modules, which correspond to four front-end chips bump bonded to a single 4×4 cm^2 sensor. The planar modules will be used in the quad configuration. The front-end chip, called ITkPix, was designed by the RD53 collaboration composed by ATLAS and CMS scientists. A first version of the chip, RD53A, was also developed and extensively tested before the final version was decided. The majority of measurements presented in this thesis, were performed with RD53A. The two versions of the chip are briefly discussed in the following subsections.

Within the 5 pixel layers of the pixel detector shown in Figure 7.1, the pixel pitch is chosen to be 50×50 μm^2 for the planar layers 1-4, and 25 ×100 μm^2 for the innermost 3D pixel layer. The sensor thickness is chosen to be 100 μm for layers 0 and 1, and 150 μm for layers 2-4.

7.5.1 RD53A

The RD53A [95] readout chip was developed using 65 nm CMOS technology and measures 20 mm×11.6 mm. With a 50×50 μm^2 pitch size, RD53A has an active area holding 400 columns with 192 pixels each. This is half of the size aimed for ITkPix, which is approximately 20mm×20mm with 400×384 pixels. The readout electronics usually consist of an analog part to amplify and shape the signal and a digital data processing logic. In order to be able to evaluate different readout designs in a single production, the chip contains three different analog frontend circuits designed to meet all the requirements needed for the high luminocity LHC,

[3] such as clock, command input, data output, low voltage and high voltage power

such as radiation tolerance in the harder radiation conditions, high hit rate, and stable operation at low thresholds. The three chip designs are usually referred to as: the synchronous (SYNC), the linear (LIN) and the differential (DIFF) analog front-end.

All three front-ends use as basic units a charge-sensitive amplifier (CSA) and a time-over-threshold counter. The SYNC and LIN use a Krummenacher circuit to discharge the feedback capacitance, while the DIFF uses a simple MOS in the feedback [96]. Moreover, the DIFF front-end uses a differential gain stage in front of the discriminator and implements a threshold by unbalancing two branches. Both the LIN and DIFF front-ends have a time-continuous discriminator, with a per-pixel trimming DAC for threshold tuning, while the SYNC has a synchronous discriminator and is using an auto-zeroing technique, consisting in a periodic acquisition of the baseline. In addition, a calibrated charge injection circuitry is available for all front-ends for testing purposes.

7.5.2 ITkPixV1

The ITkPixV1 or RD53B is the second version of the chip, specifically made for each experiment. It measures 20.7mm×20 mm with 50×50 μm^2 pixels arranged in 382 columns and 400 rows. For the ATLAS pixel modules the differential front-end has been chosen, therefore ITkPixV1 uses the DIFF readout. The new version of the chip has a very similar design to RD53A, and is used for the first batch of the ITk pixel modules production. After testing the first production batch, a final version of the chip will be developed, ITkPixV2, which will be used in the final module production for the ITk pixel detector.

7.5.3 Hybrid module assembly

As already introduced in section 7.5, a hybrid Itk module consists of three main components; a sensor, a readout chip bump-bonded to the sensor and a PCB glued to the hybrid module as shown in Figure 7.5.

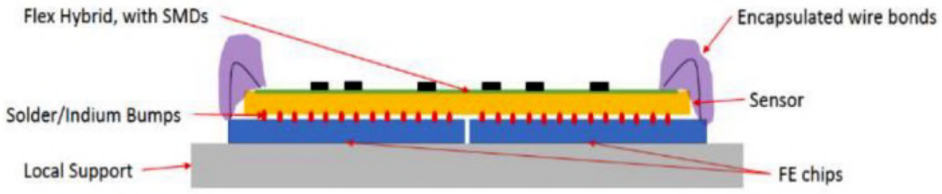

FIGURE 7.5: Schematic view of a hybrid quad module.

The bump-bonding is realized in industry while the PCB attach is performed manually using dedicated tooling specifically developed and tested for this purpose. The glue used for the PCB attach in carefully chosen in order to be radiation hard as well as, as robust against environmental influences and thermal stress as possible. To reduce material budget and gain flexibility in the detector, the PCB is a thin double sided flexible printed circuit called "flex", or "flex PCB". The accurate positioning and attachment of the hybrid module to the flex is of paramount importance for the next step to be realized; this includes the wire bonding that forms the electrical connections between the readout chip and the PCB. Through the wire bonds all possible connections to the chip, low voltage powering as well as high voltage supply (for the sensor) are realized.

8. Quality control of modules

After the module assembly described in 7.5.3, a series of quality control tests are performed in order to ensure uniformly high quality of all modules produced and spot any possible damage done during transfer or assembly. Quality control tests include visual inspection of the module, for damaged components or wire bonds, as well as a number of tests such as sensor current-voltage (IV) measurements, electrical tests of chip functionality and radioactive source tests for bump bond quality. In this chapter I am focusing on the electrical tests regarding the characterization of the front-end chip. First results for the prototype chip, RD53A, are presented in 8.1. Following, results for the first quad module assembled, are discussed in section 8.2

8.1 Electrical tests of the RD53A prototype

8.1.1 Setup

Readout board

For the characterization of the RD53A prototype, the YARR [97] data acquisition system (DAQ), developed by the Lawrence Berkeley National Laboratory in Berkeley, is used. The communication to the RD53A chip is established through an FMC adapter card equipped with four mini-display ports. The FMC adapter card is mounted on a commercial PCIe[1] FPGA card (like the Trenz TEF-100) installed in the host pc. In contract with the traditional processing usually performed in FPGAs, the YARR system allows for data processing in software, which relaxes the dependency on the used hardware. In this configuration, the FPGA has a simple firmware implementing only a basic buffer for commands and data, while all of the scans and analysis are implemented in the software on the host PC. Moreover, YARR is optimized for multi-threaded processing, allowing data processing to occur in parallel, which greatly improves the performance of the system. The YARR board is shown in Figure 8.1.

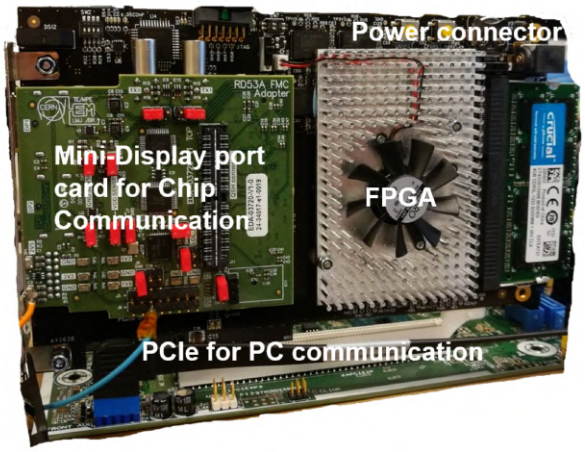

FIGURE 8.1: The YARR readout board with the most important components labelled [98]

[1]Peripheral Component Interconnect Express

Single Chip Card

The single chip card (SCC) is a printed circuit board carrying a single RD53A chip located in the center of the board as shown in Figure 9.2. On the bottom part of the SCC the connectors that are used in order to supply the low voltage (LV) for powering the readout chip and the data acquisition (DAQ) communication are visible. An indication for the temperature of the module can be obtained through the negative temperature coefficient thermistor (NTC) which is located next to the module. In addition the SCCs feature a set of jumpers that, amongst other things, can be used to choose between powering options (direct powering, or powering through the LDO with or without the integrated shunt capability[2]) and to set some of the RD53A trim bits. The SCC board is shown in Figure 8.2.

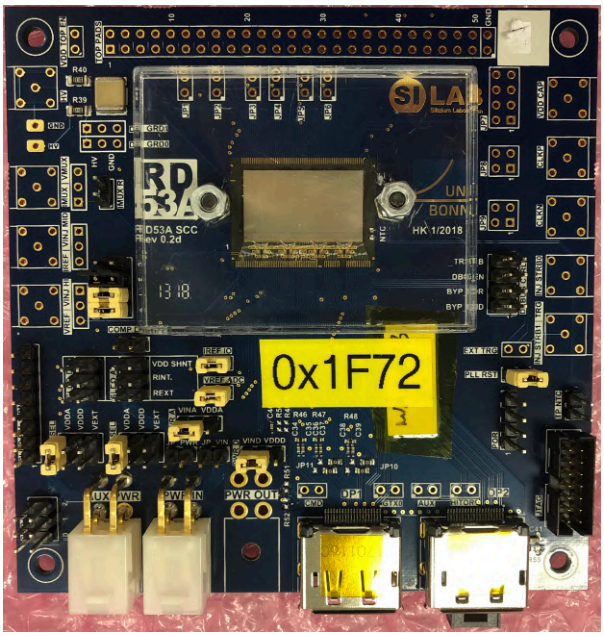

FIGURE 8.2: The RD53A single chip card.

8.1.2 Pixel matrix performance

Every readout pixel of the RD53A frontend chip has its own analog and digital circuitry as well as a calibrated charge injection circuitry allowing individual charge deposition through an injection capacitor. The characterization of the pixel matrix is performed using the charge injection circuitry. Dedicated tuning procedures and scans have been developed in order to tune and measure the performance of the pixel matrix. The most important scans include; analog, digital and threshold tests and are briefly discussed in the following subsections.

The tuning of the pixel matrix is also of paramount importance. When a signal pulse with amplitude higher than the threshold of the discriminator passes, the time over threshold (ToT) is measured. The ToT value gives direct information of the charge deposited in the sensor and though the energy of the initial particle. For this reason, a uniform ToT pixel matrix response is ensuring a good detector performance. Due to process variations, the pixel matrix does not have, in general, a uniform response, which makes recorded data not-exploitable. Figure 8.3 shows the threshold distribution of an un-tuned RD53A chip. The width of a gaussian fit to the threshold distribution is about 217e. A similar result for the TOT response to test charge injections of 10 ke is plotted in Figure 8.4. A large dispersion of the ToT values is also noticed. In addition, even for an initially uniform pixel matrix response, the exposition of the

[2]discussed in more detail in 9.1.1

chip to radiation will create un-uniformities along the matrix. Hence, a constant adjustment of the pixel response, called tuning, is necessary. The tuning procedure is briefly introduced in subsection 8.1.6

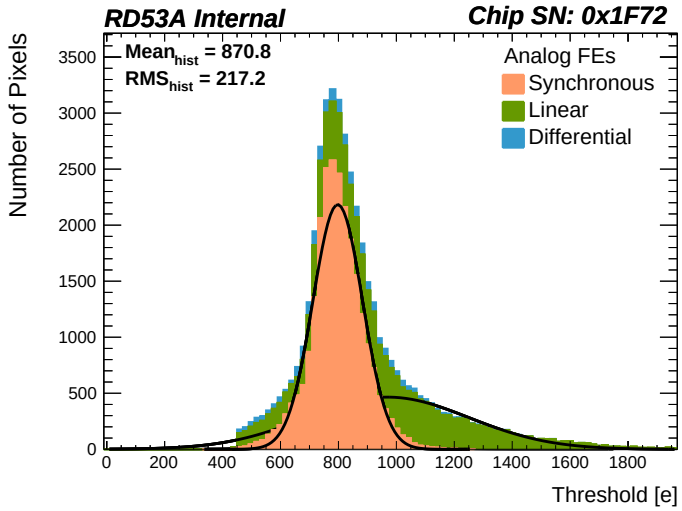

FIGURE 8.3: Untuned threshold distribution of an RD53A chip. The three front-ends are plotted in different colors. The printed mean and RMS values correspond to the combined distribution.

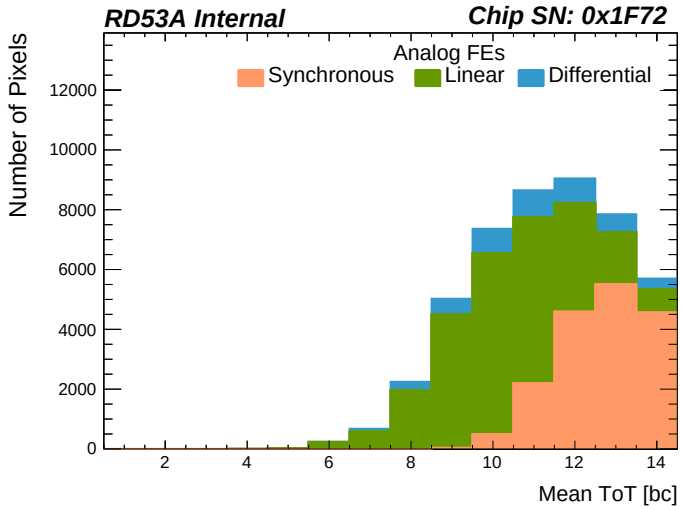

FIGURE 8.4: Untuned ToT distribution of an RD53A chip. The three front-ends are plotted in different colors. The ToT is measured in values of bunch crossings (25 ns)

8.1.3 Analog scan

A first functionality test is the injection of a test charge to each pixel. The injection is performed N times and the occupancy per pixel is recorded. The output occupancy map is plotted in Figure 8.5. A number of 100 injections at an input charge of 10ke has been performed to all pixels. The majority of pixels have been responded 100 times as expected. A few pixels in the DIFF front-end are problematic and have an occupancy close to zero. A significant amount of pixels have also fired more than 100 times. These correspond to noisy pixels, or cross-talk effects between pixels.

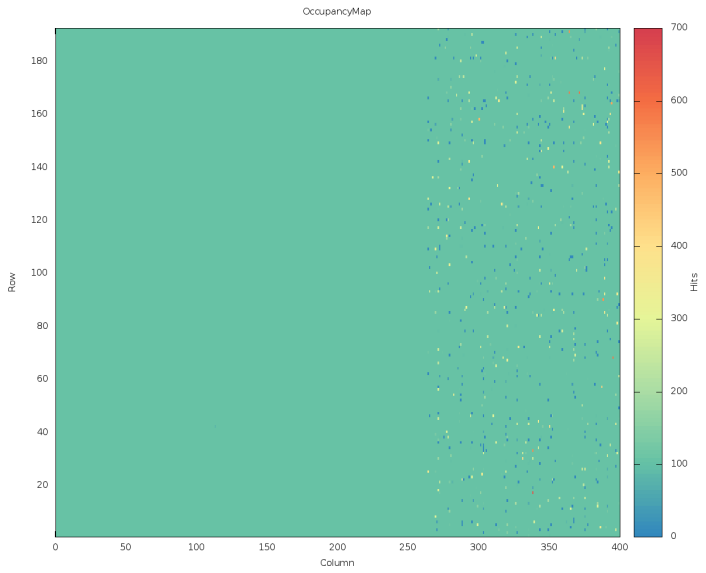

FIGURE 8.5: Occupancy map of the RD53A pixel matrix when performing an analog scan.

8.1.4 Digital scan

To disentangle errors in the analog circuit from errors in the digital one, digital scans are performed. In the digital scan a number of digital hits is injected after the discriminator stage to simulate the discriminator?s output. If all the logic units are functioning correctly the same number of hits should be recorded in the output. The result of a digital scan is plotted in Figure 8.6. A number of 100 injections has been performed. All pixels responded with an occupancy of 100.

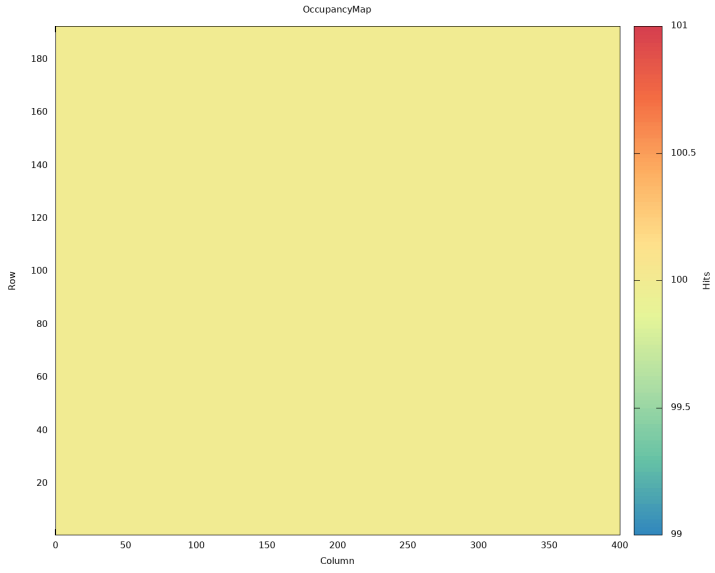

FIGURE 8.6: Occupancy map of the RD53A pixel matrix when performing a digital scan.

8.1.5 Threshold scan

A threshold scan measures the occupancy of the pixel at different injected charges. The injected charge value, which results to a 50% efficiency of the pixel, is then indicated as the mean threshold. The response curve of Figure 8.7 may be fitted with a sigmoid curve (S-Curve), where the slope is a characteristic of the leakage current, sensor capacitance and electronic

(FE) noise. The number of electrons in the efficiency region of 30% to 70%, is therefore, used in order to describe the noise. Ideally, in the absence of noise, this S-curve would have a shape of a step function.

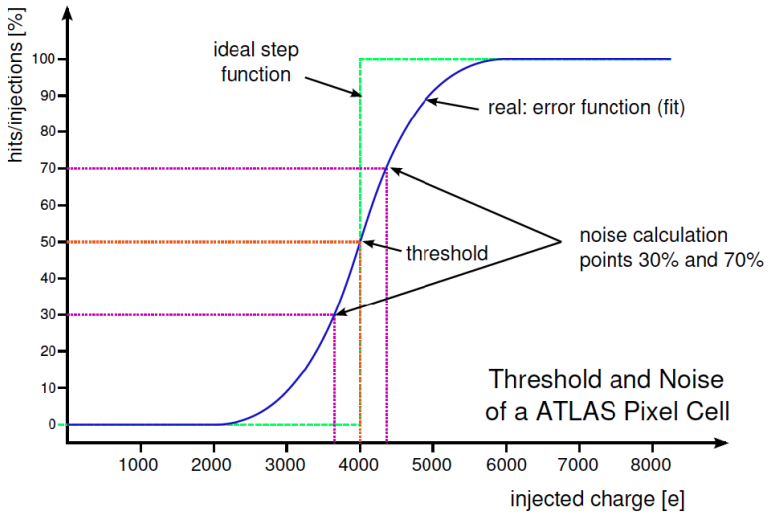

FIGURE 8.7: Example of an S-curve for a pixel cell tuned to 4ke [99].

8.1.6 Pixel tuning

The pixel threshold consists of a global component, which is constant for all pixels, and a local component, which can be adjusted for each pixel individually. The global threshold is adjustable for all three front-ends (SYN, LIN and DIFF) while the local threshold tuning is available only for the LIN and DIFF front-ends. The absence of local tuning for the SYN front-end is due to its preamplifier design which uses a so called auto zeroing process to compensate for local threshold variations. The global and local threshold values are controlled through dedicated registers (DACs) which are different for each front-end design.

Per-pixel threshold adjustment is performed using the charge injection circuit. First, the global threshold is set for all pixels to the desired value. Following, a charge equal to the desired threshold value is injected into the preamplifier of the front-end chip N times. Then triggers are sent to all pixels and the per pixel occupancy is estimated. If a pixel has an occupancy much lower than 50%, its threshold is decreased (by adjusting the relevant DAC registers), while it is increased in the case where the occupancy is found to be higher than 50%. The procedure is repeated probing each time small subsets of the pixel matrix. The final DAC values achieved at the end of this procedure are chosen as the tuning settings.

The ToT response of the pixel matrix to a given injection charge is also adjustable through a dedicated register. The tuning procedure is usually an iterative process of threshold and ToT adjustments since they both influence each other. The Itk pixel modules are tuned to a threshold of 1000e and a ToT of 8 for an injected charge of 10ke. The 10ke charge corresponds to the most probable charge generated by a MIP in the sensor. The choice of the threshold setting is an interplay between the need to achieve a high hit detection efficiency, and low noise occupancy. In a similar way, the ToT value should also be chosen in a way that allows the resolution of small hits, due to charge sharing with neighboring pixels, but also keeping the possibility of detecting larger deposited charges.

The ToT and threshold tunings are performed separately for the three front-ends. A threshold and ToT scans are performed after tuning in order to check the quality of tuning. In the ToT scan a test charge of 10 ke is injected in every pixel and the time over threshold is measured. The threshold, noise and ToT distributions after tuning are plotted in Figure 8.8.

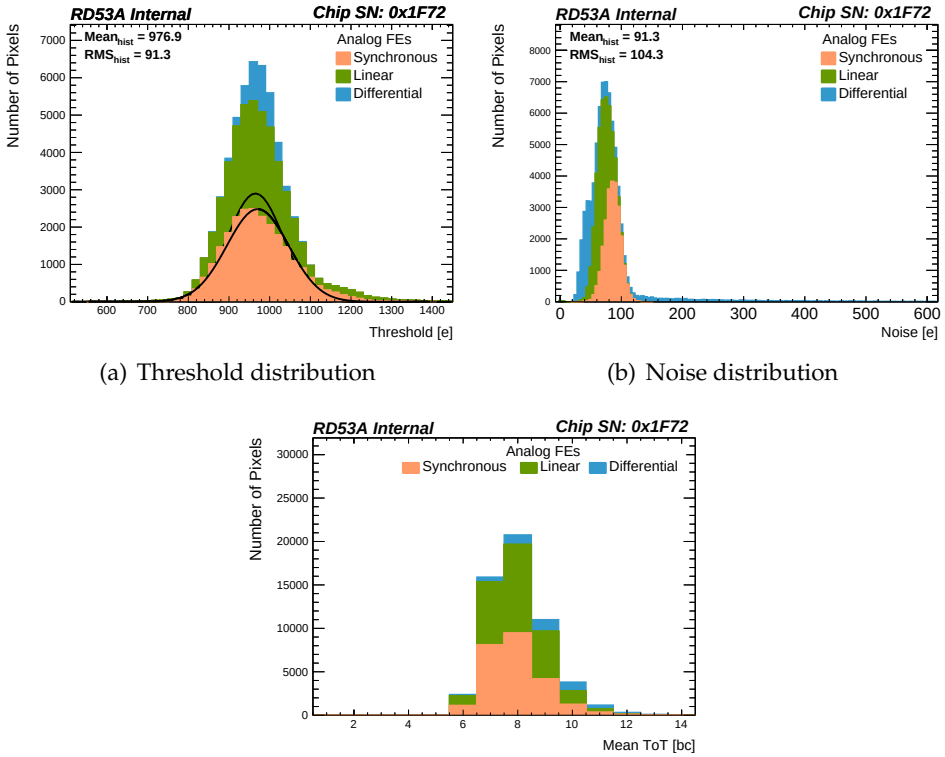

(a) Threshold distribution

(b) Noise distribution

(c) ToT distribution

FIGURE 8.8: Threshold, Noise and ToT distributions for a tuned RD53A chip. The three front-ends are plotted in different colors.

8.1.7 Noise occupancy

In the noise occupancy scan random triggers are sent to the pixel matrix without injecting any charge and the occupancy is measured. Any hits recorded correspond to noisy pixels. The noise occupancy is required to be less than $10^{?6}$ for the ATLAS pixel detector. Pixels with higher occupancy numbers, are identified as noisy and a mask is applied in order to remove them. In Figure 8.9 the noise occupancy for 10^6 sent triggers is plotted. A large number of pixels in the DIFF front-end recorded hits. This is due to a known timing issue in the analog cores of the DIFF front-end which results to large number of the DIFF pixels to be in particular noisy. This effect is not present in future versions of the chip.

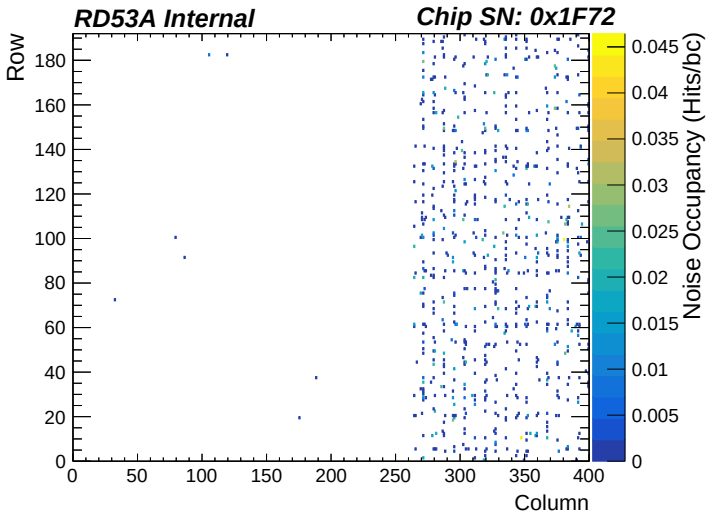

FIGURE 8.9: Noise occupancy map of the RD53A pixel matrix.

8.2 Electrical tests of quad module

8.2.1 Visual Inpection

After the module assembly described in 7.5.3, a visual inspection of the module is performed in order to spot any possible damages or missing/damaged wirebonds. The visual inspection is done using a Keyence VHX-7000 series digital microscope. In Figure 8.10 the assembled module and zoom in images of the wirebonds are shown. No problematic wirebonds were spotted.

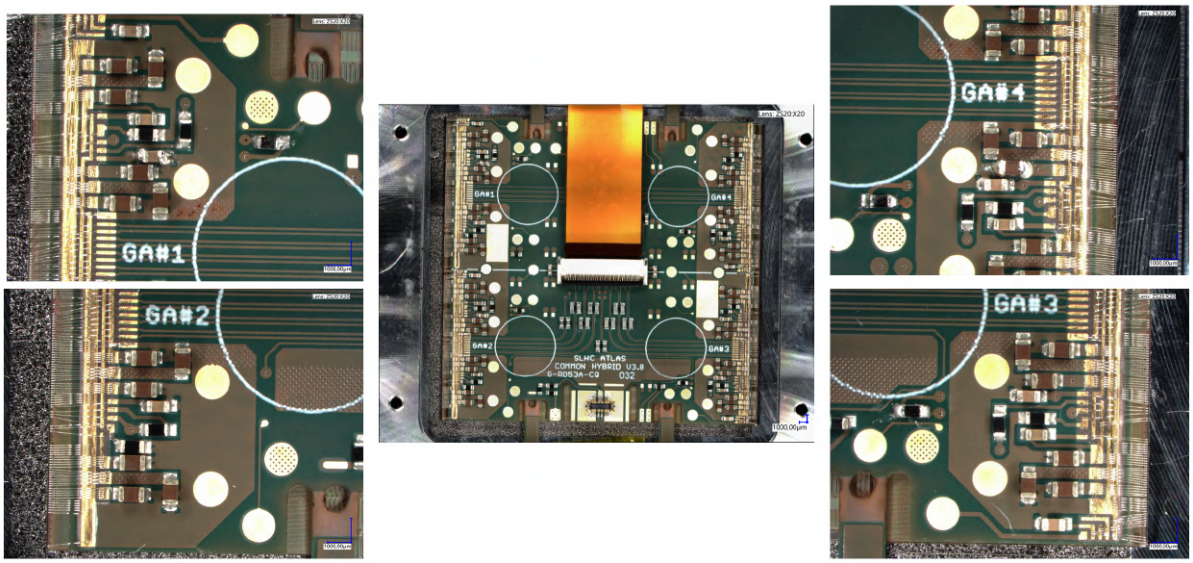

FIGURE 8.10: Visual inspection of quad module.

8.2.2 Trimming chip references

There are two internal voltage rails for powering the chip core, analog (VDDA) and digital (VDDD). Special voltage regulators called Shunt-LDOs are used in order to generate these voltages independently of the external supply voltage. The chip requires a voltage of 1.2V applied to both the analog and digital circuits in order to operate optimally. Due to process variations, the regulated voltages are not always generated at the desired value of 1.2V. However, they can be adjusted by trimming the regulator reference voltages. This can be achieved through dedicated DAC registers.

The trimming results for the quad module are shown in Table 8.12. In order for the regulators to generate the internal voltages VDDA and VDDD, a sufficient supply voltage of about 1.53V should be supplied. Then, the generated VDDA(D) value can be trimmed by changing the corresponding DAC register and probing the generated output voltage on the chip. The DAC settings are written to the chips through software. The probe points on the chip are summarized in Figure 8.12

8.2.3 Setup

The setup used for the electrical tests of the RD53A quad modules is shown in Figure 8.13. The low voltage (LV) supply to the chips is done through a programmable HMP4040 power supply. The chips are designed for serial powering operation, therefore are configured to run in Shunt-LDO mode. This means that a constant current should be supplied; each chip needs approximately 1.1A (separately for analog and digital rails) in order to generate the

			VDDA (V)			VDDD (V)		
Chip	Chip SN	Vin (V)	Default	Trimmed	DAC	Default	Trimmed	DAC
GA 1	0x7237	1.530	1.200	1.199	16	1.172	1.208	21
GA 2	0x7239	1.530	1.180	1.207	19	1.072	1.207	28
GA 3	0x7243	1.532	1.167	1.214	20	1.129	1.251	27
GA 4	0x723B	1.531	1.159	1.212	21	1.079	1.218	28

FIGURE 8.11: Trimming of chip references.

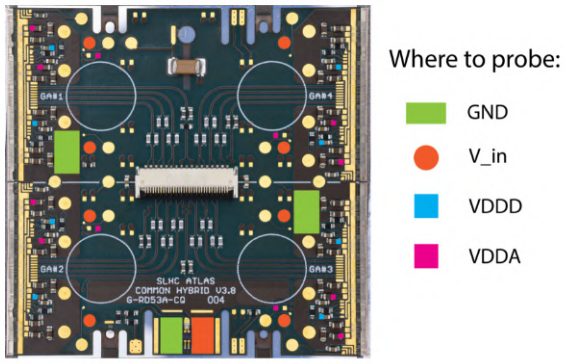

FIGURE 8.12

necessary regulated voltages. Since a current supply is not available, a low voltage supply is used instead, configured to run in a constant current mode (by hitting compliance). The current supplied to the module is 4.4A. The module is connected to the readout board through an adapter card as shown in Figure 8.13(b). The readout board is integrated in the host PC. The Yarr DAQ system is used. The temperature of the module is continuously monitored through an arduino board by measuring the resistance of the NTC thermistor, located near to one of the chips, and converting the resistance to a temperature reading.

8.2.4 Pixel matrix performance

The tests described in 8.1 are repeated for all four chips of the quad module. The chips were tuned to a target threshold of 1000 e and ToT of 7 at 10ke injection charge. The results of the analog, digital and threshold scans after tuning are discussed in the following subsections.

8.2.5 Analog scans

A charge of 10 ke is injected to all pixels of each of the 4 chips, 100 times. The output occupancy maps are plotted in Figure 8.14 . The majority of pixels recorded 100 hits. A few very noisy pixels are spotted in particular for chips GA1 and GA2.

8.2.6 Digital scans

A number of 500 injections is performed to all pixels through the digital injection circuit. The output occupancy maps are plotted in Figure 8.15. The maps are uniform around an occupancy of 500 with very few pixels firing to higher values.

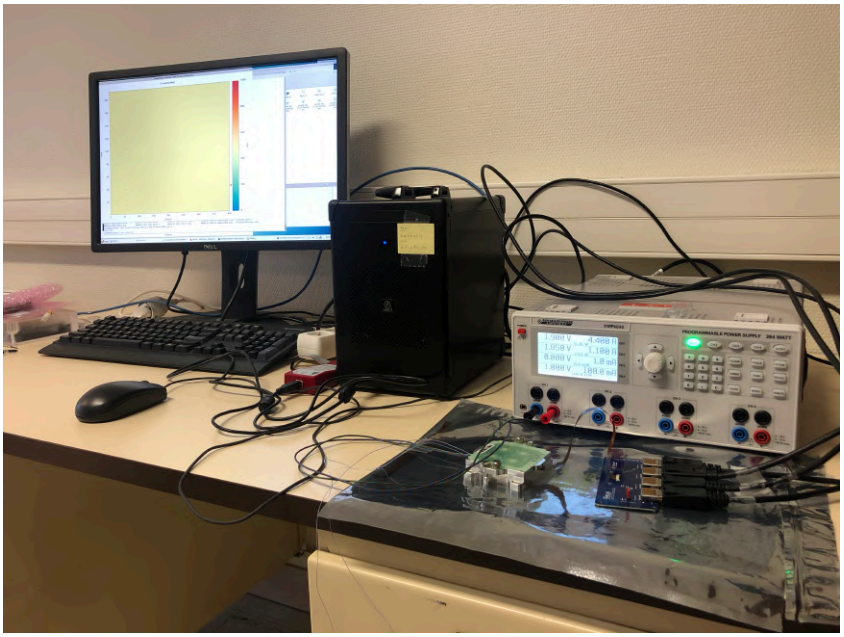

(a)

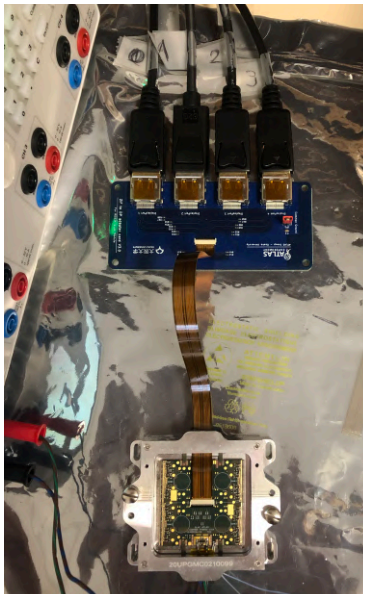

(b)

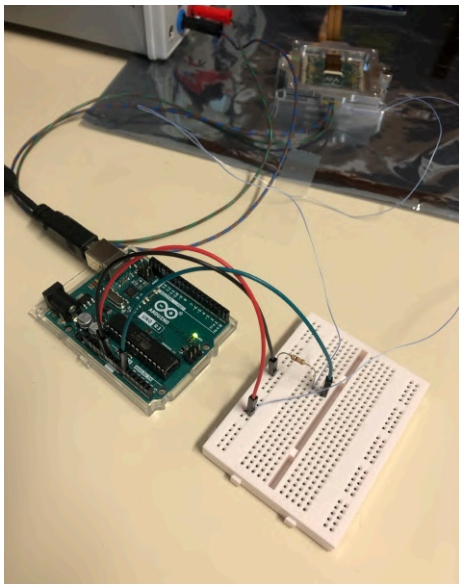

(c)

FIGURE 8.13: Setup for quad module testing

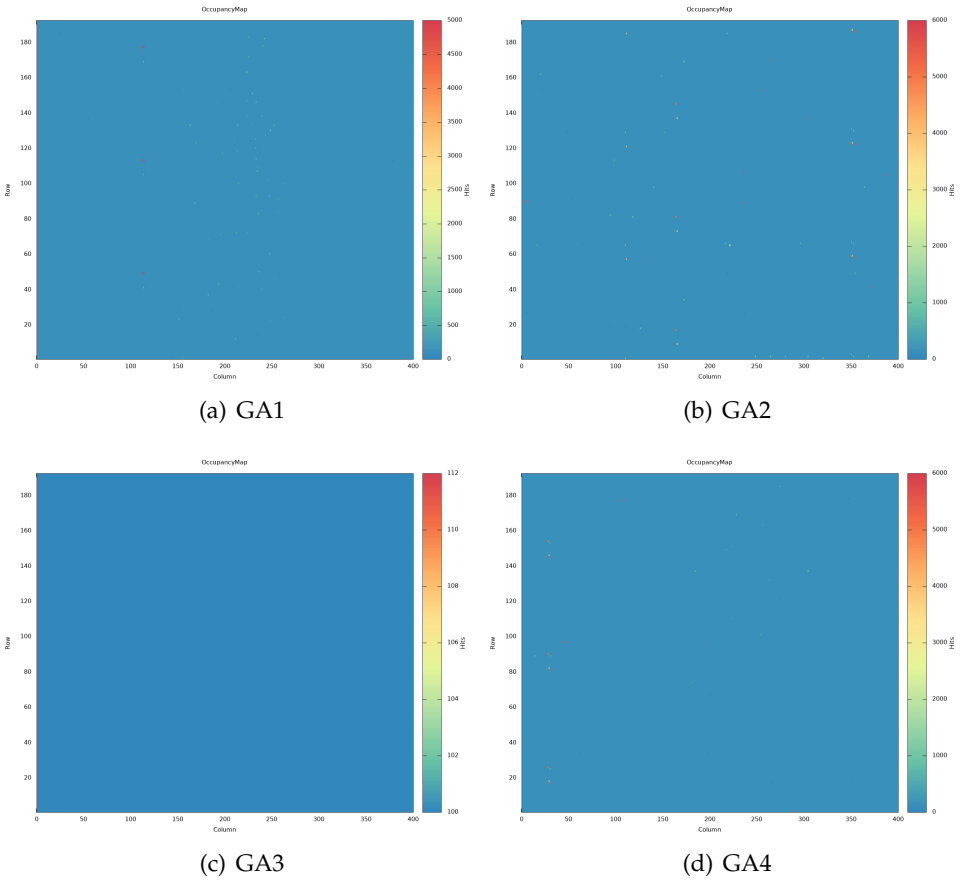

(a) GA1 (b) GA2

(c) GA3 (d) GA4

FIGURE 8.14: Analog scans for the RD53A quad module

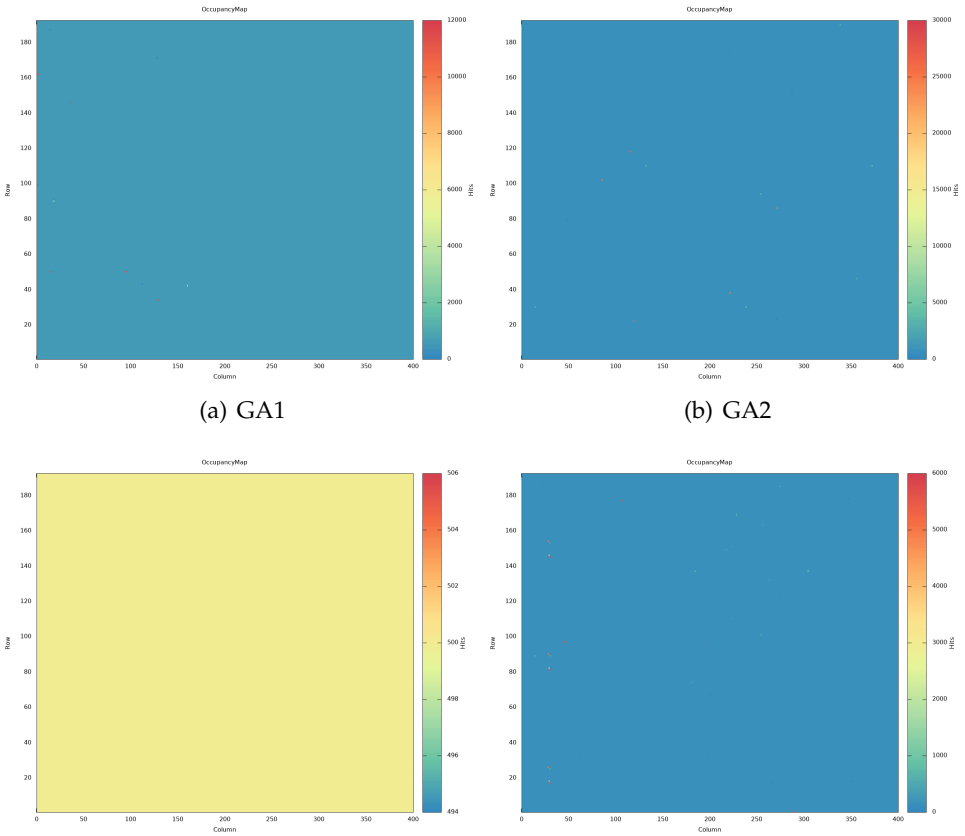

(a) GA1 (b) GA2

(c) GA3 (d) GA4

FIGURE 8.15: Digital scans for the RD53A quad module

8.2.7 Threshold and ToT scans

Threshold and ToT scans are performed after the chips are tuned to a threshold of 1000 e and ToT of 7 at 10ke injection charge. The threshold and ToT distributions are plotted in Figures 8.16 and 8.17 respectively. All chips were successfully tuned to the desired threshold and ToT values, with in general small dispersion from the mean values. The secondary peak seen in the threshold distribution of chip GA2 correspond to the SYN front-end, as shown in the threshold map of Figure 8.18.

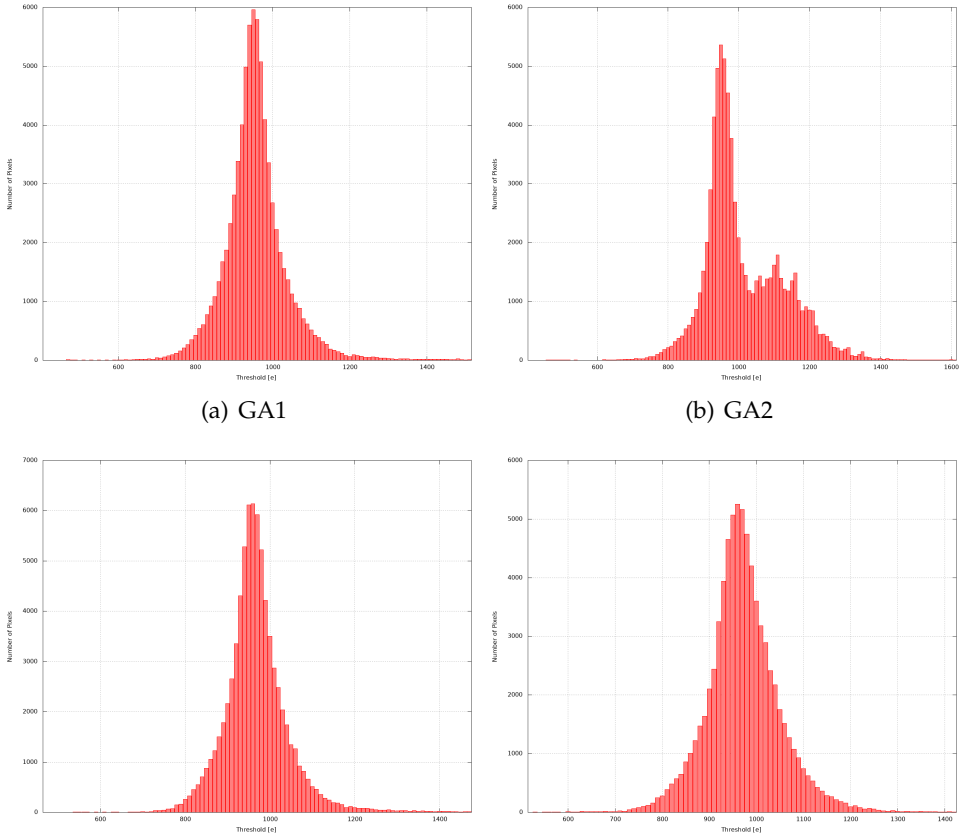

(a) GA1 (b) GA2

(c) GA3 (d) GA4

FIGURE 8.16: Threshold scans for the RD53A quad module

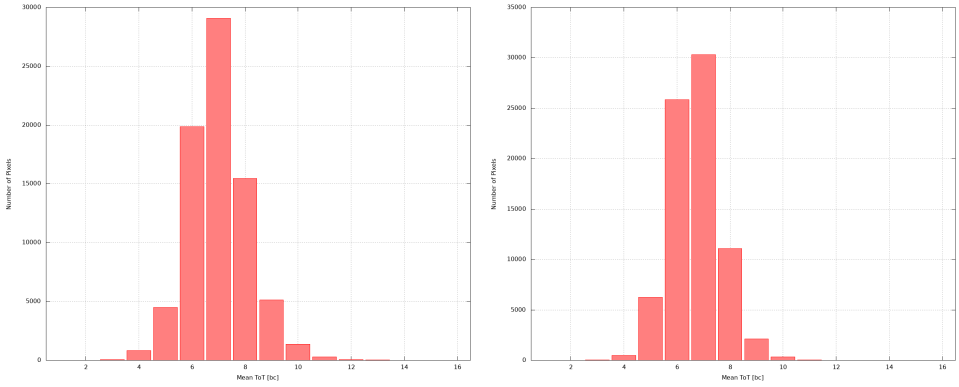

(a) GA1 (b) GA2

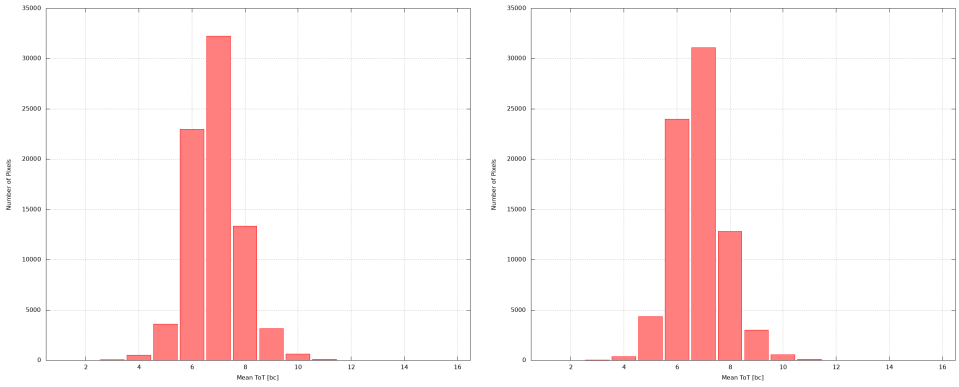

(c) GA3 (d) GA4

FIGURE 8.17: ToT scans for the RD53A quad module

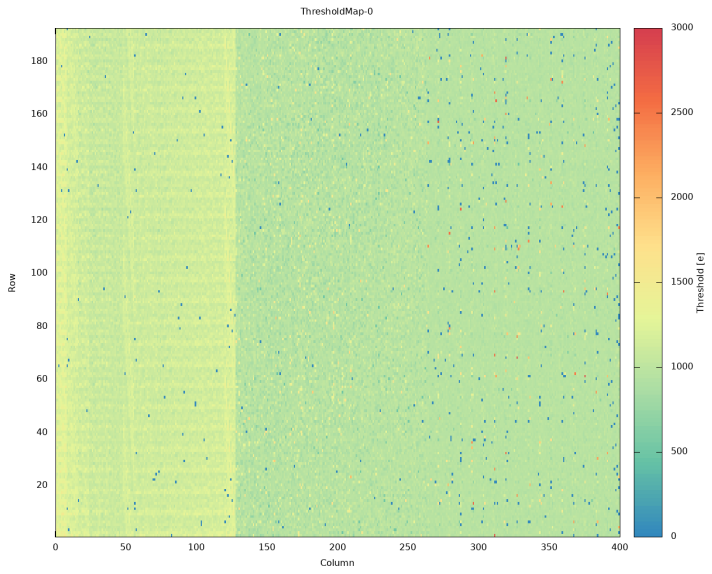

FIGURE 8.18: Threshold map after tuning for GA2 chip

9. Serial powering chain of irradiated RD53A modules

The much larger number of modules and the much finer granularity used by the ITk pixel detector with respect to the current pixel detector, results in a significant increase in the power density. For this reason a serial powering (SP) scheme has been chosen for the ITk pixel detector. In this scheme, the readout chips of the pixel modules are powered in series by a constant current; the sensors of several modules on the other hand will be connected in parallel to a common supply line for the depletion high voltage. In combination with the ITk grounding requirements and the properties of most commercially available power supplies this architecture results in an effective forward bias on some sensors under certain operating conditions. Although the forward bias will be small, it can still lead to non negligible currents between the sensor backside and the readout chip, in particular for irradiated sensors with large saturation currents. In this chapter, the behavior of such a serial powering chain is studied.

9.1 Serial powering in ITk

The ITk pixel detector design features a much higher active area of about $13\,\mathrm{m}^2$, roughly six times the active area of the current pixel detector, while the number of pixels is increased by a factor of 60. The increased granularity results in a higher current consumption by the module while the much larger active area requires the increase in the number of such modules to be used. A conventional, parallel powering scheme without point-of-load DC-DC conversion for the ITk detector would hence result in unacceptably large power losses on the electrical services (about 75% of the entire detector power) or unaccetably thick power cables (more than ten times the amount of copper that can reasonably be installed in the ITk pixel detector). Point-of-load DC-DC conversion has been ruled out due to space constraints in the service channels of the detector, such that a serial powering scheme [100, 101, 102] has been chosen for the ITk Pixel Detector.

The basic building blocks of a serial powering chain are power units. In the four outermost layers of the ITk pixel detector, a power unit is equivalent to a quad module already introduced in 7.5, while in the innermost layer a power unit is a triplet module. The three or four readout chips on one such unit are powered in parallel, i.e. they share a common input voltage and a common local ground. In the ITk serial powering scheme, between 3 and 14 such power units are connected in series, powered by a constant supply current. An immediate consequence of such a powering scheme is that the modules in the chain must have an independent on-chip voltage regulation, capable of powering the chip while taking constant current from the supply. This regulator, referred to as Shunt Low-Dropout Regulator (SLDO), is discussed in the following sub section.

9.1.1 Shunt low-dropout regulator

In order to be able to generate the necessary voltages (VDDA for analog and VDDD for digital) to power the chip irrespective of changes to the supply current or load conditions, RD53A is equipped with a shunt low-dropout regulator (SLDO) [95, 103]. The SLDO regulator is a combination of a low-drop linear voltage regulator (LDO) and a shunt regulator. Every chip has two independent such SLDO regulators, one for the digital and one for the analog domain of the chip. A simplified circuit of the SLDO regulator is shown in Figure 9.1. The

LDO regulator part is formed by the error amplifier A1, the PMOS pass transistor M1 and the voltage divider formed by the resistors R1 and R2 [95]. The LDO provides a constant regulated voltage VDD while the shunt regulator drains any excess of current not drawn by the load connected to VDD. The last is achieved with the help of the shunt transistor M4 which is added to provide an additional current path to GND: it is controlled to drain all the current which is not drawn by the load. For this purpose the current flow through transistor M1 is compared with a reference current which is defined by use of the external resistor R_{ext}, amplifier A4 and transistor M7. The reference current is given by:

$$I_{ref} = \frac{V_{IN} - V_{OFS}}{R_{ext}} \tag{9.1}$$

The generated offset voltage is $VOFS = 2I_{OFS}R_{OFS}$, where R_{OFS} is the external resistor connected to the I_{OFS} pin.

Thanks to the SLDO design, extra currents created by single point failures in the chain are shunted. The SLDO is able to shunt currents about twice the required by the chip. The regulator behaves as an ohmic load to the power supply with the impedance being constant in time and for a particular supply current. The impedance value can be set by the external resistor R_{ext}.

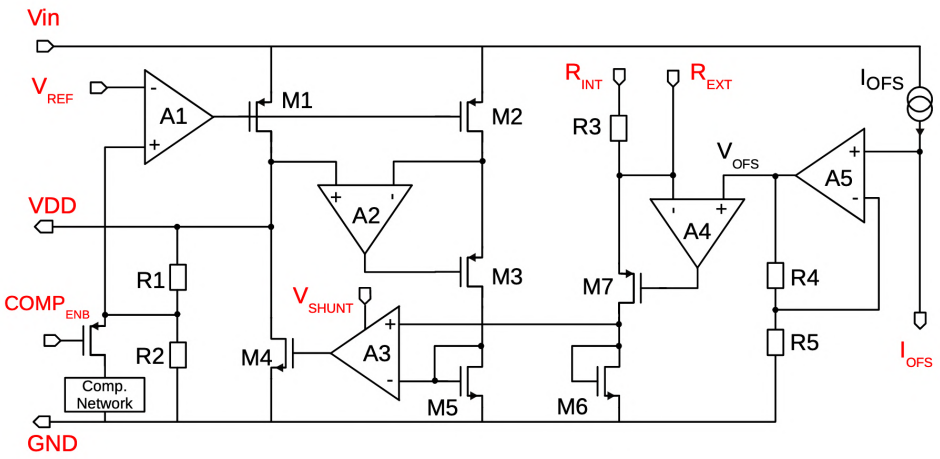

FIGURE 9.1: Schematic of Shunt-LDO regulator [104]

9.1.2 High voltage distribution design

In the outer layers (Layer 1 to Layer 4) of ITk, the high voltage (HV) supply, providing the bias to the sensors, will be connected in parallel to several sensors in the same serial powering chain. Any leakage current is returned through a single HV return line, which is tied to the last module in the chain (the one with the lowest local ground potential in the serial powering chain). A schematic of this architecture is shown in Figure 9.5. The motivation for choosing this particular design is the limited number of HV channels that can reasonably be supplied to and installed in the ITk Pixel Detector. The choice of a common HV return line being tied to the local ground of the last module in the serial powering chain is dictated by the ITk grounding requirements. The innermost layer of ITk Pixel Detector features 3D silicon sensors; these sensors typically have a significantly lower depletion and breakdown voltage than planar sensors. Therefore, a different HV distribution scheme is chosen in the innermost layer; a single HV line is connected to each power unit individually. This is possible due to the small number of power units that will be installed in the innermost layer.

An important consequence of grouping together all modules in a SP chain to one HV power supply, are the different local reference voltages for the sensor bias voltages. Each module in the SP chain has a different local ground, therefore a sensor in the chain that is connected to a common HV line will be exposed to a slightly different effective bias voltage based on its position in the chain. Starting at the module in the serial powering chain with the lowest local ground potential, the effective bias voltage for the sensor in the $i+1$th module will be larger by ΔV compared to the effective bias voltage for the sensor in the ith module. Since the depletion voltage is usually chosen close to the middle of the saturation region of the characteristic sensor I-V curve, therefore far away from the breakdown voltage or the linear region where the sensor is not fully depleted, small ΔV variations in the depletion voltage should not affect the sensor performance.

9.1.3 Potential issue of current HV distribution design

Under certain conditions (for instance while the LHC is being filled with protons), the readout chips in a serial powering may be powered while for safety reasons the sensor bias voltage will be interlocked. The available HV power supplies have a high impedance between HIGH and LOW power ports when switched off. This would mean that the potential on the common HV line will float to a potential between the local ground of the module with the highest local ground potential in the chain and the one with the lowest local ground potential. This will lead to an effective reverse bias voltage on most of the sensors in the serial powering chain. However, for the sensors on modules with the lowest local ground potentials in the chain, it will lead to a forward bias. The forward bias is expected to be small in the case of un-irradiated modules. However, when the modules are irradiated, the leakage current of the sensors can contribute significantly to the forward bias. If the forward bias voltage on the sensor with the lowest local ground potential becomes too high, the total current going through the sensor of this module might damage either the sensor, or the readout chip, or both. In that case, the problem could be mitigated by requiring the HV power supplies to have a low-ohmic off-mode, which however seems to be a costly and special requirement. The effect of such forward bias is studied in the following subsections.

9.2 Setup

9.2.1 RD53A Single Chip Cards

All tests presented in this note have been performed using Single Chip Cards (SCCs). The SCC is a printed circuit board carrying a single RD53A module located in the center of the board as shown in Figure 9.2. On the bottom part of the SCC the connectors that are used in order to supply the low voltage (LV) for powering the readout chip and the data acquisition (DAQ) communication are visible. The high voltage (HV) supply for the sensor is connected through a Lemo connector located on the top left of the SCC. An indication for the temperature of the module can be obtained through the negative temperature coefficient thermistor (NTC) which is located next to the module. The offset and slope values, R_{ext} and R_{OFS}, for the SLDO regulators on the readout chip are set through SMD resistors on the SCC. In addition, the SCCs feature a set of jumpers that, amongst other things, can be used to choose between powering options (direct powering, or powering through the LDO with or without the integrated shunt capability) and to set some of the RD53A trim bits.

Configuration of the Used SCCs

The modules on the available SCCs are first tested standalone in order to ensure good functionality and then in a serial powering chain. For the characterization of the RD53A

chips, the BDAQ53 [105] data acquisition system is used. The jumpers on the SCCs were set for powering in SLDO mode; the slope and offset resistors for all chips were set to the values through the resistors on the SCC (R_{ext}=806 Ohm, R_{iofs}= 250 kOhm for both analog and digital domains of the readout chip). For some chips the output of the analog regulators (VDDA) took much lower values (e.g. <1.09 V) than the nominal 1.2 V, making communication with the chip difficult. In these cases an extra pull-up resistor of 150 kOhm was mounted, increasing VDDA roughly by 0.1 V.

Modifications to the HV Connections on the SCCs

In order to build a serial powering chain with the same HV distribution scheme that will be used in the ITk Pixel Detector, the HV connection configuration on the SCCs had to be changed. The relevant part of the schematics is shown on the left hand side of Figure 9.3. Two resistors are mounted: R_{39}, in between the input depletion voltage (HV_IN) and the sensor back side, and R_{40}, in between the HV return and the chip local ground. By measuring the voltage drop across R_{39} a measurement of the leakage current through the sensors is done. In the ITk Pixel Detector, the value of R_{39} is limited by power and voltage considerations, as a leakage current of several mA per sensor is expected at the end of lifetime. A decision for the value of this resistor on the ITk Pixel modules had not been chosen at the time the presented measurements have been performed. However, a value of $R_{39} = 10$ kOhms has been chosen for the tested modules, which is expected to be close to the final design choice[1]. In addition the resistor R_{40}, which is connecting the chip's local ground to the HV return line, has to be removed due to the fact that all modules in the serial powering chain have a common return line that is tied to the local ground of the module with the lowest local ground potential in the serial powering chain only. On the right hand side of Figure 9.3 the HV path after performing the modifications described above is shown for one SCC. With these modifications, a serial powering chain according to the architecture shown in Figure 9.5 can be built using the available SCCs.

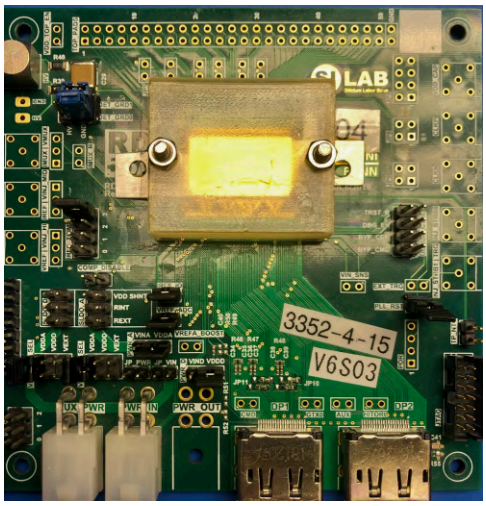

FIGURE 9.2: RD53A SCC with a mounted single chip module

[1]In the meantime, the preliminary choice for the corresponding resistor on the ITk Pixel quad chip modules has been fixed to a value of 5 kOhms; hence the value chosen for the presented tests is reasonably close to the preliminary design value.

9.2.2 Irradiated RD53A SCCs

The RD53A modules that were available for the presented tests have been irradiated with 70 MeV protons up to a total of approximately 2, 5 or $10{\cdot}10^{15}$ n_{eq}/cm^2 (1 MeV neutron equivalent) fluence. These fluences are close to the expected levels at the end of lifetime of the ITk Pixel Detector. Out of the available SCCs, a total of seven cards have been chosen to build the serial powering chain. A summary of the irradiation conditions of the chosen modules is shown in Table 9.1.

Position in Chain	Module ID	NIEL $10^{15} \cdot 1\,\text{MeV}\ n_{eq} cm^{-2}$)
1st	V6S02	1.65
2nd	V3S03	3.33
3rd	V3S11	4.35
4th	V3S02	3.33
5th	V3S01	1.18
6th	V2S11	1.66
7th	V6S03	3.34

TABLE 9.1: Summary of flunces for the modules and the position of the modules used in the serial powering chain. The module with the highest ground potential is considered the first module in the chain.

9.2.3 Serial Powering Chain

For the serial powering chain all the seven modules presented in Table 9.1 were used. The RD53A modules are connected in series through banana to Molex adapters provided by the stands shown in Figure 9.4. The backside of the sensor of each module is connected to a common HV line which is left floating. The choice of leaving the common HV line floating in this setup is a conservative choice compared to the conditions in the experimental cavern, because it will lead to a small increase in the potential that the common HV line will float to; this is due to the fact that in the detector the HV power supply will usually be connected to the common HV line, providing an additional return path for any leakage current to the ITk reference voltage through the HV power supply. However, assuming that the ID pixel HV supply units are representative for the units used in the ITk Pixel Detector, the impact of leaving the HV line floating is negligible - in a system test performed with FE-I4 modules less than 2% of the total induced leakage currents were returned through the HV power supply. The choice of number of modules is motivated by the ITk design where fourteen modules are connected in serial powering with two HV lines per chain (thus seven sensors will share a common HV line). Although, the ITk design features the use of quad chip modules or triplet modules, the expected leakage current per pixel in the last module of the chain is expected to be similar (see section **??**). The assembled setup is shown in Figure 9.4. In order to avoid reverse annealing of the irradiated sensors, the setup is placed in a climate chamber operated constantly at low temperatures.

9.3 Measurements

The measurements were arranged in four main stages. In the first stage the RD53A modules were characterized standalone in order to re-assure good functionality before mounting in the chain. The standalone tests include; HV I-V measurements of the sensor, SLDO V-I curves of the chip, analog (injection of test charges in the analog circuitry of each pixel), digital (injection of test hits into the digital circuiry of each pixel) and threshold scans (response of each pixel to analog test injections with increasing signal strength). All measurements were

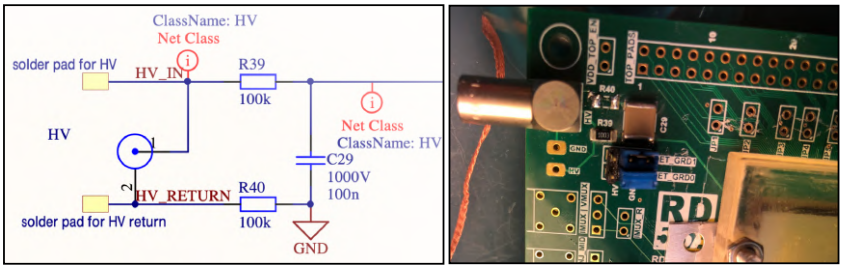

FIGURE 9.3: RD53A HV path on the SCC

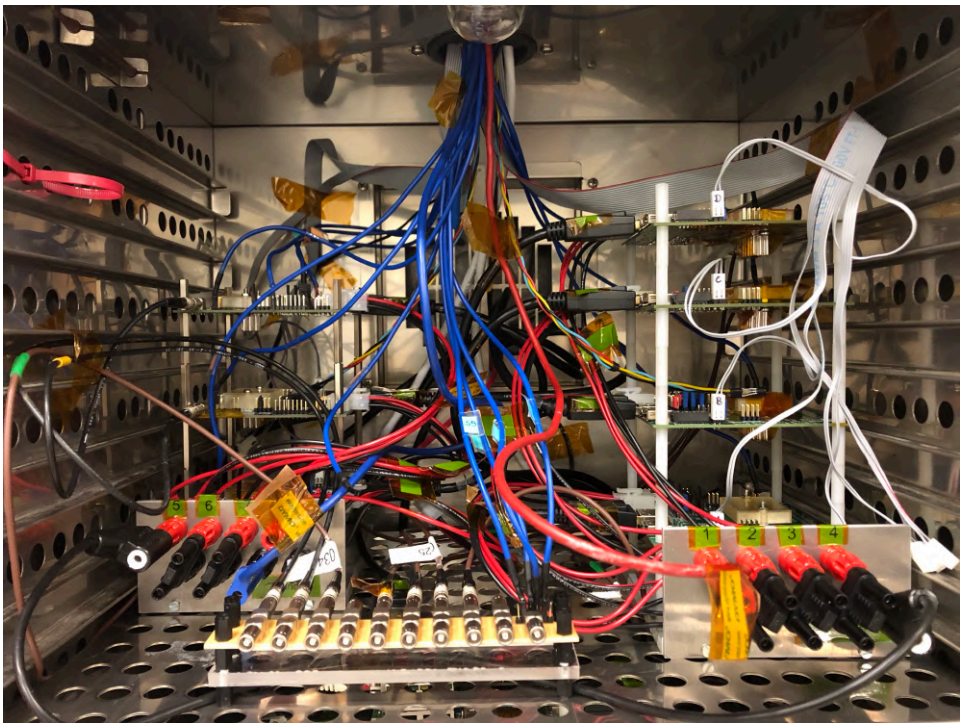

FIGURE 9.4: Assembled setup with seven modules in the climate chamber

performed in cold environment with the chip temperatures constantly monitored. After successfully passing these tests, modules were mounted in the serial chain.

The second stage of measurements includes the characterization of the assembled chain. The used modules, together with their position in the serial powering chain, are summarized in Table 9.1. The module with the highest local ground potential is considered the first module in the chain. In this stage, LV V-I curves were recorded while ramping up and down the chain supply current. Voltages were measured at the inputs of each module with respect to the corresponding module ground. The outputs of the analog (VDDA) and the digital (VDDD) regulators were also recorded. Due to the known start-up issues of RD53A chips which have also been observed with the modules used for this test, the supply current for all modules to turn on successfully was determined and chosen as the operational current of the serial powering chain. During this stage, no bias voltage was applied to the sensors, and the HV lines for the different sensors were not connected to each other.

For the third stage all the sensors were connected to a common HV line which was left floating. A schematic of the setup is shown in Figure 9.5. As explained in section 9.2, this biasing configuration is a sufficiently close approximation to the current ITk Pixel biasing scheme in the layers 1 to 4 assuming the use of high-ohmic off-mode HV power supplies. The chain was operated with a supply current of $I_{in} = 1.4\,\text{A}$, selected during the chain characterization stage. In order to spot any potential damage caused to the last module of the chain (due to the dynamically built forward bias) the chain is operated for a total time of 9 hours, running scans in regular intervals. During this period the voltage drop (ΔV) across R_{39} for all modules is monitored. The corresponding leakage current (I_{leak}) for each module in the chain is then calculated by $I_{leak} = \Delta V / R_{39}$.

As a final step, the last module in the SP chain, which was exposed to the highest forward bias (V6S03), was tested again according to the procedure used for the first stage, i.e. standalone testing, in order to compare the performance of this module before and after having been operated with a forward bias on the sensor.

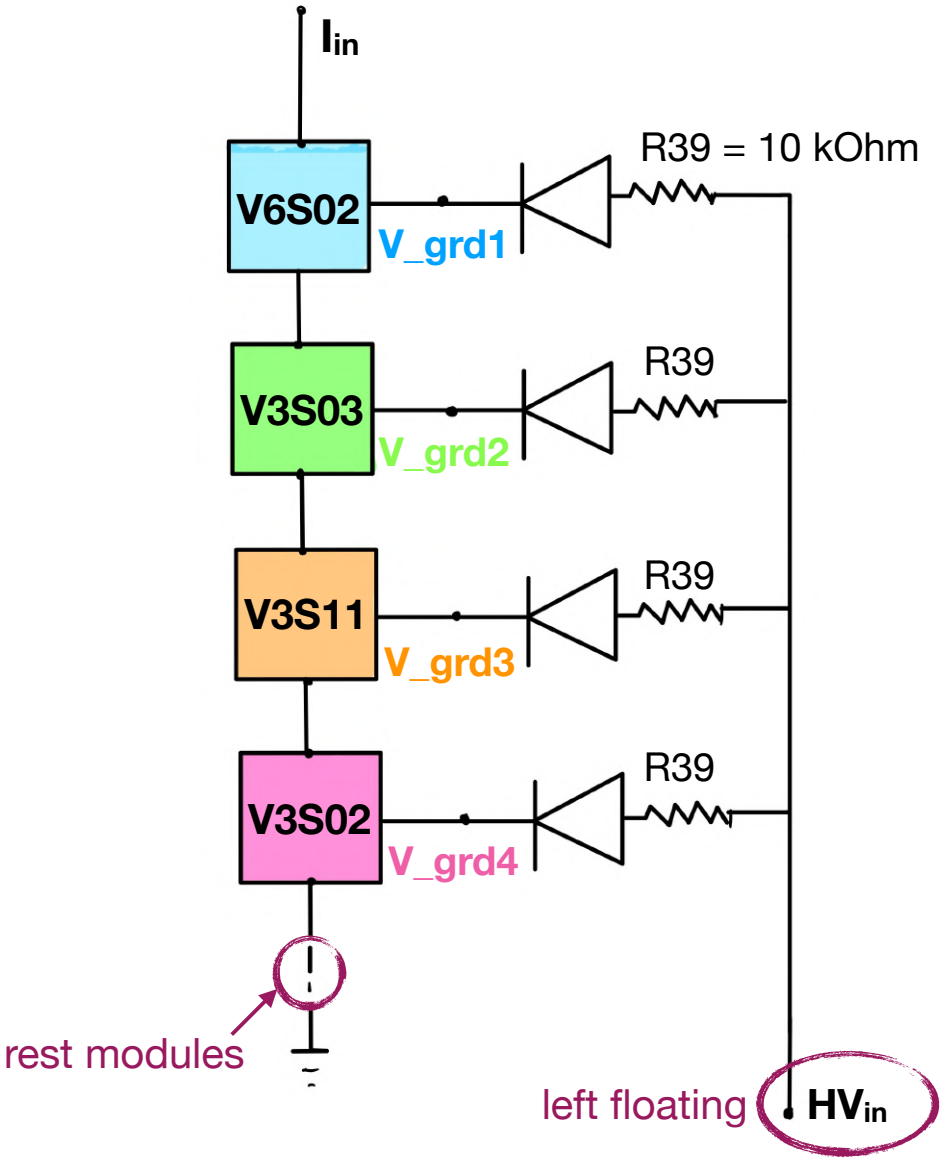

FIGURE 9.5: Schematic of the setup used for the common HV line tests. The sensor part of each module is represented as a diode while the chip side is drawn as a square.

9.4 Results

9.4.1 Stage 1: Standalone module testing

The results of the standalone module tests described in 9.3 are presented in this sub-section for module V6S03. For all the measurements the climate chamber was operating at a temperature of -35 °C and the corresponding temperature on the chip (as measured by the NTC) was stable at -27 °C.

SLDO V-I measurements

The SLDO V-I scan result for V6S03 is plotted in Figure 9.6. The input voltage voltage and outputs of the analog (VDDA) and digital (VDDD) regulators are recorded while ramping up the supply current to the chip. The input current is shared between the analog and digital SLDO regulators. For a sufficient value of the supplied current, of about 1 A, the regulators are able to produce the necessary output voltages (of about 1.2 V) to power the chip. At this point the regulators behave as an ohmic load to the power supply. Due to process variations, the required current for a regulator to switch on might be different for the analog and digital domains of the chip.

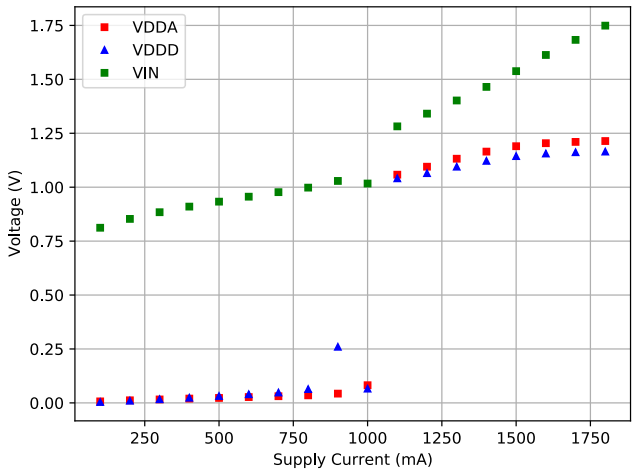

FIGURE 9.6: SLDO V-I measurement for module V6S03.

Sensor I-V measurement

The sensor I-V characteristic is performed by ramping up the reverse bias voltage applied to the sensor and measuring the leakage current. The sensor temperature as measured by the NTC located close to the module, was stable at -27 °C. The I-V curve for the sensor of module V6S03 is plotted in Figure 9.7. After irradiation, the leakage current increases considerably while the sensor shows a more resistive behavior. The sensor temperature has also a significant effect on the measured leakage current; although the climate chamber was operating at -35 °C, the module temperature was only at -27 °C. This is much higher than the expected module temperature in ITk (which is around -35 °C). Moreover, the supply current for the SLDO regulators influences as well the observed leakage current. Any additional current going through the regulators warm up the module, leading to significantly larger leakage currents.

Pixel matrix performance

Threshold, noise and Time-over-Threshold (ToT) distributions for module V6S03 are shown in Figure 9.8 and 9.9. During the tests the sensor was biased to a HV of -300 V and the leakage current was stable at 80 µA. The module was tuned to a target mean threshold of 1740 e^- and ToT of 8 BC at 10 ke^-. For the ToT scan of Figure 9.9 an input charge of 8 ke^- was injected to each pixel and therefore the ToT distribution is centered at 6. It should be noted that the combined distributions for all three analog front-ends on the RD53A chip are shown in all figures, explaining for instance the occurence of three separate peaks in the noise distribution. The left most peak in this plot correspond to the DIFF front-end, while the second and third peaks to the LIN and SYN frontends respectively. Someone might notice that the noise levels are much higher with respect to what is reported in chapter 8. This is mainly because the results presented in chapter 8 correspond to bare RD53A chips. The extra capacitance of the sensors is expected to increase the noise level, especially when the module is not fully depleted (which is the case here). This effect is amplified when considering irradiated modules.

9.4.2 Stage 2: Chain characterization

As a first step for the chain characterization, similar V-I measurements with what is shown in are repeated; the input voltage and outputs of the analog and digital regulators are recorded while ramping up the supply current to the chip. The scan result is plotted in Figure 9.11(a). Due to the limited number of readout channels, VDDA and VDDD measurements were only recorded for 5 out of the 7 modules in the chain. The input voltage V_{in} is measured between the input of the first module and output of the last one in the chain, as shown in Figure 9.10. The majority of modules have successfully started up at a supply current of 1.2A.; a problematic analog regulator is spotted for module V3S02 which didn't start up. Moreover the analog regulator of V3S03 switched on much later around 1.5A. A similar measurement when ramping down the supply current starting from a value of 1.7A is plotted in Figure 9.11(b). All the regulators have successfully switched on. It has been noticed that some modules have issues on starting up at cold temperatures. In this case a much higher supply current is needed for the regulators to switch on. However as shown in Figure 9.11(b), after a proper start up, the regulators are much less sensitive to current fluctuations allowing for chain operation to much lower supply currents than 1.7A.

Similar measurements are repeated when ramping up and down the supply current and measuring the voltage drop across each module as indicated in Figure 9.12. The corresponding plots are shown in Figure 9.13. The voltage drop is recorded for all seven modules in the chain. Sharp jumps in V_{in} correspond to the start up of the SLDO regulators. Two different jumps are recorded for a few modules in Figure 9.13(a). These correspond to the analog and digital regulators switching on at different supply currents. As already introduced in section 9.1.1, the SLDO output and offset voltages are generated by two band-gaps; V_{ref} and V_{OFS}, respectively. It is known that the main issue during power-up of the RD53A SLDOs is related with the band-gaps minimum voltage and current needed to start-up [106]. In addition, due to the variance off the start-up behavior of the analog and digital SLDOs, current sharing distribution issues during start-up can occur. This behavior is being solved in the next SLDO version using a new band-gap scheme [106]. Much smoother V-I curves are obtained after the proper start-up of the SLDOS in Figure 9.13(c). For comparison reasons similar scans, when ramping up the supply current and powering cycling at each measurement step the power supply, as well as when ramping down the supply current in warmer temperatures ($T = -13\,^{\circ}$C), are also performed. These are shown in Figures 9.13(b) and 9.13(d) respectively.

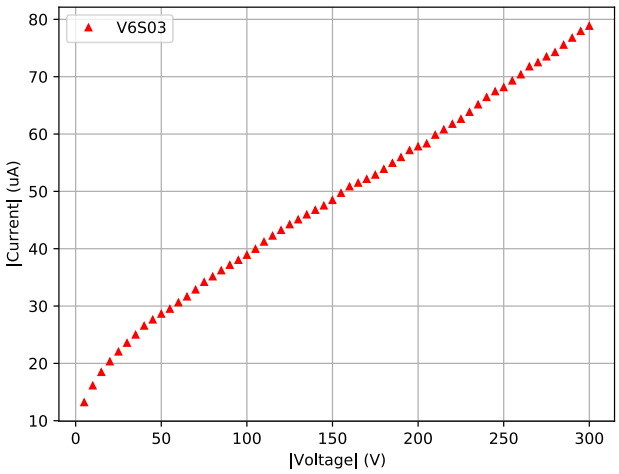

FIGURE 9.7: Sensor I-V curve for module V6S03.

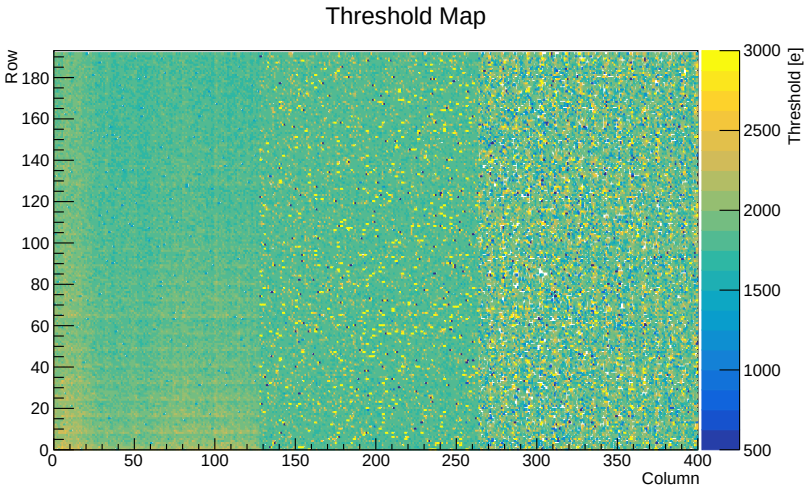

(a)

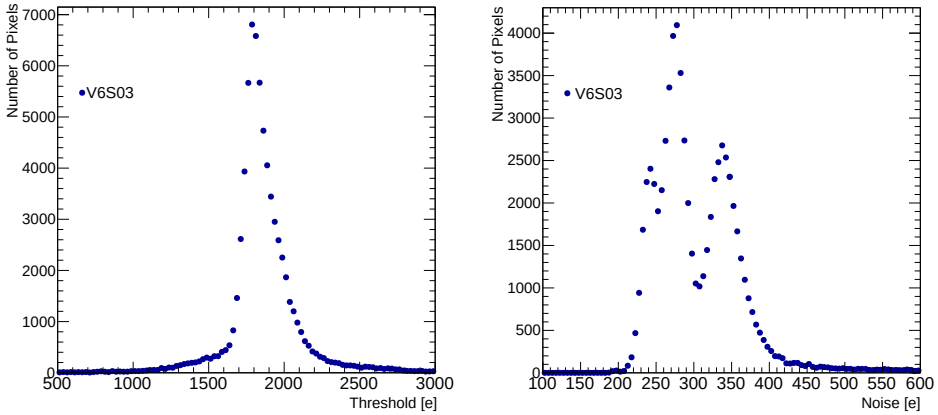

(b) (c)

FIGURE 9.8: Threshold map (a) and corresponding threshold (b) and noise (c) distributions for module V6S03

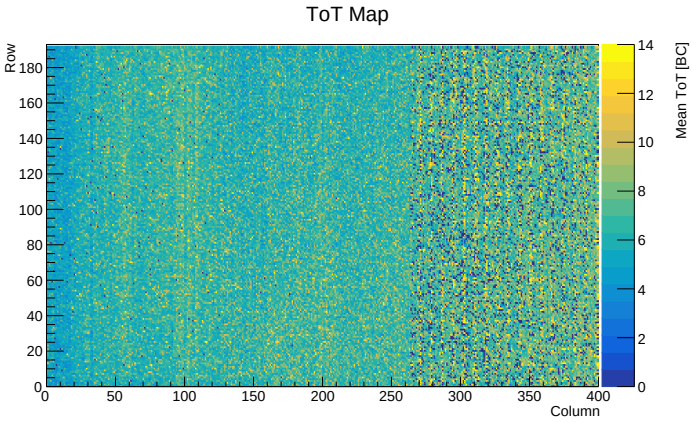

(a)

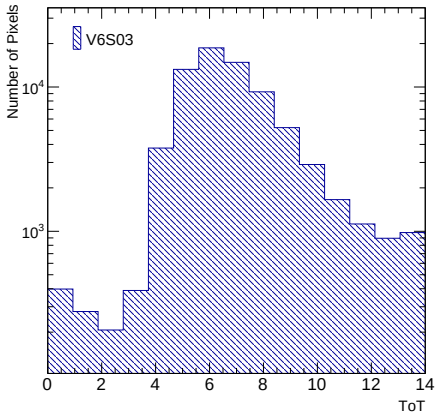

(b)

FIGURE 9.9: ToT map (a) and corresponding one-dimensional distribution (b) for module V6S03

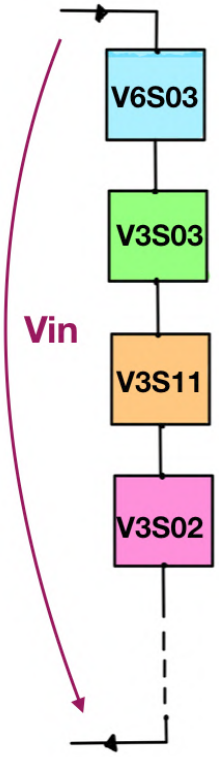

FIGURE 9.10: Schematic of the setup used during the chain characterization. During this stage, no bias voltage was applied to the sensors, and the HV lines for the different sensors were not connected to each other.

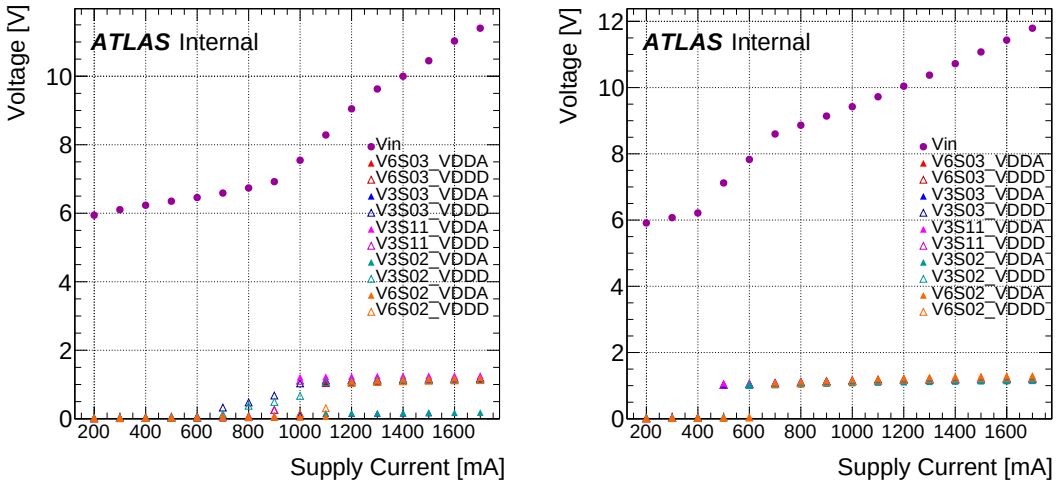

(a) Ramp up

(b) Ramp down

FIGURE 9.11: SLDO V-I measurements for the serial powering chain of seven modules summarized in Table 9.1. Measurements are performed when ramping up (a) and ramping down (b) the supply current.

After the start-up of both the analog and digital regulators in the scans of Figures 9.13(a) - 9.13(d), the impedance increases and the effective resistance depends on the choice of the external resistors used in the SLDO circuits, R_{extA} and R_{extD} (for analog and digital circuits

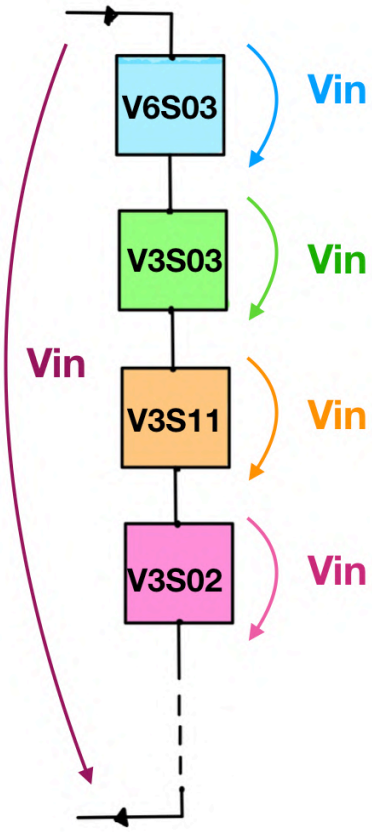

FIGURE 9.12: Schematic of the setup used during the chain characterization. During this stage, no bias voltage was applied to the sensors, and the HV lines for the different sensors were not connected to each other.

respectively). The effective resistance is approximately given by:

$$R_{eff} = \frac{1}{\frac{1}{R_{extA}} + \frac{1}{R_{extD}}}$$

. For our setup, described in 9.2.1, $R_{eff} \approx 0.4 \times 10^{-3}$ Ohm and the offset voltage V_{OFS} ≈1 V. The curves of Figures 9.13(a) - 9.13(d) are fitted using a linear function

$$V_{in} = slope * I_{in} + const$$

. The fit is performed in the range $[1600, 1800]$ mA in which all the regulators have switched on for all the scans considered. The $slope$ and $const$ fit results are summarized in Figures 9.14. The $slope$ and $const$ values are centered around 0.4×10^{-3} Ohm and 0.85 V, respectively, for the majority of modules. The slightly higher effective resistance and lower offset voltages with respect to the expected values can be attributed to parasitic inductance that derives mainly from the chip wire-bonding and the PCB routing.

As discussed in 9.1, in ITk, building blocks for a serial powering chain will be quad or triplet modules . In order to test the behavior of such a chain, the modules of Table 9.1 are re-arranged in order to form doublets; each doublet correspond to two modules powered in parallel. A serial powering chain of three doublets (D1, D2 and D3) is therefore constructed. SLDO V-I measurements are performed and the outputs of the analog and digital regulators

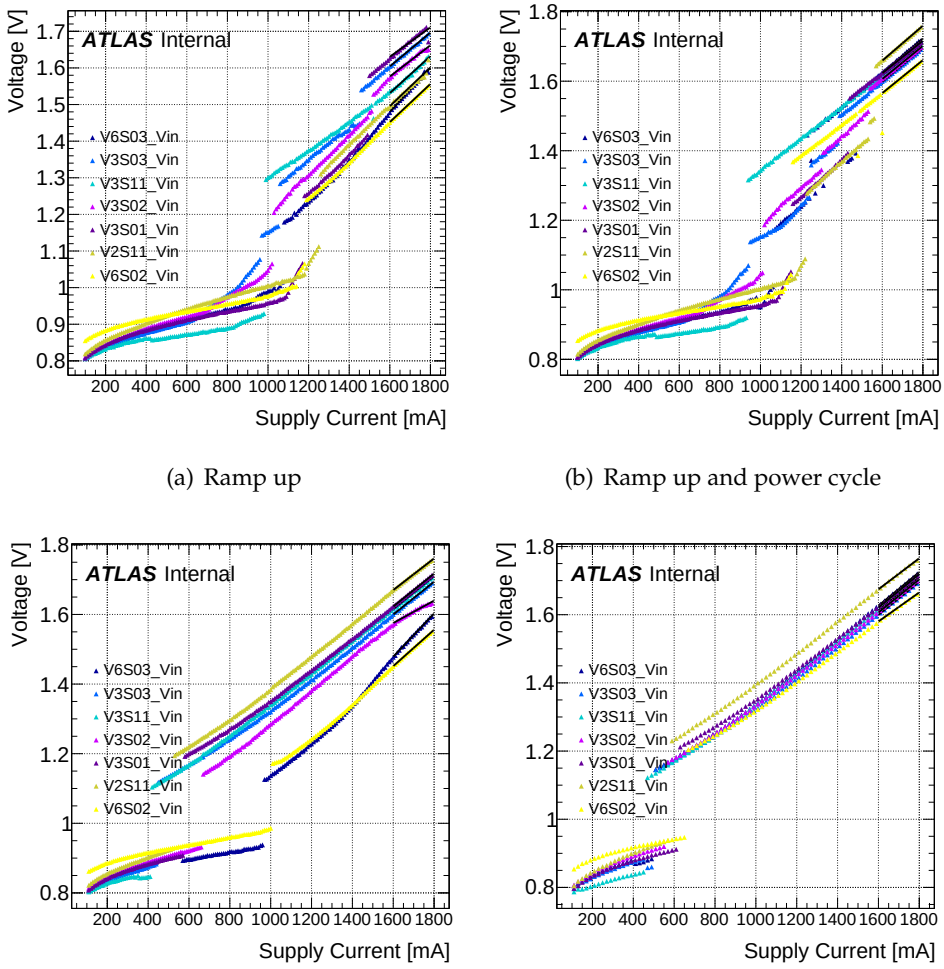

(a) Ramp up

(b) Ramp up and power cycle

(c) Ramp down

(d) Ramp down warm

FIGURE 9.13: SLDO V-I measurements for the serial powering chain of seven modules summarized in Table 9.1. The voltage drop across each module is recorded and plotted here.

for each module of the doublets is recorded. Due to the limited number of readout channels the measurements are performed in two rounds; in the first round the analog regulator outputs are recorded while in the second round the measurement is repeated for the digital regulator outputs. The SLDO scan results, when ramping up and down the supply current, are summarized in Figure 9.15. Similar behavior with the single-module configuration is noticed;

- The input behaves as an ohmic load to the current supply after the band-gaps start-up. Jumps in the input voltage correspond to the start-up of the doublets; in Figure 9.15(b), 3 jumps are recorded corresponding to the start-up of doublets D1, D2 and D3. More than 3 jumps are recorded in the ramp-up scans of Figures 9.15(a) and 9.15(c). This can attributed to the start-up issues already discussed above.
- As shown from the long-lasting plateau of Figure 9.15(b), the regulators are much less sensitive to current fluctuations after powering on at a high supply current and ramping down.
- Different doublets switch on at different supply currents. However, within a given doublet the analog and digital regulators switch on almost simultaneously. The asymmetric

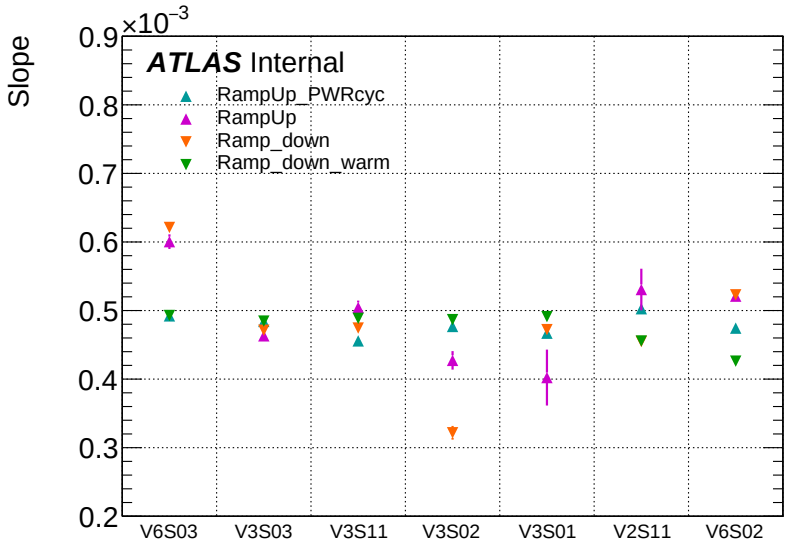

(a) Slope fit results

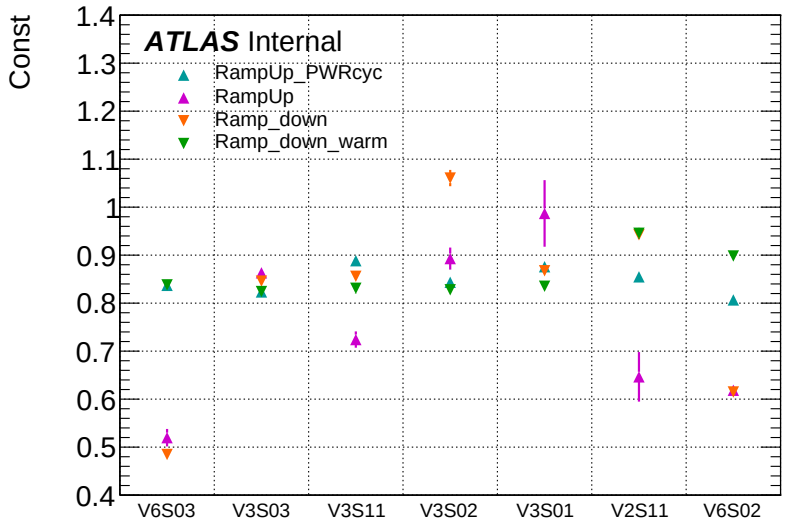

(b) Const fit results

FIGURE 9.14: Summary slope and const fit results from a linear fit to the V-I curves presented in Figures 9.13(a) - 9.13(d).

current sharing between the modules within a doublet is a possible explanation. Exceptions are the analog regulator of module V6S03[2] and module V2S11, which needs a supply current of around 1500mA for both regulators to start up as shown from Figure 9.13(b).

9.4.3 Stage 3: Common HV line tests

The chain was first powered on at an input current of I_{in}= 1.7 A and was then operated at a constant supply current of I_{in}= 1.4 A. The voltage drops across each module in the chain

[2]already discussed in the single-module serial chain

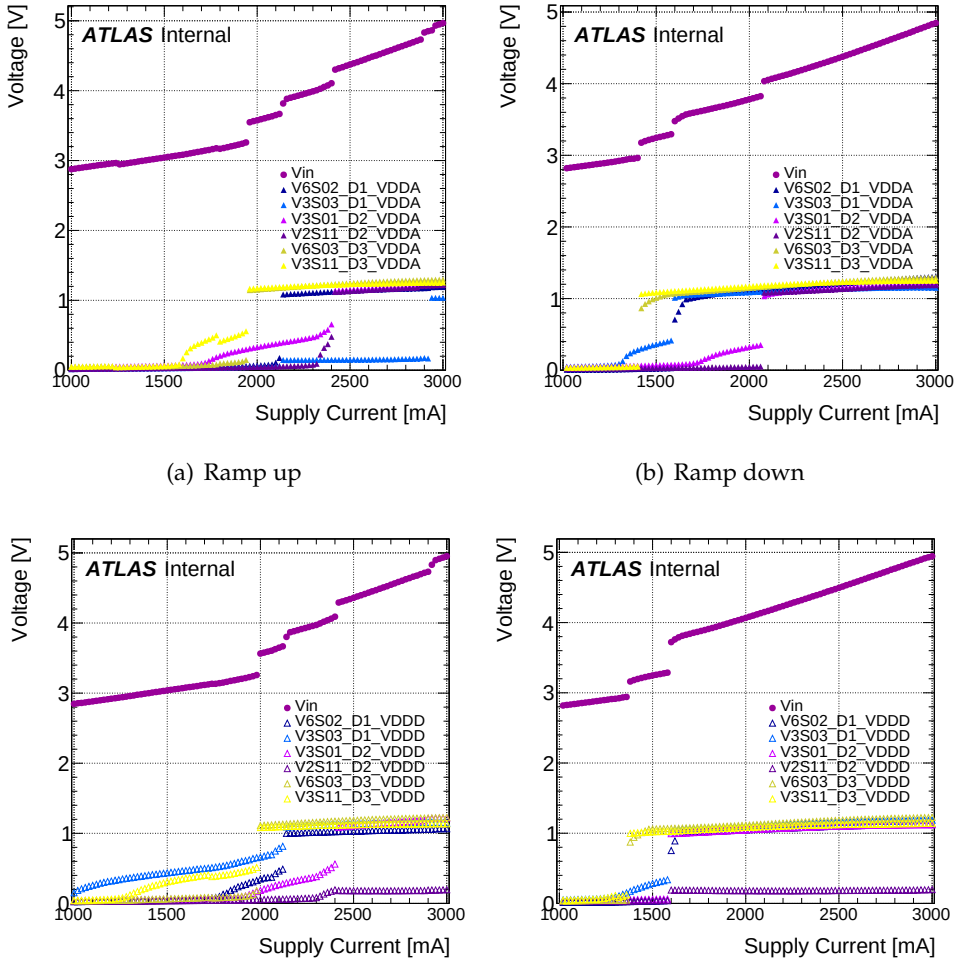

(a) Ramp up

(b) Ramp down

(c) Ramp up

(d) Ramp down

FIGURE 9.15: SLDO V-I measurements for the serial powering chain of doublets. The VDDA is recorded while ramping up (9.15(a)) and down (9.15(b)) the supply current. The corresponding plots for VDDD are shown in 9.15(c) and 9.15(d).

when it's powered by a constant supply current I_{in}= 1.4 A, are summarized in Table 9.2. For most modules the observed voltage drop is close to the design value of roughly 1.55 V. It was verified that all modules started up properly by running a series of digital and analog scans on all modules. For module V6S03, the regulator output voltages were recorded during the operation in the chain as well, with both values being reasonably close to the design value of 1.2 V (VDDD = 1.2 V, VDDA = 1.18 V). Due to the limited number of available readout channels, this measurement was not performed for the other modules in the chain.

Forward bias

In Figure 9.16 the leakage current as a function of time is plotted for each module in the chain. A positive sign in this plot corresponds to an effective reverse bias, i.e. the potential at the backside of the sensor, which is equal to the potential of the common, floating HV line, is lower than the potential at the bias grid of the sensor. A negative sign corresponds to an effective forward bias, i.e. the potential on the common HV line is higher than the potential on the bias grid on the backside of the sensor. A significant forward biasing is observed for at least two modules in the chain, the ones on the lowest ground potential (those being

Position in Chain	Module ID	Voltage Drop (V)
1st	V6S02	1.49
2nd	V3S03	1.50
3rd	V3S11	1.52
4th	V3S02	1.51
5th	V3S01	1.53
6th	V2S11	1.58
7th	V6S03	1.52

TABLE 9.2: Summary of voltage drops across each module in the chain for a supply current of 1.4A.

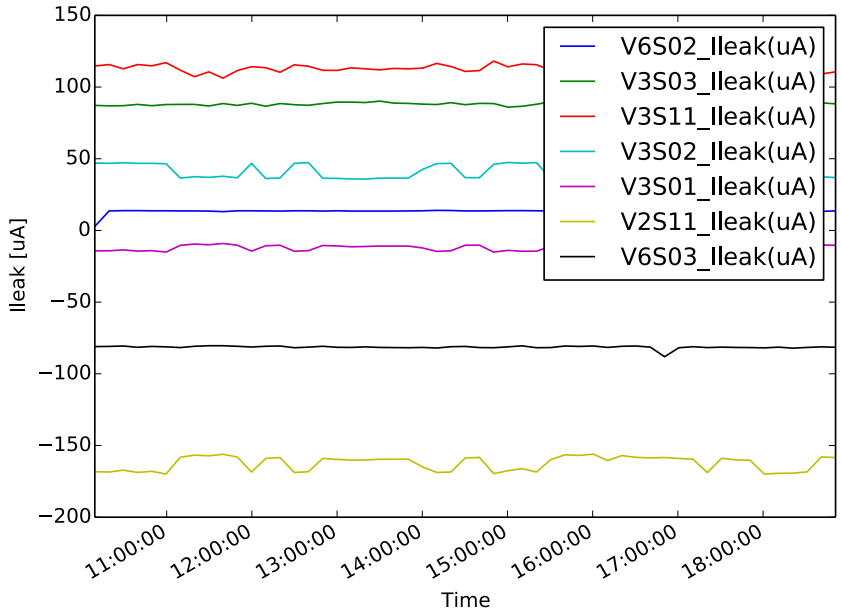

FIGURE 9.16: Leakage current measurements for all modules in the assembled chain with common HV line.

V2S11 and V6S03). The current sharing between these modules highly depends on the module temperature (which was higher for module V2S11).

Pixel matrix performance

The modules in the chain were tuned to a target threshold of 1700 e and ToT of 7 at 10 ke injection charge. The threshold and ToT distributions before and after tuning are plotted in Figures 9.17 and 9.18, respectively. In order to check the effect on the noise level, of connecting a module in a serial powering chain with respect to the standalone powering, the noise distribution for a module operated in the chain is compared to the standalone one. The noise increase per pixel is plotted in Figure 9.19. The overall increase of noise is small and it can be attributed to module temperature differences between the two tests.

9.4.4 Stage 4: Standalone Test of Module V6S03

In order to look for potential damages caused to the frontend chip due to the forward biasing, module V6S03 was re-tested standalone. The same scans that were performed before

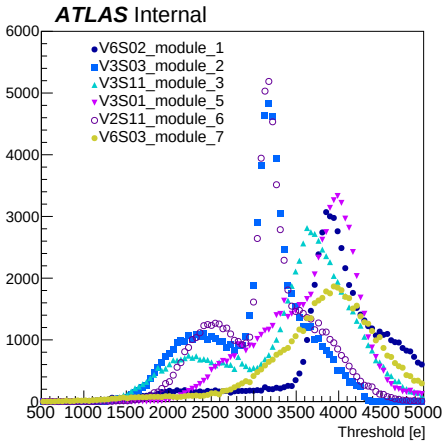

(a) Threshold - Before tuning

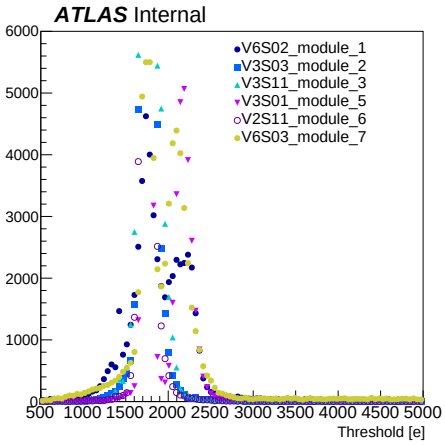

(b) Threshold - After tuning

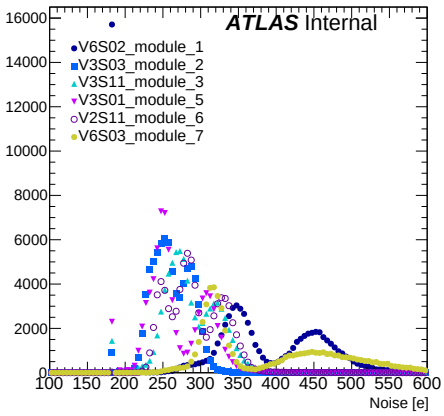

(c) Noise - Before tuning

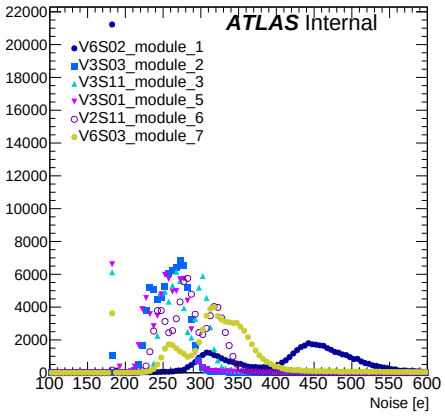

(d) Noise - After tuning

FIGURE 9.17: Threshold and noise distributions before and after tuning modules of the chain to a target threshold of 1700e.

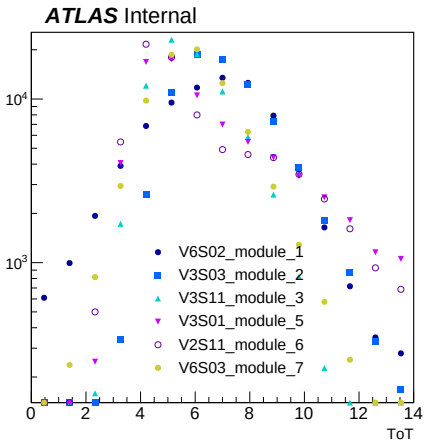

(a) ToT - Before tuning

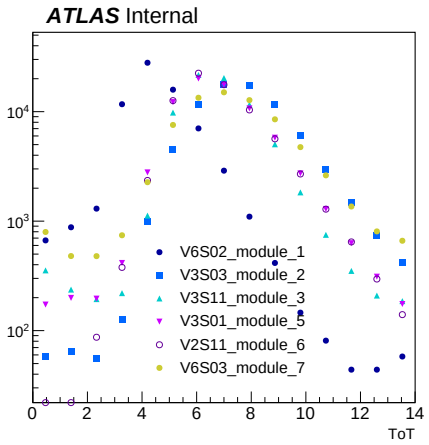

(b) ToT - After tuning

FIGURE 9.18: ToT distributions before and after tuning the modules of the chain to a ToT of 7 at 10ke injection charge.

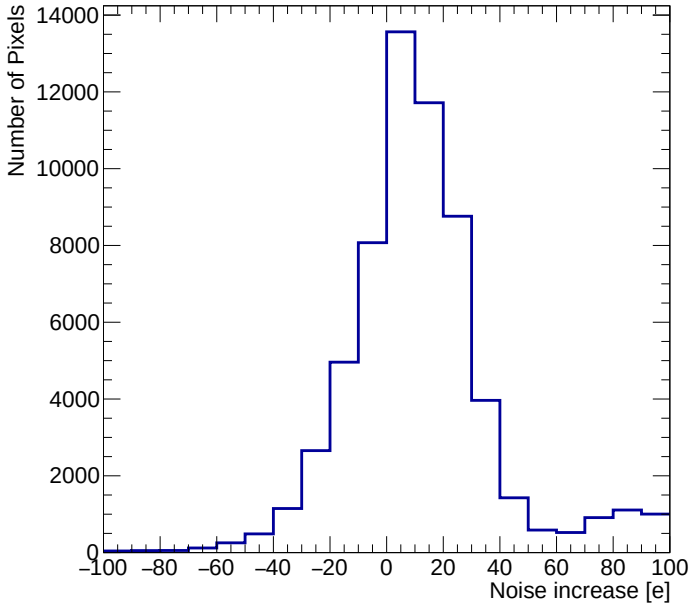

FIGURE 9.19: Noise increase for the serial powering chain. The noise is measured per pixel on a module operated standalone and in the serial powering chain.

the operation of the modules in the serial powering chain were repeated. A comparison of the threshold, noise and ToT distributions for module V6S03 before and after the long operation in the chain is shown in Figure 9.20. For all cases, the distributions are in good agreement and indicate that the module is still working properly and with the same characteristics after the operation in the serial powering chain as it was before the operation in the serial powering chain.

The sensor I-V measurement is also repeated in order to check for potential damages in the sensor side. It is plotted in Figure 9.21. The I-V curve shows very similar characteristics to the corresponding one from stage 1 testing 9.4.1.

9.4.5 Extrapolation of Results to the ITk

In the above described setup, a maximum current of roughly 2 nA per pixel for the sensors that are exposed to a forward bias is observed. While it is difficult to directly extrapolate, these results can be considered a reasonably close approximation to the ITk Pixel Detector operating conditions. The maximum potential difference between the common HV line and the local module ground is expected to be about 6 V, while the maximum leakage current is expected to be around 1 mA, resulting in a maximum of 2 nA per pixel in the module with the highest effective forward bias. This current estimate assumes that all modules in the chain have broken down completely, therefore do not have any measurable resistance any more. However, such a scenario is an overly pessimistic and quite unrealistic one to make. The reason that the per pixel current observed in the above measurements is close to this overly conservative estimate can be attributed to the higher temperature that was measured for the RD53A modules during this test compared to the expected sensor temperature in the ITk Pixel Detector.

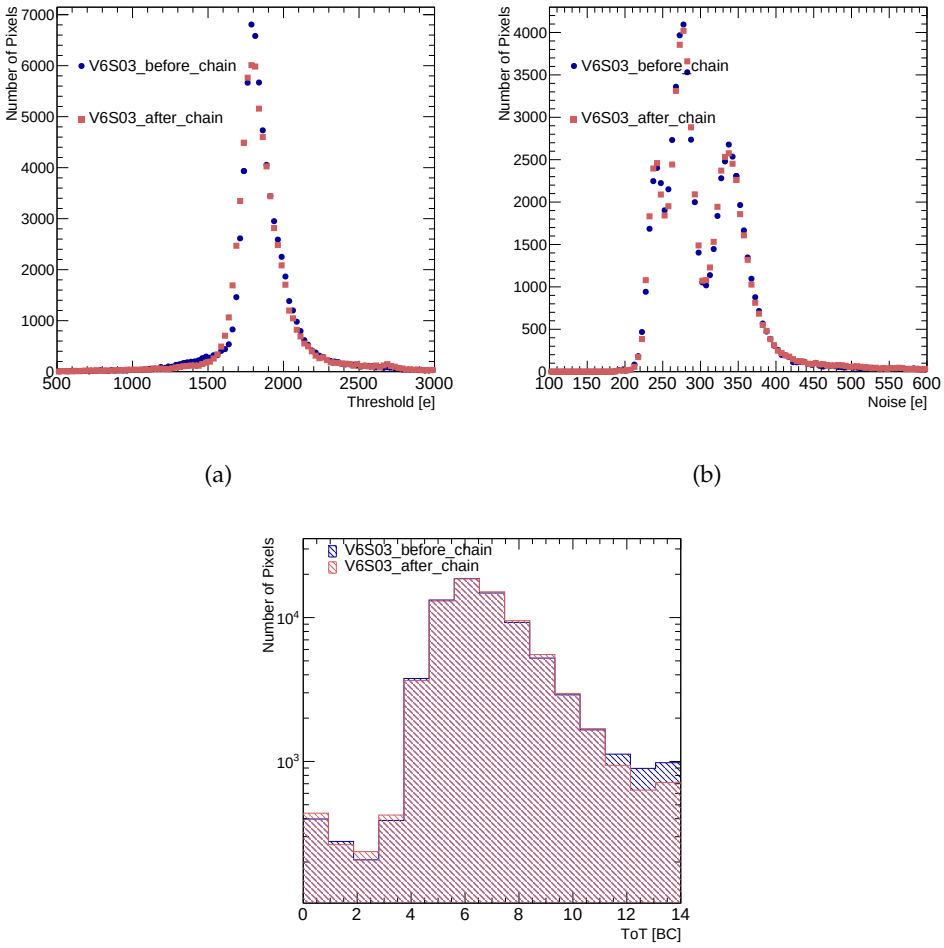

(a) (b)

(c)

FIGURE 9.20: Threshold map (a) and corresponding threshold (b) and noise distributions (c) for module V6S03

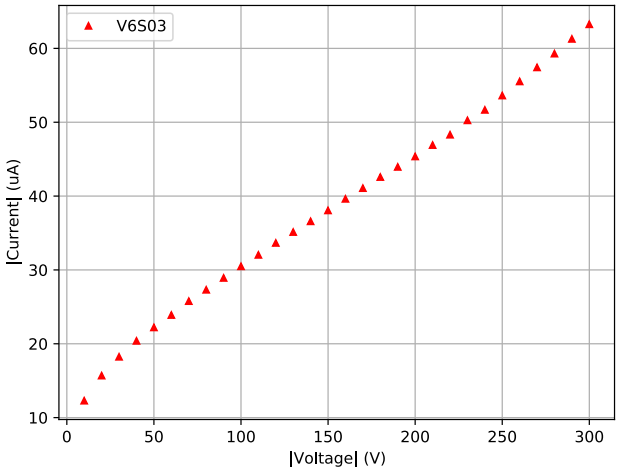

FIGURE 9.21: Sensor I-V curve for module V6S03 after in chain operation.

Measurements that were done by other colleagues with an un-irradiated ITkPixV1 module indicate that even for forward currents of up to 6.5 nA per pixel, the voltage at the pre-amplifier input stays well below the core voltage of 1.2 V. This gives us a safety factor of roughly three with respect to the maximum estimate expected for the ITk Pixel Detector. The results of this measurement are shown in figure 9.22. The relevant distributions for the tests presented in this thesis is the behavior of the pre-amplifier input voltage for the default configuration, as well as for the low power bias configuration, with the low voltage switched on. The curve for unpowered readout chips is shown for reference, only.

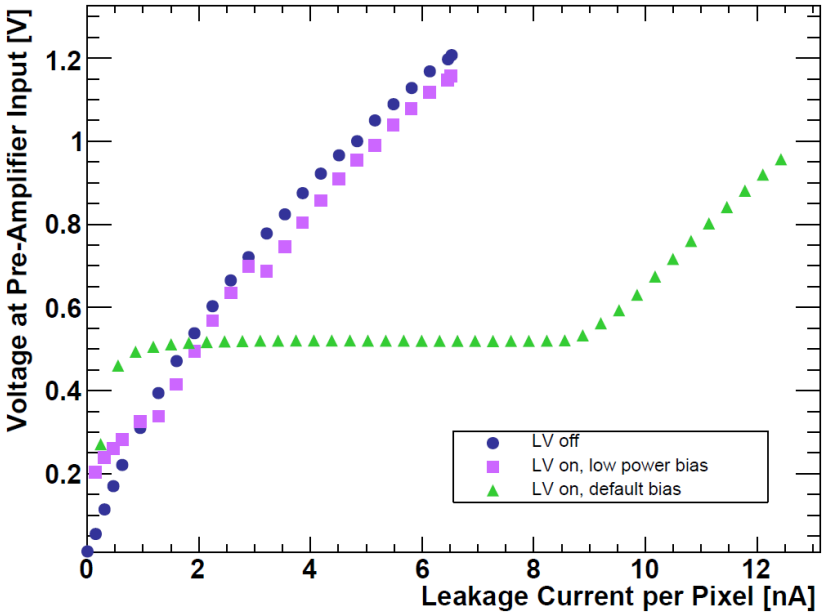

FIGURE 9.22: Pre-Amplifier input voltage as a function of the per-pixel leakage current in a forward bias configuration for an ITkPix1 module.

10. Conclusions

In this thesis work, the vector boson scattering (VBS) in semileptonic final states is studied. The advantages of semileptonic final states, with respect to other fully leptonic searches, is the higher branching ratio, as well as, the exploitation of jet substructure techniques for the W/Z identification, which allow high reconstruction efficiency in the high- p_{T} regimes, where there is higher sensitivity to anomalous quartic gauge couplings (aQGC). My thesis work highly focuses on the 2-lepton channel analysis, and it includes all steps to the signal strength measurement. The measurement is performed using the full Run-2 dataset collected during the years 2015-2018 with the ATLAS detector, corresponding to an integrated luminosity of $139 fb^{-1}$. My work starts with a detailed study of the background modelling in control regions defined for resolved and merged reconstructed boson decays. Dedicated corrections are derived in order to correct for the observed mis-modelling between data and MC in both regions. Separate BDTs are trained in the merged and resolved regimes, given the different kinematics of these regions. Next, I focused in the evaluation of the theory and modelling uncertainties related to the background and signal predictions. The modelling uncertainties related to the Z+jets prediction are found to be significantly large in the merged regions. A further study of the BDT inputs was performed in order to spot the features that cause this large mis-modelling. Such features were eliminated from the BDT and the significance drop was estimated by also considering the modelling uncertainties in the significance estimation. The loss in terms of discrimination power was found to be larger than the gain when removing such bad modelled features from the BDT. Finally, I worked on the statistical treatment of the analysis, which can be broken down in three major steps. As a first step, the model was tested with Asimov only data and the expected significance was evaluated. Next the background-only estimation with actual data, in the so called model inspection fit was performed. After gaining confidence that the background description is meaningful in data in the absence of signal, ensuring that no significant biases are observed, I moved on to the signal-dependent interpretation. The signal strength was evaluated by a combined binned maximum likelihood fit across the merged and resolved signal and control regions. The signal strength is measured to be:

$$\mu = 1.29^{+0.38}_{-0.34} = 1.29^{+0.23}_{-0.22}(\mathrm{Stat})^{+0.31}_{-0.27}(\mathrm{Syst})$$

The background only hypothesis is rejected with a significance of 4.15σ, indicating a strong evidence of the EW $VVjj$ signal in the semileptonic final state with 2 leptons. The expected significance obtained with the post-fit Asimov dataset is estimated at 3.34σ. Applying this analysis method to the $35.5 fb^{-1}$ dataset and comparing the obtained result with the corresponding publication [26], we found a $\sim$46% improvement in terms of expected significance and a $\sim$78% improvement in the observed significance.

A part of my thesis work is also dedicated to a detailed study of optimizing the forward jet identification, in particular developing an algorithm to mitigate the pileup jets in the forward region. The algorithm, referred to as fJVT, has been optimized and various methods have been tested. The fJVT is found to offer a $\sim 4\%$ increase in the observed significance and a $\sim 7\%$ increase in the expected significance when considered during the tagging jet selection.

The current ATLAS Inner Tracker is compatible with the LHC design luminosity of 10^{34} $\mathrm{cm}^{-2}\mathrm{s}^{-1}$. The foreseen increase towards High Luminosity LHC phase with peak luminosities of up to 5-7$\times 10^{34}$ $\mathrm{cm}^{-2}\mathrm{s}^{-1}$ requires a fundamental re-design of the complete inner detector due to both, increased radiation damage, and substantial occupancy of the sub-detectors. For

the HL-LHC, the current inner detector of ATLAS will be replaced by an all-silicon Inner Tracker (ITk). The ITk pixel detector design features a much higher active area and granularity with respect to the current pixel detector. The ITk pixel sensors are equipped with a new readout chip, able to meet all the requirements needed for the high luminocity LHC. As part of my thesis work, I was in charge of preparing and testing dedicated setups for the readout chip characterization at IJCLab. Several tests of the analog and digital parts of the front-end chip were performed in this context. Moreover, the much larger number of modules and the much finer granularity used by ITk, results in a significant increase in the power density in the detector. For this reason a serial powering (SP) scheme has been chosen. I was in charge of preparing and testing such a serial powering chain at CERN, composed of irradiated RD53A modules. The testing procedure comprises standalone tests of all modules, followed by the characterization of the assembled chain in various high-voltage distribution schemes, in order to spot potential damages introduced by the serial powering scheme. The obtained results show a fully functional chain with no damages caused to any of the modules in the chain.

A. Modeling plots

Modeling plots for Merged and Resolved SRs

This appendix contains the modeling plots for all the features used in the BDT trainings described in Section 6.7.

A.1 Resolved SR

Plots for the resolved SR are shown in Figures A.1- A.4. More specifically:

- Distributions for the $lljj$ system are shown in Figures A.1 a-d.
- Distributions for the full system are shown in Figures A.1 e-h.
- Variables associated to the signal jets are shown in Figures A.2
- Features linked to the tagging jets are shown in Figures A.3
- The zeppenfend and centrality related variables are plotted in Figure A.4.

A.2 Merged HP SR

Plots for the merged HP SR are shown in Figures A.5- A.8. More specifically:

- Variables related to the $sigJ$ an di-lepton system are shown in Figure A.5
- Variables related to the entire system of $sigJ$, di-lepton and tagging jets are shown in Figure A.5
- Variables associated to the $sigJ$ (identified as fatJet in plots) are shown in Figure A.6
- Tagging jet related variables are shown in Figure A.7
- The zeppenfeld and centrality variables are shown in Figure A.8

A.3 Merged LP SR

Plots for the merged LP SR are shown in Figures A.9- A.12. More specifically:

- Variables related to the $sigJ$ an di-lepton system are shown in Figure A.9.
- Variables related to the entire system of $sigJ$, di-lepton and tagging jets are shown in Figure A.9.

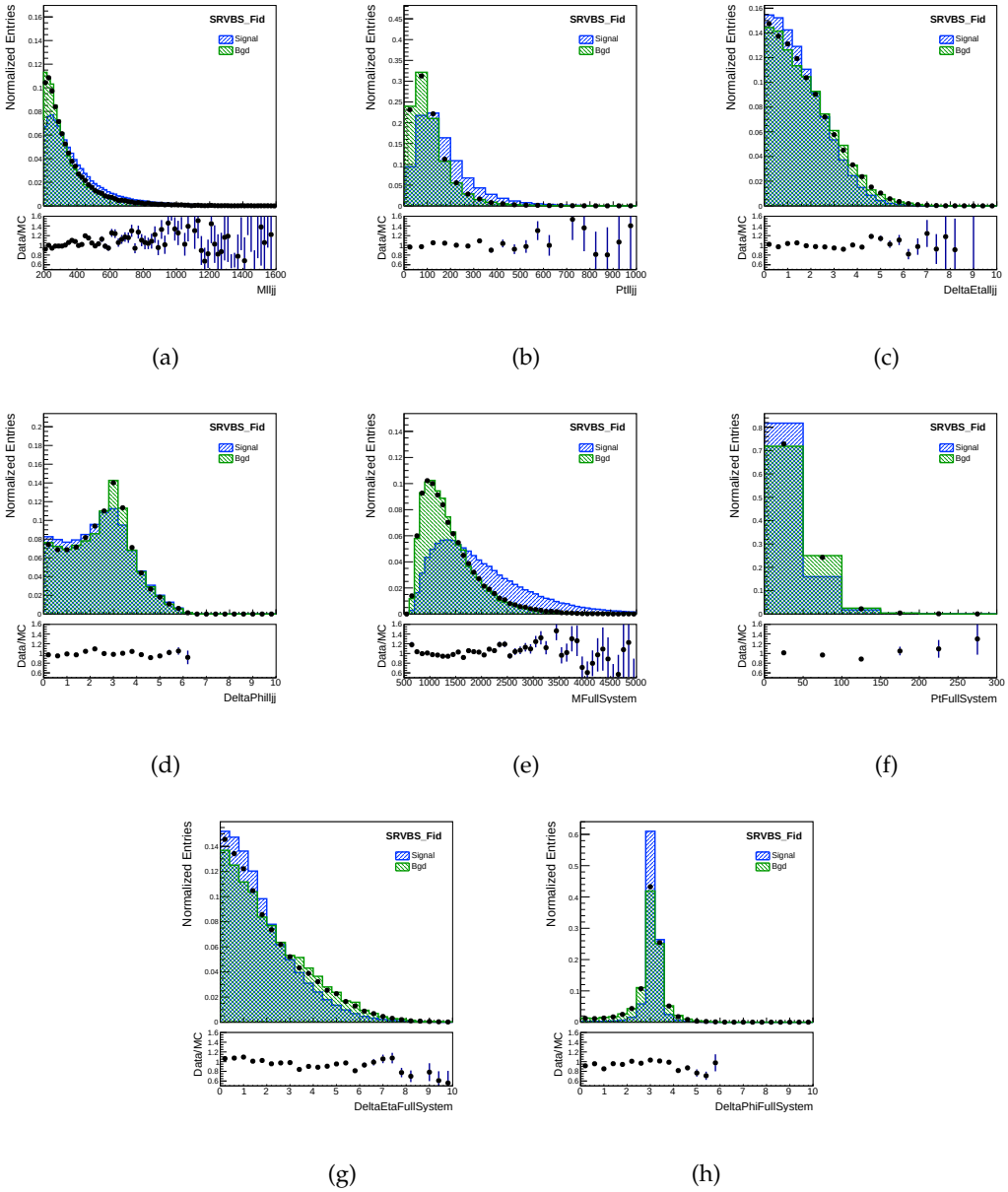

FIGURE A.1: $lljj$ and full system related plots for the resolved signal region.

- Variables associated to the $sigJ$ (identified as fatJet in plots) are shown in Figure A.10
- Tagging jet related variables are shown in Figure A.11.
- The zeppenfeld and centrality variables are shown in Figure A.12.

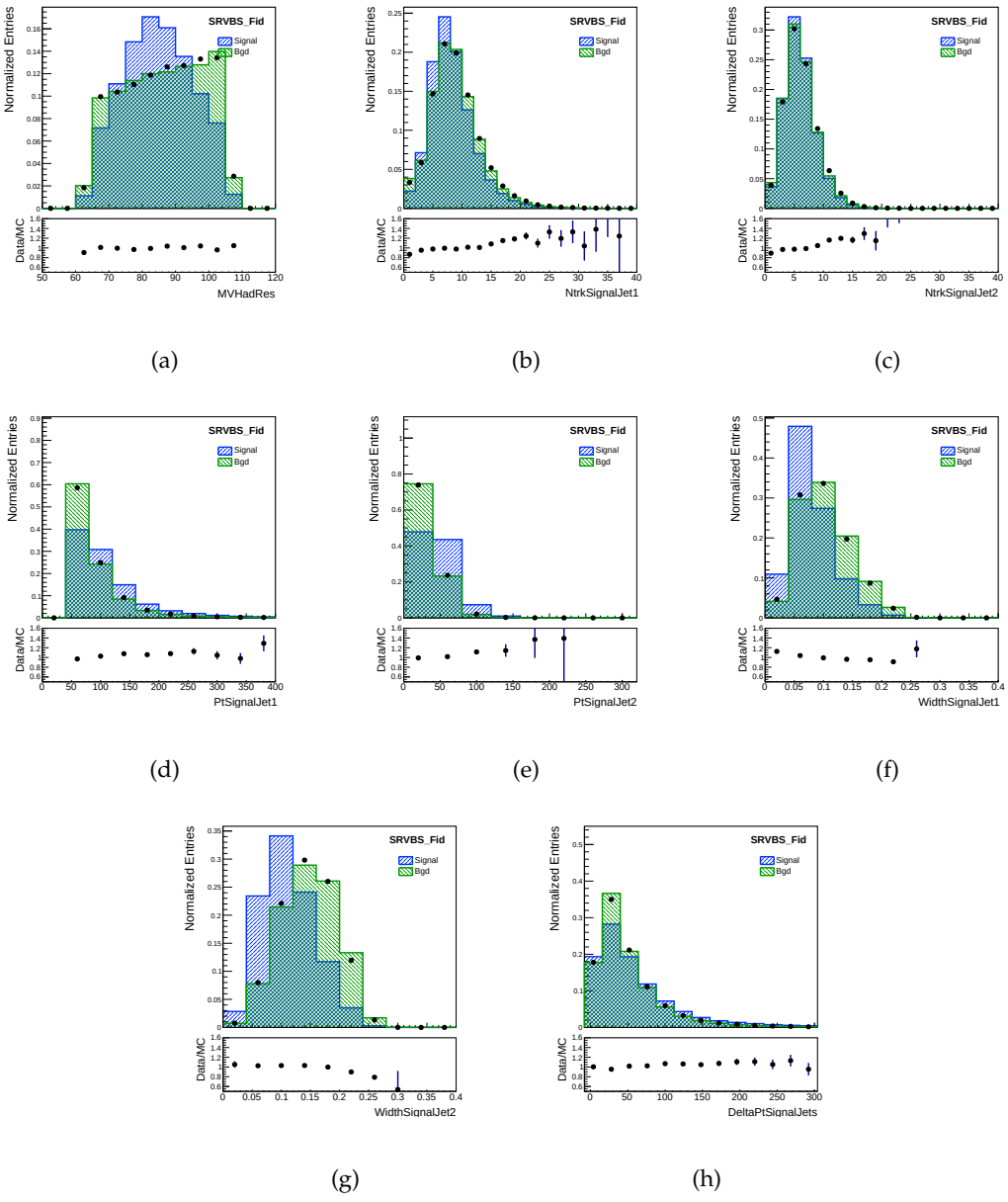

FIGURE A.2: Figures related to the signal jets for the resolved signal region.

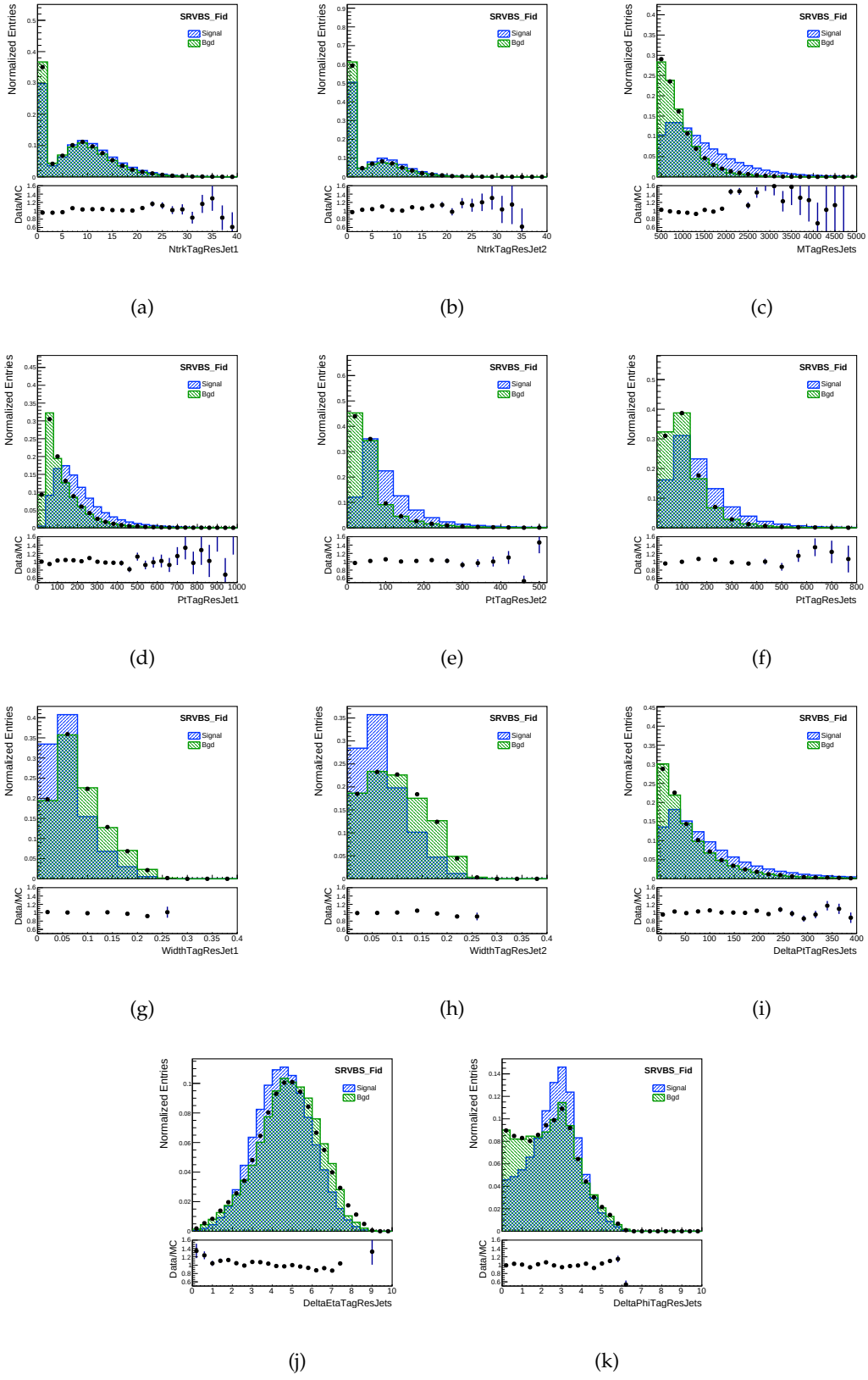

(a) (b) (c)

(d) (e) (f)

(g) (h) (i)

(j) (k)

FIGURE A.3: Figures related to the tagging jets for the resolved signal region.

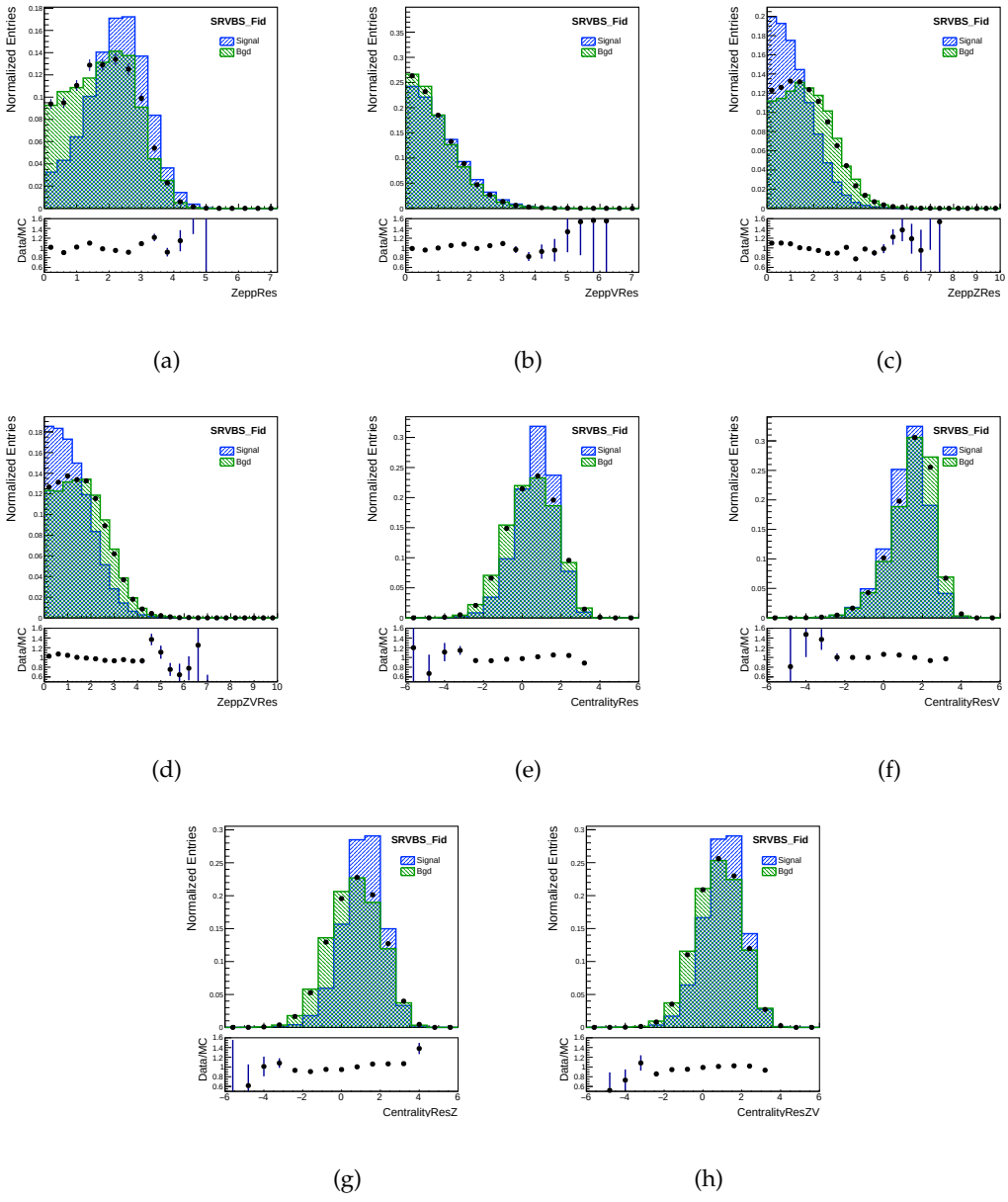

(a) (b) (c)

(d) (e) (f)

(g) (h)

FIGURE A.4: Figures related to other variables for the resolved signal region.

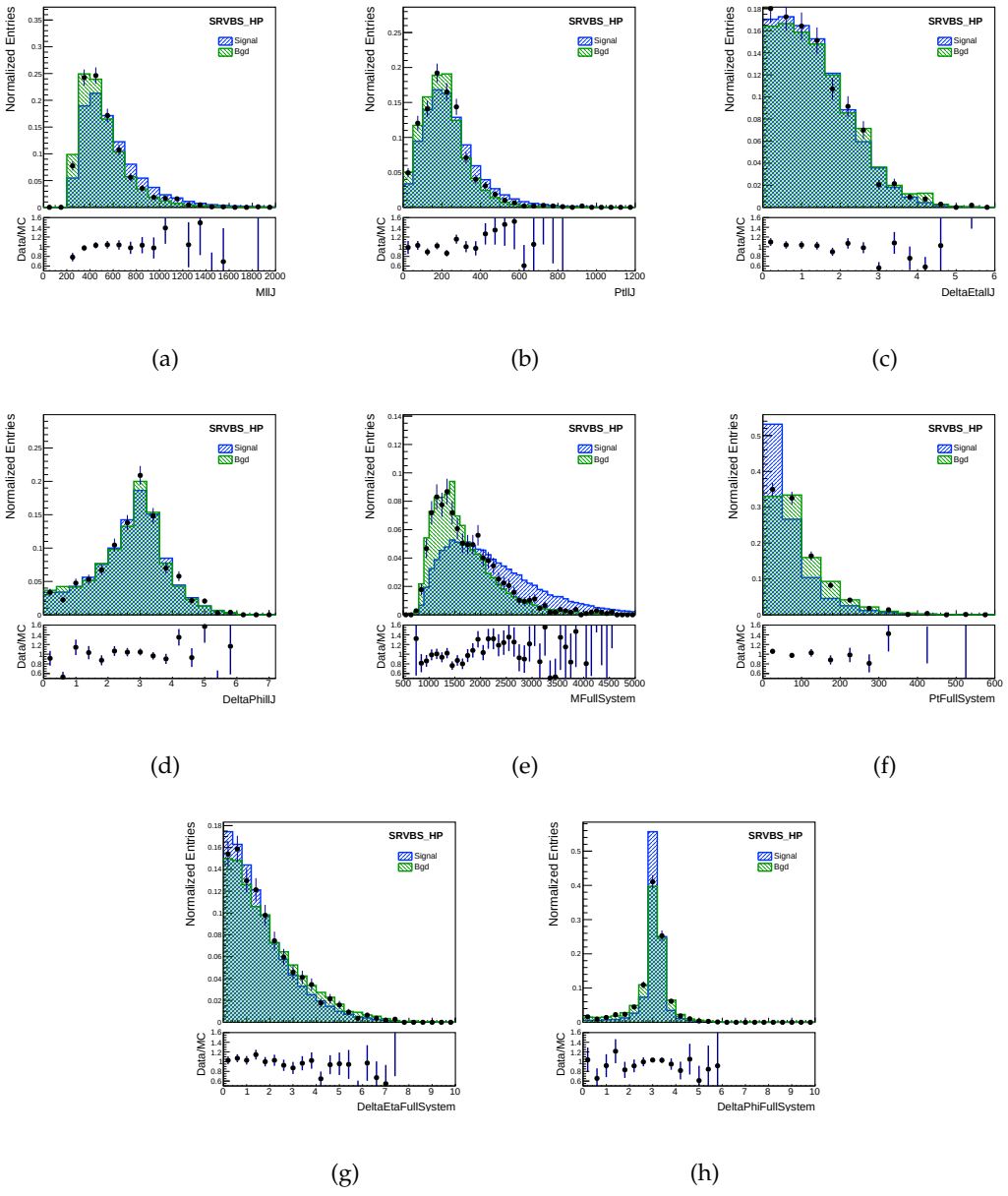

(a) (b) (c)

(d) (e) (f)

(g) (h)

FIGURE A.5: llJ and full system related plots for the merged HP signal region.

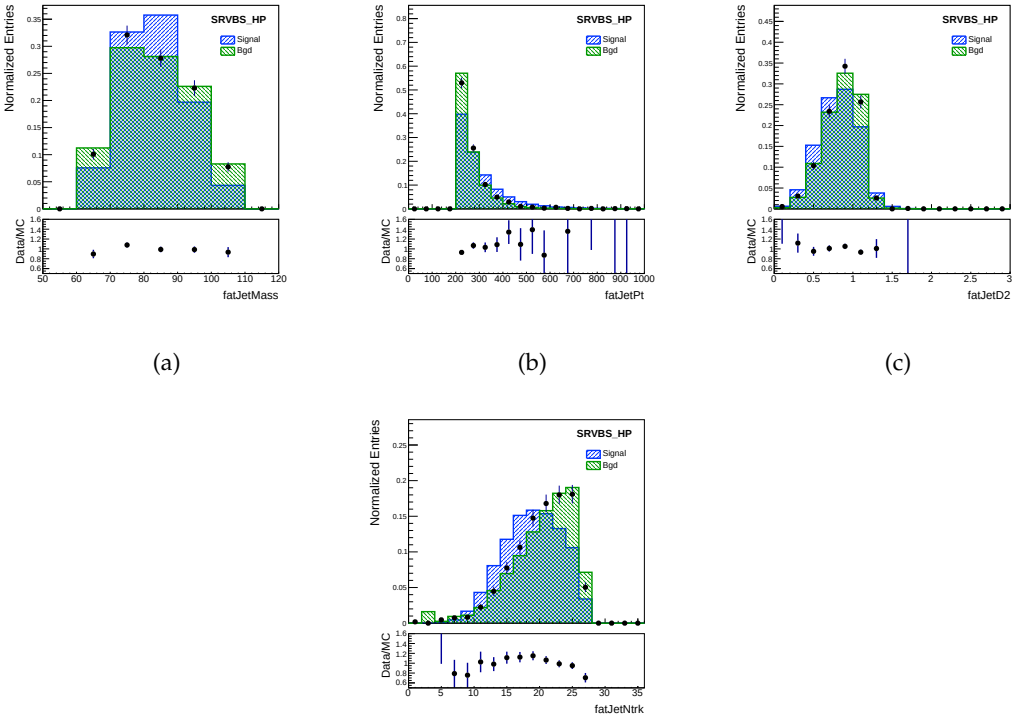

(a) (b) (c)

(d)

FIGURE A.6: Figures related to the large-R jet candidate (denoted as fatJet in the plots) for the merged HP signal region.

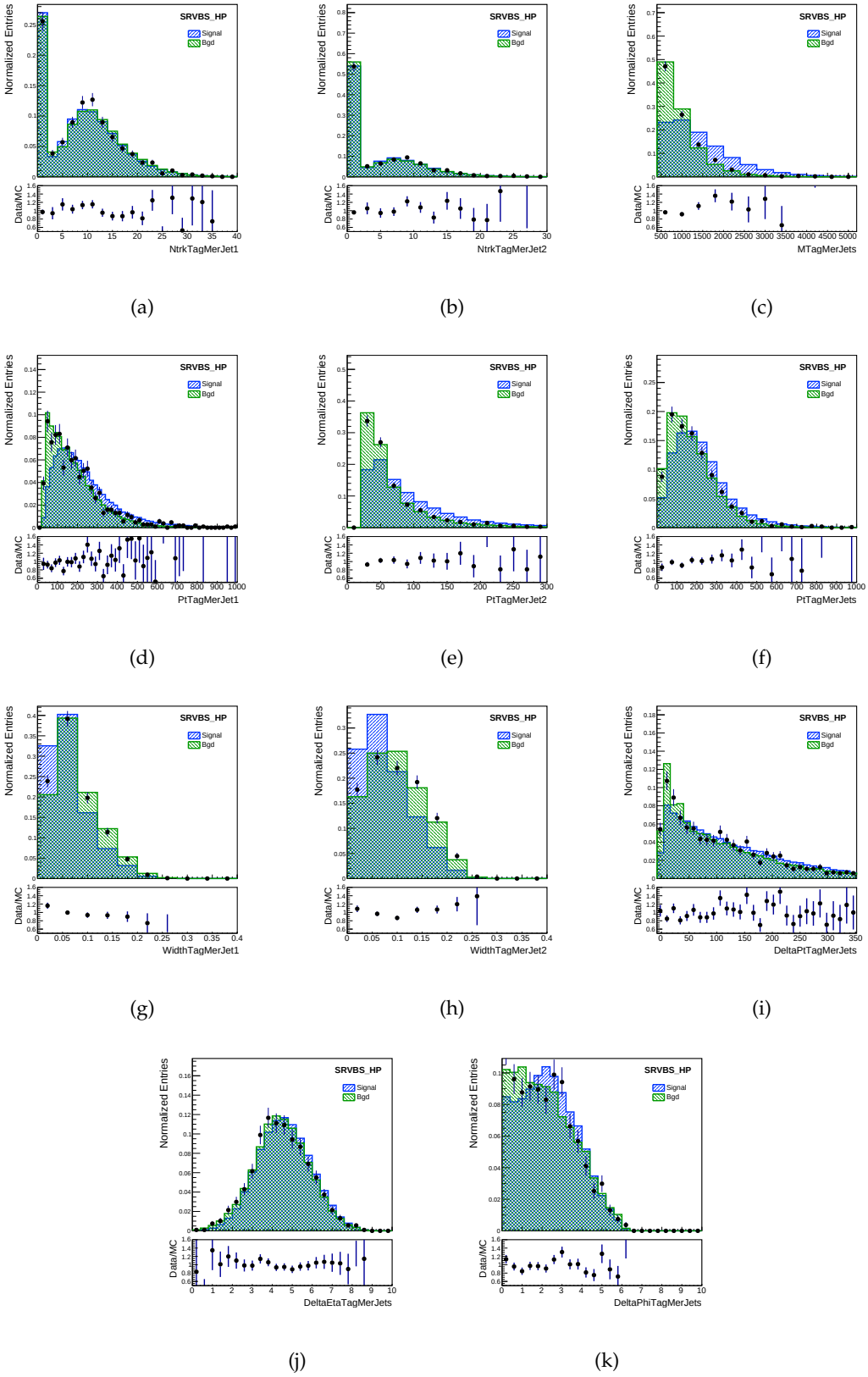

(a) (b) (c)

(d) (e) (f)

(g) (h) (i)

(j) (k)

FIGURE A.7: Figures related to the tagging jets.

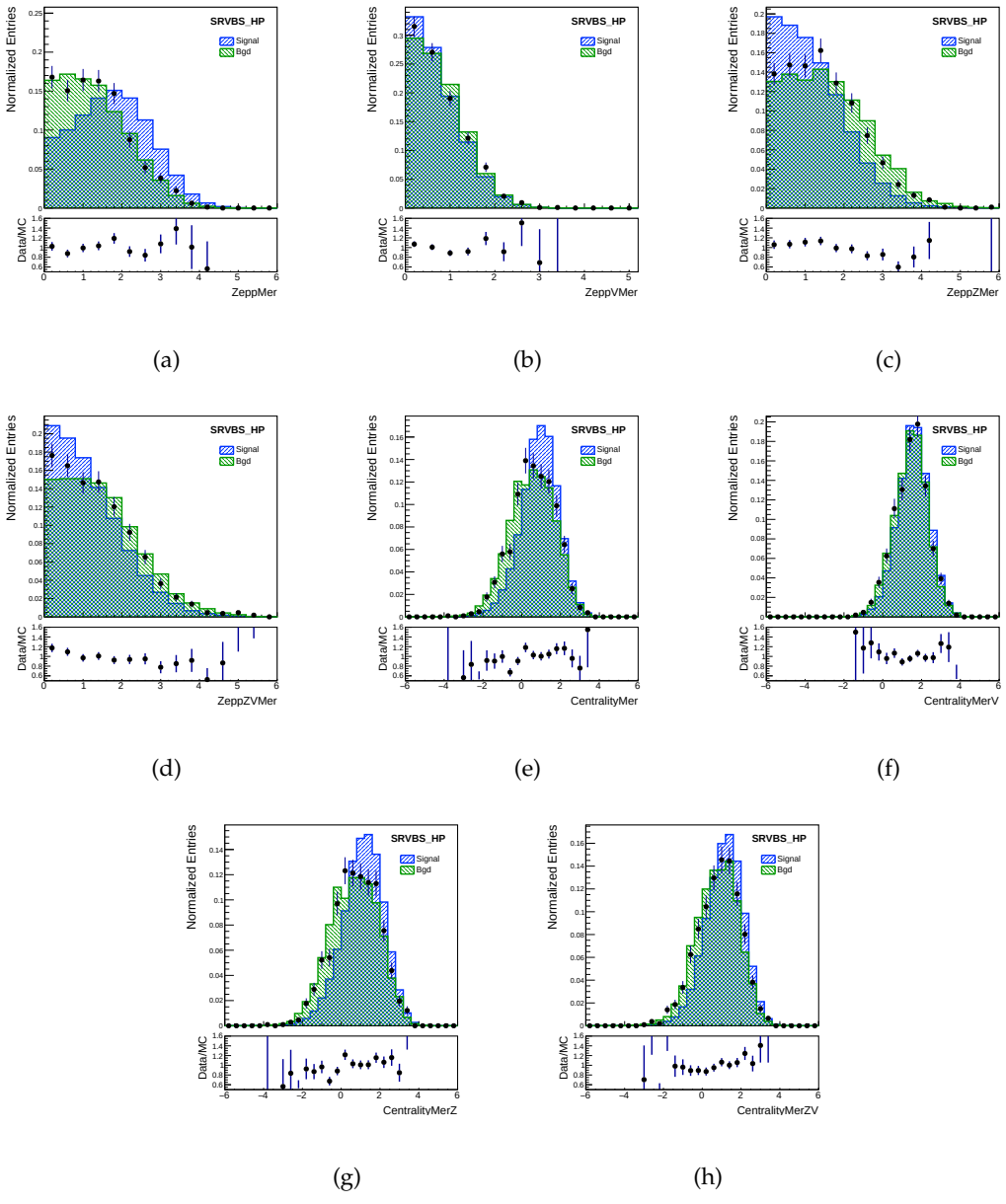

(a) (b) (c)

(d) (e) (f)

(g) (h)

FIGURE A.8: Figures related to other variables for the merged HP signal region.

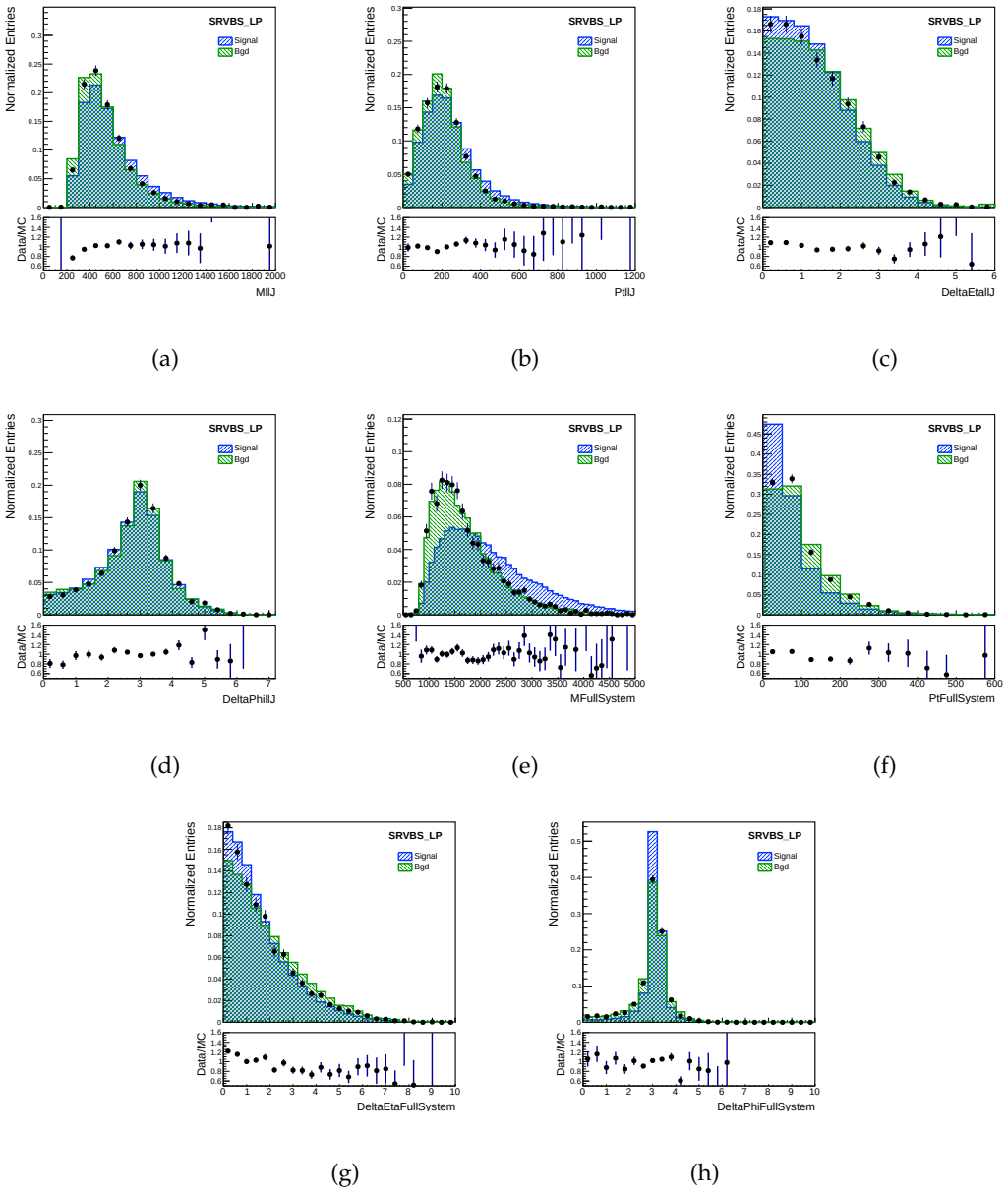

(a) (b) (c)

(d) (e) (f)

(g) (h)

FIGURE A.9: llJ and full system related plots for the merged LP signal region.

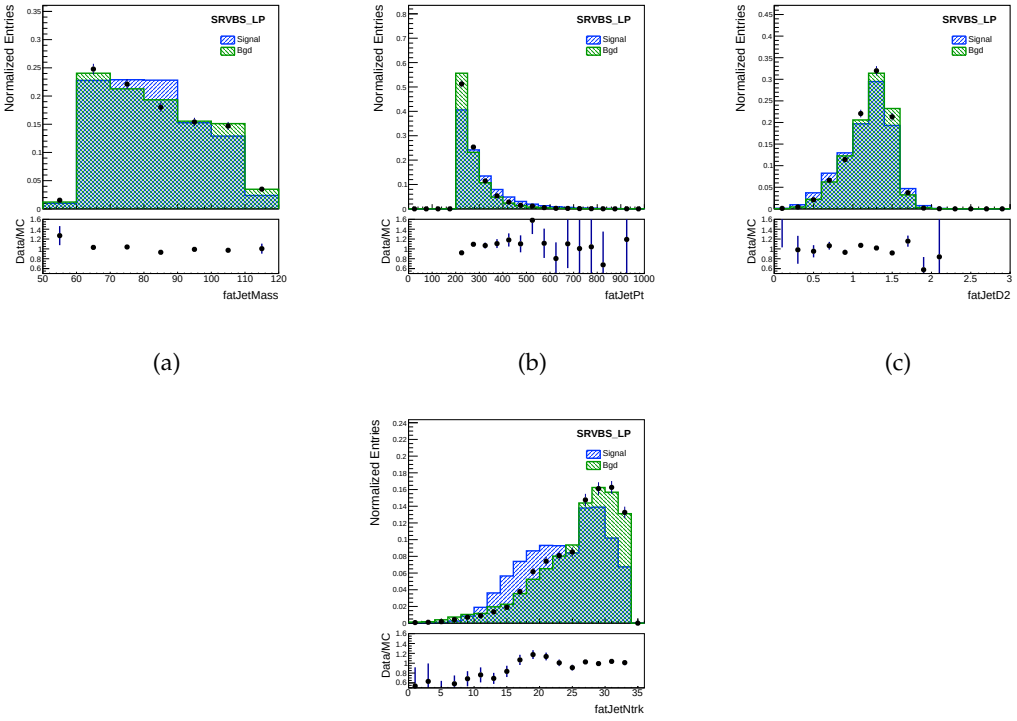

(a) (b) (c)

(d)

FIGURE A.10: Figures related to the large-R jet candidate (denoted as fatJet in the plots) for the merged LP signal region.

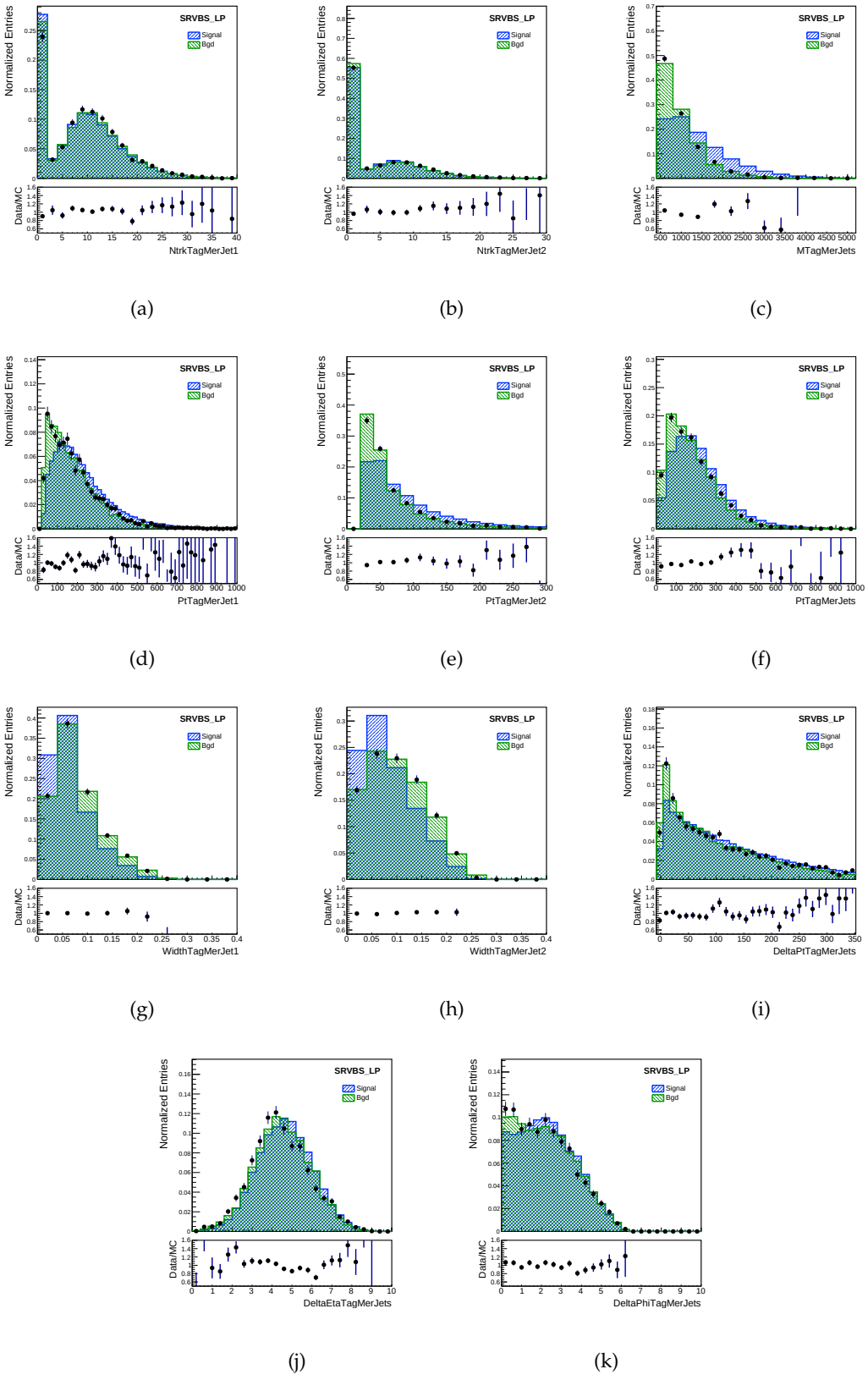

FIGURE A.11: Figures related to the tagging jets.

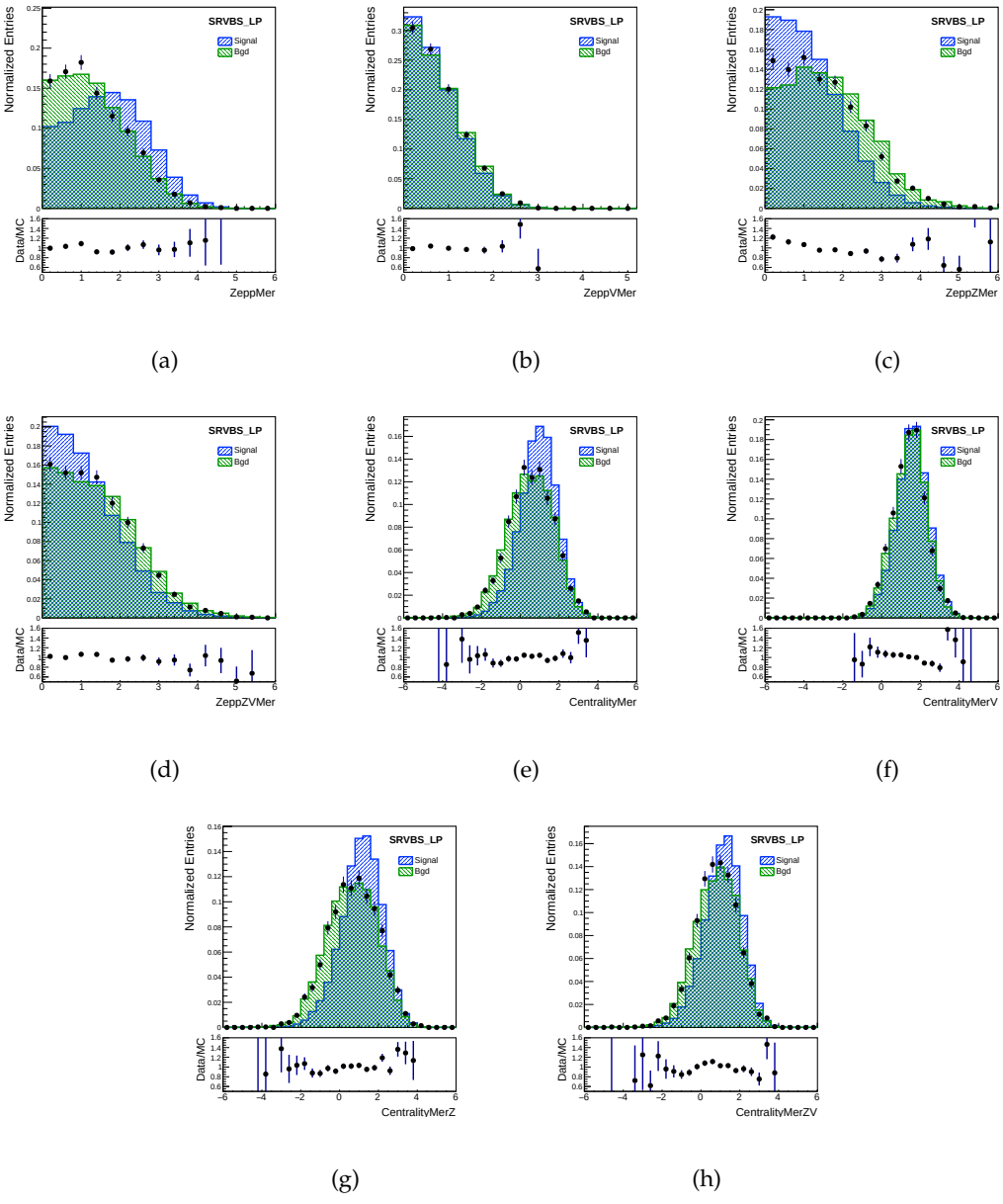

(a) (b) (c)

(d) (e) (f)

(g) (h)

FIGURE A.12: Figures related to other variables for the merged LP signal region.

B. BDT trainings

BDT training distributions

This appendix contains the modeling plots for all the features used in the BDT trainings described in Section 6.7.

B.1 Merged HP SR

The BDT score distributions, for the different folds in the merged HP SR, and for types A and B of training, are plotted in Figures B.1 and B.2 respectively.

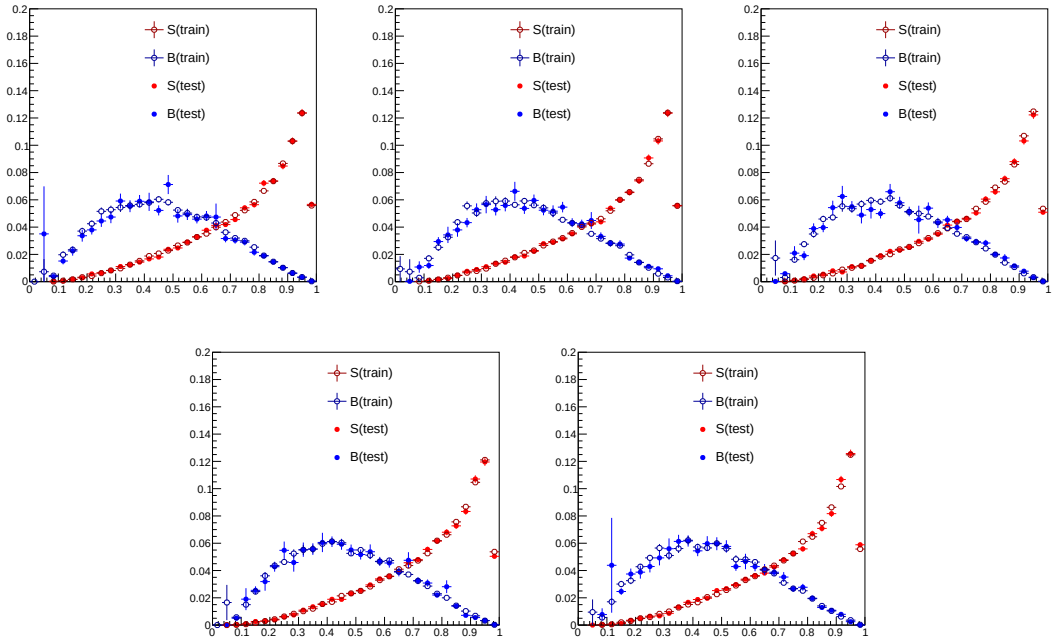

FIGURE B.1: BDT scores of the different folds in the merged HP SR . The BDTs were trained in the inclusive merged SR.

B.2 Merged LP SR

The BDT score distributions, for the different folds in the merged LP SR, and for types A and B of training, are plotted in Figures B.3 and B.4 respectively.

B.3 Resolved SR

The BDT score distributions, for the different folds in the resolved tight SR, and for types C and D of training, are plotted in Figures B.5-B.6.

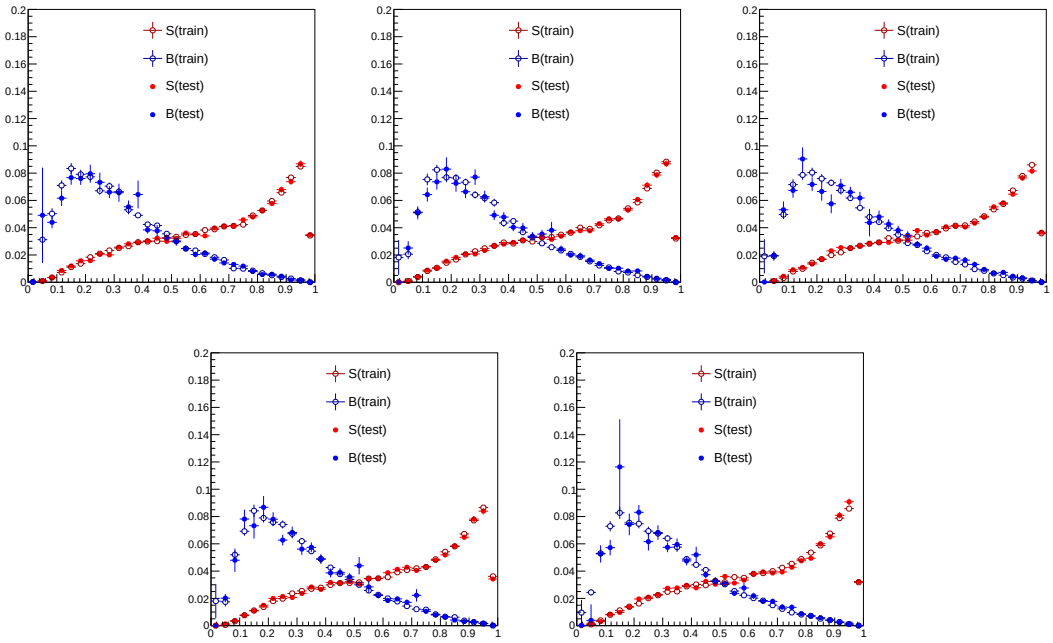

FIGURE B.2: BDT scores of the different folds in the merged HP SR . The BDTs were trained in the merged HP SR.

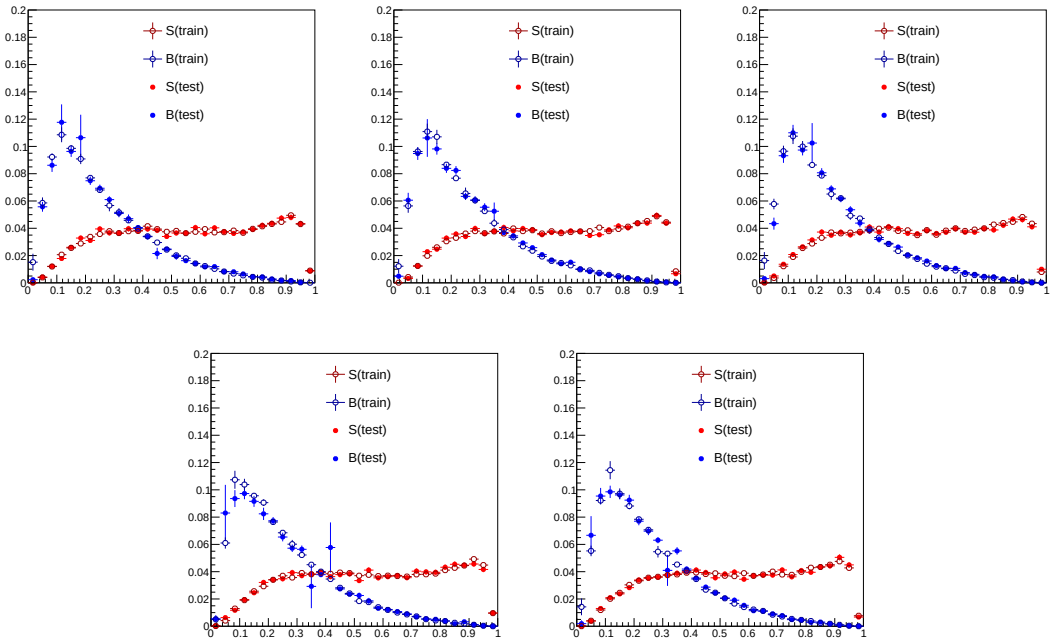

FIGURE B.3: BDT scores of the different folds in the merged LP SR . The BDTs were trained in the inclusive merged SR.

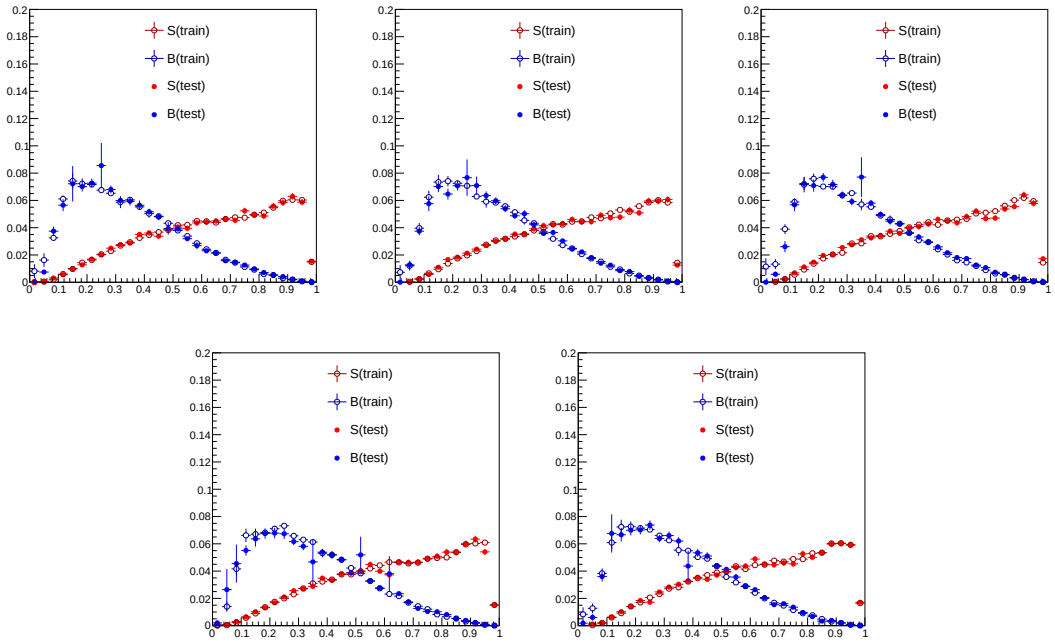

FIGURE B.4: BDT scores of the different folds in the merged LP SR . The BDTs were trained in the merged LP SR.

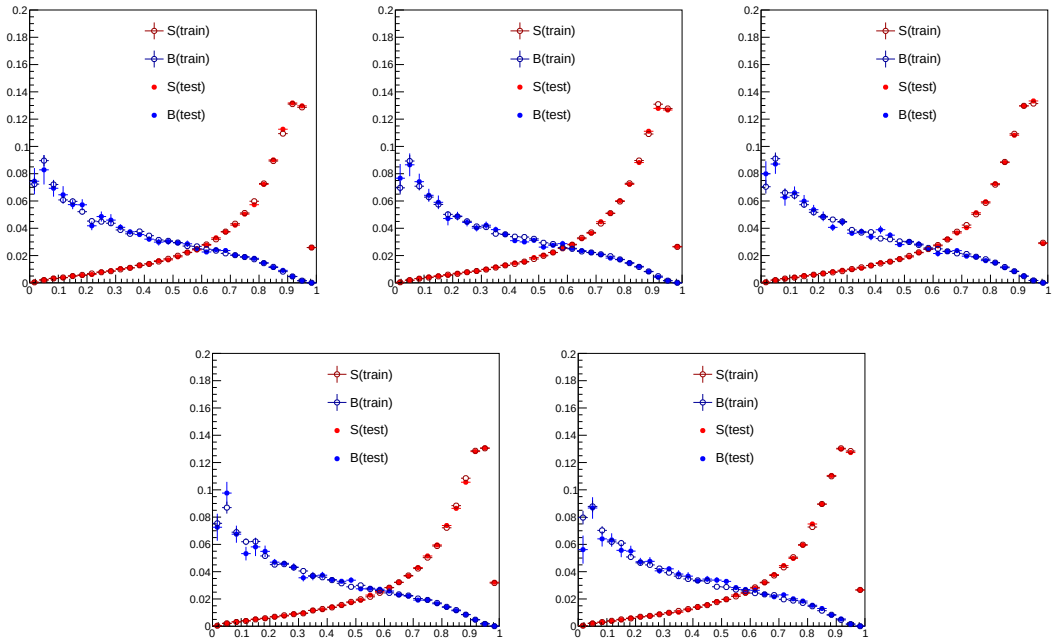

FIGURE B.5: BDT scores of the different folds in the tight resolved SR . The BDTs were trained in the loose resolved SR.

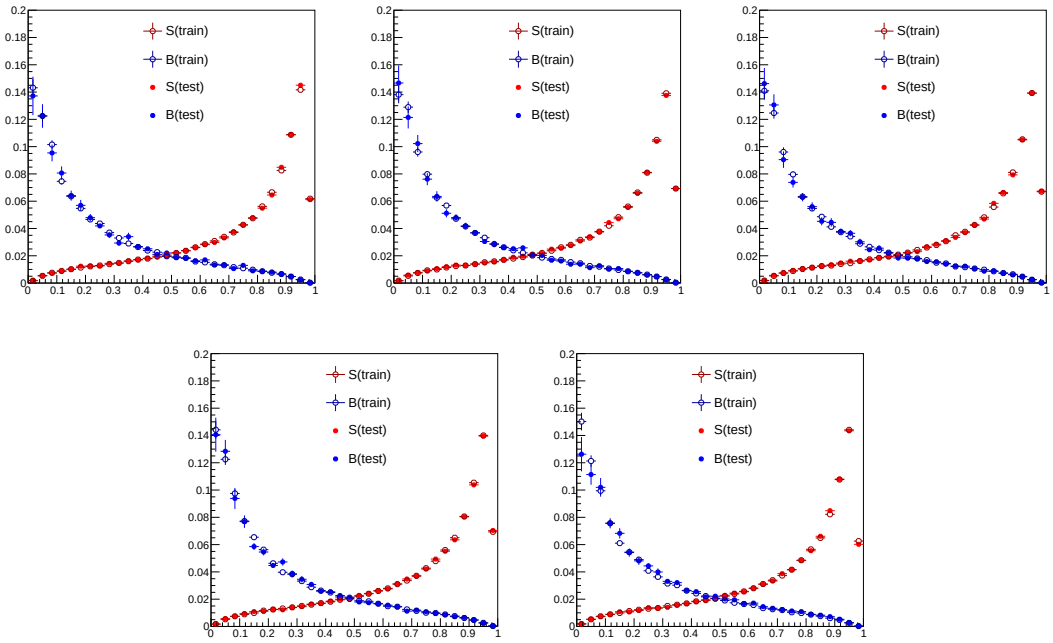

FIGURE B.6: BDT scores of the different folds in the tight resolved SR . The BDTs were trained in the tight resolved SR.

C. W/Z tagger scale factors

Effect of W/Z tagger scale factors in merged regions

C.1 Merged CR and SFs

In the left side of Figure C.1, a schematic of the merged analysis regions, as defined in the previous round of the analysis [26], is shown. In this approach a HP and LP signal region is defined by requiring the large-R jet signal candidate to pass the 50% or 80% working point (WP) tagger requirements respectively. Priority is given to the merged HP regime, thus events fulfilling the HP SR requirements are not included in the LP SR. Two separate control regions for the HP and LP regimes were used to constrain the normalization of the V+jets background in the SRs. The HP(LP) CR was defined by requiring events to pass all the cuts of the HP(LP) signal region but fail the mass requirement of the 80% working point.

A new approach for evaluating the boson tagger performance has lately been adopted by ATLAS [84]. In the new approach, scale factors (SFs) are derived in order to quantify the relative performance of the tagger in data versus MC. Efficiency scale factors (SF_{eff}) are available for large-R jets passing the 50%(80%) working point tagger requirements. Inefficiency scale factors (SF_{ineff}) for jets failing the tagger requirements are also provided and given as a function of the SF_{eff}:

$$SF_{ineff} = \frac{1 - \epsilon \times SF_{eff}}{1 - \epsilon}$$

, where ϵ is the efficiency estimated in tt-bar events for signal, and in γ+jet and multi-jet events for background.

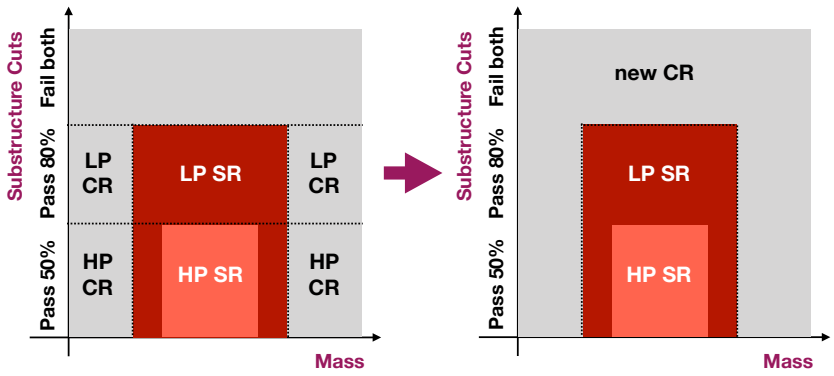

(a)

FIGURE C.1: Old (left plot) and new (right plot) region definitions for merged regime.

SFs are not defined for cases where the large-R jet passes only a number of the tagger

requirements. Therefore, the old merged CR definitions can not be used anymore, since no SFs are available for these regimes. A new single more inclusive control region is defined, as shown in the right side of Figure C.1. This is defined by events failing any of the 80% working point tagger requirements. Thus, for events falling in this region, the inefficiency scale factors, $SF_{ineff,loose}$, calculated for the 80% working point tagger are applied. The new CR is expected to constrain the normalization of the Z + jets process in both the merged HP and LP signal regions. The Z + jets contributions in the merged regions are summarized in Table C.1. The Data/MC$_{Z\,+\,\text{jets}}$ ratios are also shown, after substructing the non-Z + jets background from data. The three regions show compatible data/MC agreement, after also considering uncertainties described in 6.8.1.

The effect of the tagger SFs in the new merged CR for signal and background events is shown in Figures C.3 and C.2, respectively, plotted for various Large-R jet related variables. The effect of the SFs in the merged CR, is found to be rather flat and have negligible impact for background events(∼2%), while have a normalization impact of around 4% for signal.

TABLE C.1: Z + jets and data yields in the merged regions.

region	Merged CR	Merged LP SR	Merged HP SR
Data	6159.81	2292.39	819.07
Z + jets	7911.82	3143.88	1077.61
Data/MC$_{Z\,+\,\text{jets}}$	0.78	0.73	0.76

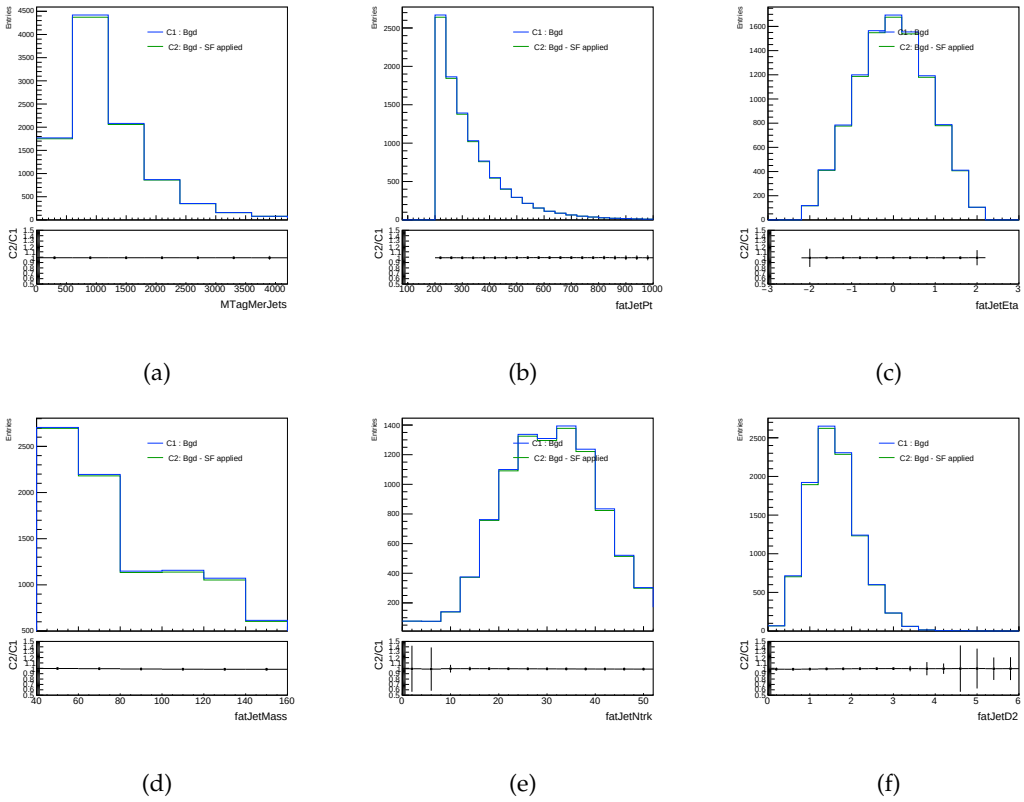

(a) (b) (c)

(d) (e) (f)

FIGURE C.2: Effect of tagger SFs on the main background in the new merged CR of the 2-lepton channel.

C.2 Merged LP SR and SFs

The LP signal region is defined by events passing the 80% but failing the 50% WP tagger requirements. Therefore the $SF_{eff,loose}$ estimated for jets passing the 80% WP can not be used alone. Instead a custom SF is used, defined as:

$$SF_{LP} = \frac{\epsilon_{loose} SF_{eff,loose} - \epsilon_{tight} SF_{eff,tight}}{\epsilon_{loose} - \epsilon_{tight}}$$

.

The effect of the tagger SFs in the merged LP SR for signal and background events is shown in Figures C.5 and C.4, respectively, plotted for various Large-R jet related variables. The SFs are found to have a negligible impact on the normalization of the signal yield, while affect up to 6% the normalization of the Z + jets background.

C.3 Merged HP SR and SFs

In the HP SR the $SF_{eff,tight}$ scale factors derived for events passing the 50% WP tagger requirements are applied. The effect of the tagger SFs in the HP SR for signal and background events is shown in Figures C.7 and C.6, respectively, plotted for various Large-R jet related variables. The SFs are found have a normalization impact of around +4% for the Z + jets background events, and a -10% normalization impact on the signal yield.

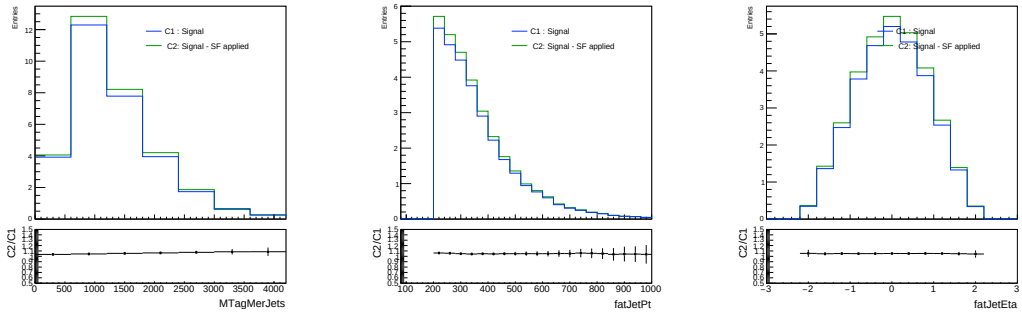

(a) (b) (c)

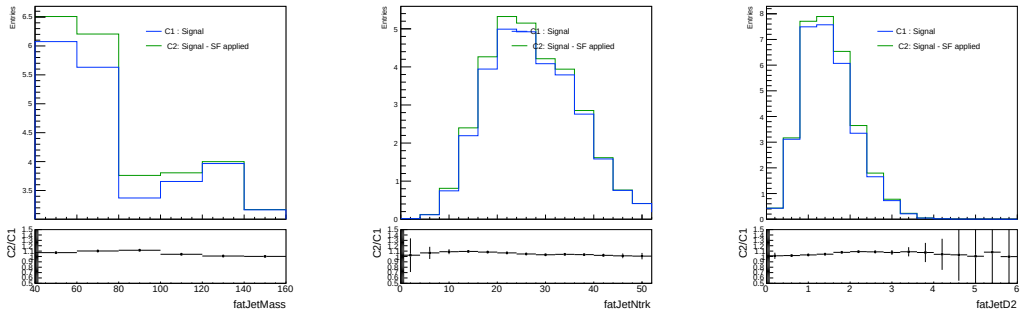

(d) (e) (f)

FIGURE C.3: Effect of tagger SFs on the signal in the new merged CR of the 2-lepton channel.

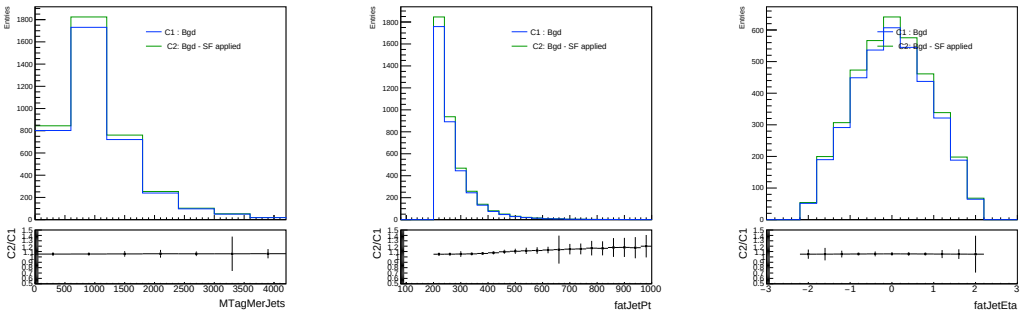

(a) (b) (c)

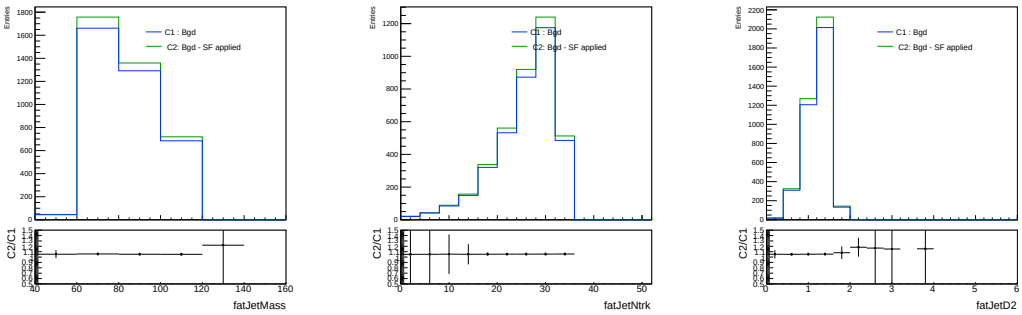

(d) (e) (f)

FIGURE C.4: Effect of tagger SFs on the main background in the LP SR of the 2-lepton channel.

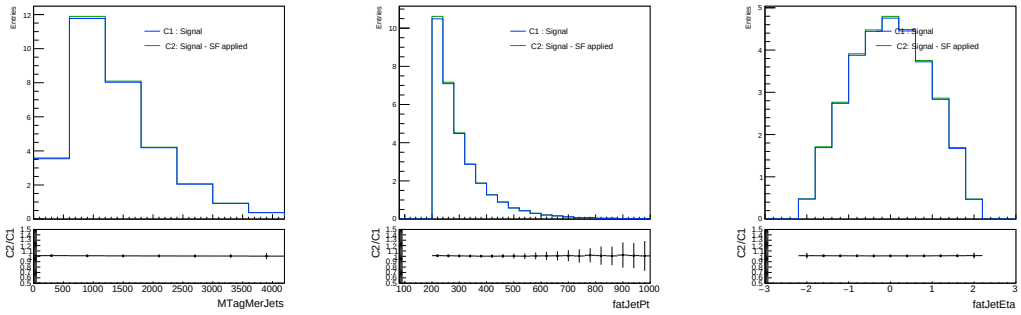

(a) (b) (c)

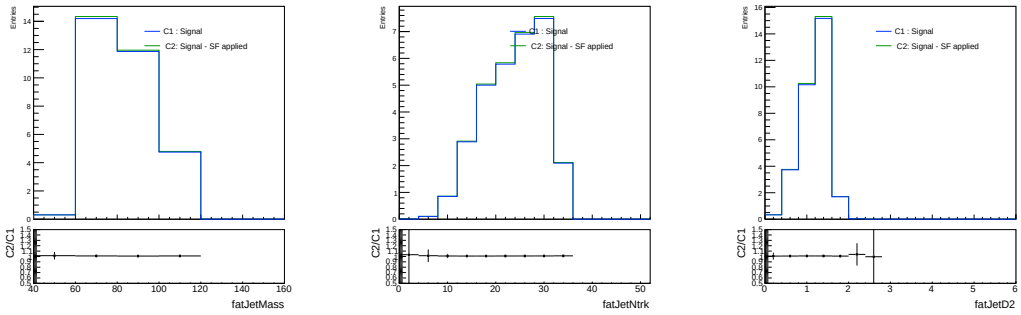

(d) (e) (f)

FIGURE C.5: Effect of tagger SFs on the signal in the LP SR of the 2-lepton channel.

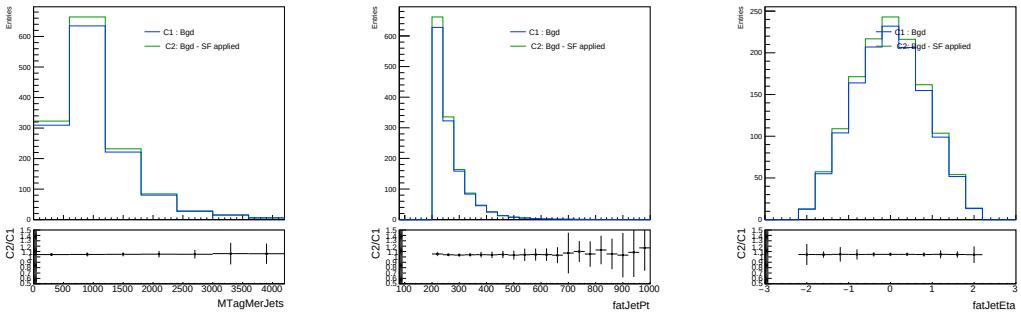

(a) (b) (c)

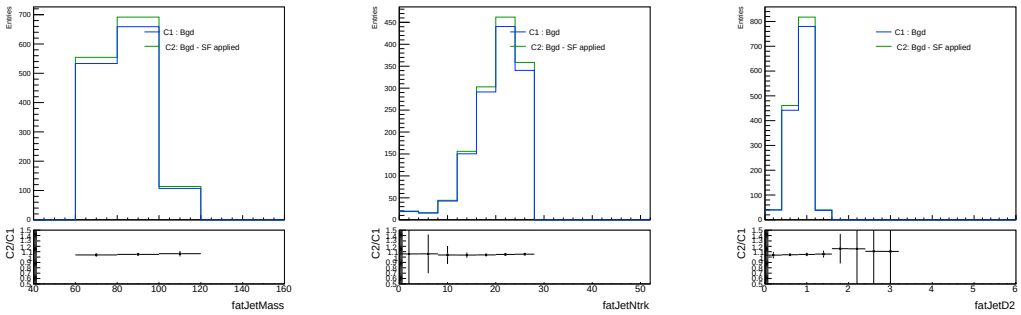

(d) (e) (f)

FIGURE C.6: Effect of tagger SFs on the main background in the HP SR of the 2-lepton channel.

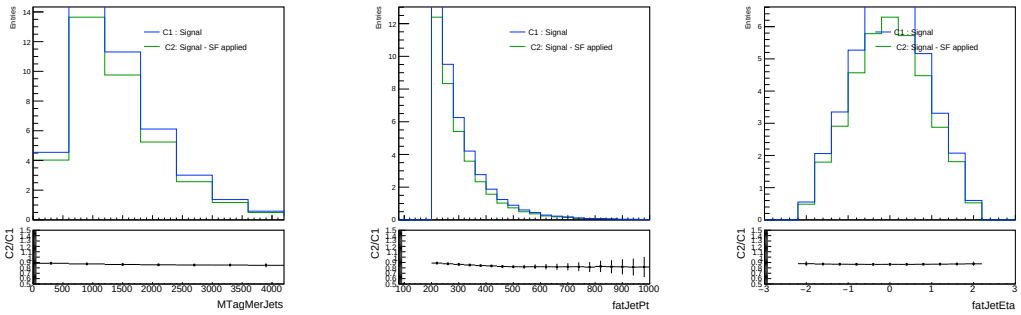

(a) (b) (c)

(d) (e) (f)

FIGURE C.7: Effect of tagger SFs on the signal in the HP SR of the 2-lepton channel.

D. Quark-Gluon fraction

Quark gluon fraction studies

The jet flavor response and composition uncertainties account for the different jet responses to quark- and gluon-initiated jets. The flavor response uncertainties are derived centrally from dijet events using alternative (Pythia 8 and Herwig++) Monte Carlo. Flavor composition uncertainties are usually derived assuming a 50/50 quark/gluon composition with a very conservative (100%) uncertainty. In VBS topologies where quark enriched regions are expected such uncertainties can limit the sensitivity of the measurement. In order to reduce such uncertainties, the gluon fraction in our analysis phase-space is studied and jet flavor related uncertainties are re derived using custom gluon fractions.

The gluon fraction in each of the analysis regions and for the different analysis samples is estimated as a function of the small-R jet p_{T} and η. Truth parton label information is used in order to estimate the number of quarks and gluons. All jets except b-quark-initiated jets are included in the denominator for the quark estimation.

In Figures D.1 and D.2 a comparison of the gluon fraction between the different analysis regions for the 2-lepton channel main MC samples is plotted as a function of p_{T} and η respectively. A clear p_{T} and η dependance of the gluon fraction is noticed.

2D histograms of the gluon fraction as a function of p_{T} and η are used as inputs to recalculate the jet flavor and composition uncertainties. A single input file per MC sample is used. The gluon fraction for a given bin in p_{T} and η is given after summing up all regions (nominal approach). This approach is very similar to computing the average gluon fraction between regions as shown by comparing the red and black histograms of Figure D.2. Additional inputs to describe the uncertainty on the gluon fraction are also provided. The uncertainty in a given p_{T}, η bin is given by:

$$\sigma_{gfrac} = \sqrt{\sigma^2_{region} + \sigma^2_{gen}}$$

where σ_{region} is the maximum difference in gluon fraction between nominal and an analysis region, σ_{gen} is the generator uncertainty derived using alternative Pythia 8 and Herwig MC samples. In Figures D.3 and D.4 a comparison of the nominal gluon fraction and gluon fraction as calculated by using alternative samples is plotted for the main background sources in the 2-lepton channel. For cases where alternative samples are not available (e.g for Signal) the region only uncertainties are considered.

The gluon fraction inputs and their corresponding uncertainties are plotted in Figures D.5 and D.6, respectively.

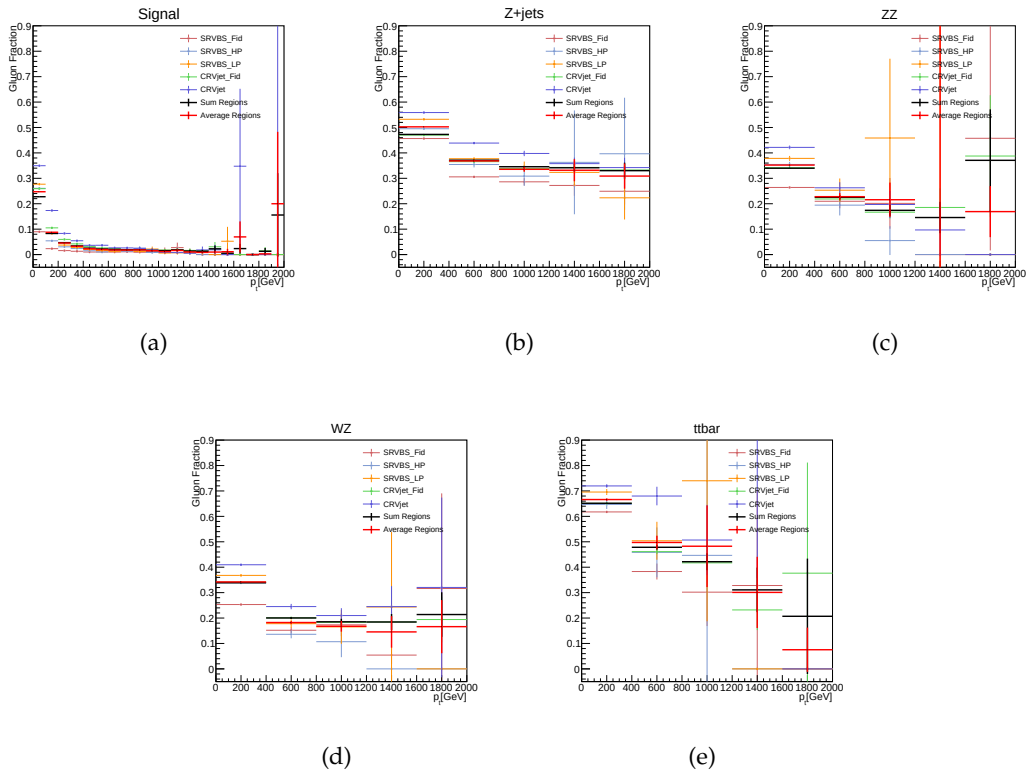

(a) (b) (c)

(d) (e)

FIGURE D.1: Gluon fraction as a function of p_T for the signal and main background sources in the 2-lepton channel.

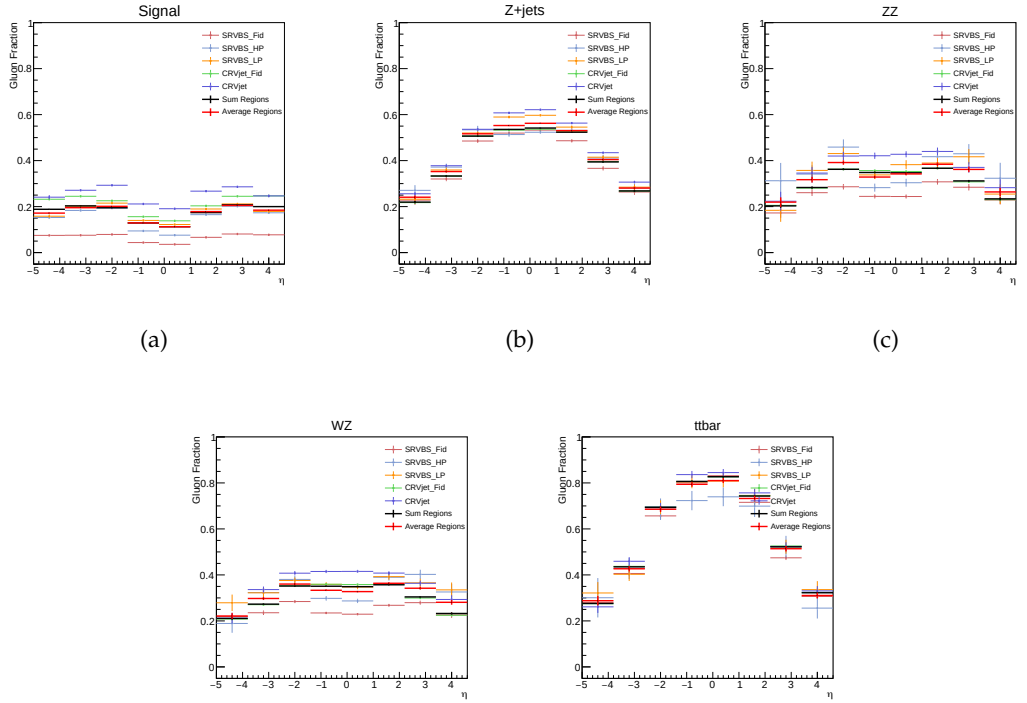

(a) (b) (c)

(d) (e)

FIGURE D.2: Gluon fraction as a function of η for the signal and main background sources in the 2-lepton channel.

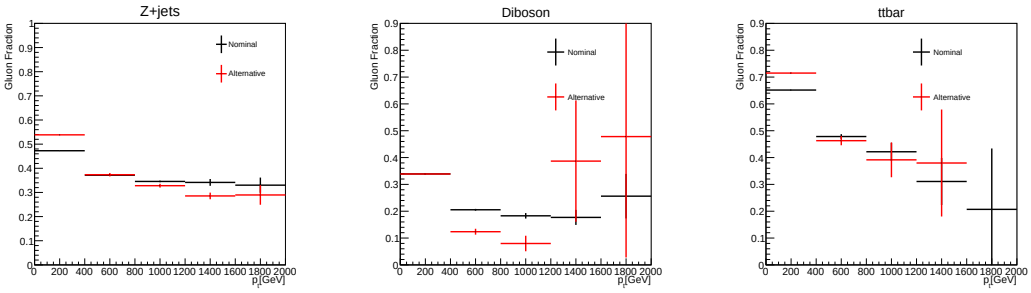

(a) (b) (c)

FIGURE D.3: Gluon fraction as a function of p_{T} for nominal and alternative samples in the 2-lepton channel. In all cases the gluon fraction is calculated after summing up all the analysis regions.

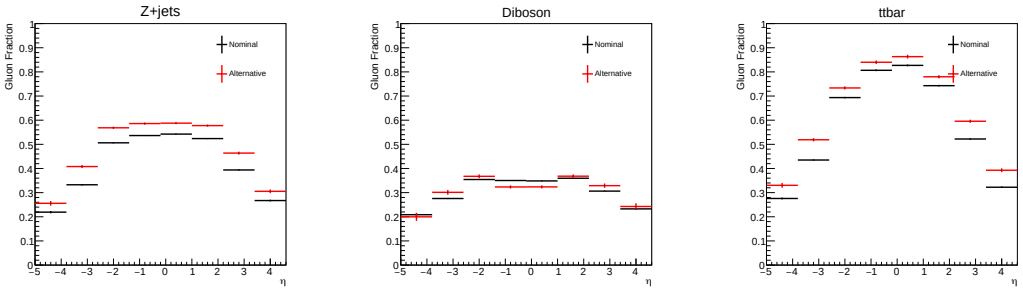

(a) (b) (c)

FIGURE D.4: Gluon fraction as a function of η for nominal and alternative samples in the 2-lepton channel. In all cases the gluon fraction is calculated after summing up all the analysis regions.

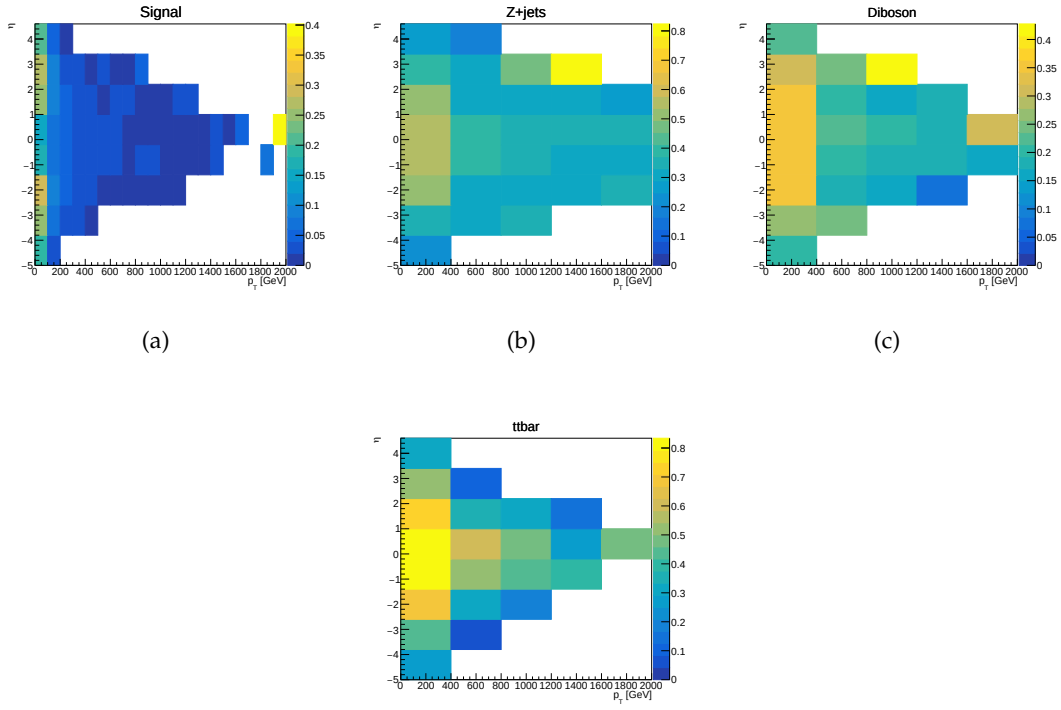

(a) (b) (c)

(d)

FIGURE D.5: Gluon fraction inputs for the 2-lepton channel.

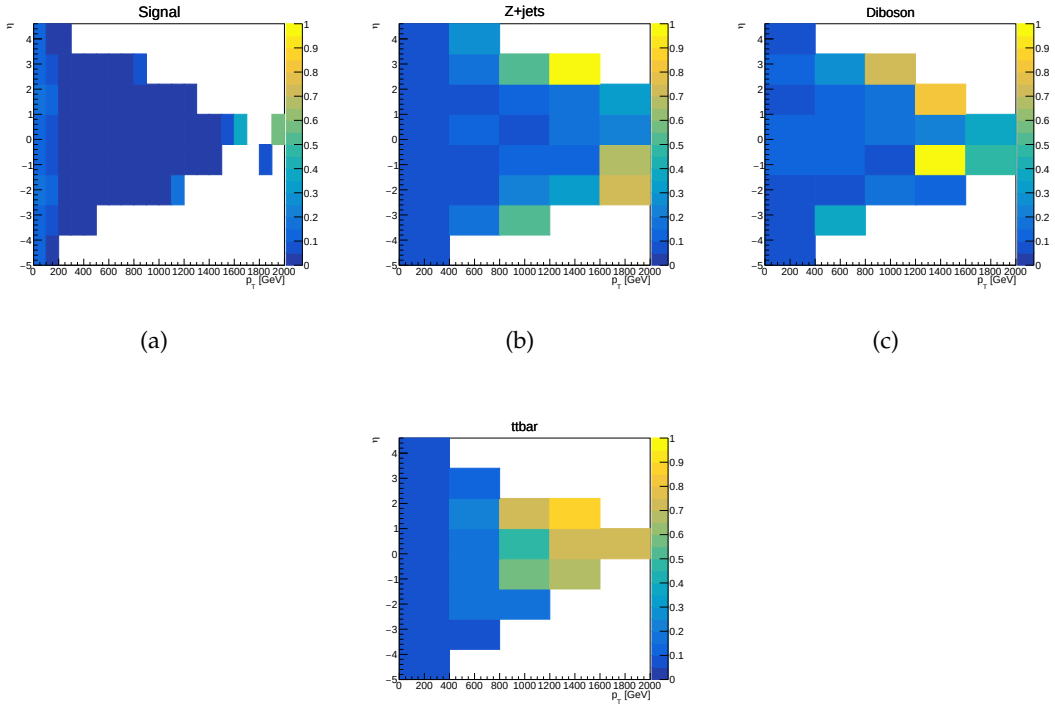

(a) (b) (c)

(d)

FIGURE D.6: Gluon fraction uncertainty inputs for the 2-lepton channel.

E. Signal jet selection for resolved

Signal jet selection in the resolved region

An optimization of the signal jet selection in the resolved regime is performed. In the baseline selection, as proposed in the previous round of the analysis [26], the signal jet pair with the invariant mass closest to the W/Z boson mass, is selected as the V_{had} candidate. In Figure E.1 , the invariant mass of the V_{had} candidate is plotted, for the baseline signal jet selection.

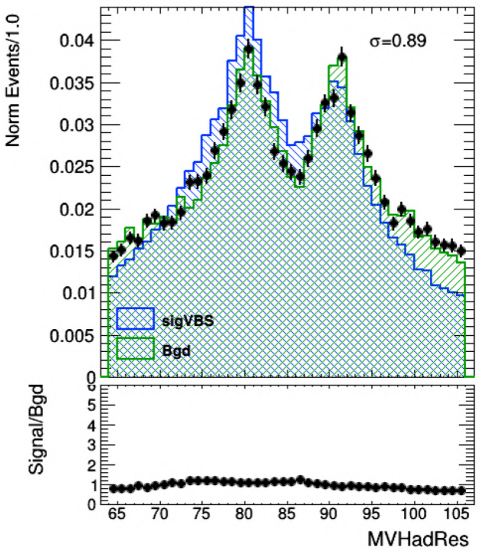

(a)

FIGURE E.1: Invariant mass of the signal jets for the baseline selection.

The binned significance for several variables is estimated, using equation 6.5 , assuming no background uncertainties. The following signal jet selections are tested:

- Baseline: Select the signal jet pair with invariant mass closest to the W/Z boson mass.
- LeadPt: Select the two small-R jets with the highest p_{T} of the event.
- Projection: Select the small-R jet pair with the largest projection of the $V_{lep}V_{had}$ system on the tagging jet system. This selection is motivated as the $V_{lep}V_{had}$ system is expected to balance the tagging jet system.
- Projection MET: This is very similar to the previous selection, but including the missing transverse energy (MET) in the projection calculation.
- Balance: Look for the $V_{lep}V_{had}$ system which best balances the tagging jet system.

The significance summary table is shown in Figure E.2. Tha baseline selection is found to overperform for the majority of variables plotted. The same test is repeated, after considering a fixed 20% uncertainty for the significance calculation. The updated summary plot is shown in Figure E.3. When considering uncertainties the baseline selection shows the worst performance. The rest of selections show very similar results. The leadPt selection is chosen for simplicity.

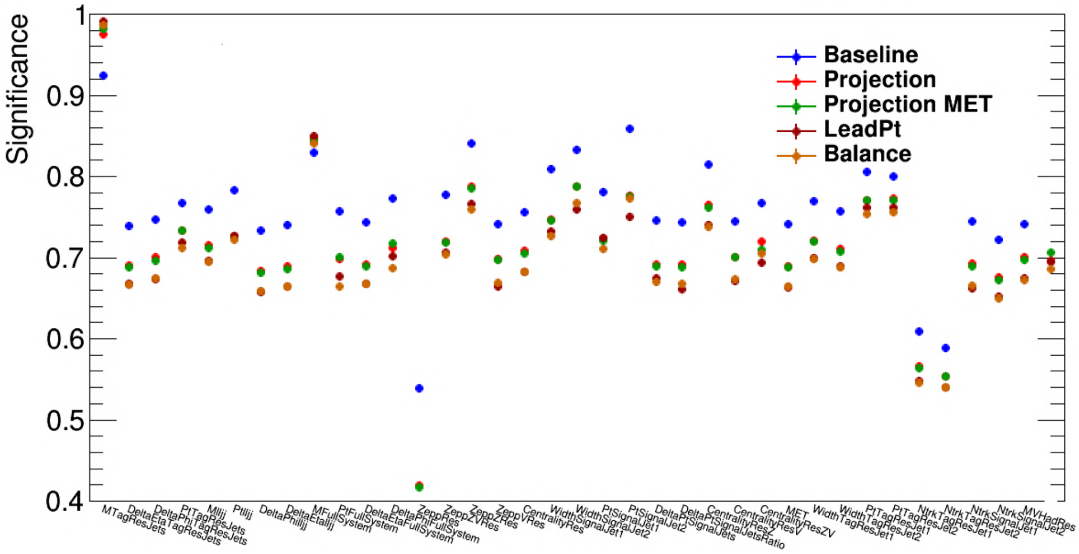

FIGURE E.2: Significance values for features in the resolved SR, estimated using Run1 data only. No background uncertainties are considered for the significance estimation.

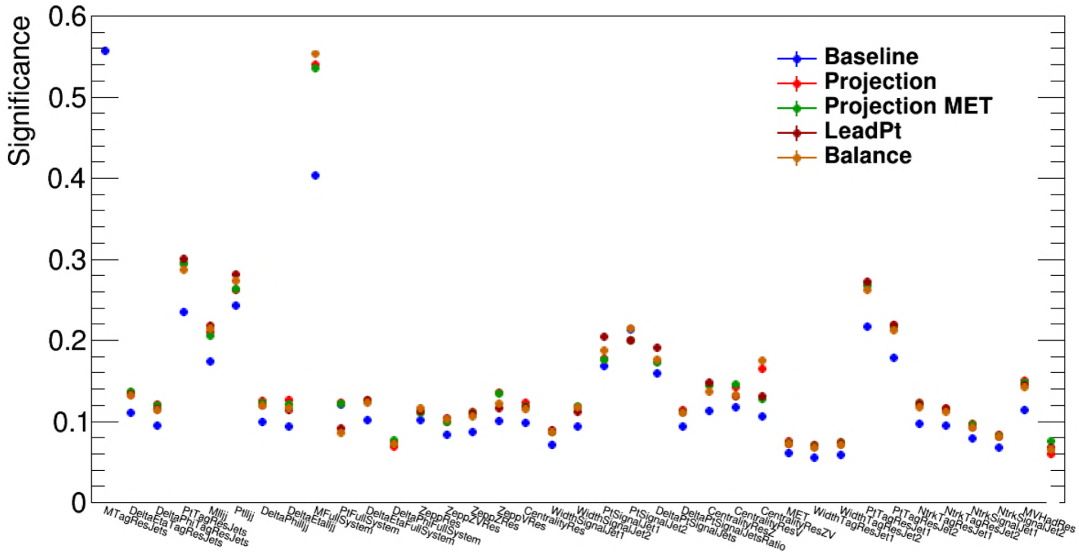

FIGURE E.3: Significance values for features in the resolved SR, estimated using Run1 data only. A 20% background uncertainty is considered for the significance estimation.

F. Model Inspection

Model inspection before un-blinding the VBS analysis

Asimov fits in full range

In Figure F.1 the nuisance parameter pulls and constraints are shown for the unconditional combined as well as individual resolved and merged fits performed to Asimov data. The corresponding correlation matrix for the combined fit is plotted in Figure F.2.

Asimov fits in blinded regions

In Figure F.3 the nuisance parameter pulls and constraints are shown for a simultaneous unconditional fit to SR and CR for the combined and individual regions to Asimov data in the 2-lepton channel. In the SRs the left bins of the BDT score are fitted only. The corresponding correlation matrix is plotted in Figure F.4.

Data fits in blinded regions

In Figure F.5 the nuisance parameter pulls and constraints are shown for a simultaneous unconditional fit to SR and CR for the combined and individual regions to observed data in the 2-lepton channel. In the SRs the left bins of the BDT score are fitted only. The corresponding correlation matrix is plotted in Figure F.6.

Figures F.7 and F.8 show the pre-fit and post-fit M_{jj}^{tag} and BDT score distributions, respectively.

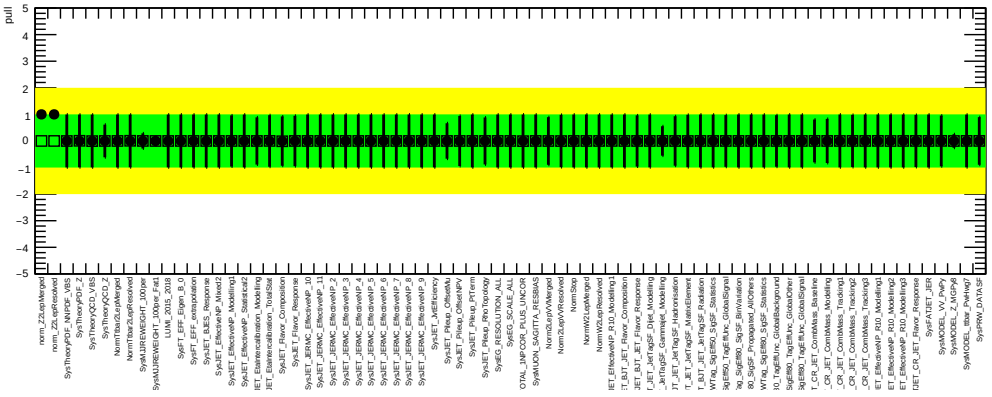

(a) Combined resolved and merged fit

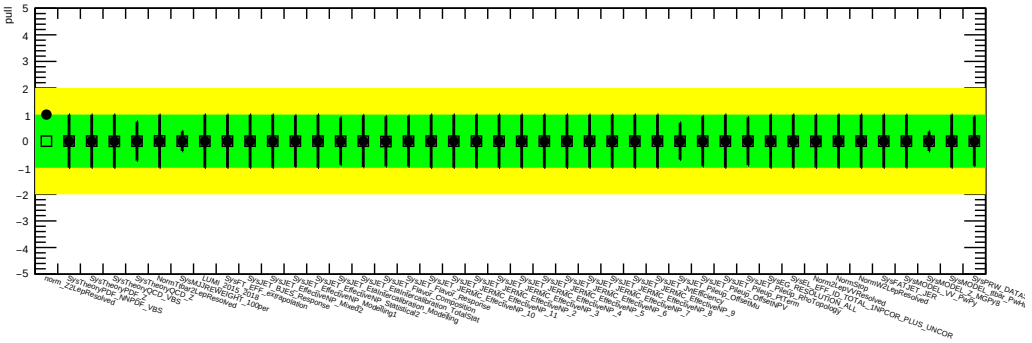

(b) Resolved only fit

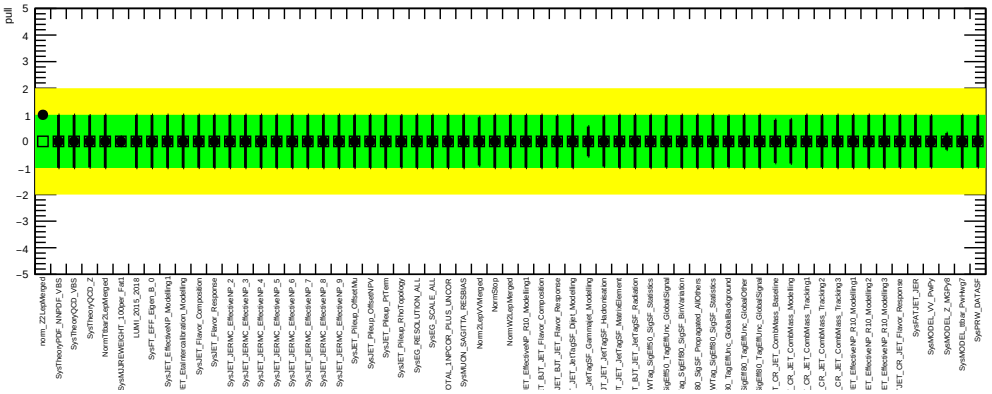

(c) Merged only fit

FIGURE F.1: Nuisance parameter pulls from the combined and individual region fits in the 2-lepton lepton channels with Asimov data. Simultaneous fits are performed in the full range of the BDT score in the SR and full range of the M_{jj}^{tag} in the CR.

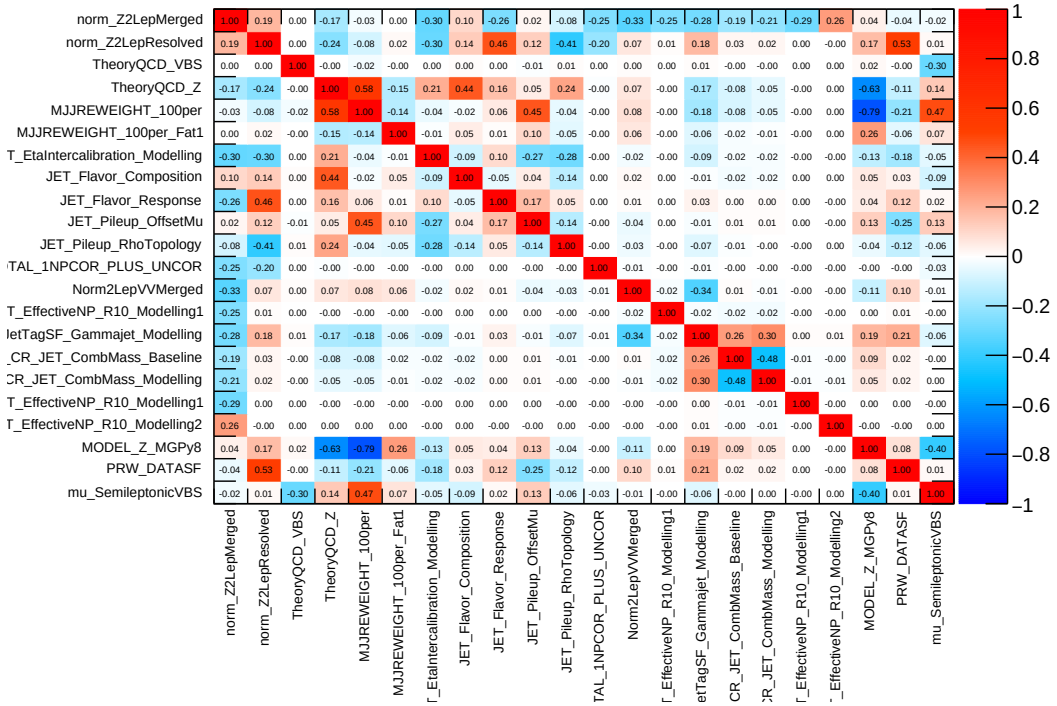

FIGURE F.2: Correlation matrix from the combined fit in the 2-lepton lepton channel with Asimov data. Simultaneous fits are performed in the full range of the BDT score in the SR and M_{jj}^{tag} distribution in the CR.

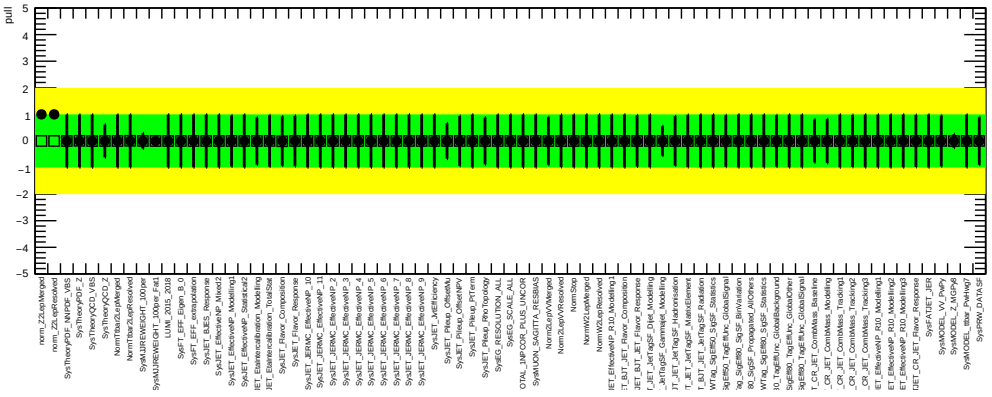

(a) Combined resolved and merged fit

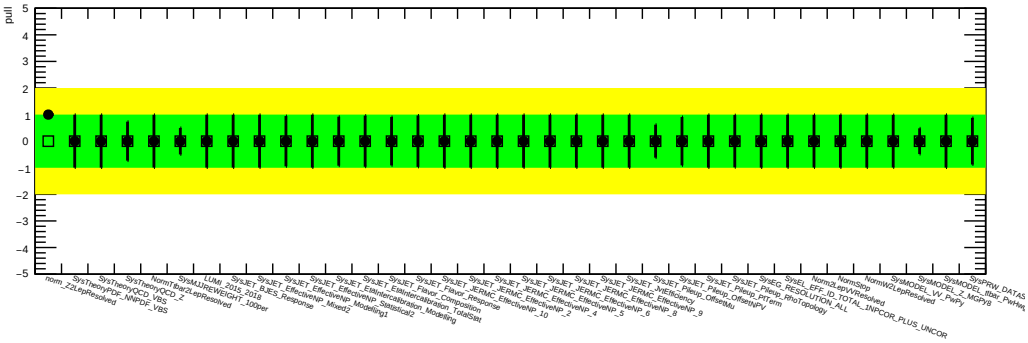

(b) Resolved only fit

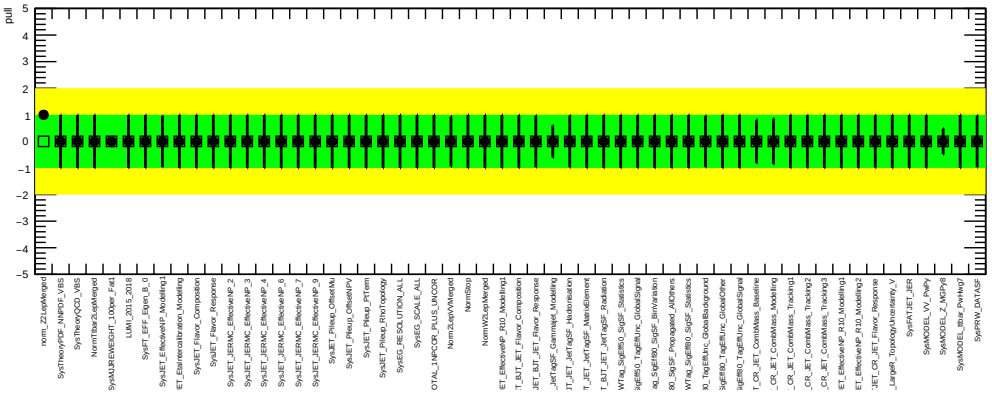

(c) Merged only fit

FIGURE F.3: Nuisance parameter pulls from the combined and individual region fits in the 2-lepton lepton channels with Asimov data. Simultaneous fits are performed in the left bins of the BDT score in the SR and full range of the M_{jj}^{tag} in the CR.

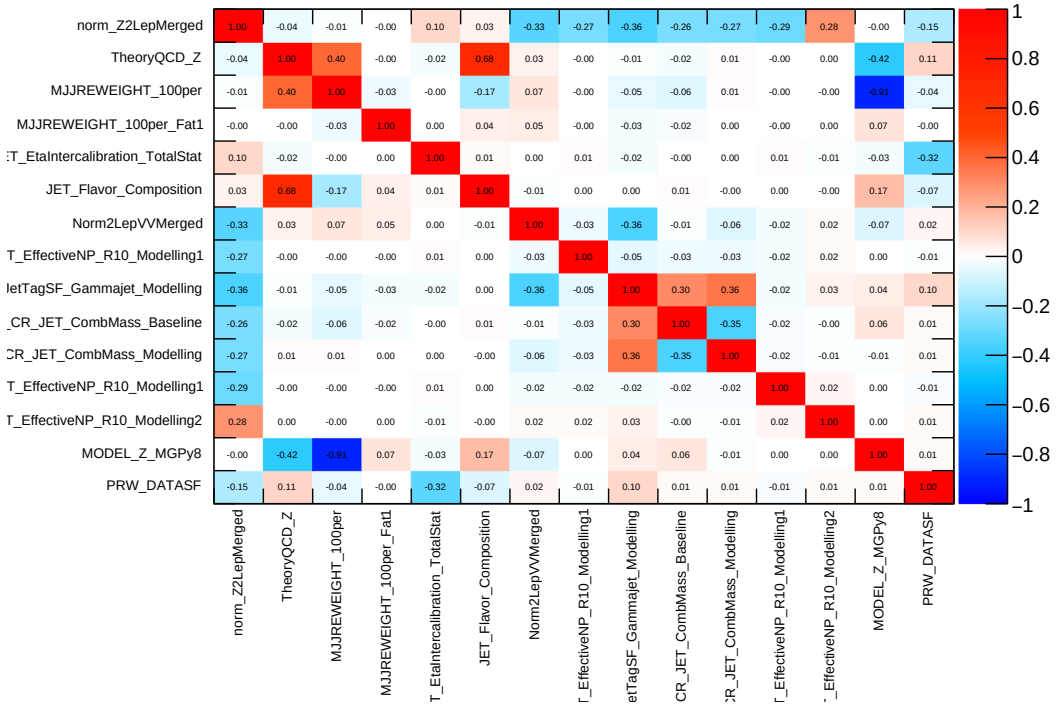

FIGURE F.4: Correlation matrix from the combined fit in the 2-lepton lepton channel with Asimov data. Simultaneous fits are performed in the left bins of the BDT score in the SR and in the full range of the M_{jj}^{tag} distribution in the CR.

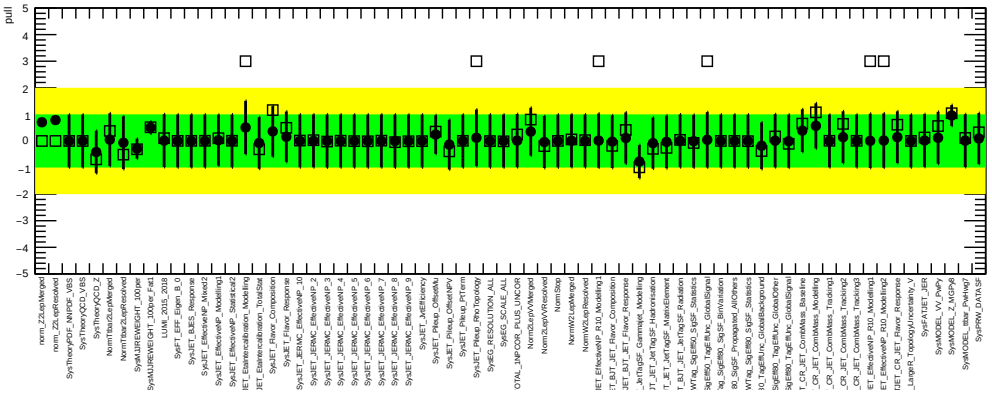

(a) Combined resolved and merged fit

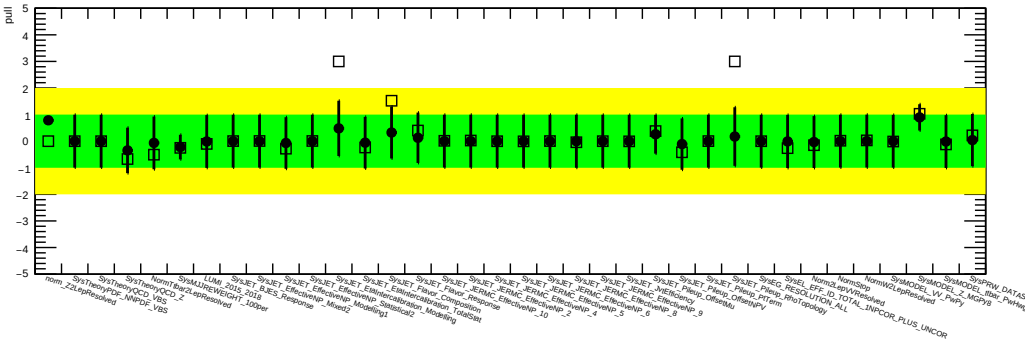

(b) Resolved only fit

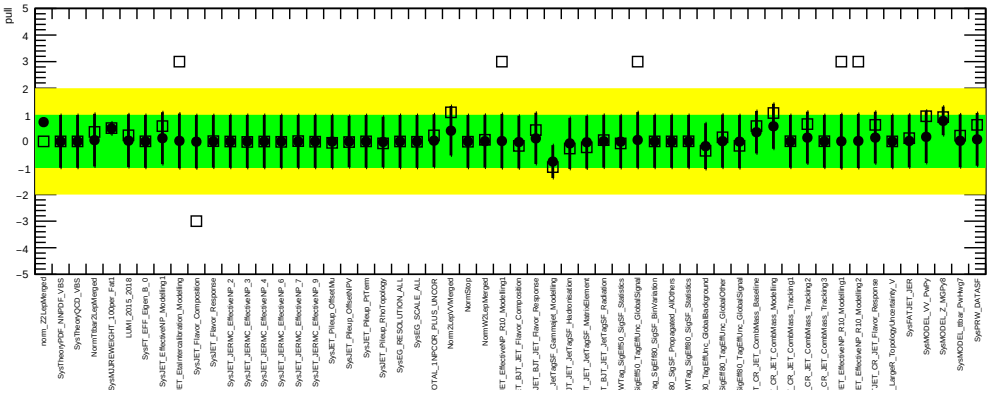

(c) Merged only fit

FIGURE F.5: Nuisance parameter pulls from the combined and individual region fits in the 2-lepton lepton channels with observed data. Simultaneous fits are performed in the left bins of the BDT score in the SR and full range of the M_{jj}^{tag} in the CR.

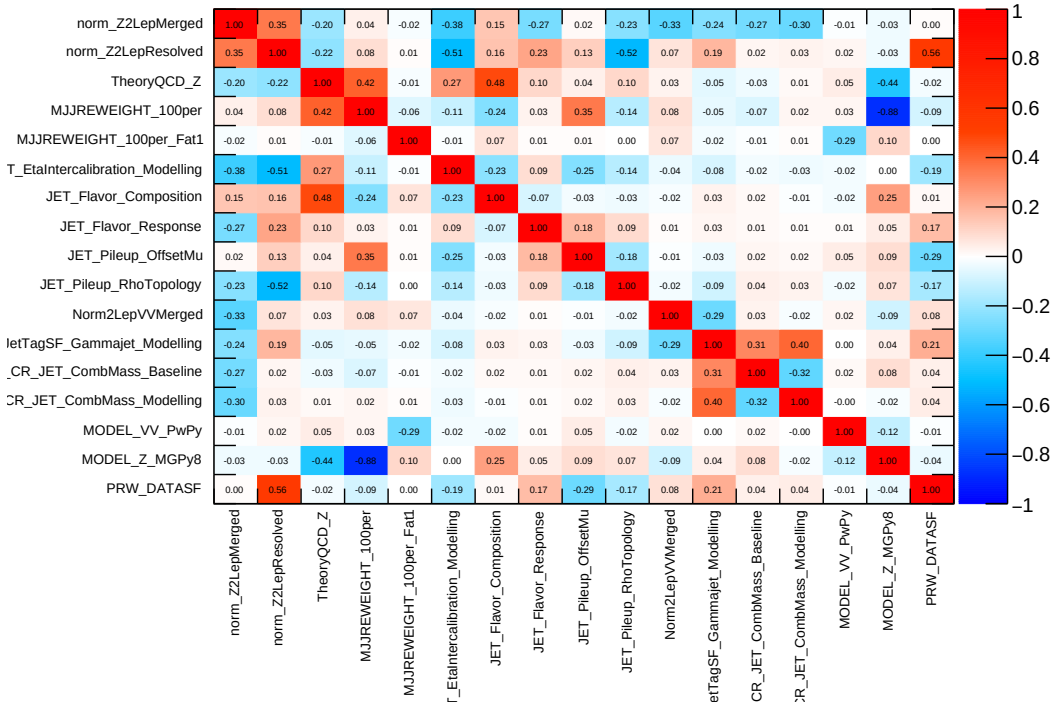

FIGURE F.6: Correlation matrix from the combined fit in the 2-lepton lepton channel with observed data. Simultaneous fits are performed in the left bins of the BDT score in the SR and in the full range of the M_{jj}^{tag} distribution in the CR.

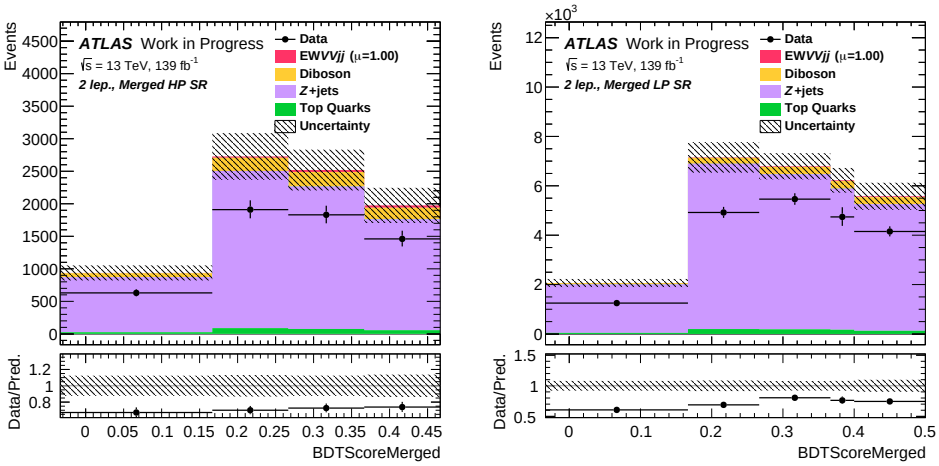

(a) Merged HP SR

(b) Merged LP SR

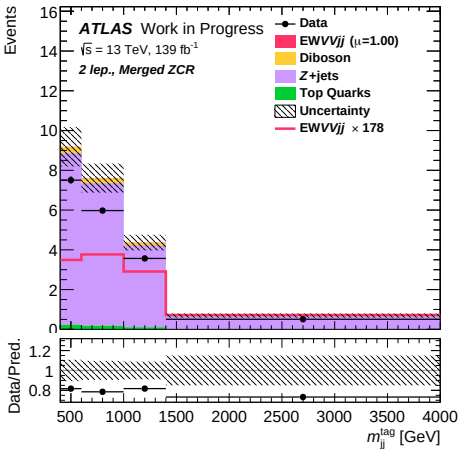

(c) Merged CR

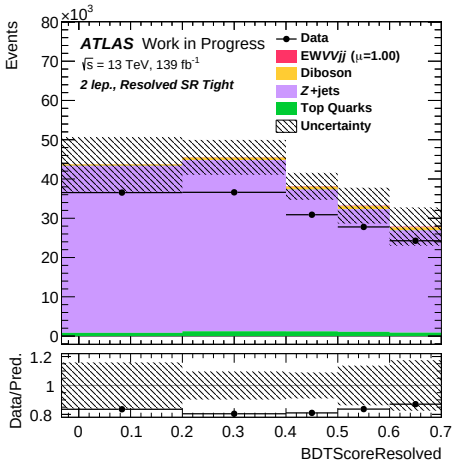

(d) Resolved SR

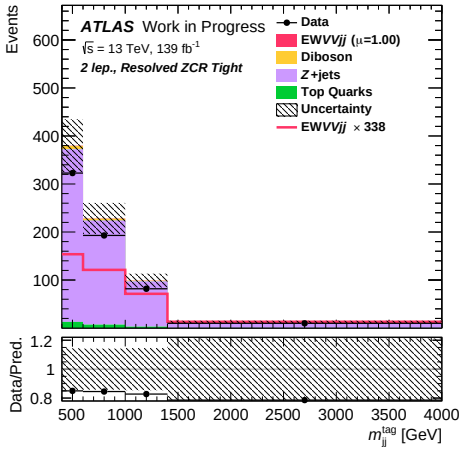

(e) Resolved CR

FIGURE F.7: Pre-fit distributions for the combined fit in the 2-lepton channel

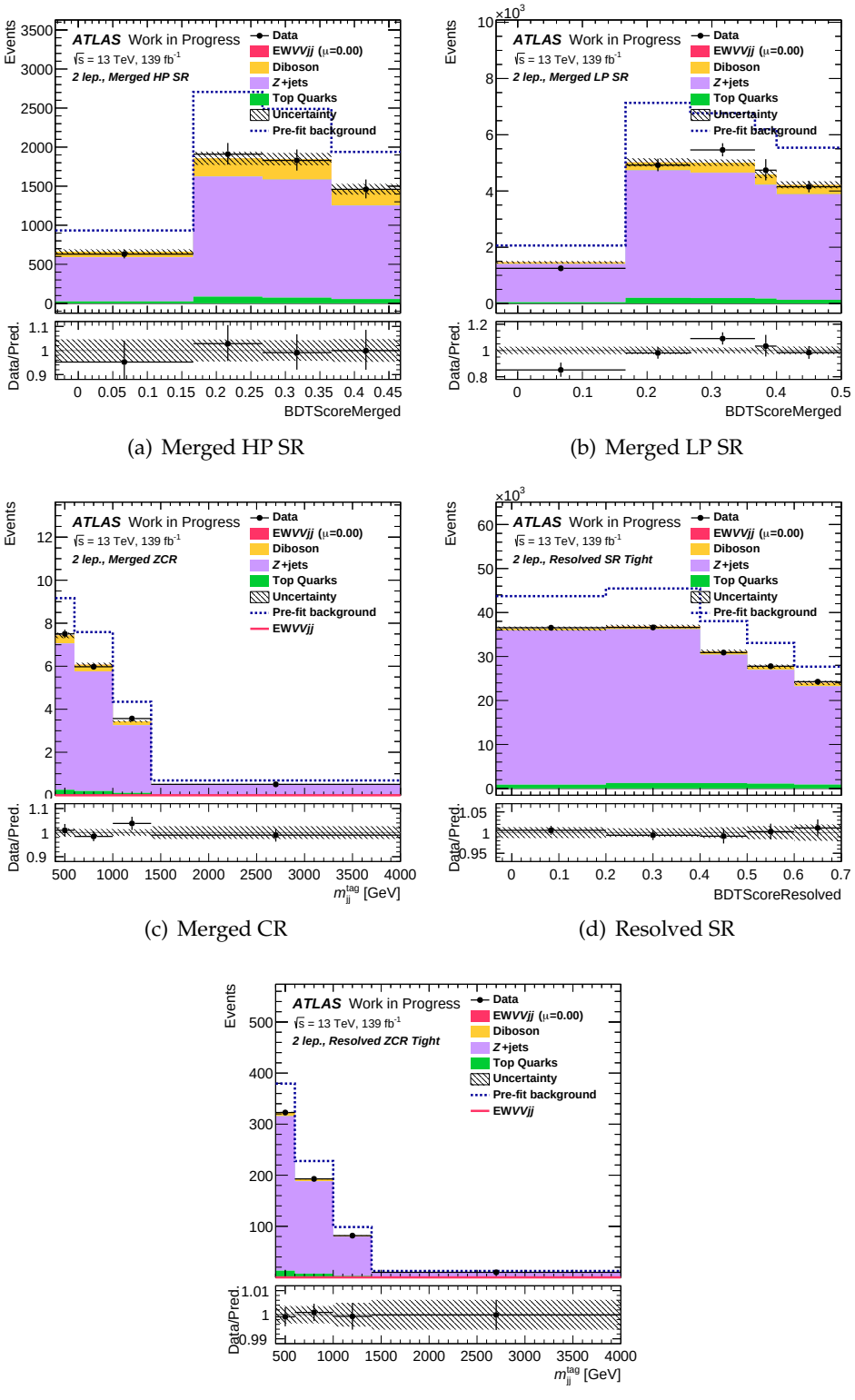

(a) Merged HP SR

(b) Merged LP SR

(c) Merged CR

(d) Resolved SR

(e) Resolved CR

FIGURE F.8: Post-fit distributions for the combined fit in the 2-lepton channel

G. Synthèse en français

G.1 Le modèle standard de la physique des particules

Le Modèle Standard (MS) est une théorie quantique des champs (TQC) qui incorpore toutes les particules fondamentales connues et décrit leurs intéractions [2] [3]. Dans ce cadre particules élémentaires apparaissent commes des excitations discrètes deschamps correspondants. Ces particules sont catégorisés comme fermions ou bosons suivant leur spin: les fermions (bosons) ont un spin demi-entier (entier). Par ailleurs, les particules sont caractérisées par leurs masses and plusieurs nombres quantiques tels que la charge électrique, la couleur et l'hyper-charge, en plus de leur nombre leptonique et baryonique. A chaque particule correspond son anti-particule ayant la même masse and le même spin mais des charges et nombres quantiques opposés. Le tableau des particules élémentaires du MS est montré à la figure G.1.

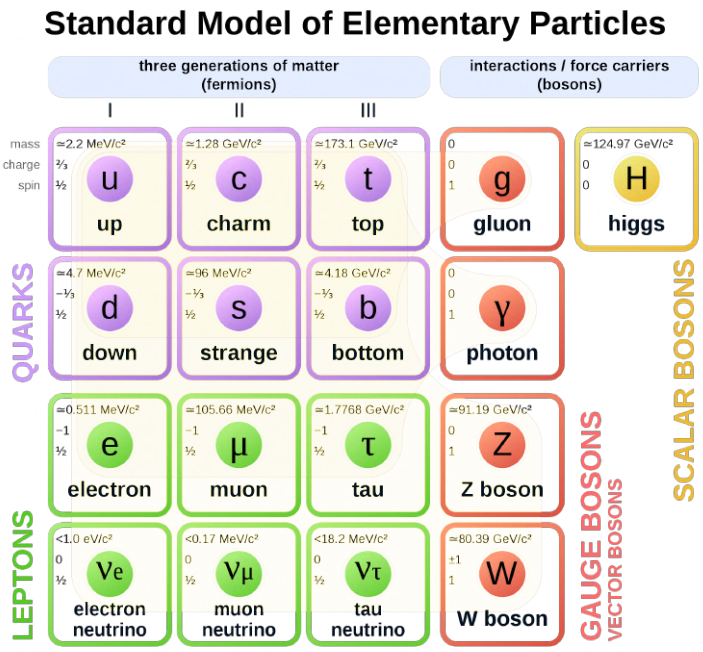

FIGURE G.1: The particle content of the Standard Model.

Dans le MS les particules décrites ci-dessus ainsi que leurs intéractions sont introduites par une théorie de Jauge basé sur un groupe unitaire spécial $SU(N)$(Yang-Mills theory [10]). Les intéractions électromagnétique et faible agissant sut les quarks et les leptons est représenté par un groupe de symétrie $SU(2)_I \times U(1)_Y$ [1]. L'intéraction forte agissant sur les quarks est décrite par la théorie de jauge $SU(3)_C$ de la Chromodynamique Quantique (QCD). Considérés ensemble, le groupe $SU(3)_C \times SU(2)_I \times U(1)_Y$ forme la théorie quantique du MS, capable de décrire les 3 forces fondamentales. Les Symétries sont tout autant importantes pour la théorie, à travers- essentiellement- du théorème de Noether [11].

[1] à cause de son caractère chiral le groupe $SU(2)_I$ est souvent notifié comme $SU(2)_L$

La non-commutativité du groupe $SU2$ permet de prédire les auto-couplages des bosons, le couplage "triple" à 3 bosons (TGC) et le couplage à 4 bosons (QGC). Les interactions à TGC sont W^+W^- et ZW^+W^- , celles QGC sont $W^+W^-W^+W^-$, W^+W^-ZZ et $W^+W^-\gamma\gamma$. Le triple couplage provient de l'équation 2.23 entre les bosons et le Higgs et est proportionnel à la masse des bosons. Le couplage du Higgs aux bosons joue un rôle important dans la diffusion des composantes longitudinales du boson, $W_LW_L \rightarrow W_LW_L$ dont la section efficace est proportionnelle à l'énergie, violant ainsi l'unitarité. Dans le MS, à haute énergie l'Unitarité est restaurée grâce au Higgs qui se couple aux bosons à travers le mécanisme de Brout-Englert-Higgs. Dans cette thèse, on étude en particulier la diffusion des Bosons Vecteurs.

G.2 Le Grand collisionneur de hadrons (LHC) et l'expérience ATLAS

Le LHC est un accélérateur circulaire de protons de 27Km situé à la frontière franco-suisse. Lors de la première prise de données(Run1) l'énergie des collisions a été de 7 et de 8 TeV, tandis que pendant le Run2 (2015-2018) elle a été montée à 13TeV. Une troisième période (Run 3) va démarrer en 2022 à une énergie de 13.6 TeV. Les protons circulant dans le LHC se croisent en 4 points de l'anneau où se situent quatre détecteurs de particules [31] [32]. Parmi eux, ATLAS et CMS sont conçus pour la détection du boson du Higgs et pour effectuer un large spectre de recherches de physique. Les deux autres expériences aont LHCb [33] conçu pour étudier la physique de la saveur et ALICE [34] qui se focalise sur l'étude des collisions d'ions lourds.

Le détecteur ATLAS [31] est le plus volumineux . Il est composé de six systèmes différents de détection organisés en couches successives autour de l'axe des faisceaux. Ces systèmes sont capables d'enregistrer l'information nécessaire à la reconstruction de la trajectoire, de l'énergie et de l'impulsion des particules ainsi que de leur type individuel. Le détecteur a une symétrie cylindrique et couvre un angle solide de presque 4π. La région centrale constitue le "barrel" et les régions avant-arrière sont les "end-caps" . Une vue schématique d'ATLAS est montrée à la figure G.2.

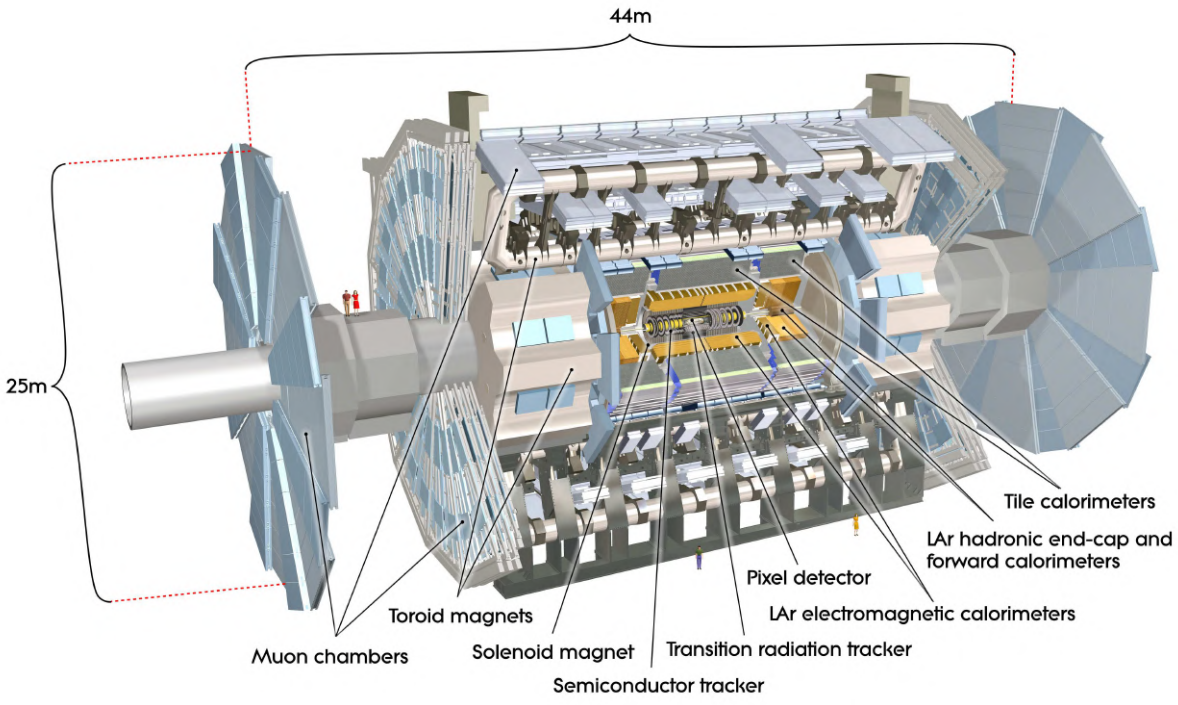

FIGURE G.2: Schematic view of the ATLAS detector.

G.3 Forward Jet Vertex Tagging dans ATLAS à l'aide de l'algorithme de particle flow

A l'ordre d'optimiser la capacité des expériences de découvrir des signes de physique au delà du MS, le LHC opère à très haute luminosité instantanée. Par conséquent, la croisée des paquets de protons donne lieu non seulement à plus d'événements intéressants mais aussi à des collisions supplémentaires pendant le même croisement, composés essentiellement de processus de Chromodynamique Quantique de faible impulsion. C'est le bruit de fond dit "pileup en temps". Par ailleurs, des résidus similaires peuvent provenir des paquets précédents ou suivants, appelés "pileup hors temps".

Dans les analyses, on se trouve confronté à l'identification et la reconstruction de la seule collision primaire dans laquelle les objets physiques sont probablement superposés à des débris supplémentaires. Les deux expériences ATLAS et CMS utilisent des techniques basés sur levertex et la forme des jets afin de minimiser les effets de pileup. L'information du vertex ne peut être utilisée que dans la région instrumentée de détecteurs de traces, qui est $\mid \eta \mid < 2.5$. Des techniques différentes doivent être construites dans les régions avant-arrière $2.5 < \mid \eta \mid < 4.5$: des corrélations topologiques entre particules des jets émergenat des interactions pileup peuvent être exploitées pour l'identification et la rejection des jets de pileup. La mise en place et les performances d'un tel algorithme (fJVT) se servant des informations de Particle Flow est présentée pour la première fois dans ATLAS.

Lors du Run 1 du LHC, ATLAS utilisait soit des informations calorimétriques, soit celles des traces afin de reconstruire les jets hadroniques ou (et) les particules "molles". La majorité des analyses avait choisi la reconstruction à partir des clusters topologiques des cellules calorimétriques (topo-clusters) [58]. Ces jets sont par la suite calibrés au niveau de particules à travers une correction de l'échelle d'energie [61, 62, 63, 64, 60]. A la fin du Run 1 et le début du Run2, des informations des traces ont été ajoutées ayant trouvé que ca améliorait significativement la résolution en énergie [61]. Dans la nouvelle méthode basée sur le flot des particules, les informations calorimétriques et de traces sont combinées pour former la signature des objets individuels. L'énergie calorimétrique correspondant aux traces chargées est soustraite. L'energie des jets est par la suite reconstruite par l'energie residuelle dans les calorimètres et les traces, en les ajustant aux points d'interaction de la collision dure.

Les principales étapes de l'algorithme fJVT est présenté à la figure G.3. Cet algorithme emploie la conservation de l'impulsion pour chaque vertex de pileup pour identifier un jjet avant-arrière comme jet de pileup.

Le discriminant fJVT est montré en figure G.4 pour différents intervalles de p_{T} de jets. Les jets de pileup ont tendance d'avoir des valeurs fJVT plus faibles que les jets de collisions dures.

La figure Fig. G.5 montre l' efficacité de reconnaissance des jets de pileup en fonction de celle des jets de collisions dures pour différentes valeurs du discriminant fJVT (fJVT$<$ cut$_{\mathrm{fjvt}}$) dans quatre intervalles de p_{T}. La performance du discriminant s'améliore à faible p_{T}. Pour une coupure à 0.53 (0.72), des efficacités de 76% (87%) sont obtenues pour les collisions dures, laissant 49% (66%) des jets pileups dans la région avant-arrière dans l'intervalle 20 < p_{T} < 60 GeV.

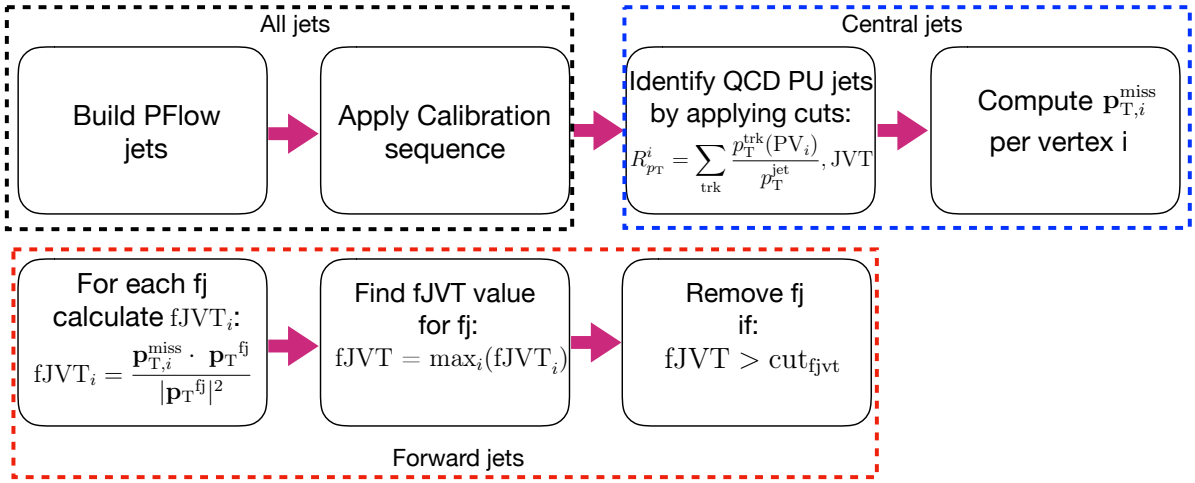

FIGURE G.3: The forward JVT algorithm using particle flow jets. Central jets correspond to jets with $|\eta| < 2.5$. Forward jets (referred to as fj) correspond to jets with $2.5 < |\eta| < 4.5$.

G.4 Recherche de production électrofaible de dibosons en association avec un système de dijet à haute masse dans des états finaux semileptoniques

Dans cette thèse on étudie la production électrofaible des di-bosons en association avec un système de deux jets de haute masse (EW $VVjj$). Le premier but de l'analyse est de distinguer cette production parmi d'autres processus contenant des dibosons. La figure G.7(a) montre a diagramme Feynman typique de diffusion de boson vecteurs (VBS) tandis que des processus non VBS (EW) and QCD contribuant au même état final son représentés à la figure G.7(b) and G.6(c). A cause de grande probabilité d'intérférences les processus non-VBS EW ne peuvent pas être distingués des ceux VBS, ils sont donc considérés comme faisant partie de la région de signal. En revanche, les processus QCD interfèrent peu et seront traités comme du bruit de fond.

L'avantage des processus VBS est que malgré leur faible section efficace ont une topologie très caractéristique. Les événements contiennent deux bosons vecteurs et deux jets situés avant- arrière ayant une grande masse invariante, appelés "tagging jets". Une illustration d'un tel événement après reconstruction est montrée à la figure G.7. L'événemnt est essentiellement identifié grâce aux deux tagging jets qui accompagnent la diffusion VV. Dans cette analyse on étudie les états finals semi-leptoniques, contenant un boson qui se désintègre en une paire de quarks et un autre qui se désintègre en leptons. Le premier est recontruit comme une paire des jets de faible rayon R ("resolved") ou comme un jet unique de grand rayon R ("merged"). En fonction du type des leptons issus de la désintégration du second boson, l'analyse est partagée en 3 canaux , 0, 1 et 2 leptons. Cette thèse se concentre à l'état final avec 2 leptons. Dans ce cas, le signal VBS-EW recherché contient les contributions des diagrammes $Z(\ell\ell)W(q\bar{q})jj$ and $Z(\ell\ell)Z(q\bar{q})jj$ seulement. Les bruits de fond principaux proviennent des événements Z + jets, de single-top et de tt-bar, ainsi que des événements di-boson d'origine QCD. Les coupures de selection appliquées sont déstinées à supprimer ces bruits de fond. La selection d'évenements dans le cas des jets resolved et merges est présentée aux tableaux G.1 et G.2, respectivement.

Afin d'améliorer la sensibilité de l'analyse au signal recherché on a utilisé une technique

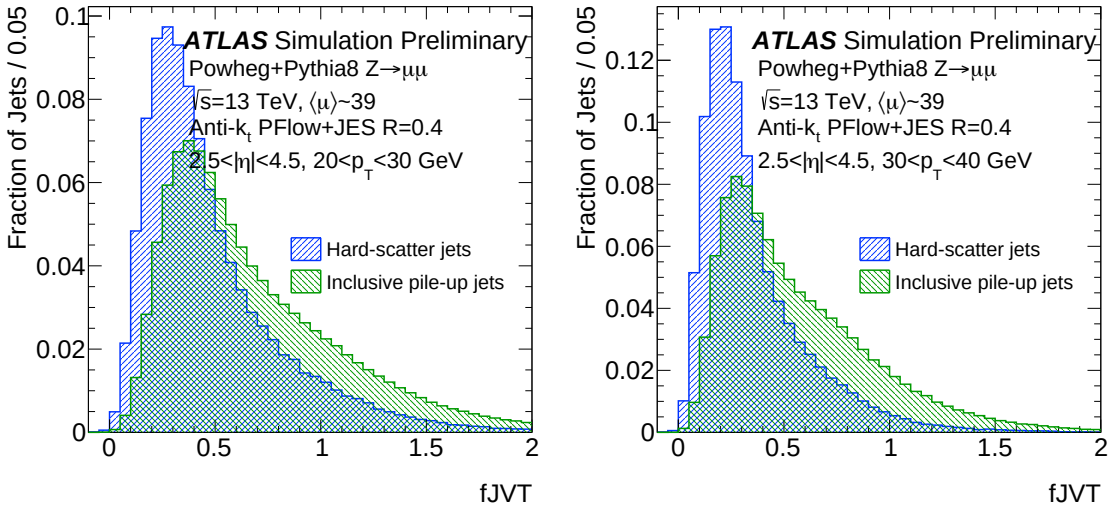

(a)

(b)

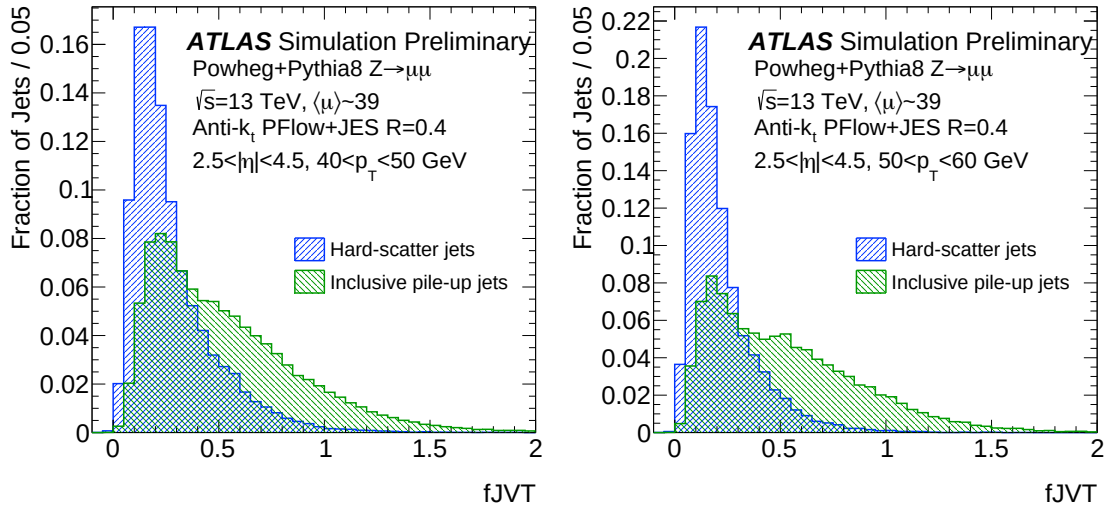

(c)

(d)

FIGURE G.4: fJVT distributions for hard-scatter (blue) and pile-up (green) forward jets with $20 < p_{\mathrm{T}}^{\mathrm{jet}} < 30\,\mathrm{GeV}$ (a) , $30 < p_{\mathrm{T}}^{\mathrm{jet}} < 40\,\mathrm{GeV}$ (b) , $40 < p_{\mathrm{T}}^{\mathrm{jet}} < 50\,\mathrm{GeV}$ (c) and $50 < p_{\mathrm{T}}^{\mathrm{jet}} < 60\,\mathrm{GeV}$ (d).

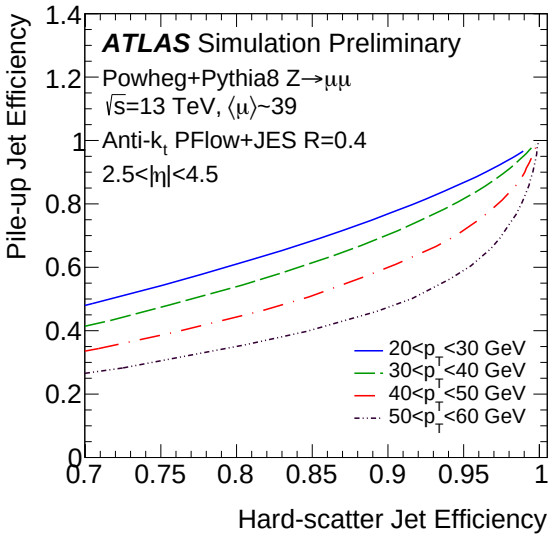

FIGURE G.5: Efficiency for pile-up jets in simulated Z + jets events as a function of the efficiency for hard-scatter jets for different jet p_{T} ranges. For a standard value of hard-scatter jet efficiency the pile-up jet efficiency is improving with p_{T} since pile-up effects are less dominant in higher p_{T} bins.

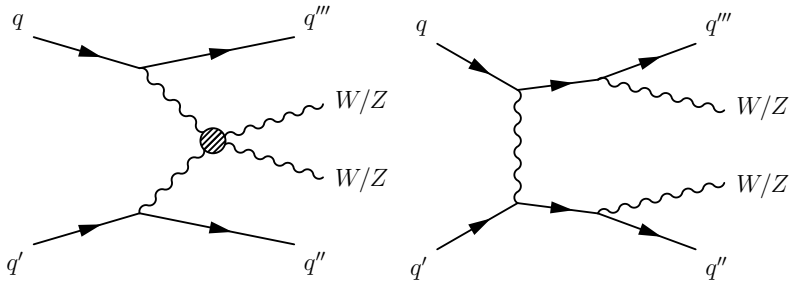

(a) EW $V_{lep}V_{had}jj$ via VBS

(b) EW $V_{lep}V_{had}jj$ via non-VBS

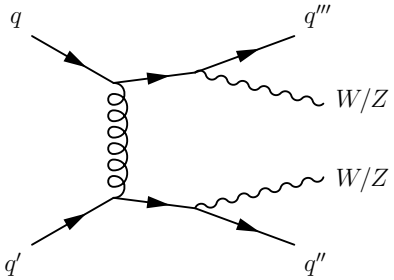

(c) QCD $V_{lep}V_{had}jj$

FIGURE G.6: Representative Feynman diagrams for (a) EW $V_{lep}V_{had}jj$ production via VBS, (b) EW $V_{lep}V_{had}jj$ production via non-VBS contribution, and (c) QCD $V_{lep}V_{had}jj$ production.

combinant plusieurs variables permettant de le séparer au mieux du bruit de fond. L'algorithme XGBoost est utilisé [85] dans ce but, qiu est un programme d'apprentissage supervisé. Pour exploiter au maximum la statistique disponible d'événements simulés tout en évitant des éventuels biais nous avons appliqué la k-fold méthode de validation avec k=5 [86]: les événements sont partagés en 5 parties égales, l'algorithme tourne 5 fois en utilisant chaque fois une partie différente pour l'entraînement et le reste pour la validation. Ainsi l'ensemble d'événements est utilisé pour l'entraînement et la validation. Les variables d'intérêt pour

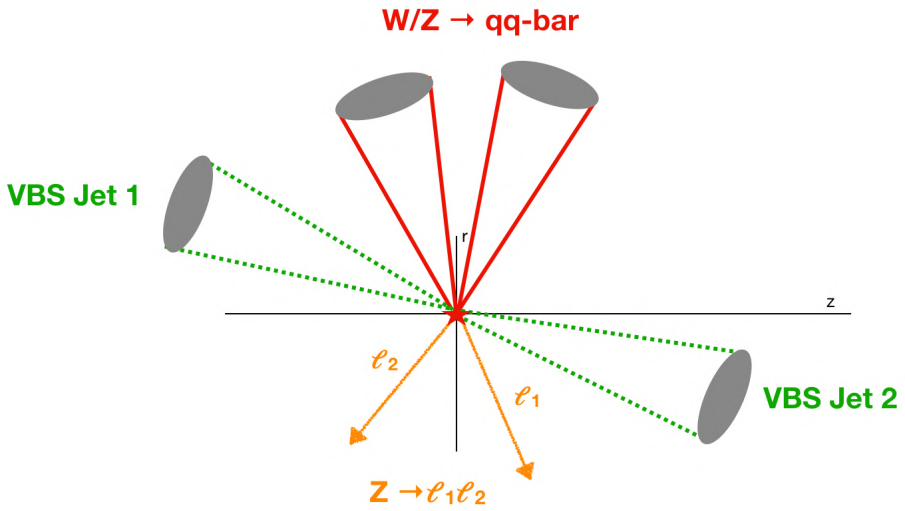

(a) Resolved reconstruction

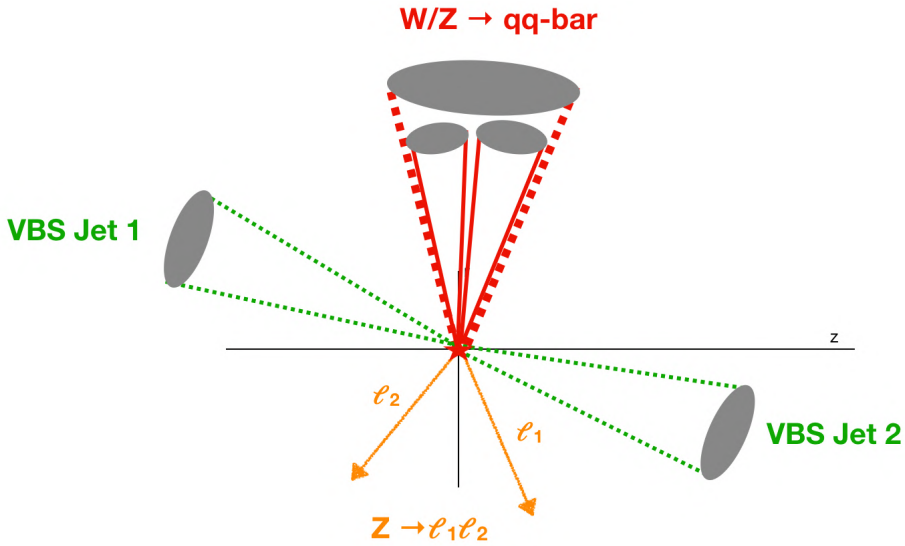

(b) Merged reconstruction

FIGURE G.7: Schematic representation of a EW $WZjj$ event with $Z \to \ell\ell$ and $W \to q\bar{q}$. The hadronic decay of W is either reconstructed as a pair of small-R jets (resolved) or a single large-R jet (merged)

l'algorithme dépendent de la région de signal (resolved ou merged). Le choix des variables se fait sur leur pouvoir de séparation signal-bruit de fond. On commence par essayer toutes les variables disponibles et on élimine progressivement de l'algorithme celles qui n'ajoutent pas de pouvoir de séparation. Les variables finalement utilisées pour l'entrainement du BDT sont exposées aux tableaux 6.11 et 6.12, pour les cas merged et resolved respectivement. La comparaison des distributions d'entraînement et de validation présentées en figure G.8 sont en bon accord et sans indication de surentraînement.

La force du signal μ est évaluée par un maximum de vraisemblance qui s'écrit comme suit:

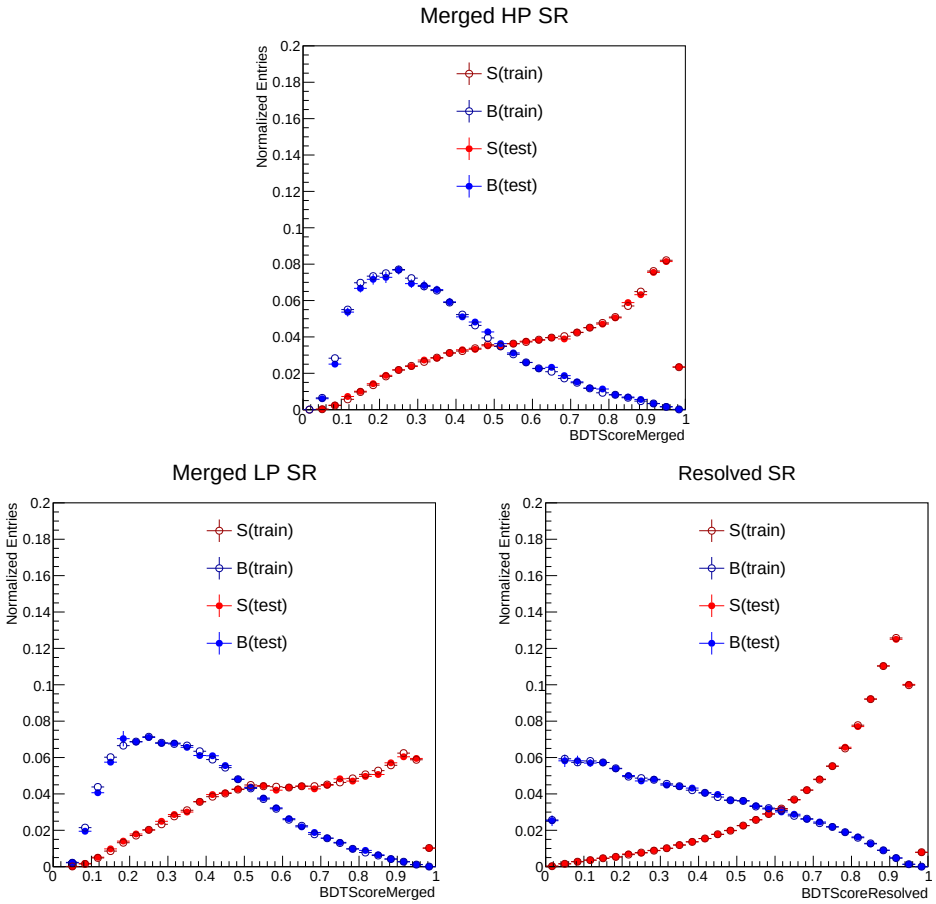

FIGURE G.8: Comparison of test and training BDT response distributions in 2-lepton channel, for the merged HP (a), LP (b) and resolved (c) regimes.

TABLE G.1: Summary of event selection for the merged regime in the 2-lepton channel.

Selection		SR		Z CR
		HP	LP	incl
$Z \to \ell\ell$	Number of Loose leptons	2		
	Same flavor	yes		
	Leading lepton p_{T}	$> 27\,\mathrm{GeV}$		
	Subleading lepton p_{T}	$> 27\,\mathrm{GeV}$		
	dilepton invariant mass	$83 < m_{ee} < 99$ GeV $(-0.0117 \times p_{\mathrm{T}}^{\mu\mu} + 85.63\,\mathrm{GeV}) < m_{\mu\mu} < (0.0185 \times p_{\mathrm{T}}^{\mu\mu} + 94\,\mathrm{GeV})$		
	Opposite sign	For $\mu\mu$ channel only		
VBS jets candidates	Leading Tag jet p_{T}	$> 30\,\mathrm{GeV}$		
	Subleading Tag jet p_{T}	$> 30\,\mathrm{GeV}$		
	m_{jj}	> 400GeV		
	$\eta_{\mathrm{tag},j_1} \cdot \eta_{\mathrm{tag},j_2}$	< 0		
$W/Z \to J$	Num of large-R jets	≥ 1		
	3-Var Tagger	pass50WP	pass80WP && !pass50WP	fail80WP

TABLE G.2: Summary of event selection for the resolved regime in the 2-lepton channel.

Selection		SR	Z CR
$Z \to \ell\ell$	Number of Loose leptons	2	
	Same flavor	yes	
	Leading lepton p_{T}	$> 27\,\mathrm{GeV}$	
	Subleading lepton p_{T}	$> 27\,\mathrm{GeV}$	
	dilepton invariant mass	$83 < m_{ee} < 99$ GeV $(-0.0117 \times p_{\mathrm{T}}^{\mu\mu} + 85.63\,\mathrm{GeV}) < m_{\mu\mu} < (0.0185 \times p_{\mathrm{T}}^{\mu\mu} + 94\,\mathrm{GeV})$	
	Opposite sign	For $\mu\mu$ channel only	
VBS jets candidates	Leading Tag jet p_{T}	$> 30\,\mathrm{GeV}$	
	Subleading Tag jet p_{T}	$> 30\,\mathrm{GeV}$	
	m_{jj}	> 400GeV	
	$\eta_{\mathrm{tag},j_1} \cdot \eta_{\mathrm{tag},j_2}$	< 0	
$W/Z \to jj$	Num of signal small-R jets	2	
	Leading signal jet p_{T}	$> 40\,\mathrm{GeV}$	
	Subleading signal jet p_{T}	$> 20\,\mathrm{GeV}$	
	$Z \to q\bar{q}$ and $W \to q\bar{q}$	$64 < m_{jj} < 106$GeV	$50 < m_{jj} < 64\,GeV$ or $m_{jj} > 106$
VBS enhancing	m_{jjj}	> 220 GeV	

$$\mathscr{L}\left(N, \tilde{\theta}|\mu, \theta\right) = P\left(\mu|\mu s + b\right) \cdot p\left(\tilde{\theta}|\theta\right) \tag{G.1}$$

Où P est le produit des termes de tous les bins des probabilités Poisson:

$$P\left(\mu|\mu s + b\right) = \prod_{i=1}^{N_{bins}} \frac{(\mu s_i(\theta) + b_i(\theta))^{N_i}}{N_i!} e^{-(\mu s_i(\theta) + b_i(\theta))} \tag{G.2}$$

où μs_i, b_i est le nombre attendu de'évenements de signal et de bruit de fond dans le bin i respectivement et N_i est le nombre d'événements observés dans ce bin. Le terme θ représente les incertitudes théoriques et expérimentales considérées dans l'analyses. Le second terme de l'équation G.1, $p(\tilde{\theta}|\theta)$, est habituellement appelé un prior et il représente la connaissance des effets systématiques. En supposant que les incertitudes sont indépendantes ce terme est donné par le produit des priors individuels: $p\left(\tilde{\theta}|\theta\right) = \prod_j p_j\left(\tilde{\theta}_j|\theta_j\right)$ où l'indice j tourne sur toutes les incertitudes and θ_j est le paramètre de nuisance associée à la source d'incertitude

j. Le résultat de l'ajustement est obtenu en maximisant la fonction de vraisemblance G.1 par rapport à tous les paramètres.

An ajustement simultané des régions de contrôle et de signal des événements resolved et merged est effectué. Dans les régions de signal le discriminant BDT est utilisé tandis que la distribution M_{jj}^{tag} est choisie pour les régions de contrôle. Afin de contraindre au mieux l'incertitude associée à la re-pondération de M_{jj}^{tag} des ajustements séparés des échantillons resolved et merged sont aussi effectués pour des vérifications. Le résumé des résultats des ajustements est donné à la figure G.9. La force du signal VBS estimé est :

$$\mu = 1.29^{+0.38}_{-0.34} = 1.29^{+0.23}_{-0.22}(\text{Stat})^{+0.31}_{-0.27}(\text{Syst})$$

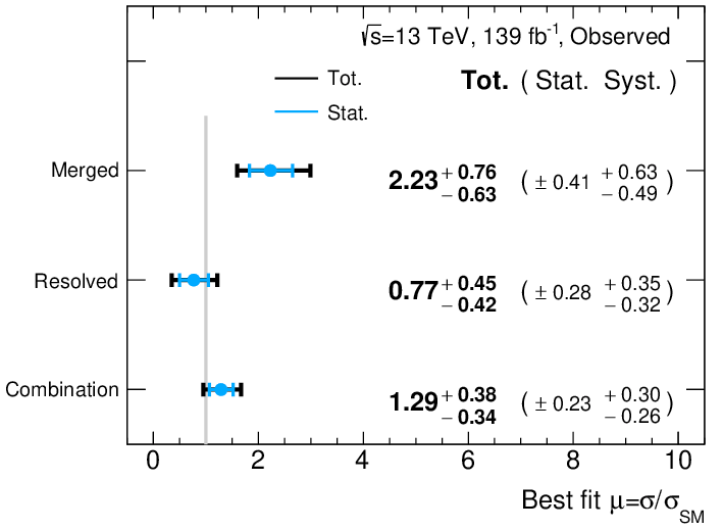

FIGURE G.9: Signal strength fit results for the merged, resolved and combined fit.

La signification correspondante est de 4.15σ, indiquant une évidence forte pour le signal EW $VVjj$ dans le canal semileptonic avec 2 leptons dans l'état final. La signification attendue obtenue par l'echantillon Asimov après-ajustement est estimée à 3.34σ. Les distributions après-ajustement de M_{jj}^{tag} et du score BDT sont présentées à la figure G.10

G.5 Contrôles de qualité et alimentation en série des modules de pixel

G.5.1 Capteurs pixel pour ITK

Le principe de base d'un module pour le détecteur à pixels de l'ITK est un module hybride avec des senseurs n-in-p sont connectés à l'électronique Front-End à travers des connexions denses appelées bump-bonds. La puce de lecture Front-End ITKPix1 a été conçue par la collaboration RD53 composée de physiciens d' ATLAS et de CMS. Une première version de cette puce, appelée RD53A a été d'abord développée et testée longuement, avant de faire le choix final. La majorité des résultats présentés dans cette thèse ont été obtenus avec la version RD53A. Afin de pouvoir tester les différentes conceptions de circuits de lecture dans la même production, chaque puce contient 3 systèmes analogues conçus pour répondre

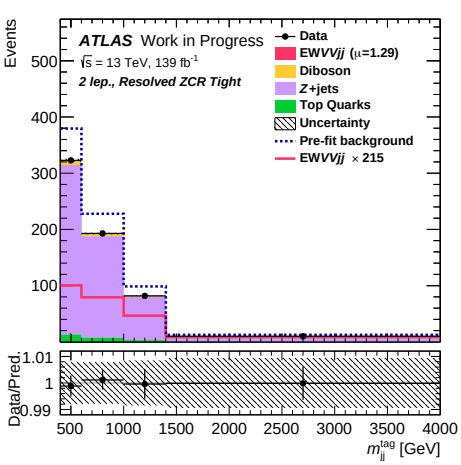

(a) Resolved CR post-fit

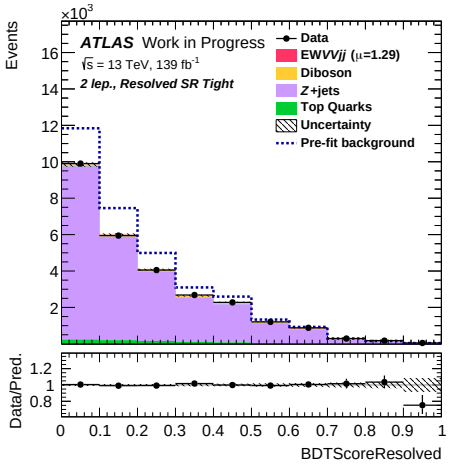

(b) Resolved SR post-fit

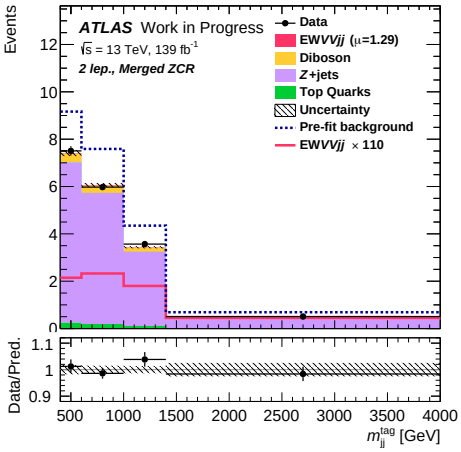

(c) Merged CR post-fit

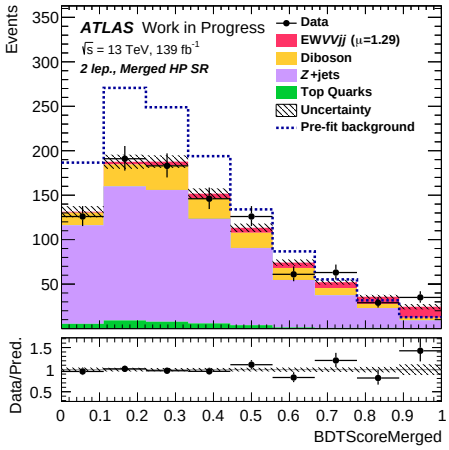

(d) Merged HP SR post-fit

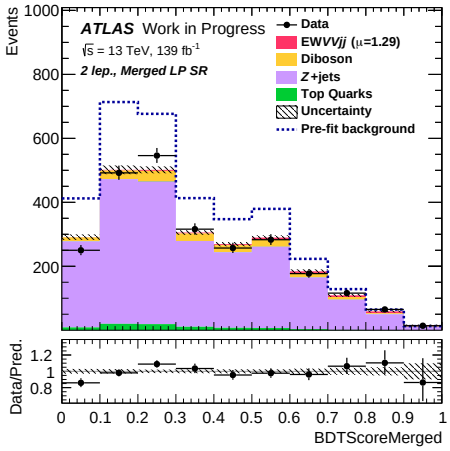

(e) Merged LP SR post-fit

FIGURE G.10: Post-fit distributions for the combined fit in the 2-lepton channel. The data correspond to an integrated luminosity of $139 fb^{-1}$.

aux exigences pour le fonctionnement à haute luminosité (comme les hautes doses de radiations, les taux élevés, l'opération stable). Les trois conceptions de puce sont connues comme "sunchrone"(SYNC), "linéaire"(LIN) et "différentielle"(DIFF).

G.5.2 Performance de la matrice des pixels

Chaque pixel de lecture de la puce RD53 possède des circuits analogues et digitaux en plus d'un système calibré d'injection de charge à travers une capacité. La caractérisation de la matrice des pixels est faite en injectant de la charge. Une série des tests et de balayage one été construits afin de mesurer les performances de la matrice des pixels. Les plus importants sont les tests digitaux, analogues et de réglage des seuils.

Le réglage de la matrice des pixels est de première importance. Quand un signal d'amplitude supérieure au seuil du discriminateur arrive, le temps passé au-dessus de ce seuil (ToT) est mesuré. Cette valeur ToT contient l'information sur la charge déposée sur le senseur et donc sur l'énergie de la particule initiale. Pour cette raison, un réponse uniforme du ToT sur l'ensemble de la matrice des pixels est souhaitée pour assurer une bonne performance. A cause des variations, ceci n'est en général pas le cas, rendant l'exploitation des données difficile. En plus, l'exposition de la puce aux radiations provoquera des non-uniformités supplémentaires à travers la matrice. Il faut donc assurer un ajustement fréquent de la réponse des pixels.

Le réglage des ToT et des seuils se fait séparément pour les 3 front-ends et un balayage des ces valeurs sont vérifiées après l'ajustement. Pendant le balayage ToT une charge de 10ke est injectée à chaque pixel et le ToT est mesuré. Des exemples des distributions de seuils, du bruit et du ToT après réglage sont montrés en figure G.11.

G.5.3 Alimentation en série des modules RD53A irradiés

Le nombre élevé des modules et la granularité fine du détecteur des Pixels ITK par rapport au détecteur actuel donneront lieu à une augmentation significative de la puissance nécessaire. Pour cette raison un schéma d'alimentation en série (SP) a été choisi. Ainsi, les puces de lecture des modules de pixels sont alimentées en série par un courant constant. Les senseurs de plusieurs modules seront eux mis en parallèle dans une source de tension pour atteindre la complète depletion. En tenant compte des spécifications pour la connexion à la terre et les propriétés des modèles commerciaux disponibles, l'architecture choisie est un biais forward sur certains senseurs. Même si ce biais est faible, il peut provoquer des courants non négligeables entre le senseur et la puce de lecture, spécialement après radiation. C'est le comportement de cette chaîne SP qui a été étudiée.

Mesures

Les mesures sont faites en 4 étapes : Premièrement tous les modules sont caractérisés individuellement afin d'assurer leur bon fonctionnement avant le montage en chaîne. Ces tests concernent les mesures IV du senseur, les courbes SLDO V-I de la puce, et les balayages des parties analogue et digitale (par injection de courant dans tous les pixels des parties correspondantes) ainsi que des seuils (injection des courants sur une gamme étendue des valeurs dans la partie analogue).

La seconde étape des mesures comprend la caractérisation de la chaine assemblée. Le positionnement des modules utilisés est présenté en tableG.3. Le module avec la plus haute tension est le premier de la chaîne. Des mesures des courbes VI sont faites en courant montant et descendant. Aussi, les voltages sont examinés à l'entrée de chaque module par rapport à

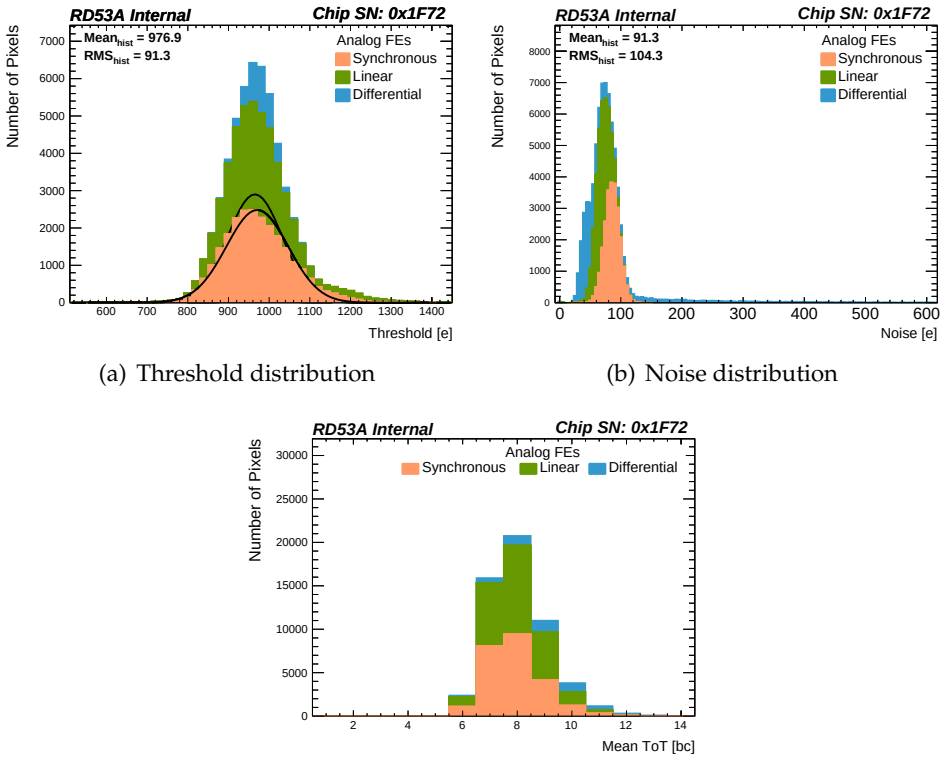

(a) Threshold distribution

(b) Noise distribution

(c) ToT distribution

FIGURE G.11: Threshold, Noise and ToT distributions for a tuned RD53A chip. The three front-ends are plotted in different colors.

la terre. Les réponses des régulateurs des circuits analogue (VDDA) et digital (VDDD) sont enregistrées. A cause des difficultés observées pendant les tests pour le démarrage des puces RD53A, le courant nécessaire pour la communication réussi avec les modules est déterminé et choisi comme valeur lors de l'alimentation en chaîne.

Position in Chain	Module ID	NIEL $10^{15} \cdot 1\,\text{MeV}\ \text{n}_{\text{eq}} cm^{-2}$)
1st	V6S02	1.65
2nd	V3S03	3.33
3rd	V3S11	4.35
4th	V3S02	3.33
5th	V3S01	1.18
6th	V2S11	1.66
7th	V6S03	3.34

TABLE G.3: Summary of flunces for the modules and the position of the modules used in the serial powering chain. The module with the highest ground potential is considered the first module in the chain.

Pour la troisième étape, tous les senseurs sont connectés à une tension commune. Le schéma de l'installation est montré à la figure G.12. La chaîne est opérée avec un courant de 1.4 A, valeur choisie pendant l'étape de caractérisation. Afin d'identifier d'éventuels dommages que pourraient subit le dernier module de la chaîne (à cause du biais positif) pendant l'opération de 9h, on suit régulièrement la réponse des modules par des tests de lecture. Pendant cette période la chute de tension (ΔV) à travers R_{39} est suivie pour tous les modules. Le courant de fuite correspondant (I_{leak}) est calculé pour chaque module de la chaîne comme $I_{leak} = \Delta V / R_{39}$.

A l'étape finale, le dernier module de la chaîne qui a été exposé à un biais positif (V6S03) est de nouveau testé suivant la procédure complète initiale, comprenant des tests individuels pour comparer ses performances avant et après la longue opération.

Résultats

Dans la figure G.13, le courant de fuite en fonction du temps est tracé pour chaque module de la chaîne au cours de la troisième étape de test décrite ci-dessus. Un signe positif dans cette graphique correspond à une polarisation inverse effective, c'est-à-dire que le potentiel à l'arrière du capteur, qui est égal au potentiel de la ligne HT flottante commune, est inférieur au potentiel sur la grille de polarisation du capteur. Un signe négatif correspond à une polarisation directe effective, c'est-à-dire que le potentiel sur la ligne HT commune est supérieur au potentiel sur la grille de polarisation à l'arrière du capteur. Une polarisation directe significative est observée pour au moins deux modules de la chaîne, ceux au potentiel de masse le plus bas (ceux étant V2S11 et V6S03). Le partage de courant entre ces modules dépend fortement de la température du module (qui était plus élevée pour le module V2S11).

Afin de rechercher les dommages potentiels causés à la puce frontale en raison de la polarisation directe, le module V6S03 a été retesté séparément à la fin de la procédure. Les mêmes scans qui ont été effectués avant le fonctionnement des modules dans la chaîne d'alimentation en série, ont été répétés. Une comparaison des distributions de seuil, de bruit et de ToT pour le module V6S03 avant et après l'opération longue dans la chaîne est présentée dans la figure G.14. Dans tous les cas, les distributions sont en bon accord et indiquent que le module fonctionne toujours correctement et avec les mêmes caractéristiques après l'opération dans la chaîne d'alimentation en série, qu'avant l'opération dans la chaîne.

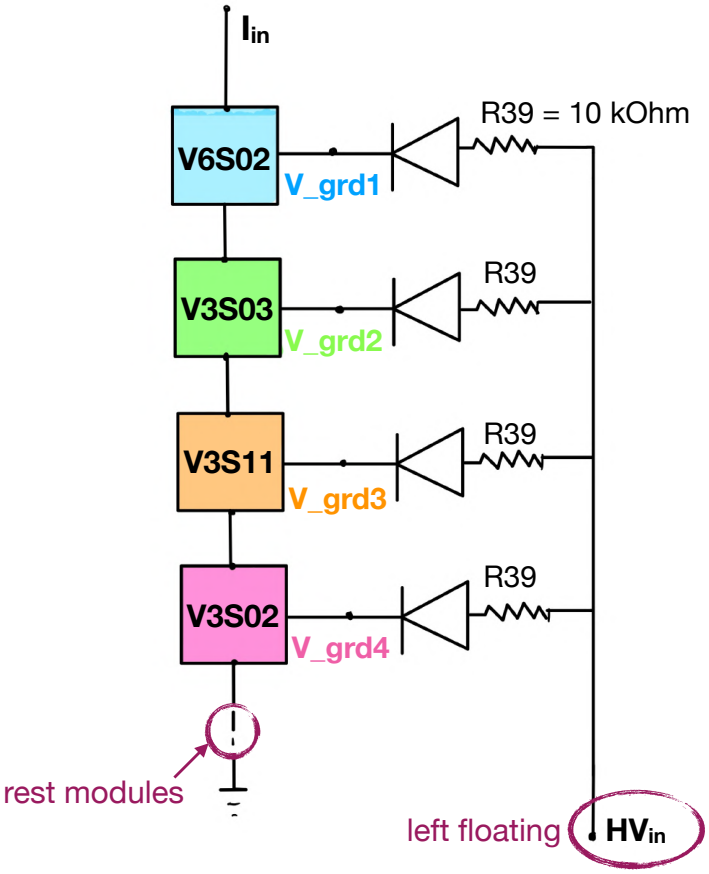

FIGURE G.12: Schematic of the setup used for the common HV line tests. The sensor part of each module is represented as a diode while the chip side is drawn as a square.

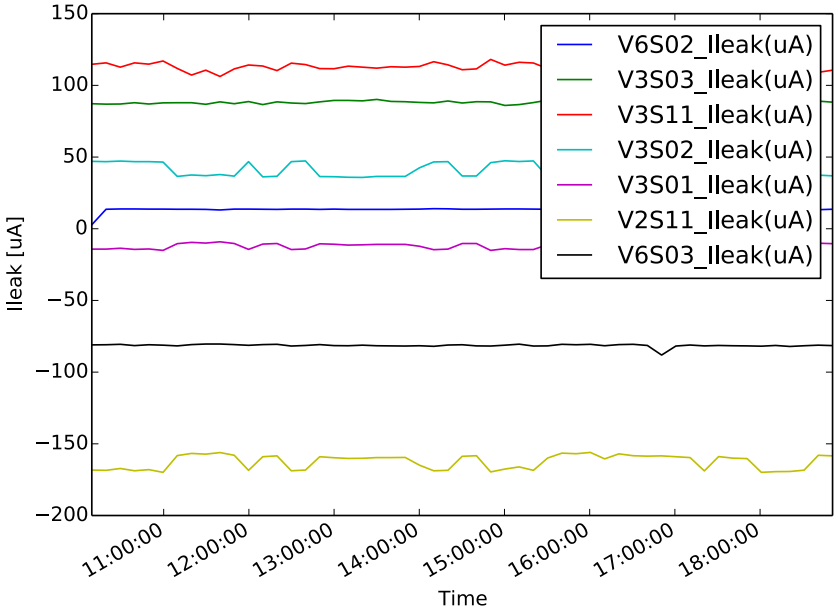

FIGURE G.13: Mesures de courant de fuite pour tous les modules de la chaîne assemblée avec ligne HT commune.

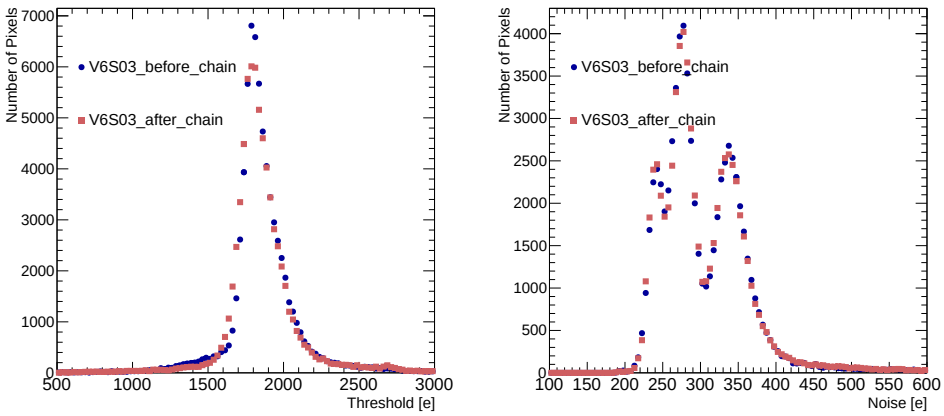

(a) (b)

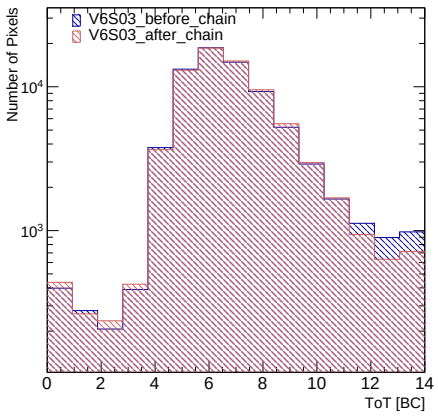

(c)

FIGURE G.14: Threshold map (a), threshold correspondant (b), et distributions de bruit (c) pour le module V6S03.

Bibliography

[1] M. Tanabashi *et al.* "Review of Particle Physics". In: *Phys. Rev.* D **98**, 030001 (2018). DOI: https://doi.org/10.1103/PhysRevD.98.030001.

[2] S.L Glashow. "Partial symmetries of Weak Interactions". In: *Nucl.Phys.* 22 (1961), pp. 579–588. DOI: 10.1016/0029-5582(61)90469-2.

[3] A. Salam and J.C. Ward. "Weak and electromagnetic Interactions". In: *Il Nuovo Cimento.* 11.4 (1959), pp. 568–577. DOI: 10.1007/BF02726525.

[4] G. T'Hooft and J.G. Veltman. "Regularisation and Renormalisation of Gauge Fields". In: *Nucl.Phys.B* 44 (1972), pp. 235–257. DOI: 10.1016/0550-3213(72)90279-9.

[5] M. Gell-Mann. "The interpretation of the new particles as displaced charge multiplets". In: *Nuovo Comento* 4.S2 (1956), pp. 848–866. DOI: 10.1007/BF02748000.

[6] M. Weinberg. "A model of leptons". In: *Phys.Rev.Lett.* 10 (1967), pp. 1264–1266. DOI: 10..1103/PhysRevLett.19.1264.

[7] Hagen C.R. Guralnik G.S. and T.W.B. Kibble. "Global conservation laws and Massless particles". In: *Phys.Rev.Lett.* 13 (1964), pp. 585–587. DOI: 10.1103/PhysRevLett.13.585.

[8] F Englert and R. Brout. "Broken Symmetry and the mass of gauge vector mesons". In: *Phys.Rev.Lett.* 13, pages = ().

[9] P.W. Higgs. "Broken symmetries and the masses of gauge bosons". In: *Phys.Rev.Lett.* 13 (1964), pp. 508–509. DOI: 10.1103/PhysRevLett.13.508.

[10] C. Yang and R. Mills. "Conservation of Isotopic spin and isotopic gauge invariance". In: *Phys.Rev.* 96 (1954), pp. 191–195. DOI: 10.1103/PhysRev.96.191.

[11] E. Noether. "Invariant variation problem". In: *Gott.Nachr.* 1918 (1971), pp. 235–257. DOI: 10.1080/00411457108231446.

[12] D. Politzer. "Reliable Perturbative Results for Strong interacions?" In: *Phys.Rev.Lett.* 30 (1973), pp. 1346–1349. DOI: 10.1103/PhysRevLett.30.1346.

[13] D. Gross and Wilczek F. "Asymptotic free Gauge Theories I". In: *Phys.Rev.D.* 8 (1973), pp. 3633–3652. DOI: 10.1103/PhysRevD.8.3633.

[14] Benjamin W. Lee, C. Quigg, and H. B. Thacker. "Weak Interactions at Very High-Energies: The Role of the Higgs Boson Mass". In: *Phys. Rev. D* 16 (1977), p. 1519. DOI: 10.1103/PhysRevD.16.1519.

[15] John C. Collins, Davison E. Soper, and George Sterman. *Factorization of Hard Processes in QCD*. 2004. arXiv: hep-ph/0409313 [hep-ph].

[16] Alan D. Martin. *Proton structure, Partons, QCD, DGLAP and beyond*. 2008. arXiv: 0802.0161 [hep-ph].

[17] H. David Politzer. "Asymptotic Freedom: An Approach to Strong Interactions". In: *Phys. Rept.* 14 (1974), pp. 129–180. DOI: 10.1016/0370-1573(74)90014-3.

[18] Matin Mojaza, Stanley J. Brodsky, and Xing-Gang Wu. "Systematic All-Orders Method to Eliminate Renormalization-Scale and Scheme Ambiguities in Perturbative QCD". In: *Physical Review Letters* 110.19 (2013). ISSN: 1079-7114. DOI: 10.1103/physrevlett.110.192001. URL: http://dx.doi.org/10.1103/PhysRevLett.110.192001.

[19] ATLAS Collaboration. "Observation of electroweak $W^{\pm}Z$ boson pair production in association with two jets in pp collisions at $\sqrt{s} = 13$ TeV with the ATLAS detector". In: *Phys. Lett. B* 793 (2019), p. 469. DOI: 10.1016/j.physletb.2019.05.012. arXiv: 1812.09740 [hep-ex].

[20] *Standard Model Summary Plots June 2021*. Tech. rep. All figures including auxiliary figures are available at https://atlas.web.cern.ch/Atlas/GROUPS/PHYSICS/PUBNOTES/ATL-PHYS-PUB-2021-032. Geneva: CERN, 2021. URL: http://cds.cern.ch/record/2777014.

[21] ATLAS Collaboration. "Measurement of $W^{\pm}W^{\pm}$ vector-boson scattering and limits on anomalous quartic gauge couplings with the ATLAS detector". In: *Phys. Rev. D* 96 (2017), p. 012007. DOI: 10.1103/PhysRevD.96.012007. arXiv: 1611.02428 [hep-ex].

[22] CMS Collaboration. "Study of vector boson scattering and search for new physics in events with two same-sign leptons and two jets". In: *Phys. Rev. Lett.* 114 (2015), p. 051801. DOI: 10.1103/PhysRevLett.114.051801. arXiv: 1410.6315 [hep-ex].

[23] CMS Collaboration. "Measurement of the cross section for electroweak production of $Z\gamma$ in association with two jets and constraints on anomalous quartic gauge couplings in proton–proton collisions at $\sqrt{s} = 8$ TeV". In: *Phys. Lett. B* 770 (2017), p. 380. DOI: 10.1016/j.physletb.2017.04.071. arXiv: 1702.03025 [hep-ex].

[24] ATLAS Collaboration. "Studies of $Z\gamma$ production in association with a high-mass dijet system in pp collisions at $\sqrt{s} = 8$ TeV with the ATLAS detector". In: *JHEP* 07 (2017), p. 107. DOI: 10.1007/JHEP07(2017)107. arXiv: 1705.01966 [hep-ex].

[25] CMS Collaboration. "Observation of Electroweak Production of Same-Sign W Boson Pairs in the Two Jet and Two Same-Sign Lepton Final State in Proton–Proton Collisions at 13 TeV". In: *Phys. Rev. Lett.* 120 (2018), p. 081801. DOI: 10.1103/PhysRevLett.120.081801. arXiv: 1709.05822 [hep-ex].

[26] ATLAS Collaboration. "Search for the electroweak diboson production in association with a high-mass dijet system in semileptonic final states in pp collisions at $\sqrt{s} = 13$ TeV with the ATLAS detector". In: *Phys. Rev. D* 100 (2019), p. 032007. DOI: 10.1103/PhysRevD.100.032007. arXiv: 1905.07714 [hep-ex].

[27] CMS Collaboration. "Evidence for WW/WZ vector boson scattering in the decay channel lvqq produced in association with two jets in proton-proton collisions at $\sqrt{s} = 13$ TeV". In: *Submitted to Phys.Lett.C* (2021). eprint: CERN-EP-2021-225 (hep-ph).

[28] Diogo Buarque Franzosi et al. *Vector Boson Scattering Processes: Status and Prospects*. 2021. arXiv: 2106.01393 [hep-ph].

[29] A. Belyaev et al. "Multiple Higgs and vector boson production beyond the Standard Model". In: *Journal of High Energy Physics* 2013.5 (2013). ISSN: 1029-8479. DOI: 10.1007/jhep05(2013)005. URL: http://dx.doi.org/10.1007/JHEP05(2013)005.

[30] Lyndon Evans and Philip Bryant. "LHC Machine". In: *JINST* 3 (2008), S08001. DOI: 10.1088/1748-0221/3/08/S08001.

[31] ATLAS Collaboration. "The ATLAS Experiment at the CERN Large Hadron Collider". In: *JINST* 3 (2008), S08003. DOI: 10.1088/1748-0221/3/08/S08003.

[32] CMS Collaboration. "The CMS experiment at the CERN LHC". In: *JINST* 3 (2008), S08004. DOI: 10.1088/1748-0221/3/08/S08004.

[33] LHCb Collaboration. "The LHCb Detector at the LHC". In: *JINST* 3 (2008), S08005. DOI: 10.1088/1748-0221/3/08/S08005.

[34] ALICE Collaboration. "The ALICE Experiment at the CERN LHC". In: *JINST* 3 (2008), S08002. DOI: 10.1088/1748-0221/3/08/S08002.

[35] *The CERN accelerator complex - August 2018. Complexe des accélérateurs du CERN - Août 2018*. URL: https://cds.cern.ch/record/2636343.

[36] *ATLAS Luminosity Public Results Run2*. URL: https://twiki.cern.ch/twiki/bin/view/AtlasPublic/LuminosityPublicResultsRun2.

[37] B. Abbott et al. "Production and integration of the ATLAS Insertable B-Layer". In: *JINST* 13 (2018), T05008. DOI: 10.1088/1748-0221/13/05/T05008. arXiv: 1803.00844 [physics.ins-det].

[38] ATLAS Collaboration. "ATLAS liquid argon calorimeter: Technical design report". In: (Dec. 1996).

[39] ATLAS Collaboration. "ATLAS tile calorimeter: Technical design report". In: (Dec. 1996).

[40] P. Adragna et al. "Testbeam studies of production modules of the ATLAS tile calorimeter". In: *Nucl. Instrum. Meth. A* 606 (2009), pp. 362–394. DOI: 10.1016/j.nima.2009.04.009.

[41] A. Artamonov et al. "The ATLAS forward calorimeters". In: *JINST* 3 (2008), P02010. DOI: 10.1088/1748-0221/3/02/P02010.

[42] ATLAS Collaboration. *ATLAS Muon Spectrometer: Technical Design Report*. ATLAS-TDR-10; CERN-LHCC-97-022. CERN, 1997. URL: https://cds.cern.ch/record/331068.

[43] ATLAS Collaboration. "Operation of the ATLAS trigger system in Run 2". In: *JINST* 15 (2020), P10004. DOI: 10.1088/1748-0221/15/10/P10004. arXiv: 2007.12539 [hep-ex].

[44] *The HL-LHC project*. URL: https://hilumilhc.web.cern.ch/content/hl-lhc-project.

[45] ATLAS Collaboration. *Technical Design Report for the ATLAS Inner Tracker Pixel Detector*. Tech. rep. CERN-LHCC-2017-021. Geneva: CERN, 2018. URL: https://cds.cern.ch/record/2285585.

[46] ATLAS Collaboration. *Technical Design Report for the ATLAS Inner Tracker Strip Detector*. Tech. rep. CERN-LHCC-2017-005 ; ATLAS-TDR-025. CERN, 2017. URL: https://cds.cern.ch/record/2257755.

[47] ATLAS Collaboration. *Technical Proposal: A High-Granularity Timing Detector for the ATLAS Phase-II Upgrade*. Tech. rep. CERN-LHCC-2018-023. Geneva: CERN, 2018. URL: https://cds.cern.ch/record/2623663.

[48] ATLAS Collaboration. *ATLAS Liquid Argon Calorimeter Phase-I Upgrade: Technical Design Report*. ATLAS-TDR-022; CERN-LHCC-2013-017. 2013. URL: https://cds.cern.ch/record/1602230.

[49] ATLAS Collaboration. *ATLAS LAr Calorimeter Phase-II Upgrade: Technical Design Report*. ATLAS-TDR-027; CERN-LHCC-2017-018. 2017. URL: https://cds.cern.ch/record/2285582.

[50] Benoit Lefebvre. "Muon Spectrometer Phase-I Upgrade for the ATLAS Experiment: the New Small Wheel project". In: *13th Conference on the Intersections of Particle and Nuclear Physics*. Oct. 2018. arXiv: 1810.01394 [physics.ins-det].

[51] Marco Valente. *The ATLAS Trigger and Data Acquisition Upgrades for the High Luminosity LHC (HL-LHC)*. Tech. rep. Geneva: CERN, 2019. URL: https://cds.cern.ch/record/2692161.

[52] ATLAS Collaboration. "Performance of the ATLAS track reconstruction algorithms in dense environments in LHC Run 2". In: *Eur. Phys. J. C* 77 (2017), p. 673. DOI: 10.1140/epjc/s10052-017-5225-7. arXiv: 1704.07983 [hep-ex].

[53] ATLAS Collaboration. "Electron reconstruction and identification in the ATLAS experiment using the 2015 and 2016 LHC proton–proton collision data at $\sqrt{s} = 13$ TeV". In: *Eur. Phys. J. C* 79 (2019), p. 639. DOI: 10.1140/epjc/s10052-019-7140-6. arXiv: 1902.04655 [hep-ex].

[54] R. Fruhwirth. "Application of Kalman filtering to track and vertex fitting". In: *Nuclear Instruments and Methods in Physics Research Section A: Accelerators, Spectrometers, Detectors and Associated Equipment* 262.2 (1987), pp. 444 –450. ISSN: 0168-9002. DOI: https://doi.org/10.1016/0168-9002(87)90887-4. URL: http://www.sciencedirect.com/science/article/pii/0168900287908874.

[55] ATLAS Collaboration. "Reconstruction of primary vertices at the ATLAS experiment in Run 1 proton–proton collisions at the LHC". In: *Eur. Phys. J. C* 77 (2017), p. 332. DOI: 10.1140/epjc/s10052-017-4887-5. arXiv: 1611.10235 [hep-ex].

[56] ATLAS Collaboration. "Muon reconstruction performance of the ATLAS detector in proton–proton collision data at $\sqrt{s} = 13$ TeV". In: *Eur. Phys. J. C* 76 (2016), p. 292. DOI: 10.1140/epjc/s10052-016-4120-y. arXiv: 1603.05598 [hep-ex].

[57] Matteo Cacciari, Gavin P. Salam, and Gregory Soyez. "The anti-k_t jet clustering algorithm". In: *JHEP* 04 (2008), p. 063. DOI: 10.1088/1126-6708/2008/04/063. arXiv: 0802.1189 [hep-ph].

[58] ATLAS Collaboration. "Topological cell clustering in the ATLAS calorimeters and its performance in LHC Run 1". In: *Eur. Phys. J. C* 77 (2017), p. 490. DOI: 10.1140/epjc/s10052-017-5004-5. arXiv: 1603.02934 [hep-ex].

[59] ATLAS Collaboration. "Jet reconstruction and performance using particle flow with the ATLAS Detector". In: *Eur. Phys. J. C* 77 (2017), p. 466. DOI: 10.1140/epjc/s10052-017-5031-2. arXiv: 1703.10485 [hep-ex].

[60] ATLAS Collaboration. "Jet energy scale measurements and their systematic uncertainties in proton–proton collisions at $\sqrt{s} = 13$ TeV with the ATLAS detector". In: *Phys. Rev. D* 96 (2017), p. 072002. DOI: 10.1103/PhysRevD.96.072002. arXiv: 1703.09665 [hep-ex].

[61] ATLAS Collaboration. *Jet global sequential corrections with the ATLAS detector in proton–proton collisions at $\sqrt{s} = 8$ TeV*. ATLAS-CONF-2015-002. 2015. URL: https://cds.cern.ch/record/2001682.

[62] ATLAS Collaboration. *Data-driven determination of the energy scale and resolution of jets reconstructed in the ATLAS calorimeters using dijet and multijet events at $\sqrt{s} = 8$ TeV*. ATLAS-CONF-2015-017. 2015. URL: https://cds.cern.ch/record/2008678.

[63] ATLAS Collaboration. *Monte Carlo Calibration and Combination of In-situ Measurements of Jet Energy Scale, Jet Energy Resolution and Jet Mass in ATLAS*. ATLAS-CONF-2015-037. 2015. URL: https://cds.cern.ch/record/2044941.

[64] ATLAS Collaboration. *Determination of the jet energy scale and resolution at ATLAS using Z/γ-jet events in data at $\sqrt{s} = 8$ TeV*. ATLAS-CONF-2015-057. 2015. URL: https://cds.cern.ch/record/2059846.

[65] ATLAS Collaboration. "Jet energy scale and resolution measured in proton?proton collisions at $\sqrt{s} = 13$ TeV with the ATLAS detector". In: *Eur. Phys. J. C* 81 (2020). 73 pages in total, author list starting page 57, 31 figures, 2 tables, submitted to Eur. Phys. J. C. All figures including auxiliary figures are available at http://atlas.web.cern.ch/Atlas/GROUPS/PHYS 2018-05, 689. 73 p. DOI: 10.1140/epjc/s10052-021-09402-3. arXiv: 2007.02645. URL: https://cds.cern.ch/record/2722869.

[66] ATLAS Collaboration. "Measurements of b-jet tagging efficiency with the ATLAS detector using $t\bar{t}$ events at $\sqrt{s} = 13$ TeV". In: *JHEP* 08 (2018), p. 089. DOI: 10.1007/JHEP08(2018)089. arXiv: 1805.01845 [hep-ex].

[67] Andreas Hoecker et al. *TMVA - Toolkit for Multivariate Data Analysis*. 2007. arXiv: physics/0703039 [physics.data-an].

[68] ATLAS Collaboration. *Calibration of light-flavour b-jet mistagging rates using ATLAS proton–proton collision data at $\sqrt{s} = 13$ TeV*. ATLAS-CONF-2018-006. 2018. URL: https://cds.cern.ch/record/2314418.

[69] ATLAS Collaboration. "Optimisation of large-radius jet reconstruction for the ATLAS detector in 13 TeV proton–proton collisions". In: (2020). arXiv: 2009.04986 [hep-ex].

[70] ATLAS Collaboration. "In situ calibration of large-radius jet energy and mass in 13 TeV proton–proton collisions with the ATLAS detector". In: *Eur. Phys. J. C* 79 (2019), p. 135. DOI: 10.1140/epjc/s10052-019-6632-8. arXiv: 1807.09477 [hep-ex].

[71] ATLAS Collaboration. "Identification and rejection of pile-up jets at high pseudorapidity with the ATLAS detector". In: *Eur. Phys. J. C* 77 (2017), p. 580. DOI: 10.1140/epjc/s10052-017-5081-5. arXiv: 1705.02211 [hep-ex].

[72] Torbjörn Sjöstrand et al. "An Introduction to PYTHIA 8.2". In: *Comput. Phys. Commun.* 191 (2015), p. 159. DOI: 10.1016/j.cpc.2015.01.024. arXiv: 1410.3012 [hep-ph].

[73] ATLAS Collaboration. *The Pythia 8 A3 tune description of ATLAS minimum bias and inelastic measurements incorporating the Donnachie–Landshoff diffractive model*. ATL-PHYS-PUB-2016-017. 2016. URL: https://cds.cern.ch/record/2206965.

[74] Richard D. Ball et al. "Parton distributions with LHC data". In: *Nucl. Phys. B* 867 (2013), p. 244. DOI: 10.1016/j.nuclphysb.2012.10.003. arXiv: 1207.1303 [hep-ph].

[75] Simone Alioli et al. "NLO vector-boson production matched with shower in POWHEG". In: *JHEP* 07 (2008), p. 060. DOI: 10.1088/1126-6708/2008/07/060. arXiv: 0805.4802 [hep-ph].

[76] ATLAS Collaboration. *Example ATLAS tunes of* PYTHIA8, PYTHIA6 *and* POWHEG *to an observable sensitive to Z boson transverse momentum*. ATL-PHYS-PUB-2013-017. 2013. URL: https://cds.cern.ch/record/1629317.

[77] J. Pumplin et al. "New generation of parton distributions with uncertainties from global QCD analysis". In: *JHEP* 07 (2002), p. 012. arXiv: hep-ph/0201195.

[78] S. Agostinelli et al. "GEANT4: A Simulation toolkit". In: *Nucl. Instrum. Meth. A* 506 (2003), p. 250. DOI: 10.1016/S0168-9002(03)01368-8.

[79] Matteo Cacciari, Gavin P. Salam, and Gregory Soyez. "FastJet User Manual". In: *Eur. Phys. J. C* 72 (2012), p. 1896. DOI: 10.1140/epjc/s10052-012-1896-2. arXiv: 1111.6097 [hep-ph].

[80] Louis Portales. "Observation of electroweak $WZjj$ production, and studies on pile-up mitigation with the ATLAS detector. Observation de la production $WZjj$ ctrofaible, et des sur la suppression des jets d?empilement avec le dcteur ATLAS". Presented 01 Oct 2020. 2020. URL: https://cds.cern.ch/record/2743491.

[81] Simone Alioli et al. "A general framework for implementing NLO calculations in shower Monte Carlo programs: the POWHEG BOX". In: *JHEP* 06 (2010), p. 043. DOI: 10.1007/JHEP06(2010)043. arXiv: 1002.2581 [hep-ph].

[82] Richard D. Ball et al. "Parton distributions for the LHC Run II". In: *JHEP* 04 (2015), p. 040. DOI: 10.1007/JHEP04(2015)040. arXiv: 1410.8849 [hep-ph].

[83] ATLAS Collaboration. "Electron reconstruction and identification in the ATLAS experiment using the 2015 and 2016 LHC proton–proton collision data at $\sqrt{s} = 13$ TeV". In: *Eur. Phys. J. C* 79 (2019), p. 639. DOI: 10.1140/epjc/s10052-019-7140-6. arXiv: 1902.04655 [hep-ex].

[84] ATLAS Collaboration. *Boosted hadronic vector boson and top quark tagging with ATLAS using Run 2 data*. ATL-PHYS-PUB-2020-017. 2020. URL: https://cds.cern.ch/record/2724149.

[85] Tianqi Chen and Carlos Guestrin. "XGBoost". In: *Proceedings of the 22nd ACM SIGKDD International Conference on Knowledge Discovery and Data Mining* (2016). DOI: 10.1145/2939672.2939785. URL: http://dx.doi.org/10.1145/2939672.2939785.

[86] Sebastian Raschka. *Model Evaluation, Model Selection, and Algorithm Selection in Machine Learning*. 2020. arXiv: 1811.12808 [cs.LG].

[87] *Formulae for Estimating Significance*. Tech. rep. All figures including auxiliary figures are available at https://atlas.web.cern.ch/Atlas/GROUPS/PHYSICS/PUBNOTES/ATL-PHYS-PUB-2020-025. Geneva: CERN, 2020. URL: https://cds.cern.ch/record/2736148.

[88] Scott Lundberg and Su-In Lee. "A Unified Approach to Interpreting Model Predictions". In: Dec. 2017.

[89] M Neal Radford. "Computing Likelihood Functions for High-Energy Physics Experiments when Distributions are Defined by Simulators with Nuisance Parameters". In: (2008). DOI: 10.5170/CERN-2008-001.111. URL: https://cds.cern.ch/record/1099977.

[90] *Luminosity determination in pp collisions at $\sqrt{s} = 13$ TeV using the ATLAS detector at the LHC*. Tech. rep. All figures including auxiliary figures are available at https://atlas.web.cern.ch/Atlas/G CONF-2019-021. Geneva: CERN, 2019. URL: https://cds.cern.ch/record/2677054.

[91] Richard D. Ball et al. "Parton distributions from high-precision collider data". In: *The European Physical Journal C* 77.10 (2017). ISSN: 1434-6052. DOI: 10.1140/epjc/s10052-017-5199-5. URL: http://dx.doi.org/10.1140/epjc/s10052-017-5199-5.

[92] Malte Backhaus. "High bandwidth pixel detector modules for the ATLAS Insertable B-Layer". Presented 30 Oct 2014. 2014. URL: https://cds.cern.ch/record/1696901.

[93] Reem Hani M Taibah. "Upgrade of the ATLAS tracking detector in preparation for the High-Luminosity phase of the LHC". Presented 17 Sep 2021. 2021. URL: https://cds.cern.ch/record/2791088.

[94] *Technical Design Report for the ATLAS Inner Tracker Pixel Detector*. Tech. rep. Geneva: CERN, 2017. URL: https://cds.cern.ch/record/2285585.

[95] Maurice Garcia-Sciveres. *The RD53A Integrated Circuit*. Tech. rep. Geneva: CERN, 2017. URL: https://cds.cern.ch/record/2287593.

[96] Natalia Emriskova. "Analog front-end characterization of the RD53A chip". In: *PoS* TWEPP2019 (2020), p. 021. DOI: 10.22323/1.370.0021.

[97] Timon Heim. "YARR - A PCIe based Readout Concept for Current and Future ATLAS Pixel Modules". In: *Journal of Physics: Conference Series* 898 (2017), p. 032053. DOI: 10.1088/1742-6596/898/3/032053. URL: https://doi.org/10.1088/1742-6596/898/3/032053.

[98] Mark Standke. "Characterization of the Joined ATLAS and CMS RD53A Pixel Chip". Presented 28 Feb 2019. 2019. URL: https://cds.cern.ch/record/2717863.

[99] Maria Elena Stramaglia. *Calibration Analysis Software for the ATLAS Pixel Detector*. Tech. rep. Geneva: CERN, 2015. DOI: 10.1016/j.nima.2015.11.120. URL: https://cds.cern.ch/record/2027805.

[100] Duc Bao Ta et al. "Serial powering: Proof of principle demonstration of a scheme for the operation of a large pixel detector at the LHC". In: *Nucl. Instrum. Meth. A* 557 (2006), pp. 445–459. DOI: 10.1016/j.nima.2005.11.115.

[101] L. Gonella et al. "A serial powering scheme for the ATLAS pixel detector at sLHC". In: *JINST* 5 (2010), p. C12002. DOI: 10.1088/1748-0221/5/12/C12002.

[102] T. Stockmanns et al. "Serial powering of pixel modules". In: *Nucl. Instrum. Meth. A* 511 (2003). Ed. by S. L. Olsen and D. Bortoletto, pp. 174–179. DOI: 10.1016/S0168-9002(03)01787-X.

[103] Michael Karagounis et al. "An integrated Shunt-LDO regulator for serial powered systems". In: *2009 Proceedings of ESSCIRC*. 2009, pp. 276–279. DOI: 10.1109/ESSCIRC.2009.5325974.

[104] Vasilije Perovic. "Serial powering in four-chip prototype RD53A modules for Phase 2 upgrade of the CMS pixel detector". In: *Nuclear Instruments and Methods in Physics Research Section A: Accelerators, Spectrometers, Detectors and Associated Equipment* 978 (2020), p. 164436. ISSN: 0168-9002. DOI: https://doi.org/10.1016/j.nima.2020.164436. URL: https://www.sciencedirect.com/science/article/pii/S0168900220308330.

[105] M. Daas et al. "BDAQ53, a versatile pixel detector readout and test system for the ATLAS and CMS HL-LHC upgrades". In: *Nuclear Instruments and Methods in Physics Research Section A: Accelerators, Spectrometers, Detectors and Associated Equipment* 986 (2021), p. 164721. ISSN: 0168-9002. DOI: 10.1016/j.nima.2020.164721. URL: http://dx.doi.org/10.1016/j.nima.2020.164721.

[106] Alvaro Pradas Luengo et al. "System level serial powering studies of RD53A chip". In: *PoS* TWEPP2018 (2019), 147. 5 p. DOI: 10.22323/1.343.0147. URL: https://cds.cern.ch/record/2710222.